Scuola Internazionale Superiore di Studi Avanzati
Area of Physics
Ph.D. in Theoretical Particle Physics

Discrete Symmetry Approach to Lepton Flavour, Neutrino Mixing and Leptonic CP Violation, and Neutrino Related Physics Beyond the Standard Theory

Candidate:
Ivan Girardi

Supervisor:
Prof. S. T. Petcov

Thesis submitted in partial fulfillment of the requirements
for the degree of Doctor Philosophiae
Academic Year 2015/2016

Abstract

The experimental evidences of neutrino oscillation, caused by non-zero neutrino masses and neutrino mixing, which were obtained in the experiments with solar, atmospheric, accelerator and reactor neutrinos, opened new field of research in elementary particle physics. The principal goal is to understand at fundamental level the mechanism giving rise to non-zero neutrino masses and neutrino mixing. The open fundamental questions include those of the nature — Dirac or Majorana — of massive neutrinos, of the type of spectrum neutrino masses obey, of the status of CP symmetry in the lepton sector, of the absolute scale of neutrino masses, and more generally, of understanding the origin of flavour in particle physics. The smallness of neutrino masses suggests that their values are related to the existence of a new fundamental mass (energy scale) in particle physics, i.e., to New Physics beyond that predicted by the Standard Theory. The New Physics can manifest itself in the Majorana nature of massive neutrinos, in the existence of sterile neutrinos with masses at the eV scale, in the existence of new non-standard interactions (NSI) of neutrinos, etc. The present Ph.D. thesis explores aspects of this neutrino-related New Physics. More specifically, we first employ the discrete flavour symmetry approach i) to construct a self-consistent theory of lepton flavour, ii) to understand the pattern of neutrino mixing and to describe it quantitatively, and iii) to derive predictions for leptonic Dirac CP violation. Next we investigate the effects of existence of sterile neutrinos with a Majorana mass at the eV scale on the predictions for the neutrinoless double beta decay effective Majorana mass. Further we present a possible interpretation of the results of the reactor neutrino and accelerator experiments (Daya Bay, RENO, Double Chooz and T2K) on the reactor angle θ_{13} in the neutrino mixing matrix in terms of non-standard interactions (NSI) of neutrinos. We also analyse the signatures of sterile neutrinos in reactor antineutrino experiments and, in particular, constrain the active-sterile mixing angle using the high-precision data of the Daya Bay reactor experiment. We finally investigate the impact of sterile neutrinos on precision measurements of the standard neutrino oscillation parameters in the upcoming neutrino experiment JUNO.

Contents

Preface

The present Ph.D. thesis is based on the following papers, listed in chronological order as they appear on Inspires [1]:

- I. Girardi, A. Meroni and S. T. Petcov,
  "Neutrinoless Double Beta Decay in the Presence of Light Sterile Neutrinos,"
  JHEP **1311** (2013) 146 [arXiv:1308.5802];

- I. Girardi, A. Meroni, S. T. Petcov and M. Spinrath,
  "Generalised geometrical CP violation in a T' lepton flavour model,"
  JHEP **1402** (2014) 050 [arXiv:1312.1966];

- I. Girardi, D. Meloni and S. T. Petcov,
  "The Daya Bay and T2K results on $\sin^2 2\theta_{13}$ and Non-Standard Neutrino Interactions,"
  Nucl. Phys. B **886** (2014) 31 [arXiv:1405.0416];

- I. Girardi, D. Meloni, T. Ohlsson, H. Zhang and S. Zhou,
  "Constraining Sterile Neutrinos Using Reactor Neutrino Experiments,"
  JHEP **1408** (2014) 057 [arXiv:1405.6540];

- I. Girardi, S. T. Petcov and A. V. Titov,
  "Determining the Dirac CP Violation Phase in the Neutrino Mixing Matrix from Sum Rules,"
  Nucl. Phys. B **894** (2015) 733 [arXiv:1410.8056].

The research activity carried out during the Ph.D. studies has also led to the following articles and contributions to conference proceedings, the content of which, however, will be not discussed in this thesis:

- I. Girardi and D. Meloni,
  "Constraining new physics scenarios in neutrino oscillations from Daya Bay data,"
  Phys. Rev. D **90** (2014) 7, 073011 [arXiv:1403.5507];

[1] https://inspirehep.net.

- A. Di Iura, I. Girardi and D. Meloni,
"Probing new physics scenarios in accelerator and reactor neutrino experiments,"
J. Phys. G **42** (2015) 065003 [arXiv:1411.5330];

- I. Girardi, S. T. Petcov and A. V. Titov,
"Predictions for the Leptonic Dirac CP Violation Phase: a Systematic Phenomenological Analysis,"
Eur. Phys. J. C **75** (2015) 7, 345 [arXiv:1504.00658];

- I. Girardi, S. T. Petcov and A. V. Titov,
"Predictions for the Dirac CP Violation Phase in the Neutrino Mixing Matrix,"
Int. J. Mod. Phys. A **30** (2015) 13, 1530035 [arXiv:1504.02402];

- I. Girardi, S. T. Petcov and A. V. Titov,
"Predictions for the Dirac Phase in the Neutrino Mixing Matrix and Sum Rules,"
J. Phys. Conf. Ser. **631** (2015) 1, 012051;

- I. Girardi, S. T. Petcov, A. J. Stuart and A. V. Titov,
"Leptonic Dirac CP Violation Predictions from Residual Discrete Symmetries,"
Nucl. Phys. B **902** (2016) 1 [arXiv:1509.02502];

- I. Girardi, D. Meloni and S. T. Petcov,
"Non-Standard Neutrino Interactions in T2K and Daya Bay,"
Nucl. Part. Phys. Proc. **265-266** (2015) 212;

- I. Girardi, S. T. Petcov and A. Titov,
"Predicting the Leptonic Dirac CP Violation Phase from Sum Rules,"
PoS EPS-**HEP2015** (2015) 039;

- I. Girardi, S. T. Petcov and A. V. Titov,
"Predictions for the Majorana CP Violation Phases in the Neutrino Mixing Matrix and Neutrinoless Double Beta Decay,"
Nucl. Phys. B **911** (2016) 754 [arXiv:1605.04172];

- I. Girardi, S. T. Petcov and A. V. Titov,
"The leptonic Dirac CP-violating phase from sum rules,"
J. Phys. Conf. Ser. **718** (2016) no.6, 062060.

CHAPTER 1

Introduction

1.1 Motivations

There have been remarkable discoveries in neutrino physics in the last 18 years, marked by the 2015 Nobel prize for Physics to Dr. T. Kajita and Prof. A. McDonald for the discovery of neutrino oscillations — transitions in flight between different types ("flavours") of neutrinos, induced by nonzero neutrino masses and non-trivial neutrino mixing. An impressive number of experiments has not only provided compelling evidence for neutrino oscillations, but neutrino mass and mixing parameters, responsible for the oscillations, have also been measured with a relatively high precision (see, e.g., [1]). In spite of this remarkable progress, one has to admit that at present we are still completely ignorant about the fundamental aspects of neutrino mixing. We have no information about the nature — Dirac or Majorana — of massive neutrinos. We do not know what kind of spectrum — with normal or inverted ordering — the neutrino masses obey. The absolute neutrino mass scale is still unknown; it follows from the current data only that the neutrino masses should be smaller than roughly 1 eV. And at present we have no information about the status of the CP symmetry in the lepton sector. Is the observed pattern of neutrino mixing related to the existence of a new fundamental symmetry of particle interactions? Is there any relation between neutrino mixing and quark mixing? Is the CP symmetry violated by the neutrino mixing? What is the mechanism at the origin of non-zero neutrino masses and mixing? What is the role of neutrinos in the unification of forces and in the mechanism which generates the observed baryon asymmetry in the Universe?

The enormous disparity between the neutrino masses and the masses of the charged leptons and quarks suggests that the existence of nonzero neutrino masses is related to a new fundamental mass scale in Particle Physics, i.e., a New Physics beyond that predicted by the Standard Theory of particle interactions. This hypothetical neutrino-related New Physics can manifest itself, in particular, i) in the Majorana nature of massive neutrinos, and/or ii) in the existence of more than three neutrinos with masses at the eV scale or heavier scales, and/or iii) in the existence of new non-standard neutrino interactions (NSI),

iv) in the existence of new particles (heavy Majorana neutrinos, doubly charged Higgs scalar, etc.) at the TeV scale, etc.

The present Ph.D. thesis is devoted to the problem of understanding at fundamental level the mechanism giving rise to neutrino masses and mixing and to the non-conservation of the individual, and possibly of the total lepton charges. This includes, in particular, understanding the origin of the patterns of neutrino mixing and masses suggested by the data. Different types of symmetries (discrete, combination of discrete and GUT symmetries, etc.) have been employed to try to understand the pattern of neutrino mixing, and the phenomenological consequences in each case have been investigated. We have analysed the possibility that the observed patterns of neutrino mixing and of neutrino mass squared differences, measured in neutrino oscillation experiments, are related to the existence of a new fundamental discrete flavour symmetry in the lepton sector of particle interactions. More specifically, we have constructed a self-consistent model with T' lepton flavor symmetry, which allows to describe quantitatively the neutrino mixing and predicts i) the value of the absolute neutrino mass scale, ii) maximal Dirac CP violation in the lepton sector, and iii) the values of the Majorana phases in the neutrino mixing matrix.

Performing these studies we have found that in a large class of theories of neutrino masses and lepton mixing, based on the idea of existence of (approximate) discrete flavour symmetry in the lepton sector, the value of the Dirac CP violation phase in the Pontecorvo, Maki, Nakagawa and Sakata (PMNS) neutrino mixing matrix U is related to (determined by) the values of the lepton mixing angles. It follows from these studies, in particular, that the measurement of the Dirac phase in the PMNS mixing matrix, together with an improvement of the precision on the lepton mixing angles, can provide unique information about the possible existence of new fundamental symmetry in the lepton sector of particle interactions. This conclusion reinforces the importance of the experiments searching for CP violation in neutrino oscillations, as well as of the experiments aiming at improving further the precision of measurements of the lepton mixing angles.

As we have already noticed, the smallness of the neutrino masses suggests the existence of a new fundamental mass scale in Particle Physics, i.e., a New Physics beyond that predicted by the Standard Theory of particle interactions. And as we have indicated, this hypothetical neutrino-related New Physics can manifest itself, in particular, i) in the Majorana nature of massive neutrinos, and/or ii) in the existence of more than three neutrinos with masses at the eV scale, and/or iii) in the existence of new non-standard neutrino interactions (NSI), etc.

We have investigated various physics aspects of these three possible manifestations of the neutrino related New Physics. More specifically, we have studied in detail the effects of the existence of one or two additional massive neutrinos with masses at the eV scale on the predictions for the effective Majorana mass in neutrinoless double beta decay — the only experimentally feasible process, the studies of which have the potential of establishing that the massive neutrinos are Majorana particles. We have also investigated the effects of the existence of new neutrino interactions on the interpretation of the recent intriguing results of the long baseline T2K experiment with accelerator neutrinos, which, when combined with the results of the Daya Bay reactor antineutrino experiment, lead to an indication

that the Dirac CP violation phase in the PMNS neutrino mixing matrix has a value close to 270 degrees. We have shown, in particular, that these data could be interpreted as an indication for existence of NSI (new non-standard neutrino interactions). Future experiments searching for CP violation and/or NSI effects in neutrino oscillations will certainly provide a critical test of the possible NSI effects discussed in our studies. We have also investigated the signatures of sterile neutrinos in reactor antineutrino experiments, in particular, constraining the active-sterile mixing angle using the high-precision data of the Daya Bay reactor experiment. And we have analysed the impact of sterile neutrinos on precision measurements of the standard neutrino oscillation parameters and the neutrino mass hierarchy.

1.2 Three neutrino mixing

All compelling data on neutrino masses, mixing and oscillations are compatible with the existence of mixing of three light neutrinos ν_i, $i = 1, 2, 3$, with masses $m_i \lesssim 1$ eV, in the weak charged lepton current (see, e.g., [1]). In the widely used standard parametrisation [1], U is expressed in terms of the solar, atmospheric and reactor neutrino mixing angles θ_{12}, θ_{23} and θ_{13}, respectively, and one Dirac — δ, and two Majorana [2] — β_1 and β_2, CP violation phases:

$$U = V(\theta_{12}, \theta_{23}, \theta_{13}, \delta)\, Q(\beta_1, \beta_2)\,, \tag{1.2.1}$$

where

$$V = \begin{pmatrix} 1 & 0 & 0 \\ 0 & c_{23} & s_{23} \\ 0 & -s_{23} & c_{23} \end{pmatrix} \begin{pmatrix} c_{13} & 0 & s_{13}e^{-\mathrm{i}\,\delta} \\ 0 & 1 & 0 \\ -s_{13}e^{\mathrm{i}\,\delta} & 0 & c_{13} \end{pmatrix} \begin{pmatrix} c_{12} & s_{12} & 0 \\ -s_{12} & c_{12} & 0 \\ 0 & 0 & 1 \end{pmatrix}\,, \tag{1.2.2}$$

or equivalently

$$V = \begin{pmatrix} c_{12}c_{13} & s_{12}c_{13} & s_{13}e^{-i\delta} \\ -s_{12}c_{23} - c_{12}s_{23}s_{13}e^{i\delta} & c_{12}c_{23} - s_{12}s_{23}s_{13}e^{i\delta} & s_{23}c_{13} \\ s_{12}s_{23} - c_{12}c_{23}s_{13}e^{i\delta} & -c_{12}s_{23} - s_{12}c_{23}s_{13}e^{i\delta} & c_{23}c_{13} \end{pmatrix}\,, \tag{1.2.3}$$

and we have used the standard notation $c_{ij} \equiv \cos\theta_{ij}$, $s_{ij} \equiv \sin\theta_{ij}$, $0 \leq \theta_{ij} \leq \pi/2$, $0 \leq \delta \leq 2\pi$. The matrix Q contains the two physical Majorana CP violation (CPV) phases:

$$Q = \mathrm{Diag}(\mathrm{e}^{-\mathrm{i}\,\beta_1/2}, \mathrm{e}^{-\mathrm{i}\,\beta_2/2}, 1)\,. \tag{1.2.4}$$

The parametrization of the phase matrix Q in Eq. (1.2.4) differs from the standard one [1] $Q = \mathrm{Diag}(1, \mathrm{e}^{\mathrm{i}\,\alpha_{21}/2}, \mathrm{e}^{\mathrm{i}\,\alpha_{31}/2})$, where

$$U = VQ\,, \quad Q = \mathrm{diag}\left(1, e^{i\frac{\alpha_{21}}{2}}, e^{i\frac{\alpha_{31}}{2}}\right)\,. \tag{1.2.5}$$

Obviously, one has $\alpha_{21} = (\beta_1 - \beta_2)$ and $\alpha_{31} = \beta_1$. In the case of the seesaw mechanism of neutrino mass generation the Majorana phases β_1 and β_2 (or α_{21} and α_{31}) vary in the

interval [3] $0 \leq \beta_{1,2} \leq 4\pi$ [1]. If CP invariance holds, we have $\delta = 0, \pi, 2\pi$, and [5] $\beta_{1(2)} = k^{(\prime)}\,\pi$, $k^{(\prime)} = 0, 1, 2, 3, 4$.

The data on neutrino oscillation allowed to determine the angles θ_{12}, θ_{23} and θ_{13} and the two neutrino mass squared differences Δm^2_{21} and Δm^2_{31} (or Δm^2_{32}), which drive the observed oscillations involving the three active flavour neutrinos and antineutrinos, ν_l and $\bar{\nu}_l$, $l = e, \mu, \tau$, with a relatively high precision [6, 7]. In Table 1.1 we give the values of the 3-flavour neutrino oscillation parameters as determined in the global analysis performed in [6].

As is well known, depending on the sign of $\Delta m^2_{31(2)}$, which cannot be fixed using the presently available neutrino oscillation data, two types of neutrino mass spectrum are possible:
i) spectrum with normal ordering (NO): $m_1 < m_2 < m_3$, $\Delta m^2_{31} > 0$, $\Delta m^2_{21} > 0$, $m_{2(3)} = (m_1^2 + \Delta m^2_{21(31)})^{\frac{1}{2}}$;
ii) spectrum with inverted ordering (IO): $m_3 < m_1 < m_2$, $\Delta m^2_{32} < 0$, $\Delta m^2_{21} > 0$, $m_2 = (m_3^2 + \Delta m^2_{23})^{\frac{1}{2}}$, $m_1 = (m_3^2 + \Delta m^2_{23} - \Delta m^2_{21})^{\frac{1}{2}}$.
Depending on the value of the lightest neutrino mass, $\min(m_j)$, the neutrino mass spectrum can be:
a) Normal Hierarchical (NH): $m_1 \ll m_2 < m_3$, $m_2 \cong (\Delta m^2_{21})^{\frac{1}{2}} \cong 8.68 \times 10^{-3}$ eV, $m_3 \cong (\Delta m^2_{31})^{\frac{1}{2}} \cong 4.97 \times 10^{-2}$ eV; or
b) Inverted Hierarchical (IH): $m_3 \ll m_1 < m_2$, with $m_{1,2} \cong |\Delta m^2_{32}|^{\frac{1}{2}} \cong 4.97 \times 10^{-2}$ eV; or
c) Quasi-Degenerate (QD): $m_1 \cong m_2 \cong m_3 \cong m_0$, $m_j^2 \gg |\Delta m^2_{31(32)}|$, $m_0 \gtrsim 0.10$ eV, $j = 1, 2, 3$.

The current data are compatible with all different types of neutrino mass spectrum listed above.

An inspection of Table 1.1 shows, in particular, that although $\theta_{13} \neq 0$, $\theta_{23} \neq \pi/4$ and $\theta_{12} \neq \pi/4$, the deviations from these values are relatively small, in fact we have $\sin\theta_{13} \cong 0.16 \ll 1$, $\pi/4 - \theta_{23} \cong 0.11$ and $\pi/4 - \theta_{12} \cong 0.20$, where we have used the relevant best fit values in Table 1.1. More recent results from global fit of neutrino oscillation data, which we will use in Chapter 3, are given in ref. [8] (for a similar analysis see also [9]). The best fit values and 3σ allowed ranges of $\sin^2\theta_{12}$, $\sin^2\theta_{23}$ and $\sin^2\theta_{13}$ found in [8] read:

$$(\sin^2\theta_{12})_{\rm BF} = 0.308\,, \qquad 0.259 \leq \sin^2\theta_{12} \leq 0.359\,, \quad (1.2.6)$$

$$(\sin^2\theta_{23})_{\rm BF} = 0.437\ (0.455)\,, \qquad 0.374\ (0.380) \leq \sin^2\theta_{23} \leq 0.626\ (0.641)\,, \quad (1.2.7)$$

$$(\sin^2\theta_{13})_{\rm BF} = 0.0234\ (0.0240)\,, \qquad 0.0176\ (0.0178) \leq \sin^2\theta_{13} \leq 0.0295\ (0.0298)\,, \quad (1.2.8)$$

where the values (values in brackets) correspond to neutrino mass spectrum with normal ordering (inverted ordering), denoted further as NO (IO) spectrum.

The status of CP symmetry in the lepton sector is still unknown. The Dirac phase δ

[1] The interval beyond 2π, $2\pi \leq \beta_{1,2} \leq 4\pi$, is relevant, e.g., in the calculations of the baryon asymmetry within the leptogenesis scenario [3], in the calculation of the neutrinoless double beta decay effective Majorana mass in the TeV scale version of the type I seesaw model of neutrino mass generation [4], etc.

Parameter	best-fit ($\pm 1\sigma$)	3σ
Δm^2_{21} [10^{-5} eV^2]	$7.54^{+0.26}_{-0.22}$	6.99 - 8.18
$\lvert\Delta m^2_{31}\rvert$ (NO) [10^{-3} eV^2]	$2.47^{+0.06}_{-0.10}$	2.19 - 2.62
$\lvert\Delta m^2_{32}\rvert$ (IO) [10^{-3} eV^2]	$2.46^{+0.07}_{-0.11}$	2.17 - 2.61
$\sin^2\theta_{12}$ (NO or IO)	$0.307^{+0.018}_{-0.016}$	0.259 - 0.359
$\sin^2\theta_{23}$ (NO)	$0.386^{+0.024}_{-0.021}$	0.331 - 0.637
(IO)	$0.392^{+0.039}_{-0.022}$	0.335 - 0.663
$\sin^2\theta_{13}$ (NO)	$0.0241^{+0.0025}_{-0.0025}$	0.0169 - 0.0313
(IO)	$0.0244^{+0.0023}_{-0.0025}$	0.0171 - 0.0315

Table 1.1: The best-fit values and 3σ allowed ranges of the 3-flavour neutrino oscillation parameters derived from a global fit of the current neutrino oscillation data (from [6]). The 3σ allowed range for θ_{23} takes into account the statistical octant degeneracy resulting from the analysis. If two values are given, the upper one corresponds to neutrino mass spectrum with normal hierarchy (NO) and the lower one to spectrum with inverted hierarchy (IO) (see text for further details).

in the neutrino mixing matrix can cause CP violating effects in neutrino oscillations, i.e., a difference between the probabilities of $\nu_l \to \nu_{l'}$ and $\bar{\nu}_l \to \bar{\nu}_{l'}$ oscillations in vacuum [10] and [2], $P(\nu_l \to \nu_{l'})$ and $P(\bar{\nu}_l \to \bar{\nu}_{l'})$, $l \neq l' = e, \mu, \tau$. The magnitude of CP violation (CPV) effects is determined, in particular, by the rephasing invariant associated with the Dirac phase present in the neutrino mixing matrix [11]:

$$J_{\rm CP} = {\rm Im}\left\{U^*_{e1}U^*_{\mu 3}U_{e3}U_{\mu 1}\right\} = \frac{1}{8}\sin\delta\sin 2\theta_{13}\sin 2\theta_{23}\sin 2\theta_{12}\cos\theta_{13}\,. \tag{1.2.9}$$

There exist hints from the current data that $\delta \cong 3\pi/2$ (see, e.g., [12]). If this result on δ will be confirmed by future data, we will have $J_{\rm CP} \cong -0.035$, where we used the best fit values of θ_{12}, θ_{23} and θ_{13}. Such a relatively large value of $|J_{\rm CP}|$ will allow to establish Dirac violation of the CP symmetry in the lepton sector at high confidence level in the future planned experiments (DUNE [13, 14], T2HK [15]).

If the neutrinos with definite masses ν_i, $i = 1, 2, 3$, are Majorana particles, the 3-neutrino mixing matrix contains two additional Majorana CPV phases [2]. However, the flavour neutrino oscillation probabilities $P(\nu_l \to \nu_{l'})$ and $P(\bar{\nu}_l \to \bar{\nu}_{l'})$, $l, l' = e, \mu, \tau$, do not depend on the Majorana phases [2, 16]. The Majorana phases can play important role in processes which are characteristic of the Majorana nature of massive neutrinos and in which the total lepton charge changes by two units, $|\Delta L| = 2$. A widely known example of such process is neutrinoless double beta decay [17–20]

$$(A, Z) \to (A, Z+2) + e^- + e^-, \tag{1.2.10}$$

of even-even nuclei ^{48}Ca, ^{76}Ge, ^{82}Se, ^{100}Mn, ^{116}Cd, ^{130}Te, ^{136}Xe, ^{154}Nd. At present this is the only $|\Delta L| = 2$ process, the experimental searches of which have reached sensitivity

that might allow to observe it if it is triggered by the exchange of the light neutrinos ν_j (see, e.g., refs. [19–21]).

Our interest in the CPV phases present in the neutrino mixing matrix is stimulated also by the intriguing possibility that the Dirac phase and/or the Majorana phases in $U_{\rm PMNS}$ can provide the CP violation necessary for the generation of the observed baryon asymmetry of the Universe [22, 23].

Data on the absolute ν mass scale from the tritium β-decay experiments performed at Mainz and Troitsk show that (see, e.g., [24–28]):

$$m(\overline{\nu}_e) \leq [2.1, 2.3] \text{ eV}/c^2 \text{ at } 95\% \text{ confidence level.} \tag{1.2.11}$$

We have $m(\overline{\nu}_e) \cong m_{\{1,2,3\}}$ for the QD spectrum. These limits have been derived analysing the end point of the spectrum of the electrons of the tritium β-decay process. The upcoming ^3H $\beta-$decay experiment KATRIN is planned to have ~ 10 times better sensitivity at 90% confidence level [29].

In what concerns the combined cosmological limits on the mass of neutrinos, they depend on the model and the data used as input in the analysis. The Planck collaboration has derived the following bounds on the sum of neutrino masses [30]:

$$\sum_i m_{\nu_i} \leq 0.23 \text{ eV}/c^2 \text{ at } 95\% \text{ confidence level (Planck+WP+BAO).} \tag{1.2.12}$$

The sensitivity to the sum of neutrino masses of the cosmological data is expected to be improved by one order of magnitude by the EUCLID mission [31, 32].

1.3 Neutrinoless double beta decay

In $(\beta\beta)_{0\nu}$-decay, and within the reference 3-neutrino mixing scheme, two neutrons of the initial nucleus (A, Z) transform by exchanging virtual Majorana neutrinos $\nu_{1,2,3}$ into two protons of the final state nucleus $(A, Z+2)$ and two free electrons. The corresponding $(\beta\beta)_{0\nu}$-decay amplitude has the form (see, e.g., refs. [17, 19]): $A((\beta\beta)_{0\nu}) = G_{\rm F}^2 \langle m \rangle M(A, Z)$, where $G_{\rm F}$ is the Fermi constant, $\langle m \rangle$ is the $(\beta\beta)_{0\nu}$-decay effective Majorana mass and $M(A, Z)$ is the nuclear matrix element (NME) of the process. The $(\beta\beta)_{0\nu}$-decay effective Majorana mass $\langle m \rangle$ contains all the dependence of $A((\beta\beta)_{0\nu})$ on the neutrino mass and mixing parameters. The expression for $|\langle m \rangle|$ (see, e.g., [17–19]), when the $(\beta\beta)_{0\nu}$-decay is induced by the exchange of the three light Majorana neutrinos ν_1, ν_2, ν_3, has the form:

$$\begin{aligned} |\langle m \rangle| &= \left| \sum_{i=1}^{3} m_i U_{ei}^2 \right| \\ &= \left| m_1 \cos^2\theta_{12} \cos^2\theta_{13} + m_2 \sin^2\theta_{12} \cos^2\theta_{13} e^{i\alpha_{21}} + m_3 \sin^2\theta_{13} e^{i(\alpha_{31} - 2\delta)} \right| , \end{aligned} \tag{1.3.1}$$

$m_{1,2,3}$ being the light Majorana neutrino masses. The effective Majorana mass $|\langle m \rangle|$ is a function of the absolute neutrino mass scale (or equivalently of $min(m_j)$), of the type of

spectrum of neutrino masses obey and of the Majorana phase α_{21} and the Majorana-Dirac phase difference $(\alpha_{31} - 2\delta)$.

Using the values of the neutrino oscillation parameters and their 3σ allowed ranges one finds that [21] (see also, e.g., [1,33]) $|\langle m \rangle^{(3\nu)}| \lesssim 0.005$ eV in the case of 3-neutrino mass spectrum of NH type, while if the spectrum is of the IH type one has [33] $0.014 \text{ eV} \lesssim |\langle m \rangle^{(3\nu)}| \lesssim 0.050$ eV.

The current experimental limits on $|\langle m \rangle|$ are in the range of $(0.1 - 0.7)$ eV. Most importantly, a large number of experiments of a new generation aim at sensitivity to $|\langle m \rangle| \sim (0.01 - 0.05)$ eV (for a detailed discussion of the current limits on $|\langle m \rangle|$ and of the currently running and future planned $(\beta\beta)_{0\nu}$-decay experiments and their prospective sensitivities see, e.g., the recent review article [20]).

1.4 Sterile neutrinos at the eV scale

A look at Table 1.1 makes evident that neutrino physics has entered the phase of precision measurements. With the future upcoming data, the focus is now to determine the missing fundamental parameters such as the neutrino mass ordering, the leptonic Dirac CP-violating phase, and the absolute neutrino mass scale. In addition to the standard neutrino parameters, theoretical and phenomenological investigations of beyond-the-Standard-Model scenarios as sub-leading effects have also full attention. Such scenarios include non-standard neutrino interactions, unitarity violation, CPT and Lorentz invariance violation, and models with sterile neutrinos.

Sterile neutrinos, or strictly speaking fermionic SM singlets, are even more elusive than ordinary active neutrinos, since their interaction with matter, if they exist, should be much weaker than the weak interaction of active (flavour) neutrinos. However, sterile neutrinos could mix with active neutrinos and can have a Majorana mass term, which calls for physics beyond the Standard Model.

At present there are a number of hints of existence of light sterile neutrinos with masses at the eV scale. They originate from the re-analyses of the short baseline (SBL) reactor neutrino oscillation data using newly calculated fluxes of reactor $\bar{\nu}_e$, which show a possible "disappearance" of the reactor $\bar{\nu}_e$ ("reactor neutrino anomaly"), from the results of the calibration experiments of the Gallium solar neutrino detectors GALLEX and SAGE ("Gallium anomaly") and from the results of the LSND and MiniBooNE experiments (for a summary of the data and complete list of references see, e.g., [34–41]). The evidences for sterile neutrinos from the different data are typically at the level of up to approximately 3σ, except in the case of the results of the LSND experiment which give much higher C.L.

Significant constraints on the parameters characterising the oscillations involving sterile neutrinos follow from the negative results of the searches for $\nu_\mu \to \nu_e$ and/or $\bar{\nu}_\mu \to \bar{\nu}_e$ oscillations in the KARMEN [42], NOMAD [43] and ICARUS [44] experiments, and from the nonobservation of effects of oscillations into sterile neutrinos in the solar neutrino experiments and in the studies of ν_μ and/or $\bar{\nu}_\mu$ disappearance in the CDHSW [45], MINOS [46] and SuperKamiokande [47] experiments.

Constraints on the number and masses of sterile neutrinos are provided by cosmological data. The recent Planck results, in particular, on the effective number of relativistic degrees of freedom at recombination epoch $N_{\rm eff}$, can be converted into a constraint on the number of (fully thermalised) sterile neutrinos [48] (see also, e.g., [49, 50] and references quoted therein). The result one obtains depends on the model complexity and the input data used in the analysis. Assuming the validity of the Λ CDM (Cold Dark Matter) model and combining the i) Planck and WMAP CMB data, ii) Planck, WMAP and Baryon Acoustic Oscillation (BAO) data, iii) Planck, WMAP, BAO and high multipole CMB data, for the best fit value and 95% C.L. interval of allowed values of $N_{\rm eff}$ it was found [48]: i) 3.08, (2.77 - 4.31), ii) 3.08, (2.83 - 3.99), ii) 3.22, (2.79 - 3.84). The prediction in the case of three light (active) neutrinos reads $N_{\rm eff} = 3.046$. The quoted values are compatible at 2σ with the existence of extra radiation corresponding to one (fully thermalised) sterile neutrino, while the possibility of existence of two (fully thermalised) sterile neutrinos seems to be disfavored by the available cosmological data. In what concerns the combined cosmological limits on the mass and number of sterile neutrinos, they depend again on data used as input in the analysis: in the case of one fully thermalised sterile neutrino, the upper limits at 95% C.L. are typically of approximately 0.5 eV, but is relaxed to 1.4 eV if one includes in the relevant data set the results of measurements of the local galaxy cluster mass distribution [51]. The existence of one sterile neutrino with a mass in the 1 eV range and couplings tuned to explain the anomalies described briefly above would be compatible with the cosmological constraints if the production of sterile neutrinos in the Early Universe is suppressed by some non-standard mechanism (as like as large lepton asymmetry, see, e.g., [52]), so that $N_{\rm eff} < 3.8$ [51].

The bounds on $N_{\rm eff}$ and on the sum of the light neutrino masses will be improved by current or forthcoming observations. For instance, the EUCLID survey [31] is planned to determine the sum of neutrino masses with a 1σ uncertainty of ~ 0.01 eV, combining the EUCLID data with measurements of the CMB anisotropies from the Planck mission. This would lead to strong constrains on extra sterile neutrino states.

Two possible "minimal" phenomenological models (or schemes) with light sterile neutrinos are widely used in order to explain the reactor neutrino and Gallium anomalies, the LSND and MiniBooNE data as well as the results of the negative searches for active-sterile neutrino oscillations: the so-called "3 + 1" and "3 + 2" models, which contain respectively one and two sterile neutrinos (right-handed sterile neutrino fields). The latter are assumed to mix with the 3 active flavour neutrinos (left-handed flavour neutrino fields) (see, e.g., [53, 54]). Thus, the "3 + 1" and "3 + 2" models have altogether 4 and 5 light massive neutrinos ν_j, which in the minimal versions of these models are Majorana particles. The additional neutrinos ν_4 and ν_4, ν_5, should have masses m_4 and m_4, m_5 at the eV scale (see further). It follows from the data that if ν_4 or ν_4, ν_5 exist, they couple to the electron and muon in the weak charged lepton current with couplings U_{ek} and $U_{\mu k}$, $k = 4;\ 4, 5$, which are approximately $|U_{ek}| \sim 0.1$ and $|U_{\mu k}| \sim 0.1$. The hypothesis of existence of light sterile neutrinos with eV scale masses and the indicated charged current couplings to the electron and muon will be tested in a number of experiments with reactor and accelerator neutrinos, and neutrinos from artificial sources, some of which are under preparation and planned to

start taking data already this year (see, e.g., [34] for a detailed list and discussion of the planned experiments).

It was noticed in [55,56] and more recently in [57–59] that the contribution of the additional light Majorana neutrinos ν_4 or $\nu_{4,5}$ to the neutrinoless double beta ($(\beta\beta)_{0\nu}$-) decay amplitude, and thus to the $(\beta\beta)_{0\nu}$-decay effective Majorana mass $|\langle m\rangle|$ (see, e.g., [17–19]), can change drastically the predictions for $|\langle m\rangle|$ obtained in the reference 3-flavour neutrino mixing scheme, $|\langle m\rangle^{(3\nu)}|$. We recall that the predictions for $|\langle m\rangle^{(3\nu)}|$ depend on the type of the neutrino mass spectrum [18,33]. The three light Majorana neutrino exchange predictions for $|\langle m\rangle|$ (see Section 1.3) are significantly modified, e.g., in the 3+1 scheme due to the contribution of ν_4 to $|\langle m\rangle|$ [57]. Now $|\langle m\rangle|$ in the NH case satisfies $|\langle m\rangle| \geq 0.01$ eV and can lie in the interval $(0.01 - 0.05)$ eV, and we can have $|\langle m\rangle| \lesssim 0.005$ eV if the 3-neutrino mass spectrum is of the IH type.

From a theoretical point of view, a lot of novel models have been constructed with the aim of embedding sterile neutrinos in a more fundamental framework. Such possibilities include models of extra dimensions with exponentially suppressed sterile neutrino masses, see for instance Ref. [60,61]. A model with slightly-broken flavor symmetry can generate a neutrino with much smaller mass than the masses of other two, allowed by the symmetry. This mechanism has been proposed in Refs. [62,63] to generate seesaw neutrinos at the keV mass scale, which can play the role of dark matter. While the commonly studied flavor models with non-Abelian discrete symmetries cannot easily produce a non-trivial hierarchy between fermion masses, the Froggatt–Nielsen mechanism is capable of doing it [64]. The latter has been proposed to generate seesaw neutrinos of eV–keV scales in Refs. [57,65]. Extensions or variants of the canonical type-I seesaw mechanism often contain additional mass scales, which can be arranged to generate light sterile neutrinos [57,66].

The important measurement of θ_{13} in 2011 by Daya Bay, RENO, Double Chooz opened the possibility for searching CPV in neutrino oscillation. The Daya Bay experiment first found evidence of non-zero θ_{13} at statistical significance more than 5σ [67]. This very precise measurement and the huge amount of data form reactor antineutrino experiments could also help us to probe new physics as non-standard effects in neutrino oscillations [68–73].

1.5 Thesis structure

This thesis is organized as follows. In Chapter 2 we analyse the interplay of generalised CP transformations and the non-Abelian discrete group T' and use the semi-direct product $G_f = T' \rtimes H_{\rm CP}$, as family symmetry acting in the lepton sector. The family symmetry is shown to be spontaneously broken in a geometrical manner. In the resulting flavour model, naturally small Majorana neutrino masses for the light active neutrinos are obtained through the type I see-saw mechanism. The known masses of the charged leptons, lepton mixing angles and the two neutrino mass squared differences are reproduced by the model with a good accuracy. The model allows for two neutrino mass spectra with normal ordering (NO) and one with inverted ordering (IO). For each of the three spectra the absolute scale of neutrino masses is predicted with relatively small uncertainty. The value of the Dirac CP

violation (CPV) phase δ in the lepton mixing matrix is predicted to be $\delta \cong \pi/2$ or $3\pi/2$. Thus, the CP violating effects in neutrino oscillations are predicted to be maximal (given the values of the neutrino mixing angles) and experimentally observable. We present also predictions for the sum of the neutrino masses, for the Majorana CPV phases and for the effective Majorana mass in neutrinoless double beta decay. The predictions of the model can be tested in a variety of ongoing and future planned neutrino experiments.

In Chapter 3 we will be concerned with the predictions for the Dirac phase δ in the PMNS matrix. More specifically, we will be interested in the predictions for the Dirac CPV phase δ which are based on the so-called "sum rules" for $\cos\delta$ [74, 75]. The sum rules of interest appear in an approach aiming at quantitative understanding of the pattern of neutrino mixing on the basis of symmetry considerations (see, e.g., [76–78]). In this approach one exploits the fact that, up to perturbative corrections, the PMNS matrix has an approximate form, U_ν, which can be dictated by symmetries. The matrix U_ν is assumed to originate from the diagonalisation of the neutrino Majorana mass term. The angles in U_ν have specific symmetry values which differ, in general, from the experimentally determined values of the PMNS angles θ_{12}, θ_{13} and θ_{23}, and thus need to be corrected. The requisite perturbative corrections, which modify the values of the angles in U_ν to coincide with the measured values of θ_{12}, θ_{13} and θ_{23}, are provided by the matrix U_e arising from the diagonalisation of the charged lepton mass matrix, $U = U_e^\dagger U_\nu$. In the sum rules derived in [75] we will analyse in detail the Dirac phase δ, more precisely, $\cos\delta$, is expressed, in general, in terms of the mixing angles θ_{12}, θ_{13} and θ_{23} of the PMNS matrix U and the angles present in U_ν, whose values are fixed, being dictated by an underlying approximate discrete symmetry of the lepton sector (see, e.g., [76–78]).

In Chapter 4 we show that the relatively large best fit value of $\sin^2 2\theta_{13} = 0.14\,(0.17)$ recently measured in the T2K experiment for fixed values of i) the Dirac CP violation phase $\delta = 0$, and ii) the atmospheric neutrino mixing parameters $\theta_{23} = \pi/4$, $|\Delta m^2_{32}| = 2.4 \times 10^{-3}$ eV^2, can be reconciled with the Daya Bay result $\sin^2 2\theta_{13} = 0.090 \pm 0.009$ if the effects of non-standard neutrino interactions (NSI) in the relevant $\bar{\nu}_e \to \bar{\nu}_e$ and $\nu_\mu \to \nu_e$ oscillation probabilities are taken into account.

In Chapter 5 we investigate the predictions of neutrinoless double beta ($(\beta\beta)_{0\nu}$-) decay effective Majorana mass $|\langle m \rangle|$ in the $3+1$ and $3+2$ schemes with one and two additional sterile neutrinos with masses at the eV scale. The two schemes are suggested by the neutrino oscillation interpretation of the reactor neutrino and Gallium "anomalies" and of the data of the LSND and MiniBooNE experiments. We analyse in detail the possibility of a complete or partial cancellation between the different terms in $|\langle m \rangle|$, leading to a strong suppression of $|\langle m \rangle|$. We determine the regions of the relevant parameter spaces where such a suppression can occure. This allows us to derive the conditions under which the effective Majorana mass satisfies $|\langle m \rangle| > 0.01$ eV, which is the range planned to be exploited by the next generation of $(\beta\beta)_{0\nu}$-experiments.

In Chapter 6, we will use the existing data of the Daya Bay experiment as well as the sensitivity of the future JUNO experiment to put constraints on sterile neutrinos using scenarios with 3+1 neutrinos [79–81]. We will show that the high-precision data of the Daya Bay experiment constrain the 3+1 neutrino scenario imposing upper bounds on the

relevant active-sterile mixing angle $\sin^2 2\theta_{14} \lesssim 0.06$ at 3σ confidence level for the mass-squared difference Δm^2_{41} in the range $(10^{-3}, 10^{-1})\,\mathrm{eV}^2$. The latter bound can be improved by six years of running of the JUNO experiment, $\sin^2 2\theta_{14} \lesssim 0.016$, although in the smaller mass range $\Delta m^2_{41} \in (10^{-4}, 10^{-3})\,\mathrm{eV}^2$. We will also investigate the impact of sterile neutrinos on precision measurements of the standard neutrino oscillation parameters θ_{13} and Δm^2_{31} (at Daya Bay and JUNO), θ_{12} and Δm^2_{21} (at JUNO), and most importantly, the neutrino mass hierarchy (at JUNO).

Chapter 7 contains an Outlook.

CHAPTER 2

Generalised Geometrical CP Violation

2.1 Introduction

Understanding the origin of the patterns of neutrino masses and mixing, emerging from the neutrino oscillation, ^3H $\beta-$decay, cosmological, etc. data is one of the most challenging problems in neutrino physics. It is part of the more general fundamental problem in particle physics of understanding the origins of flavour, i.e., of the patterns of the quark, charged lepton and neutrino masses and of the quark and lepton mixing.

The value of θ_{13} and the magnitude of deviations of θ_{23} and θ_{12} from $\pi/4$ (see Table 1.1 and text below) suggest that the observed values of θ_{13}, θ_{23} and θ_{12} might originate from certain "symmetry" values which undergo relatively small (perturbative) corrections as a result of the corresponding symmetry breaking. This idea was and continues to be widely explored in attempts to understand the pattern of mixing in the lepton sector (see, e.g., [82–91]) and [74,75]. Given the fact that the PMNS matrix is a product of two unitary matrices,

$$U = U_e^\dagger \, U_\nu \,, \tag{2.1.1}$$

where U_e and U_ν result respectively from the diagonalisation of the charged lepton and neutrino mass matrices, it is usually assumed that U_ν has a specific form dictated by a symmetry which fixes the values of the three mixing angles in U_ν that would differ, in general, by perturbative corrections from those measured in the PMNS matrix, while U_e (and symmetry breaking effects that we assume to be subleading) provide the requisite corrections. A variety of potential "symmetry" forms of U_ν, have been explored in the literature on the subject (see, e.g., [92]). Many of the phenomenologically acceptable "symmetry" forms of U_ν, as the tribimaximal (TBM) [93] and bimaximal (BM) [94, 95] mixing, can be obtained using discrete flavour symmetries (see, e.g., the reviews [76,78,96] and the references quoted there in). Discrete symmetries combined with GUT symmetries have been used also in attempts to construct realistic unified models of flavour (see, e.g., [76, 78]).

Here we will exploit the approximate flavour symmetry based on the group T', which is

the double covering of the better known group A_4 (see, e.g., [96]), with the aim to explain the observed pattern of lepton (neutrino) mixing and to obtain predictions for the CP violating phases in the PMNS matrix and possibly for the absolute neutrino mass scale and the type of the neutrino mass spectrum [98]. Flavour models based on the discrete symmetry T' have been proposed by a number of authors [97, 99–101] before the angle θ_{13} was determined with a high precision in the Day Bay [67] and RENO [102] experiments (see also [103–105]). All these models predicted values of θ_{13} which turned out to be much smaller than the experimentally determined value.

In [99–101], in particular, an attempt was made to construct a realistic unified supersymmetric model of flavour, based on the group $SU(5) \times T'$, which describes the quark masses, the quark mixing and CP violation in the quark sector, the charged lepton masses and the known mixing angles in the lepton sector, and predicts the angle θ_{13} and possibly the neutrino masses and the type of the neutrino mass spectrum as well as the values of the CPV phases in the PMNS matrix. The light neutrino masses are generated in the model by the type I seesaw mechanism [106] and are naturally small. It was suggested in [99–101] that the complex Clebsch-Gordan (CG) coefficients of T' [107] might be a source of CP violation and hence that the CP symmetry might be broken geometrically [108] in models with approximate T' symmetry. Since the phases of the CG coefficients of T' are fixed, this leads to specific predictions for the CPV phases in the quark and lepton mixing matrices. Apart from the incorrect prediction for θ_{13}, the authors of [99–101] did not address the problem of vacuum alignment of the flavon vevs, i.e., of demonstrating that the flavon vevs, needed for the correct description of the quark and lepton masses and of the mixing in both the quark and lepton sectors, can be derived from a flavon potential and that the latter does not lead to additional arbitrary flavon vev phases which would destroy the predictivity, e.g., of the leptonic CP violation of the model.

A SUSY $SU(5) \times T'$ model of flavour, which reproduces the correct value of the lepton mixing angle θ_{13} was proposed in [90], where the problem of vacuum alignment of the flavon vevs was also successfully addressed [1]. In [90] it was assumed that the CP violation in the quark and lepton sectors originates from the complexity of the CG coefficients of T'. This was possible by fixing the phases of the flavon vevs using the method of the so-called "discrete vacuum alignment", which was advocated in [109] and used in a variety of other models with discrete flavour symmetries [110]. The value of the angle θ_{13} was generated by charged lepton corrections to the TBM mixing using non-standard GUT relations [88–91, 111].

After the publication of [90] it was realised in [112, 113] that the requirement of CP invariance in the context of theories with discrete flavour symmetries, imposed before the breaking of the discrete symmetry leading to CP nonconservation and generation of the masses of the matter fields of the theory, requires the introduction of the so-called "generalised CP transformations" of the matter fields charged under the discrete symmetry. The

[1] A modified version of the model published in [99–101], which predicts a correct value of the angle θ_{13}, was constructed in [101], but the authors of [101] left open the issue of the vacuum alignment of the flavon vevs.

explicit form of the generalised CP transformations is dictated by the type of the discrete symmetry. It was noticed in [112], in particular, that due to a subtle intimate relation between CP symmetry and certain discrete family symmetries, like the one associated with the group T', it can happen that the CP symmetry does not enforce the Yukawa type couplings, which generate the matter field mass matrices after the symmetry breaking, to be real but to have certain discrete phases predicted by the family symmetry in combination with the generalised CP transformations. In the $SU(5) \times T'$ model proposed in [90], these phases, in principle, can change or modify completely the pattern of CP violation obtained by exploiting the complexity of some of the T' CG coefficients.

In the present chapter we address the problem of the relation between the T' symmetry and the CP symmetry in models of lepton flavour. After some general remarks about the connection between the T' and CP symmetries in Section 2.2, we present in Section 2.3 a fully consistent and explicit model of lepton flavour with a T' family symmetry and geometrical CP violation. We show that the model reproduces correctly the charged lepton masses, all leptonic mixing angles and neutrino mass squared differences and predicts the values of the leptonic CP violating phases and the neutrino mass spectrum. We show also that this model indeed exhibits geometrical CP violation. We clarify how the CP symmetry is broken in the model by using the explicit form of the constructed flavon vacuum alignment sector; without the knowledge of the flavon potential it is impossible to make conclusions about the origin of CP symmetry breaking in flavour models with T' symmetry. In the Appendix we give some technical details about the group T' and present a "UV completion" of the model, which is necessary in order to to select correctly certain T' contractions in the relevant effective operators.

2.2 T' Symmetry and Generalised CP Transformations

In this Section we would like to clarify the role of a generalised CP transformation combined with the non-Abelian discrete symmetry group T'. Let $G_f = T' \rtimes H_{\rm CP}$ be the symmetry group acting in the lepton sector such that both T' and $H_{\rm CP}$ act on the lepton flavour space. Motivated by this study we will present in the next section a model where G_f is broken such that all lepton mixing angles and physical CP phases of the PMNS mixing matrix can be predicted in terms of two mixing angles and two phases. The breaking of G_f will be achieved through non zero vacuum expectation values (vevs) of some scalar fields, the so-called flavons.

2.2.1 The consistency conditions

The discrete non-Abelian family symmetry group T' is the double covering of the tetrahedral group A_4 and its complete description in terms of generators, elements and representations is given in Appendix A.1. An interesting feature of this group is the fact that it is the smallest group that admits 1-, 2-, and 3-dimensional representations and for which

the three representations can be related by the multiplication rule $\mathbf{2} \otimes \mathbf{2} = \mathbf{3} \oplus \mathbf{1}$[2]. T' has seven different irreducible representations: the 1- and 3-dimensional representations $\mathbf{1}$, $\mathbf{1}'$, $\mathbf{1}''$, $\mathbf{3}$ are not faithful, i.e., not injective, while the doublet representations $\mathbf{2}$, $\mathbf{2}'$ and $\mathbf{2}''$ are faithful. One interesting feature of the T' group is related to the tensor products involving the 2-dimensional representation since the CG coefficients are complex.

We define now the transformation of a field $\phi(x)$ under the group T' and $H_{\rm CP}$ respectively as:

$$\phi(x) \to \rho_r(g)\phi(x), \qquad \phi(x) \to X_r \phi^*(x'), \tag{2.2.1}$$

where $\rho_r(g)$ is an irreducible representation r of the group element $g \in T'$, $x' \equiv (x^0, -\vec{x})$ and X_r is the unitary matrix representing the generalised CP transformation. In order to introduce consistently the CP transformation for the family symmetry group T', the matrix X_r should satisfy the consistency conditions [112, 113, 115]:

$$X_r \rho_r^*(g) X_r^{-1} = \rho_r(g')\,, \quad g, g' \in T'\,. \tag{2.2.2}$$

Following the discussion given in [112, 113, 115] it is important to remark that the consistency condition corresponds to a similarity transformation between the representation ρ_r^* and $\rho \circ \mathrm{CP}$. Since the structure of the group is preserved and an element $g \in T'$ is always mapped into an element $g' \in T'$, this map defines an automorphism of the group. In general g and g' might belong to different conjugacy classes: in this case the map defines an outer automorphism [3].

It is worth noticing that the matrices X_r are defined up to an arbitrary global phase. Indeed, without loss of generality, for each matrix X_r, one can define different phases θ_r for different irreducible representations and moreover one can define X_r up to a group transformation (change of basis): in fact the consistency conditions in Eq. (2.2.2) are invariant under $X_r \to \mathrm{e}^{\mathrm{i}\,\theta_r} X_r$ and $X_r \to \rho_r(\tilde{g}) X_r$ with $\tilde{g} \in T'$.

It proves convenient to use the freedom associated with the arbitrary phases θ_r to define the generalised CP transformation for which the vev alignments of the flavon fields can be chosen to be all real. We will show later on that the phases θ_r are not physical and therefore the results we present are independent from the specific values we assume. In the context of the T' group this choice however helps us to extract a real flavon vev structure which is a distinctive feature of some models proposed in the literature where the origin of the physical CP violation arising in the lepton sector is tightly related to the combination of real vevs, complex CGs [4] and eventual phases arising from the requirement of invariance of the superpotential under the generalised CP transformation.

Before going into details of the computations, let us comment that in the analysis presented in [112] related to the group T', the CP transformations are defined as elements of the outer automorphism group and are derived up to inner automorphisms of T' (up

[2] The only other 24-element group that has representation of the same dimensions is the octahedral group O (which is isomorphic to S_4). In this case, however, the product of two doublet reps does not contain a triplet [114].

[3] For details concerning the group of outer and inner automorphisms, $\mathrm{Out}(G)$ and $\mathrm{Inn}(G)$, see [112, 115].

[4] This idea was pioneered in [99].

to conjugacy transformations). In the present work we will consider instead all the possible transformations including the inner automorphism group and we will discuss all the convenient CP transformations which can be used to clarify the role of a generalised CP symmetry in the context of the group T'.

2.2.2 Transformation properties under generalised CP

We give now all the possible equivalent choices of generalised CP transformations for any irreducible representation of T'.

The group T' is defined by the group generators T and S, then from the consistency conditions in Eq. (2.2.2) it is sufficient to require that

$$X_r \rho_r^*(S) X_r^{-1} = \rho_r(\hat{S})\,, \qquad X_r \rho_r^*(T) X_r^{-1} = \rho_r(\hat{T})\,. \tag{2.2.3}$$

It is easy to show that the CP transformation leaves invariant the order of the element of the group g meaning that denoting $n(g)$ the order of g, we have $n(g) = n(g')$. Since the element S has order four and the element T has order three we have $\hat{S} \in 6\,C^4$ and $\hat{T} \in 4'C^3$ [116]. The latter result is derived using the action of CP on the one-dimensional representations, i.e. $\rho_{1,1',1''}(\hat{T}) = \rho^*_{1,1',1''}(T)$ which can be satisfied only if $\hat{T} \in 4'C^3$.

The conjugacy classes $6\,C^4$ and $4'C^3$ contain the group elements

$$\begin{aligned} \hat{S} \in 6\,C^4 &= \left\{S, S^3, TST^2, T^2ST, S^2TST^2, S^2T^2ST\right\}\,, \\ \hat{T} \in 4'C^3 &= \left\{T^2, S^2TST, S^2T^2S, S^3T^2\right\}\,. \end{aligned} \tag{2.2.4}$$

We recall that we have the freedom to choose arbitrary phases θ_r, so for instance in the case of X_1, $X_{1'}$ and $X_{1''}$ we are allowed to write the most general CP transformations for the three inequivalent singlets of T' as

$$\mathbf{1} \to \mathrm{e}^{\mathrm{i}\,\theta_1}\mathbf{1}^*\,, \quad \mathbf{1'} \to \mathrm{e}^{\mathrm{i}\,\theta_{1'}}\mathbf{1'}^*\,, \quad \mathbf{1''} \to \mathrm{e}^{\mathrm{i}\,\theta_{1''}}\mathbf{1''}^*\,. \tag{2.2.5}$$

Differently from the case of the A_4 family symmetry discussed in [115] in which one can show that the generalised CP transformation can be represented as a group transformation, in the case of T' we will show that this is true only for the singlet and the triplet representations. For the doublets the action of the CP transformation cannot be written as an action of a group element (i.e. $\nexists\ g \in T'$ such that $X_r = \rho_r(g)$ for $r = \mathbf{2}, \mathbf{2'}, \mathbf{2''}$).

We give a list of all the possible forms of X_r, which can be in general different for each representation: the CP transformations on the singlets, $X_{\mathbf{1},\mathbf{1'},\mathbf{1''}}$, are complex phases, as mentioned above while the CP transformations on the doublets, $X_{\mathbf{2},\mathbf{2'},\mathbf{2''}}$, and the triplets $X_{\mathbf{3}}$, are given respectively in Table 2.1 and 2.2. We stress that all the possible forms of X_r are defined up to a phase, which can be in general different for each representation. Each CP transformation we found generates a Z_2 symmetry.

The generalised CP transformation $H_{\rm CP}$, acting on the lepton flavour space is given by, see also [112],

$$u : \begin{cases} T \to T^2\,, \\ S \to S^2T^2ST\,. \end{cases} \tag{2.2.6}$$

g, g'	$X_{\mathbf{3}} = \rho_3(g) = \rho_3(g')$	$T \to \hat{T}$	$S \to \hat{S}$
T, S^2T	$\begin{pmatrix} 1 & 0 & 0 \\ 0 & \omega & 0 \\ 0 & 0 & \omega^2 \end{pmatrix}$	T^2	S^3
T^2, S^2T^2	$\begin{pmatrix} 1 & 0 & 0 \\ 0 & \omega^2 & 0 \\ 0 & 0 & \omega \end{pmatrix}$	T^2	S^2TST^2
E, S^2	$\begin{pmatrix} 1 & 0 & 0 \\ 0 & 1 & 0 \\ 0 & 0 & 1 \end{pmatrix}$	T^2	S^2T^2ST
TS, S^2TS	$\begin{pmatrix} -1/3 & 2/3\,\omega & 2/3\,\omega^2 \\ 2/3 & -1/3\,\omega & 2/3\,\omega^2 \\ 2/3 & 2/3\,\omega & -1/3\,\omega^2 \end{pmatrix}$	S^2T^2S	S
TST^2, S^2TST^2	$\begin{pmatrix} -1/3 & 2/3 & 2/3 \\ 2/3 & -1/3 & 2/3 \\ 2/3 & 2/3 & -1/3 \end{pmatrix}$	S^2T^2S	T^2ST
S^2TST, TST	$\begin{pmatrix} -1/3 & 2/3\,\omega^2 & 2/3\,\omega \\ 2/3 & -1/3\,\omega^2 & 2/3\,\omega \\ 2/3 & 2/3\,\omega^2 & -1/3\,\omega \end{pmatrix}$	S^2T^2S	S^2TST^2
ST, S^3T	$\begin{pmatrix} -1/3 & 2/3\,\omega^2 & 2/3\,\omega \\ 2/3\,\omega^2 & -1/3\,\omega & 2/3 \\ 2/3\,\omega & 2/3 & -1/3\,\omega^2 \end{pmatrix}$	S^2TST	S^3
S^3T^2, ST^2	$\begin{pmatrix} -1/3 & 2/3 & 2/3 \\ 2/3\,\omega^2 & -1/3\,\omega^2 & 2/3\,\omega^2 \\ 2/3\,\omega & 2/3\,\omega & -1/3\,\omega \end{pmatrix}$	S^2TST	TST^2
S, S^3	$\begin{pmatrix} -1/3 & 2/3\,\omega & 2/3\,\omega^2 \\ 2/3\,\omega^2 & -1/3 & 2/3\,\omega \\ 2/3\,\omega & 2/3\,\omega^2 & -1/3 \end{pmatrix}$	S^2TST	T^2ST
S^3TS, STS	$\frac{1}{9}\begin{pmatrix} 4\omega^2+4\omega+1 & -2\omega^2-2\omega+4 & -2\omega^2-2\omega+4 \\ -2\omega^2+4\omega-2 & 4\omega^2+\omega+4 & -2\omega^2+4\omega-2 \\ 4\omega^2-2\omega-2 & 4\omega^2-2\omega-2 & \omega^2+4\omega+4 \end{pmatrix}$	S^3T^2	S
S^2T^2S, T^2S	$\begin{pmatrix} -1/3 & 2/3\,\omega & 2/3\,\omega^2 \\ 2/3\,\omega & -1/3\,\omega^2 & 2/3 \\ 2/3\,\omega^2 & 2/3 & -1/3\,\omega \end{pmatrix}$	S^3T^2	TST^2
T^2ST, S^2T^2ST	$\begin{pmatrix} -1/3 & 2/3\,\omega^2 & 2/3\,\omega \\ 2/3\,\omega & -1/3 & 2/3\,\omega^2 \\ 2/3\,\omega^2 & 2/3\,\omega & -1/3 \end{pmatrix}$	S^3T^2	S^2T^2ST

Table 2.1: The generalised CP transformation for the triplet representation of the group T' derived using the consistency conditions. We have defined $\omega = \mathrm{e}^{\mathrm{i}\,2\pi/3}$.

$X_{\mathbf{2}}$, $X_{\mathbf{2}'}$, $X_{\mathbf{2}''}$	$T \to \hat{T}$	$S \to \hat{S}$	$X_{\mathbf{2}}$, $X_{\mathbf{2}'}$, $X_{\mathbf{2}''}$	$T \to \hat{T}$	$S \to \hat{S}$
$\begin{pmatrix} \bar{p}^5 & 0 \\ 0 & p^5 \end{pmatrix}$	T^2	S^3	$\sqrt{\frac{2}{3}}\begin{pmatrix} \bar{p}^5/\sqrt{2} & 1 \\ 1 & \bar{p}^7/\sqrt{2} \end{pmatrix}$	S^2TST	S^3
$\begin{pmatrix} \bar{p} & 0 \\ 0 & p \end{pmatrix}$	T^2	S^2TST^2	$\frac{1}{\sqrt{3}}\begin{pmatrix} p^5 & \sqrt{2}q \\ \sqrt{2}q^5 & \bar{p}^5 \end{pmatrix}$	S^2TST	TST^2
$\begin{pmatrix} e^{\mathrm{i}\,\pi/4} & 0 \\ 0 & \mathrm{e}^{-i\pi/4} \end{pmatrix}$	T^2	S^2T^2ST	$\begin{pmatrix} e^{\mathrm{i}\,\pi/4} & \sqrt{2}q^5 \\ \sqrt{2}q & \mathrm{e}^{-i\pi/4} \end{pmatrix}$	S^2TST	T^2ST
$\begin{pmatrix} p & \sqrt{2}\bar{q}^5 \\ \sqrt{2}\bar{q} & \bar{p} \end{pmatrix}$	S^2T^2S	S	$\frac{1}{\sqrt{3}}\begin{pmatrix} p & \sqrt{2}\bar{q} \\ \sqrt{2}\bar{q}^5 & \bar{p} \end{pmatrix}$	S^3T^2	S
$\frac{1}{\sqrt{3}}\begin{pmatrix} e^{-i\pi/4} & -i\sqrt{2} \\ -i\sqrt{2} & \mathrm{e}^{\mathrm{i}\,\pi/4} \end{pmatrix}$	S^2T^2S	T^2ST	$\frac{1}{\sqrt{3}}\begin{pmatrix} \bar{p} & \sqrt{2} \\ \sqrt{2} & p \end{pmatrix}$	S^3T^2	TST^2
$\sqrt{\frac{2}{3}}\begin{pmatrix} q^4/\sqrt{2} & \bar{p} \\ p^5 & \bar{q}/\sqrt{2} \end{pmatrix}$	S^2T^2S	S^2TST^2	$\sqrt{\frac{2}{3}}\begin{pmatrix} e^{\mathrm{i}\,5\pi/8}/\sqrt{2} & \mathrm{e}^{-i\pi/24} \\ \mathrm{e}^{-i7\pi/24} & \mathrm{e}^{-i7\pi/8}/\sqrt{2} \end{pmatrix}$	S^3T^2	S^2T^2ST

Table 2.2: The generalised CP transformation for the doublet representation of the group T' derived using the consistency conditions. We have defined $\omega = \mathrm{e}^{\mathrm{i}\,2\pi/3}$, $p = \mathrm{e}^{\mathrm{i}\,\pi/12}$, $q = \mathrm{e}^{\mathrm{i}\,\pi/6}$ and note that $\omega\bar{p}^5 = \mathrm{e}^{\mathrm{i}\,\pi/4}$.

This definition of the CP symmetry is particularly convenient because it acts on the 3- and 1- dimensional representations trivially. This particular transformation however is related to any other possible CP transformation by a group transformation.

In other words, different choices of CP are related to each other by inner automorphisms of the group, i.e., the CP transformations listed in Tables 2.1 and 2.2 are related to each other through a conjugation with a group element. For example, another possible CP transformation would be

$$v : \begin{cases} T \to T^2 \,, \\ S \to S^3 \,, \end{cases} \tag{2.2.7}$$

which is related to u via $u = conj(T^2) \circ v$. Indeed

$$\begin{aligned} S &\overset{v}{\mapsto} S^3 \overset{conj(T^2)}{\longmapsto} T^2S^3(T^2)^{-1} = S^2T^2ST \,, \\ T &\overset{v}{\mapsto} T^2 \overset{conj(T^2)}{\longmapsto} T^2T^2(T^2)^{-1} = T^2 \,. \end{aligned} \tag{2.2.8}$$

Without loss of generality we choose as CP transformation the one defined through Eq. (2.2.6) and from Eq. (2.2.1) using the results of Table 2.1 and Table 2.2 we can write the representation of the CP transformation acting on the fields as

$$\begin{aligned} &\mathbf{1} \to \mathrm{e}^{\mathrm{i}\,\theta_1}\mathbf{1}^* \,, \quad \mathbf{1}' \to \mathrm{e}^{\mathrm{i}\,\theta_{1'}}\mathbf{1}'^* \,, \quad \mathbf{1}'' \to \mathrm{e}^{\mathrm{i}\,\theta_{1''}}\mathbf{1}''^* \,, \quad \mathbf{3} \to \mathrm{e}^{\mathrm{i}\,\theta_3}\mathbf{3}^* \,, \\ &\mathbf{2} \to \mathrm{e}^{\mathrm{i}\,\theta_2}\begin{pmatrix} \omega\bar{p}^5 & 0 \\ 0 & \bar{\omega}p^5 \end{pmatrix}\mathbf{2}^* \,, \quad \mathbf{2}' \to \mathrm{e}^{\mathrm{i}\,\theta_{2'}}\begin{pmatrix} \omega\bar{p}^5 & 0 \\ 0 & \bar{\omega}p^5 \end{pmatrix}\mathbf{2}'^* \,, \quad \mathbf{2}'' \to \mathrm{e}^{\mathrm{i}\,\theta_{2''}}\begin{pmatrix} \omega\bar{p}^5 & 0 \\ 0 & \bar{\omega}p^5 \end{pmatrix}\mathbf{2}''^* \,, \end{aligned} \tag{2.2.9}$$

where $\omega = \mathrm{e}^{\mathrm{i}\,2\pi/3}$, $p = \mathrm{e}^{\mathrm{i}\,\pi/12}$ and $\omega\bar{p}^5 = \mathrm{e}^{\mathrm{i}\,\pi/4}$. Notice that we did not specify the values of the phases θ_r. Further we can check that the CP symmetry transformation chosen

generates a Z_2 symmetry group. Indeed it is easy to show that $u^2 = E$, therefore the multiplication table of the group $H_{\rm CP} = \{E, u\}$ is obviously equal to the multiplication table of a Z_2 group, from which we can write $H_{\rm CP} \cong Z_2$.

Since we want to have real flavon vevs – following the setup given in [90] – it turns out to be convenient to select the CP transformations with $\theta_1 = \theta_{1'} = \theta_{1''} = \theta_3 = 0$ and $\theta_{2''} = -\theta_{2'} = \pi/4$ [5]. With this choice the phases of the couplings of renormalisable operators is fixed up to a sign by the CP symmetry. In fact, supposing one has a renormalisable operator of the form $\lambda\mathcal{O} = \lambda(A \times B \times C)$ where λ is the coupling constant and A, B, C represent the fields, then the generalised CP phase of the operator is defined as $\beta \equiv {\rm CP}[\mathcal{O}]/\mathcal{O}^*$. The phase of λ is hence given by the equation $\lambda = \beta\lambda^*$ which is solved by

$$\begin{cases} \arg(\lambda) = \arg(\beta)/2 \;\text{ or }\; \arg(\beta)/2 - \pi & \text{if } \arg(\beta) > 0\,, \\ \arg(\lambda) = \arg(\beta)/2 \;\text{ or }\; \arg(\beta)/2 + \pi & \text{if } \arg(\beta) \leq 0\,. \end{cases} \tag{2.2.10}$$

In Table 2.3 we give a list of the phases of λ for all renormalisable operators without fixing the θ_r and with the above choice for θ_r in Table 2.4.

Under the choice we made, the CP transformation acting on the fields using the above choice for the θ_r reads

$$\begin{gathered} \mathbf{1} \to \mathbf{1}^*\,, \quad \mathbf{1'} \to \mathbf{1'}^*\,, \quad \mathbf{1''} \to \mathbf{1''}^*\,, \quad \mathbf{3} \to \mathbf{3}^*\,, \\ \mathbf{2'} \to \begin{pmatrix} 1 & 0 \\ 0 & -\mathrm{i} \end{pmatrix} \mathbf{2'}^*\,, \quad \mathbf{2''} \to \begin{pmatrix} \mathrm{i} & 0 \\ 0 & 1 \end{pmatrix} \mathbf{2''}^*\,, \end{gathered} \tag{2.2.11}$$

where we have again skipped the **2** representation because we will not need it later on.

2.2.3 Conditions to violate physical CP

In this section we try to clarify the origin of the phases entering the Lagrangian after T' breaking which are then responsible for physical CP violation. We will use the choice of the θ_r discussed in the previous section, i.e. $\theta_1 = \theta_{1'} = \theta_{1''} = \theta_3 = 0$ and $\theta_{2''} = -\theta_{2'} = \pi/4$.

We already know that the singlets and triplets do not introduce CP violation, see also [112]. Therefore we only want to consider the doublets. Suppose we couple the doublet flavons ψ_i to an operator $\mathcal{O}_r$ containing matter fields and transforming in the representation r of T'. This means that the superpotential contains the operator

$$\mathcal{W} \supset \mathcal{O}_r \Phi_{\bar{r}}\,, \text{ where } \Phi_{\bar{r}} = \left(\prod_i \psi_i \right)_{\bar{r}}\,. \tag{2.2.12}$$

In order to obtain a singlet, the flavons (the doublets) have to be contracted to the representation $\bar{r}$ which is the complex conjugate representation of r.

[5] Since in our model later on we do not have fields in a **2** representation of T' the phase θ_2 is irrelevant in our further discussion and we do not fix its value. A possible convenient choice might be $\theta_2 = 0$ which makes the mass term of a two-dimensional representation real.

$\lambda\mathcal{O} = \lambda(A \times B \times C)$	$\beta \equiv \mathrm{CP}[\mathcal{O}]/\mathcal{O}^*$
$(\mathbf{2} \times \mathbf{2})_{\mathbf{1}} \times \mathbf{1}$	$\mathrm{e}^{\mathrm{i}(\theta_1+2\theta_2)}$
$(\mathbf{2'} \times \mathbf{2''})_{\mathbf{1}} \times \mathbf{1}$	$\mathrm{e}^{\mathrm{i}(\theta_1+\theta_{2'}+\theta_{2''})}$
$(\mathbf{2'} \times \mathbf{2'})_{\mathbf{1''}} \times \mathbf{1'}$	$\mathrm{e}^{\mathrm{i}(\theta_{1'}+2\theta_{2'})}$
$(\mathbf{2} \times \mathbf{2''})_{\mathbf{1''}} \times \mathbf{1'}$	$\mathrm{e}^{\mathrm{i}(\theta_{1'}+\theta_2+\theta_{2''})}$
$(\mathbf{2''} \times \mathbf{2''})_{\mathbf{1'}} \times \mathbf{1''}$	$\mathrm{e}^{\mathrm{i}(\theta_{1''}+2\theta_{2''})}$
$(\mathbf{2} \times \mathbf{2'})_{\mathbf{1'}} \times \mathbf{1''}$	$\mathrm{e}^{\mathrm{i}(\theta_{1''}+\theta_2+\theta_{2'})}$
$[(\mathbf{2} \times \mathbf{2})_{\mathbf{3}} \times \mathbf{3}]_{\mathbf{1}}$	$-\,\mathrm{i}\ \mathrm{e}^{\mathrm{i}(2\theta_2+\theta_3)}$
$[(\mathbf{2'} \times \mathbf{2''})_{\mathbf{3}} \times \mathbf{3}]_{\mathbf{1}}$	$-\,\mathrm{i}\ \mathrm{e}^{\mathrm{i}(\theta_{2'}+\theta_{2''}+\theta_3)}$
$[(\mathbf{2'} \times \mathbf{2'})_{\mathbf{3}} \times \mathbf{3}]_{\mathbf{1}}$	$-\,\mathrm{i}\ \mathrm{e}^{\mathrm{i}(2\theta_{2'}+\theta_3)}$
$[(\mathbf{2} \times \mathbf{2''})_{\mathbf{3}} \times \mathbf{3}]_{\mathbf{1}}$	$-\,\mathrm{i}\ \mathrm{e}^{\mathrm{i}(\theta_2+\theta_{2''}+\theta_3)}$
$[(\mathbf{2''} \times \mathbf{2''})_{\mathbf{3}} \times \mathbf{3}]_{\mathbf{1}}$	$-\,\mathrm{i}\ \mathrm{e}^{\mathrm{i}(2\theta_{2''}+\theta_3)}$
$[(\mathbf{2} \times \mathbf{2'})_{\mathbf{3}} \times \mathbf{3}]_{\mathbf{1}}$	$-\,\mathrm{i}\ \mathrm{e}^{\mathrm{i}(\theta_2+\theta_{2'}+\theta_3)}$
$[(\mathbf{3} \times \mathbf{3})_{\mathbf{1}} \times \mathbf{1}]_{\mathbf{1}}$	$\mathrm{e}^{\mathrm{i}(\theta_1+2\theta_3)}$
$[(\mathbf{3} \times \mathbf{3})_{\mathbf{1'}} \times \mathbf{1''}]_{\mathbf{1}}$	$\mathrm{e}^{\mathrm{i}(\theta_{1''}+2\theta_3)}$
$[(\mathbf{3} \times \mathbf{3})_{\mathbf{1''}} \times \mathbf{1'}]_{\mathbf{1}}$	$\mathrm{e}^{\mathrm{i}(\theta_{1'}+2\theta_3)}$
$[(\mathbf{3} \times \mathbf{3})_{\mathbf{3_S},\mathbf{3_A}} \times \mathbf{3}]_{\mathbf{1}}$	$\mathrm{e}^{3i\theta_3}$
$[(\mathbf{1} \times \mathbf{1})_{\mathbf{1}} \times \mathbf{1}]_{\mathbf{1}}$	$\mathrm{e}^{\mathrm{i}(3\theta_1)}$
$[(\mathbf{1'} \times \mathbf{1'})_{\mathbf{1''}} \times \mathbf{1'}]_{\mathbf{1}}$	$\mathrm{e}^{\mathrm{i}(3\theta_{1'})}$
$[(\mathbf{1''} \times \mathbf{1''})_{\mathbf{1'}} \times \mathbf{1''}]_{\mathbf{1}}$	$\mathrm{e}^{\mathrm{i}(3\theta_{1''})}$
$[(\mathbf{1'} \times \mathbf{1''})_{\mathbf{1}} \times \mathbf{1}]_{\mathbf{1}}$	$\mathrm{e}^{\mathrm{i}(\theta_1+\theta_{1'}+\theta_{1''})}$

Table 2.3: List of operators, which form a singlet and constraints on the phase of the coupling λ from the invariance under the generalised CP transformations Eq. (2.2.9).

$\lambda\mathcal{O} = \lambda(A \times B \times C)$	$\beta \equiv \mathrm{CP}[\mathcal{O}]/\mathcal{O}^*$	$\arg(\lambda)$
$(\mathbf{2'} \times \mathbf{2''})_{\mathbf{1}} \times \mathbf{1}$	1	$0,\, \pi$
$(\mathbf{2'} \times \mathbf{2'})_{\mathbf{1''}} \times \mathbf{1'}$	$-\mathrm{i}$	$\pm\bar{\Omega}$
$(\mathbf{2''} \times \mathbf{2''})_{\mathbf{1'}} \times \mathbf{1''}$	i	$\pm\Omega$
$[\mathbf{2'} \times (\mathbf{2''} \times \mathbf{3})_{\mathbf{2''}}]_{\mathbf{1}}$	1	$0,\, \pi$
$[\mathbf{2''} \times (\mathbf{2'} \times \mathbf{3})_{\mathbf{2'}}]_{\mathbf{1}}$	1	$0,\, \pi$
$[(\mathbf{2'} \times \mathbf{2''})_{\mathbf{3}} \times \mathbf{3}]_{\mathbf{1}}$	$-\mathrm{i}$	$\pm\bar{\Omega}$
$[(\mathbf{2'} \times \mathbf{2'})_{\mathbf{3}} \times \mathbf{3}]_{\mathbf{1}}$	-1	$\pm\pi/2$
$[(\mathbf{2''} \times \mathbf{2''})_{\mathbf{3}} \times \mathbf{3}]_{\mathbf{1}}$	1	$0,\, \pi$
$[(\mathbf{3} \times \mathbf{3})_{\mathbf{1}} \times \mathbf{1}]_{\mathbf{1}}$	1	$0,\, \pi$
$[(\mathbf{3} \times \mathbf{3})_{\mathbf{1'}} \times \mathbf{1''}]_{\mathbf{1}}$	1	$0,\, \pi$
$[(\mathbf{3} \times \mathbf{3})_{\mathbf{1''}} \times \mathbf{1'}]_{\mathbf{1}}$	1	$0,\, \pi$
$[(\mathbf{3} \times \mathbf{3})_{\mathbf{3_S}, \mathbf{3_A}} \times \mathbf{3}]_{\mathbf{1}}$	1	$0,\, \pi$
$[(\mathbf{1} \times \mathbf{1})_{\mathbf{1}} \times \mathbf{1}]_{\mathbf{1}}$	1	$0,\, \pi$
$[(\mathbf{1'} \times \mathbf{1'})_{\mathbf{1''}} \times \mathbf{1'}]_{\mathbf{1}}$	1	$0,\, \pi$
$[(\mathbf{1''} \times \mathbf{1''})_{\mathbf{1'}} \times \mathbf{1''}]_{\mathbf{1}}$	1	$0,\, \pi$
$[(\mathbf{1'} \times \mathbf{1''})_{\mathbf{1}} \times \mathbf{1}]_{\mathbf{1}}$	1	$0,\, \pi$

Table 2.4: List of some operators, for which it is possible construct a singlet, and constraints on the phase of the coupling λ from invariance under the generalised CP transformations Eq. (2.2.9) with the choice $\theta_1 = \theta_{1'} = \theta_{1''} = \theta_3 = 0$ and $\theta_{2''} = -\theta_{2'} = \pi/4$. We have omitted the transformations which include the **2** representation of T' because they do not appear in our model, but they can be read off from Table 2.3 after choosing θ_2.

If the operator $\mathcal{O}_r$ by itself conserves physical CP – by which we mean that it does not introduce any complex phases into the Lagrangian including the associated coupling constant – the only possible source of CP violation is coming from the doublet vevs and the complex CG factors appearing in the contraction with the operator and the doublets. For illustrative purpose we want to discuss this explicitly if we have two doublets $\psi' \sim \mathbf{2'}$ and $\psi'' \sim \mathbf{2''}$.

For $r = \mathbf{1}$ there is only one possible combination using only ψ' and ψ'' which is $(\psi' \otimes \psi'')_{\mathbf{1}}$. Using the tensor products of T' —see for example [90]— we find that the combination is real if the vevs fulfill the following conditions

$$\psi' = \begin{pmatrix} X_1 \, \mathrm{e}^{\mathrm{i}\,\alpha} \\ X_2 \, \mathrm{e}^{\mathrm{i}\,\beta} \end{pmatrix} , \quad \psi'' = \begin{pmatrix} Y_1 \, \mathrm{e}^{-\mathrm{i}\,\beta} \\ Y_2 \, \mathrm{e}^{-\mathrm{i}\,\alpha} \end{pmatrix} , \tag{2.2.13}$$

with X_1, X_2, Y_1, Y_2, α and β real parameters. For $r = \mathbf{1'}$ and $r = \mathbf{1''}$ the only possible contractions $(\psi' \otimes \psi')_{\mathbf{1''}}$ and $(\psi'' \otimes \psi'')_{\mathbf{1'}}$ vanish due to the antisymmetry of the contraction.

For $r = \mathbf{1}$ there are three possible contractions. Either a flavon with itself or both flavons together.

- For the selfcontractions $(\psi' \otimes \psi')_{\mathbf{3}}$ and $(\psi'' \otimes \psi'')_{\mathbf{3}}$ the Lagrangian will not contain a phase if the flavon fields ψ' and ψ'' have the following structure

$$\psi' = \begin{pmatrix} X_1 \, \mathrm{e}^{\mathrm{i}\,\alpha} \\ X_2 \, \mathrm{e}^{-\mathrm{i}(\alpha+\pi/4)} \end{pmatrix} , \quad \psi'' = \begin{pmatrix} Y_1 \, \mathrm{e}^{-\mathrm{i}(\beta-\pi/4)} \\ Y_2 \, \mathrm{e}^{\mathrm{i}\,\beta} \end{pmatrix} , \tag{2.2.14}$$

  with X_1, X_2, Y_1, Y_2 being real and α, $\beta = 0$, $\pm\pi/2$, π.

- The contraction $(\psi' \otimes \psi'')_{\mathbf{3}}$ does not introduce phases if ψ', ψ'' have the following structure:

$$\psi' \sim \begin{pmatrix} X_1 \, \mathrm{e}^{\mathrm{i}(\beta-\pi/4)} \\ X_2 \, \mathrm{e}^{\mathrm{i}(\alpha+\pi/4)} \end{pmatrix} , \quad \psi'' \sim \begin{pmatrix} Y_1 \, \mathrm{e}^{-i\beta} \\ Y_2 \, \mathrm{e}^{-i\alpha} \end{pmatrix} , \tag{2.2.15}$$

  with X_1, X_2, Y_1, Y_2 real and $\beta - \alpha = -\pi/4$.

The previous results allow us to distinguish in a particular model the alignments which can introduce phases with a specific superpotential in the Yukawa sector. For example, if we consider a model in which one entry of the Yukawa matrix is filled by a term of the form $(\psi' \otimes \psi'')_{\mathbf{3}}$ and another entry by $(\psi' \otimes \psi'')_{\mathbf{1}}$ we see that we cannot fulfill both conditions simultaneously if the doublet vevs do not vanish. That means we would expect CP violation if both of these contractions are present in a given model.

Later on in our model we will have real doublet alignments with

$$\psi' \sim \begin{pmatrix} 1 \\ 0 \end{pmatrix} \text{ and } \psi'' \sim \begin{pmatrix} 0 \\ 1 \end{pmatrix} . \tag{2.2.16}$$

These alignments would conserve CP for sure only if the model contains only the contractions $(\psi' \otimes \psi')_{\mathbf{3}}$, $(\psi'' \otimes \psi'')_{\mathbf{3}}$ and $(\psi' \otimes \psi'')_{\mathbf{1}}$. Adding the contraction $(\psi' \otimes \psi'')_{\mathbf{3}}$ would add a phase to the Yukawa matrix resulting possibly in physical CP violation.

2.3 The Model

In this section we discuss a supersymmetric model of lepton flavour based on T' as a family symmetry. Because it considers only the lepton sector we can consider it as a toy model. The generalised CP symmetry will be broken in a geometrical way as we will discuss later on and we can fit all the available data of masses and mixing in the lepton sector.

The gauge symmetry of the model is the Standard Model gauge group $G_{\text{SM}} = SU(3)_c \times SU(2)_L \times U(1)_Y$. The discrete symmetries of the model are $T' \rtimes H_{\text{CP}} \times Z_8 \times Z_4^2 \times Z_3^2 \times Z_2$, where the Z_n factors are the shaping symmetries of the superpotential required to forbid unwanted operators.

There are a few comments about this symmetry in order. First of all, the symmetry seems to be rather large but in fact compared to the first works on T' with geometrical CP violation [99–101] we have only added a factor of $Z_8 \times Z_2$ but included the full flavon vacuum alignment and messenger sector. This symmetry is also much smaller than the shaping symmetry we have used before in [90].

One might wonder where this symmetry originates from and it might be embedded into (gauged) continuous symmetries or might be a remnant of the compactification of extra-dimensions. But a discussion of such an embedding goes clearly beyond the scope of this work where we just want to discuss the connection of a T' family symmetry with CP and illustrate it by a toy model which is nevertheless in full agreement with experimental data.

In this section we will only discuss the effective operators generated after integrating out the heavy messenger fields. The full renormalisable superpotential including the messenger fields is given in Section 2.4.

2.3.1 The Flavon Sector

We will start the discussion of the model with the flavon sector which is self-contained. How the flavons couple to the matter sector will be discussed afterwards.

The model contains 14 flavon fields in 1-, 2- and 3-dimensional representations of T' and 5 auxiliary flavons in 1-dimensional representations. Before we will discuss the superpotential which fixes the directions and phases of the flavon vevs we will first define them. We have four flavons in the 3-dimensional representation of T' pointing in the directions

$$\langle\phi\rangle = \begin{pmatrix} 0 \\ 0 \\ 1 \end{pmatrix} \phi_0 \,, \quad \langle\tilde{\phi}\rangle = \begin{pmatrix} 0 \\ 1 \\ 0 \end{pmatrix} \tilde{\phi}_0 \,, \quad \langle\hat{\phi}\rangle = \begin{pmatrix} 1 \\ 0 \\ 0 \end{pmatrix} \hat{\phi}_0 \,, \quad \langle\xi\rangle = \begin{pmatrix} 1 \\ 1 \\ 1 \end{pmatrix} \xi_0 \,. \tag{2.3.1}$$

The first three flavons will be used in the charged lepton sector and the fourth one couples only to the neutrino sector. These flavon vevs, like all the other flavon vevs, are real.

Further we introduce three doublets of T': $\psi' \sim \mathbf{2'}$, $\psi'' \sim \mathbf{2''}$ and $\tilde{\psi}'' \sim \mathbf{2''}$. We recall that the doublets are the only representations of the family group T' which introduce phases, due to the complexity of the Clebsh-Gordan coefficients. For the doublets we will

	$G_{\rm SM}$	T'	$U(1)_R$	Z_8	Z_4	Z_4	Z_3	Z_3	Z_2
ϕ	$(\mathbf{1},\mathbf{1},0)$	$\mathbf{3}$	0	2	0	0	1	0	1
$\tilde{\phi}$	$(\mathbf{1},\mathbf{1},0)$	$\mathbf{3}$	0	2	0	2	0	1	0
$\hat{\phi}$	$(\mathbf{1},\mathbf{1},0)$	$\mathbf{3}$	0	5	0	3	2	0	0
ξ	$(\mathbf{1},\mathbf{1},0)$	$\mathbf{3}$	0	0	2	2	0	0	0
ψ'	$(\mathbf{1},\mathbf{1},0)$	$\mathbf{2}'$	0	3	2	3	2	0	0
ψ''	$(\mathbf{1},\mathbf{1},0)$	$\mathbf{2}''$	0	7	2	1	2	0	1
$\tilde{\psi}''$	$(\mathbf{1},\mathbf{1},0)$	$\mathbf{2}''$	0	1	2	3	0	1	1
ζ	$(\mathbf{1},\mathbf{1},0)$	$\mathbf{1}$	0	5	0	1	2	0	1
ζ'	$(\mathbf{1},\mathbf{1},0)$	$\mathbf{1}'$	0	4	0	2	0	0	1
$\tilde{\zeta}'$	$(\mathbf{1},\mathbf{1},0)$	$\mathbf{1}'$	0	2	0	2	0	1	0
ζ''	$(\mathbf{1},\mathbf{1},0)$	$\mathbf{1}''$	0	2	0	0	1	0	1
$\tilde{\zeta}''$	$(\mathbf{1},\mathbf{1},0)$	$\mathbf{1}''$	0	0	0	0	0	1	0
ρ	$(\mathbf{1},\mathbf{1},0)$	$\mathbf{1}$	0	0	2	2	0	0	0
$\tilde{\rho}$	$(\mathbf{1},\mathbf{1},0)$	$\mathbf{1}$	0	0	2	2	0	0	0
ϵ_1	$(\mathbf{1},\mathbf{1},0)$	$\mathbf{1}$	0	4	1	0	0	0	0
ϵ_2	$(\mathbf{1},\mathbf{1},0)$	$\mathbf{1}$	0	4	2	2	0	0	1
ϵ_3	$(\mathbf{1},\mathbf{1},0)$	$\mathbf{1}$	0	4	2	0	0	0	0
ϵ_4	$(\mathbf{1},\mathbf{1},0)$	$\mathbf{1}$	0	0	0	0	1	1	0
ϵ_5	$(\mathbf{1},\mathbf{1},0)$	$\mathbf{1}$	0	0	0	0	2	2	0

Table 2.5: List of the flavon fields and their transformation properties. We also list here the auxiliary flavon fields ϵ_i, $i = 1, \ldots, 5$, which are needed to fix the phases of the vevs of the other flavon fields.

	$G_{\rm SM}$	T'	$U(1)_R$	Z_8	Z_4	Z_4	Z_3	Z_3	Z_2
D_ϕ	$(\mathbf{1},\mathbf{1},0)$	$\mathbf{3}$	2	0	2	0	1	0	0
$\tilde{D}_\phi$	$(\mathbf{1},\mathbf{1},0)$	$\mathbf{3}$	2	0	3	0	0	1	0
$\hat{D}_\phi$	$(\mathbf{1},\mathbf{1},0)$	$\mathbf{3}$	2	6	0	2	1	2	0
D_ψ	$(\mathbf{1},\mathbf{1},0)$	$\mathbf{3}$	2	2	0	2	2	0	0
$\bar{D}_\psi$	$(\mathbf{1},\mathbf{1},0)$	$\mathbf{3}$	2	2	0	2	2	0	0
$\tilde{D}_\psi$	$(\mathbf{1},\mathbf{1},0)$	$\mathbf{3}$	2	6	0	2	0	1	0
D_ξ	$(\mathbf{1},\mathbf{1},0)$	$\mathbf{3}$	2	4	2	2	0	0	1
S_ζ	$(\mathbf{1},\mathbf{1},0)$	$\mathbf{1}$	2	6	0	2	2	0	0
S'_ζ	$(\mathbf{1},\mathbf{1},0)$	$\mathbf{1}'$	2	0	0	0	0	0	0
$\tilde{S}'_\zeta$	$(\mathbf{1},\mathbf{1},0)$	$\mathbf{1}'$	2	4	0	0	0	1	0
P	$(\mathbf{1},\mathbf{1},0)$	$\mathbf{1}$	2	0	0	0	0	0	0

Table 2.6: List of the driving fields and their T' transformation properties. The field P stands for the fields $\tilde{S}_\zeta$, S_ξ, S_ρ and S_{ε_i}, with $i = 1,\ldots,5$, which all have the same quantum numbers.

find the alignments

$$\langle\psi'\rangle = \begin{pmatrix} 1 \\ 0 \end{pmatrix} \psi'_0 \,, \quad \langle\psi''\rangle = \begin{pmatrix} 0 \\ 1 \end{pmatrix} \psi''_0 \,, \quad \langle\tilde{\psi}''\rangle = \begin{pmatrix} 0 \\ 1 \end{pmatrix} \tilde{\psi}''_0 \,. \tag{2.3.2}$$

And finally, we introduce 7 flavon fields in one-dimensional representations of the family group. In particular, we have (the primes indicate the types of singlet)

$$\langle\zeta'\rangle = \zeta'_0 \,, \quad \langle\zeta''\rangle = \zeta''_0 \,, \quad \langle\tilde{\zeta}'\rangle = \tilde{\zeta}'_0 \,, \quad \langle\tilde{\zeta}''\rangle = \tilde{\zeta}''_0 \,, \quad \langle\zeta\rangle = \zeta_0 \,, \quad \langle\rho\rangle = \rho_0 \,, \quad \langle\tilde{\rho}\rangle = \tilde{\rho}_0 \,. \tag{2.3.3}$$

The ρ and $\tilde{\rho}$ couple only to the neutrino sector while the other one-dimensional flavons couple only to the charged lepton sector. Also the five auxiliary flavons ϵ_i, $i = 1,\ldots,5$ get real vevs which we do not label here explicitly.

The flavon quantum numbers are summarized in Table 2.5. In this table we have also included the five auxiliary flavon fields ϵ_i which are only needed to fix the phases of the other flavon vevs and all acquire real vevs by themselves.

We discuss now the superpotential in the flavon sector which "aligns" the flavon vevs. We will use so-called F-term alignment where the vevs are determined from the F-term conditions of the driving fields. The driving fields are listed with their quantum numbers in Table 2.6, where we have indicated for simplicity $P = \tilde{S}_\zeta$, S_ξ, S_ρ and S_{ε_i}, with $i = 1,\ldots,5$, because they have all the same quantum numbers under the whole symmetry group.

The fields labeled as P play a crucial role in fixing the phases of the flavon vevs. They are fixed by the discrete vacuum alignment method as it was first proposed in [109]. Having a flavon ϵ (for the moment we assume it is a singlet under the family symmetry) charged

under a Z_n symmetry the superpotential will contain a term

$$\mathcal{W} \supset P\left(\frac{\epsilon^n}{\Lambda^{n-2}} \mp M^2\right) \ . \tag{2.3.4}$$

Remember that the P fields are total singlets. Due to CP symmetry in this simple example all parameters and couplings are real. The F-term equation for P reads

$$|F_P|^2 = \left|\frac{\epsilon^n}{\Lambda^{n-2}} \mp M^2\right|^2 = 0. \tag{2.3.5}$$

which gives for the phase of the flavon vev

$$\arg(\langle\epsilon\rangle) = \begin{cases} \frac{2\pi}{n} q \ , \quad q = 1, \ldots, n & \text{for ``}-\text{'' in Eq. (2.3.5)}, \\ \frac{2\pi}{n} q + \frac{\pi}{n} \ , \quad q = 1, \ldots, n & \text{for ``}+\text{'' in Eq. (2.3.5)}. \end{cases} \tag{2.3.6}$$

This method will be used to fix the phases of the singlet and triplet flavon vevs (including the ϵ_i). Note that we have to introduce for every phase we fix in this way a P field and only after a suitable choice of basis for this fields we end up with the simple structure we show later, see also the appendix of [109]. For the directions of the triplets we use standard expressions, cf. also the previous paper [90].

For the doublets, nevertheless, we use here a different method. Take for example the term $D_\psi \left[(\psi'')^2 - \phi\,\zeta'\right]$. The F-term equations read

$$|F_{D_{\psi_1}}| = (\psi_2'')^2 - \phi_3\,\zeta' = 0 \ , \tag{2.3.7}$$

$$|F_{D_{\psi_1}}| = \mathrm{i}(\psi_1'')^2 - \phi_2\,\zeta' = 0 \ , \tag{2.3.8}$$

$$|F_{D_{\psi_1}}| = (1-\mathrm{i})\psi_1''\,\psi_2'' - \phi_1\,\zeta' = 0 \ . \tag{2.3.9}$$

Note the phases coming from the complex CG coefficients of T'. Plugging in the (real) vevs of ϕ and ζ' it turns out that only the second component of ψ'' does not vanish and is indeed real as well.

The full superpotential for the flavon vacuum alignment reads

$$\begin{aligned}
\mathcal{W}_f = {} & \frac{D_\phi\,\varepsilon_3}{\Lambda}\left[\phi^2 - \phi\,\zeta''\right] + \frac{\tilde{D}_\phi\,\varepsilon_1}{\Lambda}\left[\tilde{\phi}^2 - \tilde{\phi}\,\tilde{\zeta}'\right] + \frac{\hat{D}_\phi}{\Lambda}\left[\varepsilon_4\,\hat{\phi}\,\hat{\phi} + \varepsilon_5\,\tilde{\phi}\,\tilde{\zeta}'' + \frac{\varepsilon_4^2\,\tilde{\zeta}''\,\tilde{\phi}}{\Lambda}\right] \\
& + D_\psi\left[(\psi'')^2 - \phi\,\zeta'\right] + \bar{D}_\psi\left(\mathrm{i}\,\psi'\,\psi' + \phi\,\zeta'\right) + \tilde{D}_\psi\left[\left(\tilde{\psi}''\right)^2 - \tilde{\phi}\,\tilde{\zeta}'' - \frac{\varepsilon_4^2\,\hat{\phi}\,\hat{\phi}}{\Lambda^2}\right] \\
& + S'_\zeta\left(\zeta'\,\zeta' - \xi\,\xi - \frac{\varepsilon_2^2\,\xi^2}{\Lambda^2}\right) + \tilde{S}'_\zeta\left(\tilde{\zeta}'\,\tilde{\zeta}' - \tilde{\phi}\,\tilde{\phi}\right) + \frac{\tilde{S}_\zeta}{\Lambda}\left[\left(\tilde{\zeta}''\right)^3 - M_{\tilde{\zeta}''}^3\right] \\
& + S_\zeta\left(\zeta\,\zeta + \hat{\phi}\,\hat{\phi}\right) + \frac{S_{\varepsilon_1}}{\Lambda^2}\left(\varepsilon_1^4 - M_{\varepsilon_1}^4\right) + S_{\varepsilon_4}\left(\frac{\varepsilon_4^3}{\Lambda} - M_{\varepsilon_4}^2\right) \\
& + S_{\varepsilon_3}\left(\varepsilon_2^2 - M_{\varepsilon_2}^2\right) + S_{\varepsilon_3}\left(\varepsilon_3^2 - M_{\varepsilon_3}^2\right) + S_{\varepsilon_5}\left(\varepsilon_4\,\varepsilon_5 - M_{\varepsilon_5}^2\right) \\
& + \frac{D_\xi\,\varepsilon_2}{\Lambda}\left(\xi^2 + \xi\rho + \xi\tilde{\rho}\right) + S_\xi\left(\xi^2 - M_\xi^2\right) + S_\rho\left(\rho^2 + \tilde{\rho}^2 - M_\rho^2\right) \ .
\end{aligned} \tag{2.3.10}$$

	L	$\bar{E}$	$\bar{E}_3$	N_R	H_d	H_u
$SU(2)_L$	**2**	**1**	**1**	**1**	**2**	**2**
$U(1)_Y$	-1	2	2	0	-1	1
T'	**3**	**2″**	**1″**	**3**	**1**	**1**
$U(1)_R$	1	1	1	1	0	0
Z_8	5	7	2	4	7	7
Z_4	1	3	1	3	2	2
Z_4	1	2	1	3	2	2
Z_3	0	0	2	0	0	0
Z_3	2	0	0	0	1	1
Z_2	0	1	1	0	0	0

Table 2.7: List of the matter and Higgs fields of the model and their transformation properties under T', $U(1)_R$ and the shaping symmetries. We also give the quantum numbers under $SU(2)_L \times U(1)_Y$. All fields are singlets of $SU(3)_C$.

We will not go through all the details and discuss each F-term condition but this potential is minimized by the vacuum structure as in Eqs. (2.3.1), (2.3.2) and (2.3.3). Finally, we want to remark that the F-term equations do not fix the phase of the field ζ. However, the phase of this field will turn out to be unphysical because it can be canceled out through an unphysical unitary transformation of the right-handed charged lepton fields as we will show later explicitly.

2.3.2 The Matter Sector

Since we have discussed now the symmetry breaking flavon fields we will now proceed with the discussion on how these fields couple to the matter sector and generate the Yukawa couplings and right-handed Majorana neutrino masses.

The model contains three generations of lepton fields, the left-handed $SU(2)_L$ doublets are organized in a triplet representation of T', the first two families of right-handed charged lepton fields are organized in a two dimensional representation, $\mathbf{2''}$, and the third family sits in a $\mathbf{1''}$. There are two Higgs doublets as usual in supersymmetric models. They are both singlets, $\mathbf{1}$ under T'. The model includes three heavy right-handed Majorana neutrino fields N, which are organized in a triplet. The light active neutrino masses are generated through the type I seesaw mechanism [106]. At leading order tri-bimaximal mixing (TBM) is predicted in the the neutrino sector which is corrected by the charged lepton sector allowing a realistic fit of the measured parameters of the PMNS mixing matrix. The quantum numbers of the matter fields are summarized in Table 2.7.

In this work we use the right-left convention for the Yukawa matrices

$$-\mathcal{L} \supset (\mathrm{Y}_e)_{ij}\ \bar{e}_{Ri}\, e_{Lj} H_d + \text{ H.c. }, \tag{2.3.11}$$

i.e. there exists a unitary matrix U_e which diagonalizes the product $\mathrm{Y}_e^\dagger \mathrm{Y}_e$ and contributes to the physical PMNS mixing matrix.

The Charged Lepton Sector

The Yukawa matrix Y_e is generated after the flavons acquire their vevs and T' is broken. The effective superpotential describing the couplings of the matter sector to the flavon sector is given by

$$\begin{aligned}\mathcal{W}_{\mathrm{Y}_e} = & \frac{y_{33}^{(e)}}{\Lambda}\left(\bar{E}_3\, H_d\right)_{\mathbf{1''}}\left(L\,\phi\right)_{\mathbf{1'}} + \frac{y_{32}^{(e)}}{\Lambda^2}\left(\bar{E}_3\, H_d\right)_{\mathbf{1''}}\left(L\,\hat{\phi}\right)_{\mathbf{1'}}\zeta + \frac{\hat{y}_{32}^{(e)}}{\Lambda^2}\,\bar{\Omega}\,\left(\bar{E}_3\, H_d\right)_{\mathbf{1''}}\left[L\left(\psi'\,\psi''\right)_{\mathbf{3}}\right]_{\mathbf{1'}} \\ & + \frac{y_{22}^{(e)}}{\Lambda^2}\left(\bar{E}\,\psi'\right)_{\mathbf{1}} H_d\left(L\,\phi\right)_{\mathbf{1}} + \frac{y_{21}^{(e)}}{\Lambda^3}\,\bar{\Omega}\,\left(\bar{E}\,\psi'\right)_{\mathbf{1}} H_d\left[\left(\psi'\,\psi''\right)_{\mathbf{3}}\,L\right]_{\mathbf{1}} \\ & + \frac{y_{11}^{(e)}}{\Lambda^3}\,\Omega\,\left(\bar{E}\,\tilde{\psi}''\right)_{\mathbf{1'}} H_d\,\tilde{\zeta}'\left(L\,\tilde{\phi}\right)_{\mathbf{1'}}\,,\end{aligned} \tag{2.3.12}$$

where Λ denotes a generic messenger scale. Note the explicit phase factors $\Omega = (1+\mathrm{i})/\sqrt{2}$ and $\bar{\Omega} = (1-\mathrm{i})/\sqrt{2}$ appearing in some of the operators. They are determined by the invariance under the generalised CP transformations and they can be evaluated from Table 2.4. We also give here explicitly the contraction of T' as indices at the brackets. These contractions are determined by the messenger sector which will be discussed in Appendix 2.4.

After plugging in the flavon vevs from Eqs. (2.3.1)-(2.3.3) we find for the structure of the Yukawa matrix Y_e

$$\mathrm{Y}_e = \begin{pmatrix} \Omega\, a & 0 & 0 \\ \mathrm{i}\, b & c & 0 \\ 0 & d+\mathrm{i}\, k & e \end{pmatrix} \equiv \begin{pmatrix} \Omega\, a & 0 & 0 \\ \mathrm{i}\, b & c & 0 \\ 0 & \rho\, \mathrm{e}^{\mathrm{i}\,\eta} & e \end{pmatrix}\,, \tag{2.3.13}$$

where we define $\rho = \sqrt{d^2+k^2}$ and $\eta = \arg\left(d+\mathrm{i}\, k\right)$.

The parameters a, b, c, d, e, k depend on the unfixed phase of the vev of ζ, ζ_0, which can be explicitly factorized as

$$\mathrm{Y}_e = \begin{pmatrix} \Omega\,\bar{a}(\zeta_0) & 0 & 0 \\ \mathrm{i}\,\zeta_0^3\,\overline{b} & \zeta_0^3\,\overline{c} & 0 \\ 0 & \zeta_0^2(\overline{d}+\mathrm{i}\,\overline{k}) & \zeta_0^2\,\overline{e} \end{pmatrix} = \begin{pmatrix} \mathrm{e}^{\mathrm{i}\arg(\Omega\,\bar{a}(\zeta_0))} & 0 & 0 \\ 0 & \zeta_0^3 & 0 \\ 0 & 0 & \zeta_0^2 \end{pmatrix} \begin{pmatrix} |\Omega\,\bar{a}(\zeta_0)| & 0 & 0 \\ \mathrm{i}\,\overline{b} & \overline{c} & 0 \\ 0 & \overline{d}+\mathrm{i}\,\overline{k} & \overline{e} \end{pmatrix}\,, \tag{2.3.14}$$

from which it is clear that an eventual phase of ζ_0 drops out in the physical combination $\mathrm{Y}_e^\dagger \mathrm{Y}_e$ and we can choose the parameters in the Yukawa matrix to be real.

We remind that there are in principle three possible sources of complex phases which can lead to physical CP violation: complex vevs, complex couplings whose phases are determined by the invariance under the generalised CP symmetry and complex CG coefficients. In our model all vevs are real due to our flavon alignment and the convenient choice of the θ_r phases.

Then the (physical) phases in Y_e are completely induced by the complex couplings and complex CG coefficients. In fact the insights we have gained before in Section 2.2.3 can be used here. The phase in the 1-1 element is unphysical (it drops out in the combination $\mathrm{Y}_e^\dagger \mathrm{Y}_e$. So the physical CP violation is to leading order given by the phases of the ratios $(\mathrm{Y}_e)_{21}/(\mathrm{Y}_e)_{22}$ and $(\mathrm{Y}_e)_{32}/(\mathrm{Y}_e)_{33}$. Let us study for illustration the second ratio which has two components, one with a non-trivial relative phase and one without. The real ratio d/e is coming from the operators with the coefficients $y_{32}^{(e)}$ and $y_{33}^{(e)}$ and from the viewpoint of $T' \rtimes H_{\mathrm{CP}}$ there is not really any difference between the two because we have only added a singlet which cannot break CP in our setup as we said before.

For the second ratio $\mathrm{i}\,k/e$ this is different. Using the notation from Section 2.2.3 we have $\mathcal{O}_{\mathbf{3}}\Phi_{\mathbf{3}} = \left(\bar{E}_3\, H_d\right)_{\mathbf{1}''} \left(L\,\Phi_{\mathbf{3}}\right)_{\mathbf{1}'}$. If $\Phi_{\mathbf{3}} = \phi$ (the operator with $y_{32}^{(e)}$) we cannot have a phase because ϕ is a triplet flavon. For $\Phi_{\mathbf{3}} = (\psi'\psi'')_{\mathbf{3}}$ (the operator with $\hat{y}_{32}^{(e)}$) we can check if condition (2.2.15) is fulfilled which is not the case because both vevs are real, while the condition demands a relative phase difference between the vevs of $\pi/4$. This demonstrates the usefulness of the conditions given in Section 2.2.3 in understanding the origin of physical CP violation in this setup.

The Neutrino Sector

The neutrino sector is constructed using a superpotential similar to that used in [90]: the light neutrino masses are generated through the type I see-saw mechanism, i.e. introducing right-handed heavy Majorana states which are accommodated in a triplet under T'. We have the effective superpotential

$$\mathcal{W}_{\mathrm{Y}_\nu} = \lambda_1 N\, N\, \xi + N\, N\, (\lambda_2 \rho + \lambda_3 \tilde{\rho}) + \frac{y_\nu}{\Lambda}(NL)_1(H_u\rho)_1 + \frac{\tilde{y}_\nu}{\Lambda}(NL)_1(H_u\tilde{\rho})_1 \,. \tag{2.3.15}$$

The Dirac and the Majorana mass matrices obtained from this superpotential are identical to those described in [90] and we quote them here for completeness

$$M_R = \begin{pmatrix} 2Z+X & -Z & -Z \\ -Z & 2Z & -Z+X \\ -Z & -Z+X & 2Z \end{pmatrix} \,, \quad M_D = \begin{pmatrix} 1 & 0 & 0 \\ 0 & 0 & 1 \\ 0 & 1 & 0 \end{pmatrix} \frac{\rho'}{\Lambda} \,, \tag{2.3.16}$$

where X, Z and ρ' are real parameters which can be written explicitly as

$$X = \frac{\lambda_2}{\sqrt{3}}\rho_0 + \frac{\lambda_3}{\sqrt{3}}\tilde{\rho}_0 \,, \quad Z = \frac{\lambda_1}{\sqrt{18}}\xi_0 \;\text{ and }\; \rho' = \frac{y_\nu}{\sqrt{3}}\rho_0 v_u + \frac{\tilde{y}_\nu}{\sqrt{3}}\tilde{\rho}_0 v_u \,. \tag{2.3.17}$$

The right-handed neutrino mass matrix M_R is diagonalised by the TBM matrix [93]

$$U_{\mathrm{TBM}} = \begin{pmatrix} \sqrt{2/3} & \sqrt{1/3} & 0 \\ -\sqrt{1/6} & \sqrt{1/3} & -\sqrt{1/2} \\ -\sqrt{1/6} & \sqrt{1/3} & \sqrt{1/2} \end{pmatrix} \,, \tag{2.3.18}$$

such that the heavy RH neutrino masses read:

$$\begin{aligned} U_{\rm TBM}^T\, M_R\, U_{\rm TBM} &= D_N = {\rm Diag}(3Z+X, X, 3Z-X) \\ &= {\rm Diag}(M_1\, {\rm e}^{{\rm i}\,\phi_1}, M_2\, {\rm e}^{{\rm i}\,\phi_2},\, M_3\, {\rm e}^{{\rm i}\,\phi_3})\ ,\ \ M_{1,2,3} > 0\,. \end{aligned} \tag{2.3.19}$$

Since X and Z are real parameters, the phases ϕ_1, ϕ_2 and ϕ_3 take values 0 or π. A light neutrino Majorana mass term is generated after electroweak symmetry breaking via the type I see-saw mechanism:

$$M_\nu \ = \ -M_D^T\, M_R^{-1}\, M_D = U_\nu^*\, {\rm Diag}\,(m_1, m_2, m_3)\, U_\nu^\dagger\,, \tag{2.3.20}$$

where

$$U_\nu = {\rm i}\ U_{\rm TBM}\ {\rm Diag}\left({\rm e}^{{\rm i}\,\phi_1/2}, {\rm e}^{{\rm i}\,\phi_2/2}, {\rm e}^{{\rm i}\,\phi_3/2}\right) \equiv {\rm i}\ U_{\rm TBM}\, \Phi_\nu\,,\quad \Phi_\nu \equiv {\rm Diag}\left({\rm e}^{{\rm i}\,\phi_1/2}, {\rm e}^{{\rm i}\,\phi_2/2}, {\rm e}^{{\rm i}\,\phi_3/2}\right)\,, \tag{2.3.21}$$

and $m_{1,2,3} > 0$ are the light neutrino masses,

$$m_i = \left(\frac{\rho'}{\Lambda}\right)^2\, \frac{1}{M_i}\,,\ \ i = 1,2,3\,. \tag{2.3.22}$$

The phase factor i in Eq. (2.3.21) corresponds to an unphysical phase and we will drop it in what follows. Note also that one of the phases ϕ_k, say ϕ_1, is physically irrelevant since it can be considered as a common phase of the neutrino mixing matrix. In the following we will always set $\phi_1 = 0$. This corresponds to the choice $(X + 3Z) > 0$.

2.3.3 Comments about the θ_r

At this point we want to comment on the role of the phases θ_r appearing in the definition of the CP transformation in Eq. (2.2.11). These phases are arbitrary and hence they should not contribute to physical observables. This means, for instance, that these arbitrary phases must not appear in the Yukawa matrices after T' is broken. However it is not enough to look at the Yukawa couplings alone but one also has to study the flavon vacuum alignment sector. We want to show next a simple example for which, as expected, these phases turn out to be unphysical.

In order to show this we consider as example $({\rm Y}_e)_{22}$ and $({\rm Y}_e)_{21}$ respectively generated by the following operators:

$$({\rm Y}_e)_{22} \sim \left(\bar{E}\,\psi'\right)_{\mathbf{1}}\,(L\,\phi)_{\mathbf{1}}\,\zeta\,H_d\ ,\quad ({\rm Y}_e)_{21} \sim \left(\bar{E}\,\psi'\right)_{\mathbf{1}}\,(L\,\phi)_{\mathbf{1''}}\,\zeta'\,H_d\ . \tag{2.3.23}$$

The fields together with their charges have been defined before in Table 2.5. We will now be more explicit and consider all the possible phases arising in each of the given operators under the CP transformation of Eq. (2.2.9) where the θ_r were included explicitly. For each flavon vev in the operators we will denote the arising phase with a bar correspondingly, i.e. for the vev of the flavon ϕ we will have $\phi \to {\rm e}^{{\rm i}\,\bar{\phi}}\phi_0$ where ϕ_0 is the modulus of the vev. Then using the transformations in Eq. (2.2.9) and Table 2.2.9 we get

$$\arg\left(({\rm Y}_e)_{22} - ({\rm Y}_e)_{21}\right) = \bar{\zeta} - \bar{\zeta}' + (\theta_{\mathbf{1}} - \theta_{\mathbf{1'}})/2\ . \tag{2.3.24}$$

The vevs of the flavons ζ and ζ' are determined at leading order by

$$S_\zeta \left[\zeta^2 - (\hat{\phi}\,\hat{\phi})_{\mathbf{1}}\right] \text{ and } S_{\zeta'} \left[(\zeta')^2 - (\xi\,\xi)_{\mathbf{1''}}\right]. \tag{2.3.25}$$

where $S_{\zeta,\zeta'}$ are two of the so-called "driving fields" which in this case are singlet of type $\mathbf{1}$ and $\mathbf{1'}$ under T'. From the F-term equations one gets that $\bar{\zeta} = \bar{\hat{\phi}} + (\theta_{\mathbf{3}} - \theta_{\mathbf{1}})/2$ and $\bar{\zeta}' = \bar{\xi} + (\theta_{\mathbf{3}} - \theta_{\mathbf{1'}})/2$ and thus in the physical phase difference

$$\arg\left((\mathrm{Y}_e)_{22} - (\mathrm{Y}_e)_{21}\right) = \bar{\hat{\phi}} - \bar{\xi}\,. \tag{2.3.26}$$

the phases $\theta_{\mathbf{1}}$, $\theta_{\mathbf{1'}}$ and $\theta_{\mathbf{3}}$ cancel out.

This shows how the θ_r cancel out in a complete model and become unphysical. Including them only in one sector, for instance, in the Yukawa sector they might appear to be physical and only after considering also the flavon alignment sector it can be shown that they are unphysical which is nevertheless quite cumbersome in a realistic model due to the many fields and couplings involved.

2.3.4 Geometrical CP violation and residual symmetries

In this section we want to provide a better understanding of the quality of symmetry breaking our model exhibits. To be more precise we will argue that our model breaks CP in a geometrical fashion and then we will discuss the residual symmetries of the mass matrices.

Geometrical CP violation was first defined in [108] and there it is tightly related to the so-called "calculable phases" which are phases of flavon vevs which do not depend on the parameters of the potential but only on the geometry of the potential. This applies also to our model. All complex phases are determined in the end by the (discrete) symmetry group of our model. In particular the symmetries $T' \rtimes H_{\mathrm{CP}}$ and the Z_n factors play a crucial role here. For the singlets and triplets in fact the Z_n symmetries (in combination with CP) make the phases calculable using the discrete vacuum alignment technique [109]. For the doublets then the symmetry $T' \rtimes H_{\mathrm{CP}}$ enters via fixing the phases of the couplings and fixing relative phases between different components of the multiplets. In particular, all flavon vevs are left invariant under the generalised CP symmetry and hence protected by it. However the calculable phases are necessary but not sufficient for geometrical CP violation. For this we have to see if CP is broken or not.

For this we will have a look at the residual symmetries of the mass matrices after $T' \rtimes H_{\mathrm{CP}}$ is broken. First of all, we observe that the vev structure mentioned in Section 2.3 gives a breaking pattern which is different in the neutrino and in the charged lepton sector, i.e. the residual groups G_ν and G_e are different.

In the charged lepton sector the group T' is fully broken by the singlet, doublet and triplet vevs. If it exists, the residual group in the charged lepton sector is defined through the elements which leave invariant the flavon vevs and satisfy

$$\begin{aligned} \rho^\dagger(g_{e_i})\,\mathrm{Y}_e^\dagger\,\mathrm{Y}_e\,\rho(g_{e_i}) &= \mathrm{Y}_e^\dagger\,\mathrm{Y}_e \text{ with } g_{e_i} \in G_e < T' \rtimes H_{\mathrm{CP}}\,, \\ X_e^\dagger\,\left(\mathrm{Y}_e^\dagger\,\mathrm{Y}_e\right)\,X_e &= \left(\mathrm{Y}_e^\dagger\,\mathrm{Y}_e\right)^* \text{ with } X_e \in G_e < T' \rtimes H_{\mathrm{CP}}\,. \end{aligned} \tag{2.3.27}$$

The first condition is the ordinary condition to study residual symmetries while the second one is relevant only for models with spontaneous CP violation.

In our model this conditions are not satisfied for any $\rho(g)$ or X_e. Hence there is no residual symmetry group in the charged lepton sector and even more CP is broken spontaneously. Together with the fact that all our phases are determined by symmetries (up to signs and discrete choices) we have demonstrated now that our model exhibits geometrical CP violation.

In the neutrino sector we can write similar relations that take into account the symmetrical structure of the Majorana mass matrix, and in particular as before the residual symmetry is defined through the elements which leave invariant the flavon vevs and satisfy

$$\begin{aligned} \rho^T(g_{\nu_i})\, M_\nu\, \rho(g_{\nu_i}) = M_\nu \text{ with } g_{\nu_i} \in G_\nu < T' \rtimes H_{\rm CP}\ , \\ X_\nu^T\, M_\nu\, X_\nu = M_\nu^* \text{ with } X_\nu \in G_\nu < T' \rtimes H_{\rm CP}\ . \end{aligned} \tag{2.3.28}$$

In our model M_ν is a real matrix and therefore $\rho(g_{\nu_i})$ and X_ν are defined through the same conditions. Defining O as the orthogonal matrix which diagonalizes the real symmetric matrix M_ν we find from Eq. (2.3.28)

$$(O\, X_\nu^T\, O^T)\, M_\nu^{\rm diag}\, (O\, X_\nu\, O^T) = M_\nu^{\rm diag} \tag{2.3.29}$$

and hence the matrix $D = O\, X_\nu\, O^T$ has to be of the form

$$D = \begin{pmatrix} (-1)^p & 0 & 0 \\ 0 & (-1)^q & 0 \\ 0 & 0 & (-1)^{p+q} \end{pmatrix}\ . \tag{2.3.30}$$

The same argument can be applied to the matrix $\rho(g_{\nu_i})$, because the matrices X_ν, $\rho(g_{\nu_i})$ and M_ν are simultaneously diagonalisable by the same orthogonal matrix O. It is easy to find that

$$O = \begin{pmatrix} 1/\sqrt{3} & 1/\sqrt{3} & 1/\sqrt{3} \\ 0 & -1/\sqrt{2} & 1/\sqrt{2} \\ -\sqrt{2/3} & 1/\sqrt{6} & 1/\sqrt{6} \end{pmatrix}\ , \tag{2.3.31}$$

which is expected since M_ν is diagonalized by $U_{\rm TBM}$ and O is just a permutation of $U_{\rm TBM}^T$ which corresponds to a permutation of the eigenvalues.

The residual symmetry coming from T' is generated only by

$$T\, S\, T^2 = O^T \cdot \begin{pmatrix} 1 & 0 & 0 \\ 0 & -1 & 0 \\ 0 & 0 & -1 \end{pmatrix} \cdot O\ , \tag{2.3.32}$$

which also leaves invariant the vev structure. This symmetry is a Z_2 symmetry. In summary the residual symmetry in the neutrino sector is a Klein group $K_4 \cong Z_2 \times Z_2$, in which one Z_2 comes from $H_{\rm CP}$ and the other one from T'. $H_{\rm CP}$ is conserved because in the neutrino sector X_ν can be chosen as the identity matrix and M_ν is real.

Combining the two we find

$$G_f \equiv T' \rtimes H_{\rm CP} \equiv T' \rtimes Z_2 \longrightarrow \begin{cases} G_e & = \emptyset \,, \\ G_\nu & = K_4 \,, \end{cases} \tag{2.3.33}$$

so that $T' \rtimes H_{\rm CP}$ is completely broken and there is no residual symmetry left.

2.3.5 Predictions

Absolute Neutrino Mass Scale

Before we consider the mixing angles and phases in the PMNS matrix we first will discuss the neutrino spectra predicted by the model. We get the same results as in [90] because our neutrino mass matrix has exactly the same structure. The forms of the Dirac and Majorana mass terms given in Eq. (2.3.16) imply that in the model considered by us both light neutrino mass spectra with normal ordering (NO) and with inverted ordering (IO) are allowed (see also [90]). In total three different spectra for the light active neutrinos are possible. They correspond to the different choices of the values of the phases ϕ_i in Eq. (2.3.21)). More specifically, the cases $\phi_1 = \phi_2 = \phi_3 = 0$ and $\phi_1 = \phi_2 = 0$ and $\phi_3 = \pi$ correspond to NO spectra of the type A and B, respectively. For $\phi_1 = \phi_2 = 0$ and $\phi_3 = \pi$ also IO spectrum is possible. The neutrino masses in cases of the three spectra are given by:

$$\text{NO spectrum A}: \quad (m_1, m_2, m_3) = (4.43, 9.75, 48.73) \cdot 10^{-3} \text{ eV} \,, \tag{2.3.34}$$

$$\text{NO spectrum B}: \quad (m_1, m_2, m_3) = (5.87, 10.48, 48.88) \cdot 10^{-3} \text{ eV} \,, \tag{2.3.35}$$

$$\text{IO spectrum}: \quad (m_1, m_2, m_3) = (51.53, 52.26, 17.34) \cdot 10^{-3} \text{ eV} \,, \tag{2.3.36}$$

where we have used the best fit values of Δm^2_{21} and $|\Delta m^2_{31(32)}|$ given in Table 1. Employing the 3σ allowed ranges of values of the two neutrino mass squared differences quoted in Table 1, we find the intervals in which $m_{1,2,3}$ can vary:

- NO spectrum A:
  $m_1 \in [4.23, 4.66] \cdot 10^{-3}$ eV, $m_2 \in [9.23, 10.17] \cdot 10^{-3}$ eV, $m_3 \in [4.28, 5.56] \cdot 10^{-2}$ eV;

- NO spectrum B:
  $m_1 \in [5.56, 6.20] \cdot 10^{-3}$ eV, $m_2 \in [9.83, 11.20] \cdot 10^{-3}$ eV, $m_3 \in [4.23, 5.74] \cdot 10^{-2}$ eV;

- IO spectrum:
  $m_1 \in [4.57, 5.87] \cdot 10^{-2}$ eV, $m_2 \in [4.63, 5.96] \cdot 10^{-2}$ eV, $m_3 \in [1.53, 1.98] \cdot 10^{-2}$ eV.

Correspondingly, we get for the sum of the neutrino masses:

$$\text{NO A}: \quad \sum_{j=1}^{3} m_j = 6.29 \times 10^{-2}\ \text{eV}\,, \quad 5.63 \times 10^{-2} \leq \sum_{j=1}^{3} m_j \leq 7.04 \times 10^{-2}\ \text{eV}\,, \tag{2.3.37}$$

$$\text{NO B}: \quad \sum_{j=1}^{3} m_j = 6.52 \times 10^{-2}\ \text{eV}\,, \quad 5.77 \times 10^{-2} \leq \sum_{j=1}^{3} m_j \leq 7.48 \times 10^{-2}\ \text{eV}\,, \tag{2.3.38}$$

$$\text{IO}: \quad \sum_{j=1}^{3} m_j = 12.11 \times 10^{-2}\ \text{eV}\,, \quad 10.73 \times 10^{-2} \leq \sum_{j=1}^{3} m_j \leq 13.81 \times 10^{-2}\ \text{eV}\,, \tag{2.3.39}$$

where we have given the predictions using the best fit values and the 3σ intervals of the allowed values of m_1, m_2 and m_3 quoted above.

The Mixing Angles and Dirac CPV Phase

We will derive next expressions for the mixing angles and the CPV phases in the standard parametrisation of the PMNS matrix in terms of the parameters of the model. The expression for the charged lepton mass matrix Y_e given in Eq. (2.3.13) contains altogether seven parameters: five real parameters and two phases, one of which is equal to $\pi/2$. Three (combinations of) parameters are determined by the three charged lepton masses. The remaining two real parameters and two phases are related to two angles and two phases in the matrix U_e which diagonalises the product $\mathrm{Y}_e^\dagger \mathrm{Y}_e$ and enters into the expression of the PMNS matrix: $U_{\rm PMNS} = U_e^\dagger U_\nu$, where U_ν is of TBM form (see Eq. (3.19)), while $U_e \propto R_{23} R_{12}$, R_{23} and R_{12} are orthogonal matrices describing rotations in the 2-3 and 1-2 planes, respectively. It proves convenient to adopt for the matrices U_e and U_ν the notation used in [74]:

$$\begin{cases} U_e = \Psi_e\, R_{23}^{-1}\left(\theta_{23}^e\right) R_{12}^{-1}\left(\theta_{12}^e\right) \\ U_\nu = R_{23}\left(\theta_{23}^\nu\right) R_{12}\left(\theta_{12}^\nu\right) \Phi_\nu \end{cases} \tag{2.3.40}$$

where $\Psi_e = \mathrm{diag}\left(1, \mathrm{e}^{\mathrm{i}\,\psi_e}, \mathrm{e}^{\mathrm{i}\,\omega_e}\right)$, $\theta_{23}^\nu = -\pi/4$, $\theta_{12}^\nu = \sin^{-1}(1/\sqrt{3})$, Φ_ν is a diagonal phase matrix defined in Eq. (2.3.21), and

$$R_{12}\left(\theta_{12}^e\right) = \begin{pmatrix} \cos\theta_{12}^e & \sin\theta_{12}^e & 0 \\ -\sin\theta_{12}^e & \cos\theta_{12}^e & 0 \\ 0 & 0 & 1 \end{pmatrix}\,, \quad R_{23}\left(\theta_{23}^e\right) = \begin{pmatrix} 1 & 0 & 0 \\ 0 & \cos\theta_{23}^e & \sin\theta_{23}^e \\ 0 & -\sin\theta_{23}^e & \cos\theta_{23}^e \end{pmatrix}\,. \tag{2.3.41}$$

Using the expression for the charged lepton mass matrix Y_e given in Eq. (2.3.13) and comparing the right and the left sides of the equation

$$\mathrm{Y}_e^\dagger \mathrm{Y}_e = U_e \mathrm{diag}\left(m_e^2, m_\mu^2, m_\tau^2\right) U_e^\dagger\,, \tag{2.3.42}$$

we find that $m_e^2 = a^2$, $m_\mu^2 = c^2$ and $m_\tau^2 = e^2$. For U_e given in Eq. (2.3.40) this equality holds only under the condition that $\sin\theta_{12}^e$ and $\sin\theta_{23}^e$ are sufficiently small. Using the

leading terms in powers of the small parameters $\sin\theta^e_{12}$ and $\sin\theta^e_{23}$ we get the approximate relations:

$$\sin\theta^e_{12}\,\mathrm{e}^{\mathrm{i}\,\psi_e} \simeq \pm\,\mathrm{i}\left|\frac{b}{c}\right| \;, \quad \sin\theta^e_{23}\,\mathrm{e}^{\mathrm{i}(\psi_e-\omega_e)} = \frac{e\,\rho}{c^2-e^2}\,\mathrm{e}^{\mathrm{i}\,\eta} \simeq \left|\frac{\rho}{e}\right|\,\mathrm{e}^{\mathrm{i}\,\xi_e}\;, \tag{2.3.43}$$

where $\psi_e = \pm\pi/2$, $\xi_e = \psi_e - \omega_e$, $\xi_e \in [0, 2\pi]$, $\theta^e_{12} \simeq |b/c|$ and $\theta^e_{23} \simeq |\rho/e|$.

In the discussion that follows θ^e_{12}, θ^e_{23}, ψ_e and ω_e are treated as arbitrary angles and phases, i.e., no assumption about their magnitude is made.

The lepton mixing we obtain in the model we have constructed, including the Dirac CPV phase but not the Majorana CPV phases, was investigated in detail on general phenomenological grounds in ref. [74] and we will use the results obtained in [74]. The three angles θ_{12}, θ_{23} and θ_{13} and the Dirac and Majorana CPV phases δ and β_1 and β_2 (see Eqs. (1.1) - (1.3)), of the PMNS mixing matrix $U_{\rm PMNS} = U^\dagger_e U_\nu = R_{12}(\theta^e_{12})R_{23}(\theta^e_{23})\Psi^*_e R_{23}(\theta^\nu_{23})R_{12}(\theta^\nu_{12})\;\Phi_\nu$, can be expressed as functions of the two real angles, θ^e_{12} and θ^e_{23}, and the two phases, ψ_e and ω_e present in U_e. However, as was shown in [74], the three angles θ_{12}, θ_{23} and θ_{13} and the Dirac phase δ are expressed in terms of the angle θ^e_{12}, an angle $\hat\theta_{23}$ and just one phase ϕ, where

$$\sin^2\hat\theta_{23} = \frac{1}{2}\;(1 - 2\sin\theta^e_{23}\cos\theta^e_{23}\cos(\omega_e - \psi_e))\;, \tag{2.3.44}$$

and the phase $\phi = \phi(\theta^e_{23}, \omega_e, \psi_e)$. Indeed, it is not difficult to show that (see the Appendix in [74])

$$R_{23}(\theta^e_{23})\;\Psi^*_e\;R_{23}(\theta^\nu_{23}) = P\,\Phi\,R_{23}(\hat\theta_{23})\tilde Q\,. \tag{2.3.45}$$

Here $P = \mathrm{diag}(1, 1, \mathrm{e}^{-\,\mathrm{i}\,\alpha})$, $\Phi = \mathrm{diag}(1, \mathrm{e}^{\mathrm{i}\,\phi}, 1)$ and $\tilde Q = \mathrm{diag}\left(1, 1, \mathrm{e}^{\mathrm{i}\,\beta}\right)$, where

$$\alpha = \gamma + \psi_e + \omega_e\,, \qquad \beta = \gamma - \phi\,, \tag{2.3.46}$$

and

$$\gamma = \arg\left(-\mathrm{e}^{-\,\mathrm{i}\,\psi_e}\cos\theta^e_{23} + \mathrm{e}^{-\,\mathrm{i}\,\omega_e}\sin\theta^e_{23}\right)\;,\;\; \phi = \arg\left(\mathrm{e}^{-\,\mathrm{i}\,\psi_e}\cos\theta^e_{23} + \mathrm{e}^{-\,\mathrm{i}\,\omega_e}\sin\theta^e_{23}\right)\;. \tag{2.3.47}$$

The phase α is unphysical (it can be absorbed in the τ lepton field). The phase β contributes to the matrix of physical Majorana phases, which now is equal to $\overline{Q} = \tilde Q\,\Phi_\nu$. The PMNS matrix takes the form:

$$U_{\rm PMNS} = R_{12}(\theta^e_{12})\,\Phi(\phi)\,R_{23}(\hat\theta_{23})\,R_{12}(\theta^\nu_{12})\,\overline{Q}\,, \tag{2.3.48}$$

where $\theta^\nu_{12} = \sin^{-1}(1/\sqrt{3})$. Thus, the four observables θ_{12}, θ_{23}, θ_{13} and δ are functions of three parameters θ^e_{12}, $\hat\theta_{23}$ and ϕ. As a consequence, the Dirac phase δ can be expressed as a function of the three PMNS angles θ_{12}, θ_{23} and θ_{13}, leading to a new "sum rule" relating δ and θ_{12}, θ_{23} and θ_{13} [74]. Using the measured values of θ_{12}, θ_{23} and θ_{13}, the authors of [74] obtained predictions for the values of δ and of the rephasing invariant $J_{\rm CP} = \mathrm{Im}(U^*_{e1}U^*_{\mu3}U_{e3}U_{\mu1})$, which controls the magnitude of CP violating effects in neutrino oscillations [11], as well as for the 2σ and 3σ ranges of allowed values of $\sin\theta_{12}$, $\sin\theta_{23}$ and $\sin\theta_{13}$. These predictions are valid also in the model under discussion.

To be more specific, using Eq. (2.3.48) we get for the angles θ_{12}, θ_{23} and θ_{13} of the standard parametrisation of $U_{\rm PMNS}$ [74]:

$$\begin{aligned}
&\sin\theta_{13} = |U_{e3}| = \sin\theta^e_{12}\sin\hat{\theta}_{23}, \\
&\sin^2\theta_{23} = \frac{|U_{\mu 3}|^2}{1-|U_{e3}|^2} = \frac{\sin^2\hat{\theta}_{23}-\sin^2\theta_{13}}{1-\sin^2\theta_{13}}\,, \quad \cos^2\theta_{23} = \frac{\cos^2\hat{\theta}_{23}}{1-\sin^2\theta_{13}}\,, \\
&\sin^2\theta_{12} = \frac{|U_{e2}|^2}{1-|U_{e3}|^2} = \frac{1}{3}\left(2+\frac{\sqrt{2}\,\sin 2\theta_{23}\sin\theta_{13}\cos\phi-\sin^2\theta_{23}}{1-\cos^2\theta_{23}\cos^2\theta_{13}}\right),
\end{aligned} \tag{2.3.49}$$

where the first relation $\sin\theta_{13} = \sin\theta^e_{12}\sin\hat{\theta}_{23}$ was used in order to obtain the expressions for $\sin^2\theta_{23}$ and $\sin^2\theta_{12}$. Clearly, the angle $\hat{\theta}_{23}$ differs little from the atmospheric neutrino mixing angle θ_{23}. For $\sin^2\theta_{13} = 0.024$ and $\sin^2\theta_{23} \cong 0.39$ we have $\sin\theta^e_{12} \cong 0.2$. Comparing the imaginary and real parts of $U^*_{e1}U^*_{\mu 3}U_{e3}U_{\mu 1}$, obtained using Eq. (2.3.48) and the standard parametrisation of $U_{\rm PMNS}$, one gets the following relation between the phase ϕ and the Dirac phase δ [74]:

$$\sin\delta = -\,\frac{2\sqrt{2}}{3}\,\frac{\sin\phi}{\sin 2\theta_{12}}\,, \tag{2.3.50}$$

$$\begin{aligned}
\cos\delta = {}& \frac{2\sqrt{2}}{3\sin 2\theta_{12}}\,\cos\phi\left(-1+\frac{2\sin^2\theta_{23}}{\sin^2\theta_{23}\cos^2\theta_{13}+\sin^2\theta_{13}}\right) \\
&+\frac{1}{3\sin 2\theta_{12}}\,\frac{\sin 2\theta_{23}\,\sin\theta_{13}}{\sin^2\theta_{23}\cos^2\theta_{13}+\sin^2\theta_{13}}\,.
\end{aligned} \tag{2.3.51}$$

The results quoted above, including those for $\sin\delta$ and $\cos\delta$, are exact. As can be shown, in particular, we have: $\sin^2\delta+\cos^2\delta = 1$.

Equation (2.3.49) allows to express $\cos\phi$ in terms of θ_{12}, θ_{23} and θ_{13}, and substituting the result thus obtained for $\cos\phi$ in Eqs. (2.3.50) and (2.3.51), one can get expressions for $\sin\delta$ and $\cos\delta$ in terms of θ_{12}, θ_{23} and θ_{13}. We give below the result for $\cos\delta$ [74]:

$$\cos\delta = \frac{\tan\theta_{23}}{3\sin 2\theta_{12}\sin\theta_{13}}\left[1+\left(3\sin^2\theta_{12}-2\right)\left(1-\cot^2\theta_{23}\,\sin^2\theta_{13}\right)\right]. \tag{2.3.52}$$

For the best fit values of $\sin^2\theta_{12}$, $\sin^2\theta_{23}$ and $\sin\theta_{13}$, one finds in the case of NO and IO spectra [6] (see also [74]):

$$\cos\delta \cong -0.069\,, \quad \sin\delta = \pm 0.998\,. \tag{2.3.53}$$

These values correspond to

$$\delta = 93.98^\circ \quad \text{or} \quad \delta = 266.02^\circ\,. \tag{2.3.54}$$

[6] Due to the slight difference between the best fit values of $\sin^2\theta_{23}$ and $\sin\theta_{13}$ in the cases of NO and IO spectra (see Table 1), the values we obtain for $\cos\delta$ in the two cases differ somewhat. However, this difference is equal to 10^{-4} in absolute value and we will neglect it in what follows.

Thus, our model predicts $\delta \simeq \pi/2$ or $3\pi/2$. The fact that the value of the Dirac CPV phase δ is determined (up to an ambiguity of the sign of $\sin\delta$) by the values of the three mixing angles θ_{12}, θ_{23} and θ_{13} of the PMNS matrix, (2.3.52), is the most striking prediction of the model considered. For the best fit values of θ_{12}, θ_{23} and θ_{13} we get $\delta \cong \pi/2$ or $3\pi/2$. These result implies also that in the model under discussion, the $J_{\rm CP}$ factor, which determines the magnitude of CP violation in neutrino oscillations, is also a function of the three angles θ_{12}, θ_{23} and θ_{13} of the PMNS matrix:

$$J_{\rm CP} = J_{\rm CP}(\theta_{12},\theta_{23},\theta_{13},\delta(\theta_{12},\theta_{23},\theta_{13})) = J_{\rm CP}(\theta_{12},\theta_{23},\theta_{13})\,. \tag{2.3.55}$$

This allows to obtain predictions for the range of possible values of $J_{\rm CP}$ using the current data on $\sin^2\theta_{12}$, $\sin^2\theta_{23}$ and $\sin^2\theta_{13}$. For the best fit values of these parameters (see Table 1) we find: $J_{\rm CP} \simeq \pm 0.034$.

The quoted results on δ and $J_{\rm CP}$ were obtained first on the basis of a phenomenological analysis in [74]. Here they are obtained for the first time within a selfconsistent model of lepton flavour based on the T' family symmetry.

In [74] the authors performed a detailed statistical analysis which permitted to determine the ranges of allowed values of $\sin^2\theta_{12}$, $\sin^2\theta_{23}$, $\sin\theta_{13}$, δ and $J_{\rm CP}$ at a given confidence level. We quote below some of the results obtained in [74], which are valid also in the model constructed by us.

Most importantly, the CP conserving values of $\delta = 0;\pi;2\pi$ are excluded with respect to the best fit CP violating values $\delta \cong \pi/2;3\pi/2$ at more than 4σ. Correspondingly, $J_{\rm CP} = 0$ is also excluded with respect to the best-fit values $J_{\rm CP} \simeq (-0.034)$ and $J_{\rm CP} \simeq 0.034$ at more than 4σ. Further, the 3σ allowed ranges of values of both δ and $J_{\rm CP}$ form rather narrow intervals. In the case of the best fit value $\delta \cong 3\pi/2$, for instance, we have in the cases of NO and IO spectra:

$$\text{NO}: \quad J_{\rm CP} \cong -0.034\,, \quad 0.028 \lesssim J_{\rm CP} \lesssim 0.039\,, \quad \text{or} \tag{2.3.56}$$

$$-0.039 \lesssim J_{\rm CP} \lesssim -0.028\,, \tag{2.3.57}$$

$$\text{IO}: \quad J_{\rm CP} \cong -0.034\,, \quad 0.027 \lesssim J_{\rm CP} \lesssim 0.039\,, \quad \text{or} \tag{2.3.58}$$

$$-0.039 \lesssim J_{\rm CP} \lesssim -0.026\,, \tag{2.3.59}$$

where we have quoted the best fit value of $J_{\rm CP}$ as well. The positive values are related to the χ^2 minimum at $\delta = \pi/2$.

The preceding results and discussion are illustrated qualitatively in Fig. 2.1, where we show the correlation between the value of $\sin\delta$ and $J_{\rm CP}$ for the 1σ and 2σ ranges of allowed values of $\sin^2\theta_{12}$, $\sin^2\theta_{23}$ and $\sin^2\theta_{13}$, which were taken from Table 1. The figure was produced assuming flat distribution of the values of $\sin^2\theta_{12}$, $\sin^2\theta_{23}$ and $\sin^2\theta_{13}$ in the quoted intervals around the corresponding best fit values. As can be seen from Fig. 2.1, the predicted values of both $\sin\delta$ and $J_{\rm CP}$ thus obtained form rather narrow intervals [7].

[7] The 2σ ranges of allowed values of $\sin\delta$ and $J_{\rm CP}$ shown in Fig. 2.1 match approximately the 3σ ranges of allowed values of $\sin\delta$ and $J_{\rm CP}$ obtained in [74] by performing a more rigorous statistical (χ^2) analysis.

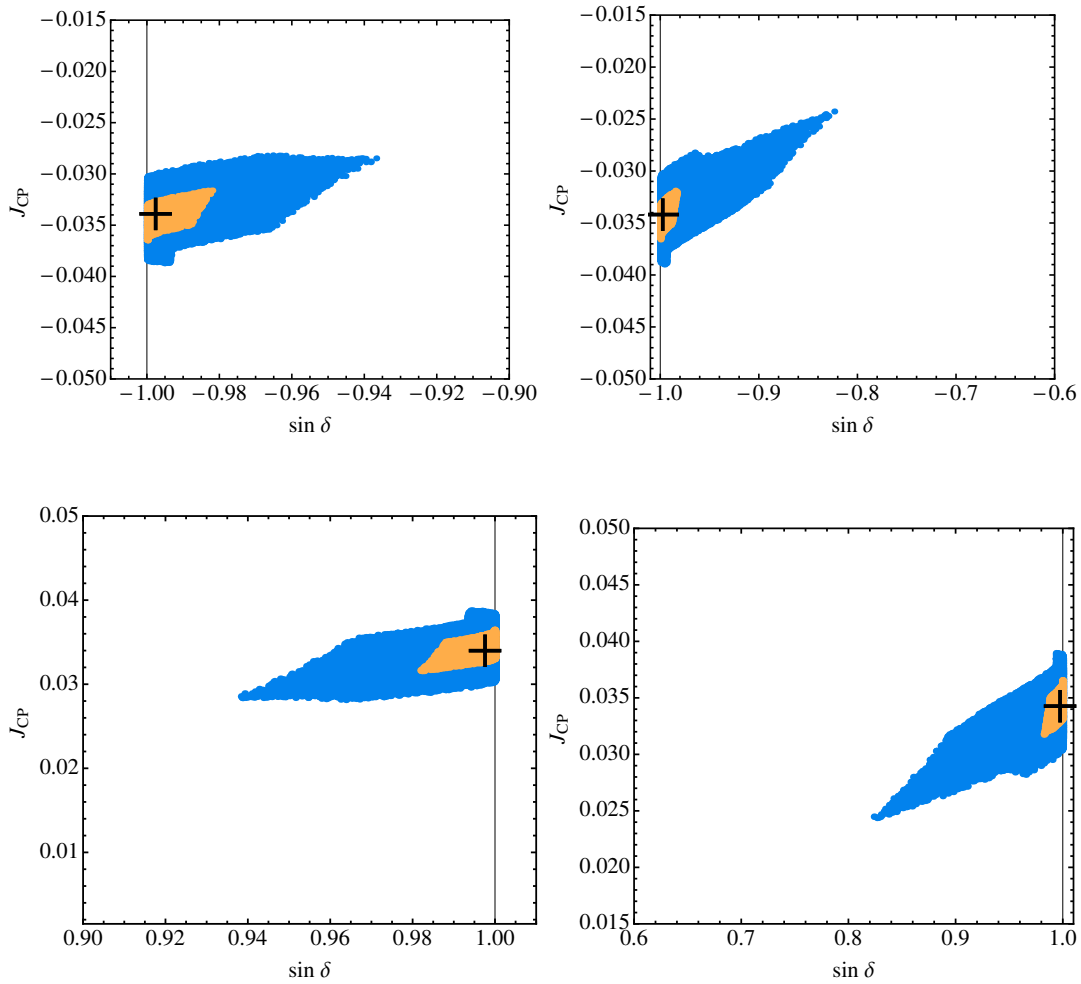

Figure 2.1: Possible values of $\sin\delta$ and $J_{\rm CP}$, obtained by using the 1σ (light brown areas) and 2σ ranges (blue + light brown areas) of allowed values of the mixing angles θ_{12}, θ_{23} and θ_{13} for NO spectrum (left panels) and IO spectrum (right panels), and for $\sin\delta < 0$ (upper panels) and $\sin\delta > 0$ (lower panels). The predictions for the best fit values of θ_{12}, θ_{23} and θ_{13}, corresponding to $\delta = 266.02^\circ$ ($\sin\delta < 0$) and $\delta = 93.98^\circ$ ($\sin\delta > 0$), are indicated with crosses. See text for further details.

As it follows from Table 1, the angle θ_{23} is determined using the current neutrino oscillation data with largest uncertainty. We give next the values of the Dirac phase δ for two values of $\sin^2\theta_{23}$ from its 3σ allowed range, $\sin^2\theta_{23} = 0.50$ and 0.60, and for the best fit values of $\sin^2\theta_{12}$ and $\sin^2\theta_{13}$:

$$\sin^2\theta_{23} = 0.50: \quad \cos\delta = -0.123\,, \quad \delta = 97.09^\circ \;\; \text{or} \;\; 262.91^\circ\,; \tag{2.3.60}$$

$$\sin^2\theta_{23} = 0.60: \quad \cos\delta = -0.176\,, \quad \delta = 100.12^\circ \;\; \text{or} \;\; 259.88^\circ\,. \tag{2.3.61}$$

These results show that $|\sin\delta|$, which determines the magnitude of the CP violation effects in neutrino oscillations, exhibits very weak dependence on the value of $\sin^2\theta_{23}$: for any value of $\sin^2\theta_{23}$ from the interval $0.39 \leq \sin^2\theta_{23} \leq 0.60$ we get $|\sin\delta| \geq 0.98$.

The predictions of the model for δ and $J_{\rm CP}$ will be tested in the experiments searching for CP violation in neutrino oscillations, which will provide information on the value of the Dirac phase δ.

The Majorana CPV Phases

Using the expressions for the angles θ_{12}^e and $\hat{\theta}_{23}$ and for $\cos\phi$ in terms of $\sin\theta_{13}$, $\sin\theta_{12}$ and $\sin\theta_{23}$ and the best fit values of $\sin\theta_{13}$, $\sin\theta_{12}$ and $\sin\theta_{23}$, we can calculate the numerical form of $U_{\rm PMNS}$ from which we can extract the values of the physical CPV Majorana phases. We follow the procedure described in [117]. Obviously, there are two such forms of $U_{\rm PMNS}$ corresponding to the two possible values of δ. In the case of $\delta = 266.02^\circ$ and $\phi \simeq 102.55^\circ$ we find:

$$U_{\rm PMNS} = \begin{pmatrix} 0.822\,e^{-i\,7.47^\circ} & 0.547\,e^{i\,16.04^\circ} & 0.155\,e^{i\,102.55^\circ} \\ 0.436\,e^{-i\,104.08^\circ} & 0.658\,e^{i\,114.67^\circ} & 0.614\,e^{i\,102.55^\circ} \\ 0.365 & -0.517 & 0.774 \end{pmatrix} \overline{Q}\,. \tag{2.3.62}$$

Recasting this expression in the form of the standard parametrisation of $U_{\rm PMNS}$ we get:

$$U_{\rm PMNS} = P \begin{pmatrix} 0.822 & 0.547 & 0.155\,e^{i\,93.98^\circ} \\ 0.436\,e^{i\,169.41^\circ} & 0.658\,e^{i\,4.65^\circ} & 0.614 \\ 0.365\,e^{i\,16.04} & 0.517\,e^{i\,172.53} & 0.774 \end{pmatrix} Q_2\,\overline{Q}\,, \tag{2.3.63}$$

where $P = {\rm diag}(e^{i(16.04-7.47)^\circ}, e^{i\,102.55^\circ}, 1)$, $Q_2 = {\rm diag}(e^{-i\,16.04^\circ}, e^{i\,7.47^\circ}, 1)$ and $e^{i\,93.98^\circ} = e^{-\,i(360-93.98)^\circ} = e^{-\,i\,266.02^\circ}$.
Similarly, in the case of $\delta = 93.98$ and $\phi \simeq 257.45^\circ$ we obtain:

$$U_{\rm PMNS} = \begin{pmatrix} 0.822\,e^{i\,7.47^\circ} & 0.547\,e^{-i\,16.04^\circ} & 0.155\,e^{-i\,102.55^\circ} \\ 0.436\,e^{i\,104.08^\circ} & 0.658\,e^{-i\,114.67^\circ} & 0.614\,e^{-i\,102.55^\circ} \\ 0.365 & -0.517 & 0.774 \end{pmatrix} \overline{Q}\,. \tag{2.3.64}$$

Extracting again phases in diagonal matrices on the right hand and left hand sides to get the standard parametrisation of $U_{\rm PMNS}$ we find:

$$U_{\rm PMNS} = \tilde{P} \begin{pmatrix} 0.822 & 0.547 & 0.155\, e^{-i\,93.98^\circ} \\ 0.436\, e^{-i\,169.41^\circ} & 0.658\, e^{-i\,4.65^\circ} & 0.614 \\ 0.365\, e^{-i\,16.04} & 0.517\, e^{-i\,172.53} & 0.774 \end{pmatrix} \tilde{Q}_2\, \overline{Q}\,, \tag{2.3.65}$$

where $P = {\rm diag}(e^{i(-16.04+7.47)^\circ}, e^{-i\,102.55^\circ}, 1)$ and $\tilde{Q}_2 = {\rm diag}(e^{i\,16.04^\circ}, e^{-i\,7.47^\circ}, 1)$. The phases in the matrices P and $\tilde{P}$ can be absorbed by the charged lepton fields and are unphysical. In contrast, the phases in the matrices Q_2 and $\tilde{Q}_2$ contribute to the physical Majorana phases. We can finally write the Majorana phase matrix in the parametrization given in (1.2.1) ($\phi_1 = 0$):

$$-\frac{\beta_1}{2} = \mp 16.04^\circ - \beta - \frac{\phi_3}{2}\,, \quad \sin\delta = \mp\, 0.976\,, \tag{2.3.66}$$

$$-\frac{\beta_2}{2} = \pm 7.47^\circ - \beta - \frac{\phi_3 - \phi_2}{2}\,, \quad \sin\delta = \mp\, 0.976\,. \tag{2.3.67}$$

In order to calculate the phase $\beta = \gamma - \phi$ we have to find the value of γ. It follows from Eqs. (3.1.8) and (3.1.11) that

$$\cos\gamma = \frac{\sin\theta^e_{23}\cos\omega_e}{\sqrt{2}\sin\hat{\theta}_{23}}\,, \quad \sin\gamma = \frac{\pm\cos\theta^e_{23} - \sin\theta^e_{23}\sin\omega_e}{\sqrt{2}\sin\hat{\theta}_{23}}\,, \tag{2.3.68}$$

$$\cos\phi = \frac{\sin\theta^e_{23}\cos\omega_e}{\sqrt{2}\cos\hat{\theta}_{23}}\,, \quad \sin\phi = \frac{\mp\cos\theta^e_{23} - \sin\theta^e_{23}\sin\omega_e}{\sqrt{2}\cos\hat{\theta}_{23}}\,, \tag{2.3.69}$$

where we used the fact that $\psi_e = \pm\pi/2$. These equations imply the following relations:

$$\cos\gamma = \cos\phi\,\frac{\cos\hat{\theta}_{23}}{\sin\hat{\theta}_{23}}\,, \tag{2.3.70}$$

$$\sin\phi\cos\hat{\theta}_{23} + \sin\gamma\sin\hat{\theta}_{23} = -\sqrt{2}\sin\theta^e_{23}\sin\omega_e\,. \tag{2.3.71}$$

It is clear from Eq. (2.3.70) that the value of $\cos\gamma$ can be determined knowing the values of $\cos\phi$ and $\sin\hat{\theta}_{23}$, independently of the values of θ^e_{23} and ω_e. This, obviously, allows to find also $|\sin\gamma|$, but not the sign of $\sin\gamma$. In the case of $\sin\theta^e_{23}\sin\omega_e \ll 1$ of interest, Eq. (2.3.71) allows to correlate the sign of $\sin\gamma$ with the sign of $\sin\phi$ and thus to determine γ for a given ϕ: we have $\sin\gamma < 0$ if $\sin\phi > 0$, and $\sin\gamma > 0$ for $\sin\phi < 0$. Thus, for $\phi = 102.5530^\circ$ (corresponding to $\delta = 266.02^\circ$) we find $\gamma = -105.4118$ and $\beta = \gamma - \phi = -207.9648^\circ = -(180 + 27.9648)^\circ$, while for $\phi = -102.5530^\circ$ (corresponding to $\delta = 93.98^\circ$) we obtain $\gamma = +105.4118$ and $\beta = +207.96^\circ = +(180 + 27.96)^\circ$.

The results thus derived allow us to calculate numerically the Majorana CPV phases. For the best fit values of the neutrino mixing angles we get:

$$\beta_1 = (23.84 + 360 + \phi_3)^\circ\,,\ \beta_2 = (70.88 + 360 - \phi_2 + \phi_3)^\circ \text{ for } \phi = -102.55^\circ\ (\delta = 93.98^\circ)\,; \tag{2.3.72}$$

$$\beta_1 = (-23.84 - 360 + \phi_3)^\circ = (-23.84 + 360 + \phi_3)^\circ \,,$$
$$\beta_2 = (-70.88 - 360 - \phi_2 + \phi_3)^\circ = (-70.88 + 360 - \phi_2 + \phi_3)^\circ \text{ for } \phi = 102.55^\circ \ (\delta = 266.02^\circ) \,, \tag{2.3.73}$$

where we have used the fact that $\beta_{1(2)}$ and $\beta_{1(2)} + 4\pi$ lead to the same physical results. In the cases of the three types of neutrino mass spectrum allowed by the model, which are characterised, in particular, by specific values of the ϕ_2 and ϕ_3 we find:

- NO A spectrum, i.e., $\phi_2 = \phi_3 = 0$:

$$\beta_1 = (23.84 + 360)^\circ \,,\ \beta_2 = (70.88 + 360)^\circ \text{ for } \phi = -102.55^\circ \ (\delta = 93.98^\circ) \,,$$
$$\beta_1 = (-23.84 + 360)^\circ \,,\ \beta_2 = (-70.88 + 360)^\circ \text{ for } \phi = 102.55^\circ \ (\delta = 266.02^\circ) \,; \tag{2.3.74}$$

- NO B spectrum, i.e., $\phi_2 = 0$ and $\phi_3 = \pi$:

$$\beta_1 = (23.84 + 540)^\circ \,,\ \beta_2 = (70.88 + 540)^\circ \text{for } \phi = -102.55^\circ \ (\delta = 93.98^\circ) \,,$$
$$\beta_1 = (-23.84 + 540)^\circ \,,\ \beta_2 = (-70.88 + 540)^\circ \text{for } \phi = 102.55^\circ \ (\delta = 266.02^\circ) \,; \tag{2.3.75}$$

- IO spectrum, $\phi_3 = 0$ and $\phi_2 = \pi$:

$$\beta_1 = (23.84 + 360)^\circ \,,\ \beta_2 = (70.88 + 180)^\circ \text{ for } \phi = -102.55^\circ \ (\delta = 93.98^\circ) \,,$$
$$\beta_1 = (-23.84 + 360)^\circ \,,\ \beta_2 = (-70.88 + 180)^\circ \text{ for } \phi = 102.55^\circ \ (\delta = 266.02^\circ) \,, \tag{2.3.76}$$

where again we have used the fact that $\beta_{1(2)}$ and $\beta_{1(2)} + 4\pi$ are physically indistinguishable.

The Neutrinoless Double Beta Decay Effective Majorana Mass

Knowing the values of the neutrino masses and the Majorana and Dirac CPV phases we can derive predictions for the neutrinoless double beta ($(\beta\beta)_{0\nu}$-) decay effective Majorana mass $|\langle m \rangle|$ (see, e.g., [17]). Since $|\langle m \rangle|$ depends only on the cosines of the CPV phases, we get the same result for $\phi = +102.55^\circ$ ($\delta = 266.02^\circ$) and $\phi = -102.55^\circ$ ($\delta = 93.98^\circ$).

Thus, for $\phi = \pm 102.55^\circ$, using the best fit values of the neutrino mixing angles, we obtain:

$$|\langle m \rangle| = 4.88 \times 10^{-3}\,\text{eV} \,, \quad \text{NO A spectrum} \,; \tag{2.3.77}$$

$$|\langle m \rangle| = 7.30 \times 10^{-3}\,\text{eV} \,, \quad \text{NO B spectrum} \,; \tag{2.3.78}$$

$$|\langle m \rangle| = 26.34 \times 10^{-3}\,\text{eV} \,, \quad \text{IO spectrum} \,. \tag{2.3.79}$$

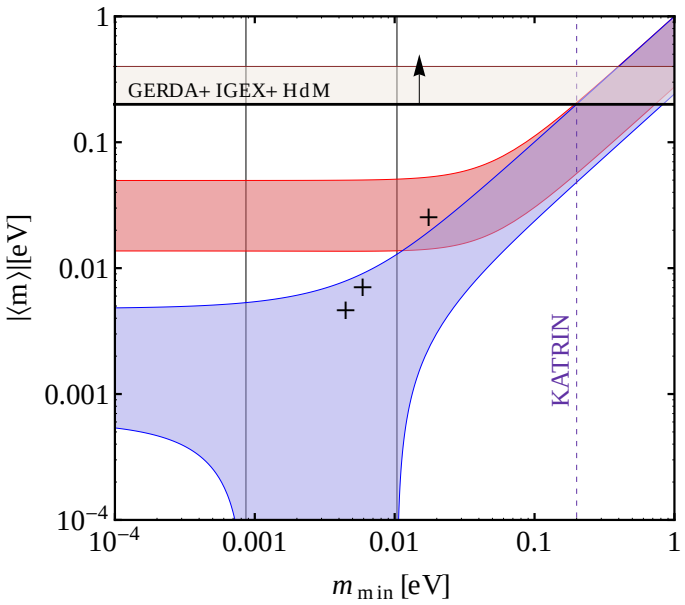

Figure 2.2: The 3σ allowed regions of values of the effective Majorana mass $|\langle m\rangle|$ as functions of the lightest neutrino mass m_{min} for the NO (blue area) and IO (red area) neutrino mass spectra. The regions are obtained by using the experimentally determined values of the neutrino oscillation parameters (including the 1σ uncertainties) quoted in Table 1. The black crosses correspond to the predictions of the model constructed in the present chapter, Eqs. (2.3.77) - (2.3.79). The horizontal band indicates the upper bound $|\langle m\rangle| \sim 0.2 - 0.4$ eV obtained using the 90 % C.L. limit on the half-life of ^{76}Ge reported in [118]. The dotted line represents the prospective upper limit from the β-decay experiment KATRIN [29].

In Fig. 2.2 we show the general phenomenologically allowed 3σ range of values of $|\langle m\rangle|$ for the NO (blue area) and IO (red area) neutrino mass spectra as a function of the lightest neutrino mass. The values of $|\langle m\rangle|$ quoted above and corresponding to the three types of neutrino mass spectrum (NO A, NO B and IO), predicted by the model constructed in the present chapter, are indicated with black crosses. The vertical lines in Fig. 2.2 correspond to $m_{min} = 8.6 \times 10^{-4}\,\text{eV}$ and $1.0 \times 10^{-2}\,\text{eV}$; for a given value of m_{min} from the interval determined by these two values, $[8.6 \times 10^{-4}, 1.0 \times 10^{-2}]$ eV, one can have $|\langle m\rangle| = 0$ for specific values of the Majorana CPV phases.

Limiting Cases

Finally, there are two interesting limiting forms of the charged lepton Yukawa coupling (mass) matrix Y_e: they correspond to i) $k = 0$, i.e., $\eta = 0$ or π, and ii) $d = 0$, i.e., $\eta = \pm\pi/2$. In the case of $k = 0$, the TBM prediction for θ_{12} does not depend on θ_{23}^e anymore; if $d = 0$, even θ_{23} itself does not depend on θ_{23}^e anymore. Up to next-to-leading order we find:

$$\begin{aligned} &\text{i)}\ \sin^2\theta_{12} = \frac{1}{3} + \frac{1}{3}\sin^2\theta_{13} \approx \frac{1}{3} \ \text{for}\ k = 0, \eta = 0, \pi\ , \\ &\text{ii)}\ \sin^2\theta_{23} = \frac{1}{2} - \frac{1}{2}\sin^2\theta_{13} \approx \frac{1}{2} \ \text{for}\ d = 0, \eta = \pm\pi/2\ , \end{aligned} \tag{2.3.80}$$

where we have written the corrections in terms of θ_{13}. Both cases could be realised by choosing a certain set of messengers. If we remove the messenger pair $\Sigma^A_{2'}$, $\bar{\Sigma}^A_{2''}$, our model would correspond to the case i), while if we remove the messenger pair $\Sigma^C_{1''}$, $\bar{\Sigma}^C_{1'}$, the model would correspond to the case ii). The model we have constructed, which includes both messenger pairs, gives a somewhat better description of the current data on the neutrino mixing angles. This brief discussion shows how important the messenger sector can be for getting meaningful predictions.

2.4 Messenger Sector

The effective model we have considered so far contains only non-renormalisable operators allowed by the symmetry group $G_f \times Z_2 \times Z_3^2 \times Z_4^2 \times Z_8 \times U(1)_R$. But in fact using only this symmetry there would be more effective operators allowed which might spoil our model predictions.

Therefore we discuss in this section the so-called ultraviolet completion defining a renormalisable theory which gives the effective model described in the previous sections after integrating out the heavy messenger superfields. In this way we can justify why we have chosen only a certain subset of the effective operators allowed by the symmetries. The quantum numbers of the messenger fields are given in Table 2.8. We label them with Σ, Ξ and Δ for the charged lepton, neutrino and flavon sector respectively.

	$SU(2)$	$U(1)_Y$	T'	$U(1)_R$	Z_8	Z_4	Z_4	Z_3	Z_3	Z_2
Ξ_1 , $\bar{\Xi}_1$	**2** ,**2**	1,1	**1** ,**1**	0,2	7,1	0,0	0,0	0,0	1,2	0,0
Σ_1^A,$\bar{\Sigma}_1^A$	**2** ,**2**	1,1	**1** ,**1**	1,1	1,7	3,1	3,1	2,1	1,2	1,1
Σ_1^B,$\bar{\Sigma}_1^B$	**1** ,**1**	2,2	**1** ,**1**	1,1	2,6	1,3	1,3	2,1	0,0	1,1
$\Sigma_{1'}^A$,$\bar{\Sigma}_{1''}^A$	**2** ,**2**	1,1	**1′**,**1″**	1,1	7,1	3,1	3,1	0,0	2,1	0,0
$\Sigma_{1'}^B$,$\bar{\Sigma}_{1''}^B$	**1** ,**1**	2,2	**1′**,**1″**	1,1	0,0	1,3	1,3	0,0	1,2	0,0
$\Sigma_{1''}^A$,$\bar{\Sigma}_{1'}^A$	**2** ,**2**	1,1	**1″** ,**1′**	1,1	1,7	3,1	3,1	2,1	1,2	1,1
$\Sigma_{1''}^B$,$\bar{\Sigma}_{1'}^B$	**2** ,**2**	1,1	**1″** ,**1′**	1,1	1,7	3,1	1,3	0,0	0,0	0,0
$\Sigma_{1''}^C$,$\bar{\Sigma}_{1'}^C$	**2** ,**2**	1,1	**1″** ,**1′**	1,1	6,2	3,1	0,0	1,2	1,2	0,0
$\Sigma_{2'}^A$,$\bar{\Sigma}_{2''}^A$	**2** ,**2**	1,1	**2′**,**2″**	1,1	0,0	1,3	0,0	1,2	1,2	0,0
$\Sigma_{2''}^A$,$\bar{\Sigma}_{2'}^A$	**2** ,**2**	1,1	**2″** ,**2′**	1,1	0,0	1,3	0,0	1,2	1,2	0,0
Δ_1^A,$\bar{\Delta}_1^A$	**1** ,**1**	0,0	**1** ,**1**	0,2	0,0	2,2	0,0	0,0	0,0	0,0
Δ_1^B,$\bar{\Delta}_1^B$	**1** ,**1**	0,0	**1** ,**1**	0,2	0,0	0,0	0,0	2,1	2,1	0,0
$\Delta_{1'}^A$,$\bar{\Delta}_{1''}^A$	**1** ,**1**	0,0	**1′**,**1″**	0,2	0,0	0,0	0,0	0,0	2,1	0,0
$\Delta_{2'}^A$,$\bar{\Delta}_{2''}^A$	**1** ,**1**	0,0	**2′**,**2″**	0,2	0,0	0,0	3,1	1,2	1,2	1,1
Δ_3^A,$\bar{\Delta}_3^A$	**1** ,**1**	0,0	**3** ,**3**	0,2	4,4	0,0	0,0	0,0	0,0	1,1
Δ_3^B,$\bar{\Delta}_3^B$	**1** ,**1**	0,0	**3** ,**3**	0,2	6,2	2,2	0,0	1,2	0,0	1,1
Δ_3^C,$\bar{\Delta}_3^C$	**1** ,**1**	0,0	**3** ,**3**	0,2	6,2	1,3	2,2	0,0	1,2	0,0
Δ_3^D,$\bar{\Delta}_3^D$	**1** ,**1**	0,0	**3** ,**3**	0,2	5,3	0,0	3,1	0,0	1,2	0,0
Δ_3^E,$\bar{\Delta}_3^E$	**1** ,**1**	0,0	**3** ,**3**	0,2	2,6	0,0	2,2	2,1	0,0	0,0

Table 2.8: List of the messengers fields and their transformation properties.

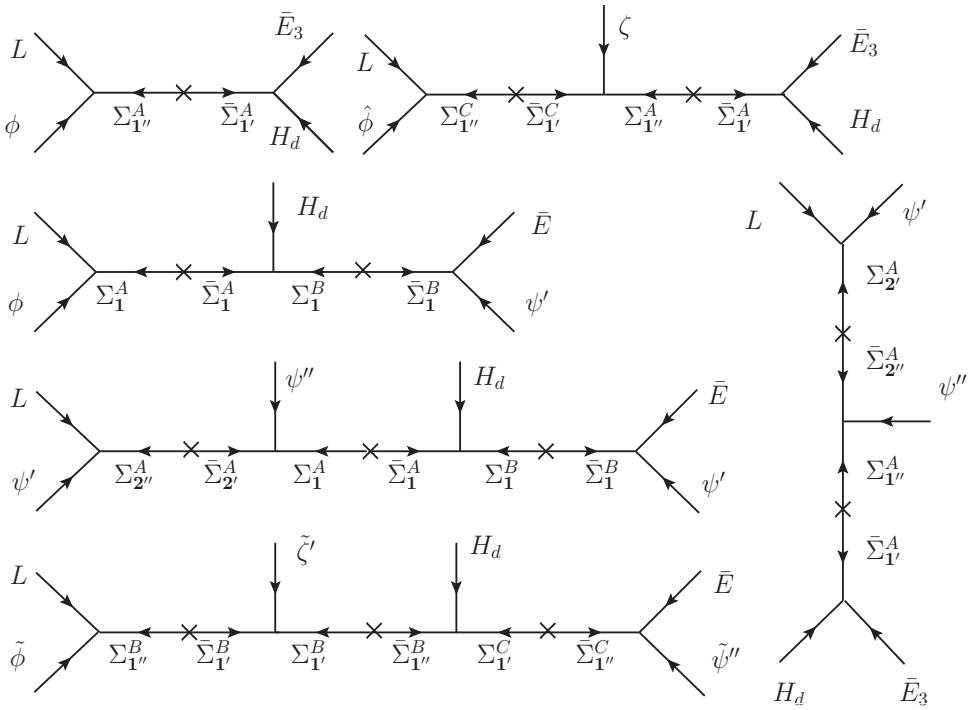

Figure 2.3: The supergraphs before integrating out the messengers for the charged lepton sector.

For the charged lepton sector we find the renormalisable superpotential $\mathcal{W}_e^{\rm ren}$

$$\begin{aligned}\mathcal{W}_e^{\rm ren} &= L\,\phi\,\Sigma^A_{1''} + L\,\phi\,\Sigma^A_{1} + \bar{E}_3\,H_d\,\bar{\Sigma}^A_{1'} + L\,\hat{\phi}\,\Sigma^C_{1''} + \zeta\,\bar{\Sigma}^C_{1'}\,\Sigma^A_{1''} + H_d\,\bar{\Sigma}^A_{1}\,\Sigma^B_{1} \\ &+ \bar{E}\,\psi'\,\bar{\Sigma}^B_{1} + L\,\psi'\,\Sigma^A_{2''} + \psi''\,\bar{\Sigma}^A_{2'}\,\Sigma^A_{1} + L\,\tilde{\phi}\,\Sigma^B_{1'} + \tilde{\zeta}'\,\bar{\Sigma}^B_{1'}\,\Sigma^B_{1'} \\ &+ H_d\,\bar{\Sigma}^B_{1''}\,\Sigma^C_{1'} + \bar{E}\,\tilde{\psi}''\,\bar{\Sigma}^C_{1''} + L\,\psi'\,\Sigma^A_{2'} + \psi''\,\bar{\Sigma}^A_{2''}\,\Sigma^A_{1''}\,,\end{aligned} \tag{2.4.1}$$

which through the diagrams of Fig. 2.3 generates at low energy the non-renormalisable superpotential $\mathcal{W}_{Y_e}$ of Eq. (2.3.12).

For the neutrino and the flavon sector we obtained similarly to the previous case

$$\mathcal{W}_\nu^{\rm ren} = N^2\xi + N^2\rho + N^2\tilde{\rho} + LN\Xi_1 + H_u\bar{\Xi}_1\rho + H_u\bar{\Xi}_1\tilde{\rho}\,, \tag{2.4.2}$$

$$\begin{aligned}\mathcal{W}_{\rm flavon}^{\rm ren} &= D_\phi\,\phi\,\Delta^B_3 + \varepsilon_3\,\phi\,\bar{\Delta}^B_3 + D_\phi\,\zeta''\,\Delta^B_3 + \tilde{D}_\phi\,\tilde{\phi}\,\Delta^C_3 + \varepsilon_1\,\tilde{\phi}\,\bar{\Delta}^C_3 + \tilde{D}_\phi\,\tilde{\zeta}'\,\Delta^C_3 \\ &+ \hat{D}_\phi\,\hat{\phi}\,\Delta^D_3 + \varepsilon_4\,\hat{\phi}\,\bar{\Delta}^D_3 + \hat{D}_\phi\,\tilde{\zeta}''\,\Delta^E_3 + \varepsilon_5\,\tilde{\phi}\,\bar{\Delta}^E_3 + \tilde{S}_\zeta\,\tilde{\zeta}''\,\Delta^A_{1'} + \tilde{\zeta}''\,\tilde{\zeta}''\,\bar{\Delta}^A_{1''} \\ &+ S_{\varepsilon_4}\,\varepsilon_4\,\Delta^B_1 + \varepsilon_4\,\varepsilon_4\,\bar{\Delta}^B_1 + \varepsilon_1\,\varepsilon_1\,\bar{\Delta}^A_1 + S_{\varepsilon_1}\,\Delta^A_1\,\Delta^A_1\,.\end{aligned} \tag{2.4.3}$$

The corresponding diagrams that generate the effective operators in the neutrino and flavon sector in our model are given in Figs. 2.4 and 2.5.

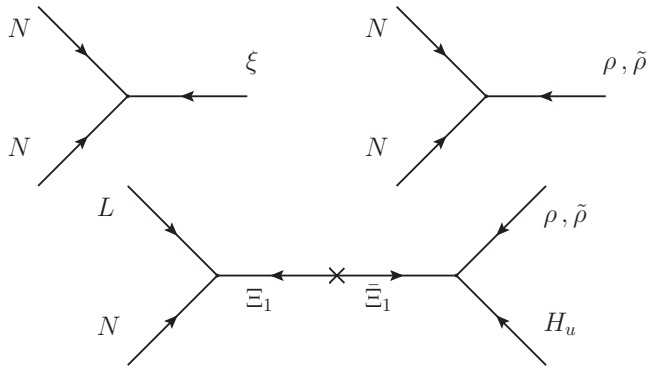

Figure 2.4: The supergraphs before integrating out the messengers for the neutrino sector.

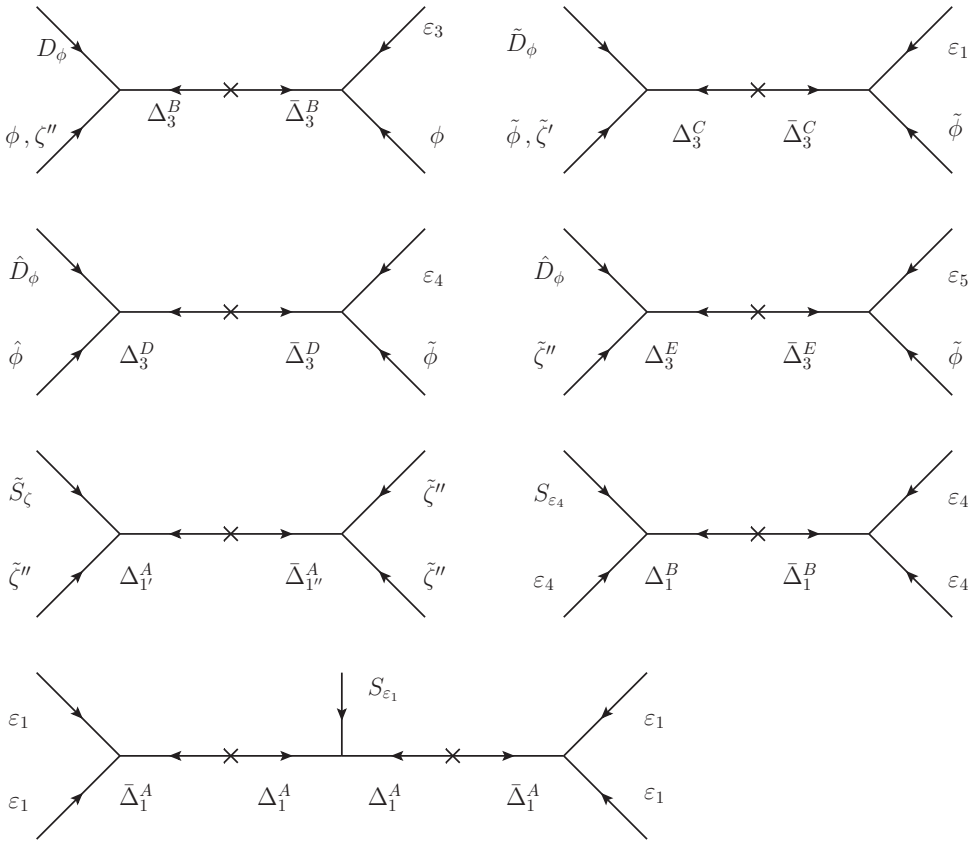

Figure 2.5: The supergraphs before integrating out the messengers for the flavon sector. We have omitted for simplicity the supergraphs of the higher order corrections in the flavon superpotential.

2.5 Summary and Conclusions

We have analyzed the presence of a generalised CP symmetry, $H_{\rm CP}$, combined with the non-Abelian discrete group T' in the lepton flavour space, i.e. the possibility of the existence of a symmetry group $G_f = T' \rtimes H_{\rm CP}$ acting among the three generations of charged leptons and neutrinos. The phenomenological implications of the breaking of such a symmetry group both in the charged lepton and neutrino sectors are thus explored especially in connection with the CP violation appearing in the leptonic mixing matrix, $U_{\rm PMNS}$.

First of all we have derived in Section 2.2 all the possible generalised CP transformations for all the representations of the T' group i.e. we found all possible outer automorphisms of the group T' following the consistency conditions given in [112, 113, 115]. We have chosen as generalised CP symmetry the transformation $u : (T, S) \to (T^2, S^2T^2ST)$ which corresponds to a Z_2 symmetry and it is defined up to an inner automorphism. The transformation u is particularly convenient since, in the basis chosen for the generators S and T, for the 1 and 3-dimensional representations it is trivially defined as the identity up to a global unphysical phase θ_r where the index r refers to the representation. More importantly we found that, given this specific generalised CP symmetry combined with T', it is possible to fix the vevs of the flavon fields to real values in such a way that no complex phases, and thus no physical CP violation, stem from the vevs themselves.

Moreover, for a list of possible renormalisable operators, namely $\lambda\mathcal{O} = \lambda(A \times B \times C)$ where λ is the coupling constant and A, B, C are fields, we derived the constraints on the phase λ under the assumption of invariance under the generalised CP transformation. This list of possible operators can be used to construct a CP-conserving renormalisable superpotential for the flavon sector and therefore can be used in order to show that real vev structures can be achieved.

Motivated by this preliminary study we constructed in Section 2.3 a supersymmetric flavour model able to describe the observed patterns and mixing for three generations of charged lepton fields and the three light active neutrinos.

We have constructed an effective superpotential with operators up to mass dimension six giving the charged lepton and neutrino Yukawa couplings and the Majorana mass term for the RH neutrinos. Naturally small neutrino masses are generated by the type I see-saw mechanism. At leading order, the mixing in the neutrino sector is described by the tri-bimaximal mixing, which is then perturbed by additional contributions coming from the charged lepton sector. The latter are responsible for the compatibility of the predictions on the mixing angles with the experimental values and, in particular, with the non-zero value of the reactor mixing angle θ_{13}.

Similarly to what was found in [90], we find that both types of neutrino mass spectrum — with normal ordering (NO) and inverted ordering (IO) — are possible within the model and that the NO spectrum can be of two varieties, A and B. They differ by the value of the lightest neutrino mass. Only one spectrum of the IO type is compatible with the model. For each of the three neutrino mass spectra, NO A, NO B and IO, the absolute scale of neutrino masses is predicted with relatively small uncertainty. This allows us to

predict the value of the sum of the neutrino masses for the three spectra. The Dirac phase δ is predicted to be approximately $\delta \cong \pi/2$ or $3\pi/2$. More concretely, for the best fit values of the neutrino mixing angles quoted in Table 1.1 we get $\delta = 93.98°$ or $\delta = 266.02°$. The deviations of δ from the values $90°$ and $270°$ are correlated with the deviation of atmospheric neutrino mixing angle θ_{23} from $\pi/4$. Thus, the CP violating effects in neutrino oscillations are predicted to be nearly maximal (given the values of the neutrino mixing angles) and experimentally observable. The values of the Majorana CPV phases are also predicted by the model. This allows us to predict the neutrinoless double beta decay effective Majorana mass in each of the three cases of neutrino mass spectrum allowed by the model, NO A, NO B and IO. The predictions of the model can be tested in ongoing and future planned i) accelerators experiments searching for CP violation in neutrino oscillations (T2K, NOνA, etc.), ii) experiments aiming to determine the absolute neutrino mass scale, and iii) experiments searching for neutrinoless double beta decay.

It is important to comment that in this model the physical CP violation emerging in the PMNS mixing matrix stems only from the charged lepton sector. Indeed, in the neutrino sector the Majorana mass matrix and the Dirac Yukawa couplings are real and the CP violation is caused by the complex CP violating phases arising in the charged lepton sector. The presence of the latter is a consequence of the requirement of invariance of the theory under the generalised CP symmetry at the fundamental level and of the complex CGs of the T' group.

We also found that the residual group in the charged lepton sector is trivial i.e. $G_e = \emptyset$ and since the phases of the flavon vevs are completely independent of the coupling constants of the flavon superpotential, the CP symmetry is broken geometrically (according to the definition of "geometrical CP violation" given in [108]). In the neutrino sector, the residual subgroup is instead a Klein group, $G_\nu = K_4 = Z_2 \times Z_2$ with one Z_2 coming from the generalised CP symmetry $H_{\rm CP}$.

Concluding, we have shown that the spontaneous breaking of a symmetry group $G_f = T' \rtimes H_{\rm CP}$ in the leptonic sector through a real flavon vev structure is possible and, at the same time, CP violation in the leptonic sector can take place. In this scenario the appearance of the CP violating phases in the PMNS mixing matrix can be traced to two factors: i) the requirement of invariance of the Lagrangian of the theory under $H_{\rm CP}$ at the fundamental level, and ii) the complex CGs of the T' group. The model we have constructed allows for two neutrino mass spectra with normal ordering (NO) and one with inverted ordering (IO). For each of the three spectra the absolute scale of neutrino masses is predicted with relatively small uncertainty. The value of the Dirac CP violation (CPV) phase δ in the lepton mixing matrix is predicted to be $\delta \cong \pi/2$ or $3\pi/2$. Thus, the CP violating effects in neutrino oscillations are predicted to be nearly maximal and experimentally observable. We present also predictions for the sum of the neutrino masses, for the Majorana CPV phases and for the effective Majorana mass in neutrinoless double beta decay. The predictions of the model can be tested in a variety of ongoing and future planned neutrino experiments.

CHAPTER 3

Dirac CP Violation Phase from Sum Rules

3.1 The Sum Rules

In the present Chapter we continue the investigation of the discrete symmetry approach to understanding of the pattern of neutrino mixing. In Chapter 2 we have done it on the example of a specific self-consistent model with T' lepton flavour symmetry we have constructed. In this Chapter we follow a more general phenomenological approach [119]. We consider several possible symmetry forms of the matrix U_ν of the PMNS matrix $U = U_e^\dagger U_\nu$ combined with the requirement that the "correcting" matrix U_e has a minimal possible form in terms of number of angles and phases it contains. We further analyse in detail the predictions for the Dirac phase δ which can be obtained for the different symmetry forms of U_ν within the outlined approach.

In the framework of the reference 3 flavour neutrino mixing we will consider in this chapter, the PMNS neutrino mixing matrix is always given by Eq. 2.1.1. We will suppose in what follows that U_ν has a form which is dictated by symmetries. More specifically, we will assume that

$$U_\nu = \Psi_1 \, \tilde{U}_\nu \, Q_0 = \Psi_1 \, R_{23}\left(\theta_{23}^\nu\right) R_{12}\left(\theta_{12}^\nu\right) Q_0 \,, \tag{3.1.1}$$

where $R_{23}(\theta_{23}^\nu)$ and $R_{12}(\theta_{12}^\nu)$ are orthogonal matrices describing rotations in the 2-3 and 1-2 planes, respectively, and Ψ_1 and Q_0 are diagonal phase matrices each containing two phases. Obviously, the phases in the matrix Q_0 give contribution to the Majorana phases in the PMNS matrix. In the present chapter we will consider the following symmetry forms of the matrix $\tilde{U}_\nu$: i) tri-bimaximal (TBM) [93], ii) bimaximal (BM), or due to a symmetry corresponding to the conservation of the lepton charge $L' = L_e - L_\mu - L_\tau$ (LC) [94, 95], iii) golden ratio type A (GRA) form [120, 121], iv) golden ratio type B (GRB) form [122], and v) hexagonal (HG) form [92, 123]. The TBM, BM, GRA, GRB and HG forms can be obtained respectively from, e.g., T'/A_4, S_4, A_5, D_{10} and D_{12} discrete (lepton) flavour symmetries (see, e.g., [77, 98, 100, 101, 120–123]). In all these cases we have $\theta_{23}^\nu = -\pi/4$,

and the matrix $\tilde{U}_\nu$ is given by

$$\tilde{U}_\nu = \begin{pmatrix} \cos\theta^\nu_{12} & \sin\theta^\nu_{12} & 0 \\ -\frac{\sin\theta^\nu_{12}}{\sqrt{2}} & \frac{\cos\theta^\nu_{12}}{\sqrt{2}} & -\frac{1}{\sqrt{2}} \\ -\frac{\sin\theta^\nu_{12}}{\sqrt{2}} & \frac{\cos\theta^\nu_{12}}{\sqrt{2}} & \frac{1}{\sqrt{2}} \end{pmatrix} . \tag{3.1.2}$$

The TBM, BM (LC), GRA, GRB and HG forms of $\tilde{U}_\nu$ correspond to different fixed values of θ^ν_{12} and thus of $\sin^2\theta^\nu_{12}$, namely, to i) $\sin^2\theta^\nu_{12} = 1/3$, ii) $\sin^2\theta^\nu_{12} = 1/2$, iii) $\sin^2\theta^\nu_{12} = (2+r)^{-1} \cong 0.276$, r being the golden ratio, $r = (1+\sqrt{5})/2$, iv) $\sin^2\theta^\nu_{12} = (3-r)/4 \cong 0.345$, and v) $\sin^2\theta^\nu_{12} = 1/4$. Thus, the matrix U_e in eq. (2.3.40) should provide corrections which not only generate nonzero value of θ_{13}, but also lead to reactor, atmospheric and solar neutrino mixing angles θ_{13}, θ_{23} and θ_{12} which have values compatible with the current data, including a possible sizeable deviation of θ_{23} from $\pi/4$. As was shown in [74], the "minimal" form of U_e, in terms of angles and phases it contains, that can provide the requisite corrections to U_ν includes a product of two orthogonal matrices describing rotations in the 2-3 and 1-2 planes, $R_{23}(\theta^e_{23})$ and $R_{12}(\theta^e_{12})$, θ^e_{23} and θ^e_{12} being two (real) angles. In what follows we will adopt this minimal form of U_e. It proves convenient to cast it in the form [74]:

$$U_e = \Psi_2^\dagger \tilde{U}_e = \Psi_2^\dagger R^{-1}_{23}(\theta^e_{23}) R^{-1}_{12}(\theta^e_{12}) , \tag{3.1.3}$$

where Ψ_2 is a diagonal phase matrix including two phases, and

$$R_{12}(\theta^e_{12}) = \begin{pmatrix} \cos\theta^e_{12} & \sin\theta^e_{12} & 0 \\ -\sin\theta^e_{12} & \cos\theta^e_{12} & 0 \\ 0 & 0 & 1 \end{pmatrix} , \quad R_{23}(\theta^e_{23}) = \begin{pmatrix} 1 & 0 & 0 \\ 0 & \cos\theta^e_{23} & \sin\theta^e_{23} \\ 0 & -\sin\theta^e_{23} & \cos\theta^e_{23} \end{pmatrix} . \tag{3.1.4}$$

Thus, the PMNS matrix in the approach we are following is given by

$$U = U_e^\dagger U_\nu = R_{12}(\theta^e_{12})\, R_{23}(\theta^e_{23})\, \Psi\, R_{23}(\theta^\nu_{23})\, R_{12}(\theta^\nu_{12})\, Q_0 , \;\; \Psi = \Psi_2\Psi_1 , \;\; \theta^\nu_{23} = -\frac{\pi}{4} . \tag{3.1.5}$$

The matrices Ψ and Q_0 are diagonal phase matrices each containing, in general, two physical CPV phases [1] [83]:

$$\Psi = \mathrm{diag}\left(1, e^{-i\psi}, e^{-i\omega}\right) , \quad Q_0 = \mathrm{diag}\left(1, e^{i\frac{\xi_{21}}{2}}, e^{i\frac{\xi_{31}}{2}}\right) . \tag{3.1.6}$$

As was explained earlier, the requirement that U_e has a "minimal" form in terms of angles and phases it contains, needed to provide the requisite corrections to U_ν, makes not necessary the inclusion in $\tilde{U}_e$ of the orthogonal matrix describing the rotation in the 1-3 plane, $R_{13}(\theta^e_{13})$. Effectively, this is equivalent to the assumption that the angle θ^e_{13}, if

[1] The diagonal phase matrix Ψ, as we see, can originate from the charged lepton or the neutrino sector, or else can receive contributions from both sectors [83].

nonzero, is sufficiently small and thus is either negligible, or leads to sub-dominant effects in the observable of interest in the present analysis, $\cos\delta$. We will use $\theta^e_{13} \cong 0$ to denote values of θ^e_{13} which satisfy the indicated condition.

We note that $\theta^e_{13} \cong 0$ is a feature of many theories of charged lepton and neutrino mass generation (see, e.g., [86, 88–91, 98, 100, 101, 120, 124]). The assumption that $\theta^e_{13} \cong 0$ was also used in a large number of studies dedicated to the problem of understanding the origins of the observed pattern of lepton mixing (see, e.g., [83–86, 91, 125, 126]). In wide class of GUT inspired models of flavour, the matrix U_e is directly related to the quark mixing matrix (see, e.g., [86, 88–91, 100, 101, 127]). As a consequence, in this class of models we have $\theta^e_{13} \cong 0$. We will comment later on the possible effects of $\theta^e_{13} \neq 0$, $|\sin\theta^e_{13}| \ll 1$, on the predictions for $\cos\delta$, which are of principal interest of the present study.

More generally, the approach to understanding the observed pattern of neutrino mixing on the basis of discrete symmetries employed here, which leads to the sum rule of interest for $\cos\delta$, is by no means unique — it is one of the several possible approaches discussed in the literature on the subject (see, e.g., [78]). It is employed in a large number of phenomenological studies (see, e.g., [83–86, 91, 125, 126]) as well as in a class of models (see, e.g., [86, 88–91, 98, 100, 101, 127]) of neutrino mixing based on discrete symmetries. However, it should be clear that the conditions which define the approach used here, are not fulfilled in all models with discrete flavour symmetries. For example, they are not fulfilled in the models with discrete flavour symmetry $\Delta(6n^2)$ studied in [128, 129], with the S_4 flavour symmetry constructed in [130] and in the models discussed in [91].

Following [74], we will use the following rearrangement of the product of matrices $R_{23}(\theta^e_{23})\Psi R_{23}(\theta^\nu_{23} = -\pi/4)$ in the expression eq. (3.1.5) for $U_{\rm PMNS}$:

$$R_{23}(\theta^e_{23})\,\Psi\,R_{23}(\theta^\nu_{23} = -\pi/4) = P_1\,\Phi\,R_{23}(\hat{\theta}_{23})\,Q_1\,, \tag{3.1.7}$$

where the angle $\hat{\theta}_{23}$ is determined by

$$\sin^2\hat{\theta}_{23} = \frac{1}{2}\,\left(1 - 2\sin\theta^e_{23}\cos\theta^e_{23}\cos(\omega - \psi)\right)\,, \tag{3.1.8}$$

and

$$P_1 = {\rm diag}\left(1, 1, e^{-\,i\alpha}\right)\,,\;\; \Phi = {\rm diag}\left(1, e^{i\phi}, 1\right)\,,\;\; Q_1 = {\rm diag}\left(1, 1, e^{i\beta}\right)\,. \tag{3.1.9}$$

In eq. (3.1.9)

$$\alpha = \gamma + \psi + \omega\,, \qquad \beta = \gamma - \phi\,, \tag{3.1.10}$$

and

$$\gamma = \arg\left(-e^{-i\psi}\cos\theta^e_{23} + e^{-i\omega}\sin\theta^e_{23}\right)\,,\;\; \phi = \arg\left(e^{-i\psi}\cos\theta^e_{23} + e^{-i\omega}\sin\theta^e_{23}\right)\,. \tag{3.1.11}$$

The phase α in the matrix P_1 can be absorbed in the τ lepton field and, thus, is unphysical. The phase β gives a contribution to the matrix $\hat{Q} = Q_1\,Q_0$; the diagonal phase matrix $\hat{Q}$ contributes to the matrix of physical Majorana phases. In the setting considered the PMNS matrix takes the form:

$$U_{\rm PMNS} = R_{12}(\theta^e_{12})\,\Phi(\phi)\,R_{23}(\hat{\theta}_{23})\,R_{12}(\theta^\nu_{12})\,\hat{Q}\,, \tag{3.1.12}$$

where θ_{12}^{ν} has a fixed value which depends on the symmetry form of $\tilde{U}_{\nu}$ used. For the angles θ_{13}, θ_{23} and θ_{12} of the standard parametrisation of the PMNS matrix U we get in terms of the parameters in the expression eq. (3.1.12) for U [74]:

$$\sin\theta_{13} = |U_{e3}| = \sin\theta_{12}^{e}\sin\hat{\theta}_{23}\,, \tag{3.1.13}$$

$$\sin^2\theta_{23} = \frac{|U_{\mu 3}|^2}{1-|U_{e3}|^2} = \sin^2\hat{\theta}_{23}\,\frac{\cos^2\theta_{12}^{e}}{1-\sin^2\theta_{12}^{e}\sin^2\hat{\theta}_{23}} = \frac{\sin^2\hat{\theta}_{23}-\sin^2\theta_{13}}{1-\sin^2\theta_{13}}\,, \tag{3.1.14}$$

$$\begin{aligned}\sin^2\theta_{12} = \frac{|U_{e2}|^2}{1-|U_{e3}|^2} &= \left(1-\cos^2\theta_{23}\cos^2\theta_{13}\right)^{-1}\,\Big[\sin^2\theta_{12}^{\nu}\sin^2\theta_{23} \\ &+ \cos^2\theta_{12}^{\nu}\cos^2\theta_{23}\sin^2\theta_{13} + \frac{1}{2}\,\sin 2\theta_{12}^{\nu}\sin 2\theta_{23}\sin\theta_{13}\cos\phi\Big]\,,\end{aligned} \tag{3.1.15}$$

where eq. (3.1.13) was used in order to obtain the expression for $\sin^2\theta_{23}$ in terms of $\hat{\theta}_{23}$ and θ_{13}, and eqs. (3.1.13) and (3.1.14) were used to get the last expression for $\sin^2\theta_{12}$. Within the approach employed, the expressions in eqs. (3.1.13) – (3.1.15) are exact.

It follows from eqs. (1.2.5), (1.2.3) and (3.1.12) that the four observables θ_{12}, θ_{23}, θ_{13} and δ are functions of three parameters θ_{12}^{e}, $\hat{\theta}_{23}$ and ϕ. As a consequence, the Dirac phase δ can be expressed as a function of the three PMNS angles θ_{12}, θ_{23} and θ_{13} [74], leading to a new "sum rule" relating δ and θ_{12}, θ_{23} and θ_{13}. For an arbitrary fixed value of the angle θ_{12}^{ν} the sum rule for $\cos\delta$ reads [75]:

$$\cos\delta = \frac{\tan\theta_{23}}{\sin 2\theta_{12}\sin\theta_{13}}\,\left[\cos 2\theta_{12}^{\nu} + \left(\sin^2\theta_{12}-\cos^2\theta_{12}^{\nu}\right)\,\left(1-\cot^2\theta_{23}\,\sin^2\theta_{13}\right)\right]\,. \tag{3.1.16}$$

For $\theta_{12}^{\nu} = \pi/4$ and $\theta_{12}^{\nu} = \sin^{-1}(1/\sqrt{3})$ the expression eq. (3.1.16) for $\cos\delta$ reduces to those found in [74] in the BM (LC) and TBM cases, respectively. A similar sum rule for an arbitrary θ_{12}^{ν} can be derived for the phase ϕ [74, 75]. It proves convenient for our further discussion to cast the sum rules for $\cos\delta$ and $\cos\phi$ of interest in the form:

$$\sin^2\theta_{12} = \cos^2\theta_{12}^{\nu} + \frac{\sin 2\theta_{12}\sin\theta_{13}\cos\delta - \tan\theta_{23}\cos 2\theta_{12}^{\nu}}{\tan\theta_{23}(1-\cot^2\theta_{23}\,\sin^2\theta_{13})}\,, \tag{3.1.17}$$

$$\sin^2\theta_{12} = \cos^2\theta_{12}^{\nu} + \frac{1}{2}\sin 2\theta_{23}\,\frac{\sin 2\theta_{12}^{\nu}\,\sin\theta_{13}\,\cos\phi - \tan\theta_{23}\cos 2\theta_{12}^{\nu}}{(1-\cos^2\theta_{23}\,\cos^2\theta_{13})}\,. \tag{3.1.18}$$

The phases δ and ϕ are related by [75]:

$$\sin\delta = -\,\frac{\sin 2\theta_{12}^{\nu}}{\sin 2\theta_{12}}\,\sin\phi\,, \tag{3.1.19}$$

$$\begin{aligned}\cos\delta = \frac{\sin 2\theta_{12}^{\nu}}{\sin 2\theta_{12}}\,\cos\phi\,\left(-1+\frac{2\sin^2\theta_{23}}{\sin^2\theta_{23}\cos^2\theta_{13}+\sin^2\theta_{13}}\right) \\ + \frac{\cos 2\theta_{12}^{\nu}}{\sin 2\theta_{12}}\,\frac{\sin 2\theta_{23}\,\sin\theta_{13}}{\sin^2\theta_{23}\cos^2\theta_{13}+\sin^2\theta_{13}}\,.\end{aligned} \tag{3.1.20}$$

Within the scheme considered the sum rules eqs. (3.1.16) – (3.1.18) and the relations eqs. (3.1.19) and (3.1.20) are exact. In a complete self-consistent theory of (lepton) flavour based on discrete flavour symmetry, the indicated sum rules and relations are expected to get corrections due to, e.g., $\theta_{13}^e \neq 0$, renormalisation group (RG) effects, etc. Analytic expression for the correction in the expression for $\cos\delta$, eq. (3.1.16), due to $|\sin\theta_{13}^e| \ll 1$ was derived in [75]. As was shown in [75], for the best fit values of the lepton mixing angles θ_{12}, θ_{13} and θ_{23}, a nonzero $\theta_{13}^e \lesssim 10^{-3}$ produces a correction to the value of $\cos\delta$ obtained from the "exact" sum rule eq. (3.1.16), which does not exceed 11% (4.9%) in the TBM (GRB) cases and is even smaller in the other three cases of symmetry forms of $\tilde{U}_\nu$ analysed here. A value of $\theta_{13}^e \lesssim 10^{-3}$ is a feature of many theories and models of charged lepton and neutrino mass generation (see, e.g., [86, 88–91, 98, 100, 101, 120, 124]). The RG effects on the lepton mixing angles and the CPV phases are known to be negligible for hierarchical neutrino mass spectrum (see, e.g., [131,132] and the references quoted therein); these effects are relatively small for values of the lightest neutrino mass not exceeding approximately 0.05 eV [2]. We will call the sum rules and the relations given in eqs. (3.1.16) – (3.1.18), (3.1.19) and (3.1.20) "exact", keeping in mind that they can be subject to corrections, which, however, in a number of physically interesting cases, if not absent, can only be sub-dominant.

A parametrisation of the PMNS matrix, similar to that given in eq. (3.1.5), has been effectively employed in ref. [86]: the hierarchy of values of the angles in the matrices U_e and U_ν assumed in [86] leads the authors to consider the angles θ_{13}^e and θ_{13}^ν of the 1-3 rotations in U_e and U_ν as negligibly small. As a consequence, the PMNS matrix is effectively parametrised in [86] with four angles θ_{12}^e, θ_{23}^e, θ_{12}^ν, θ_{23}^ν and [3] four phases δ_{12}^e, δ_{23}^e, δ_{12}^ν, δ_{23}^ν. As is shown in Appendix C.1 (see also ref. [75]), these phases are related to the phases ψ, ω, ξ_{21} and ξ_{31} present in the parametrisation in eq. (3.1.5) as follows:

$$\psi = \delta_{12}^e - \delta_{12}^\nu + \pi\,, \quad \omega = \delta_{23}^e + \delta_{12}^e - \delta_{23}^\nu - \delta_{12}^\nu\,, \tag{3.1.21}$$

$$\xi_{21} = -2\delta_{12}^\nu\,, \quad \xi_{31} = -2(\delta_{12}^\nu + \delta_{23}^\nu)\,. \tag{3.1.22}$$

Treating $\sin\theta_{12}^e$ and $\sin\theta_{23}^e$ as small parameters, $|\sin\theta_{12}^e| \ll 1$, $|\sin\theta_{23}^e| \ll 1$, neglecting terms of order of, or smaller than, $O((\theta_{12}^e)^2)$, $O((\theta_{23}^e)^2)$ and $O(\theta_{12}^e\theta_{23}^e)$, and taking into account that in this approximation we have $\sin\theta_{12}^e = \sqrt{2}\sin\theta_{13}$, the following "leading order" sum rule was obtained in [86]:

$$\theta_{12} \cong \theta_{12}^\nu + \theta_{13}\cos\delta\,. \tag{3.1.23}$$

This sum rule can be derived from the sum rule

$$\sin\theta_{12} \cong \sin\theta_{12}^\nu + \frac{\sin 2\theta_{12}^\nu}{2\sin\theta_{12}^\nu}\sin\theta_{13}\cos\delta\,, \tag{3.1.24}$$

[2] In supersymmetric theories this result is valid for moderate values of the parameter $\tan\beta \lesssim 10$ (see [131,132]); for $\tan\beta = 50$ the same statement is true for values of the lightest neutrino mass smaller than approximately 0.01 eV.

[3] In contrast to $\theta_{23}^\nu = \pi/4$ employed in [86], we use $\theta_{23}^\nu = -\pi/4$. The effect of the difference in the signs of $\sin\theta_{12}^e$ and $\sin\theta_{23}^e$ utilised by us and in [86] is discussed in Appendix C.1.

by treating $\sin 2\theta^{\nu}_{12} \sin\theta_{13} \cos\delta \cong \sin 2\theta^{\nu}_{12}\theta_{13} \cos\delta$ as a small parameter and using the Taylor expansion $\sin^{-1}(a + b\,x) \cong \sin^{-1}(a) + b\,x/\sqrt{1-a^2}$, valid for $|bx| \ll 1$.

From eqs. (3.1.17) and (3.1.18), employing the approximations used in ref. [86], we get:

$$\sin^2\theta_{12} \cong \sin^2\theta^{\nu}_{12} + \sin 2\theta_{12} \sin\theta_{13} \cos\delta\,, \tag{3.1.25}$$

$$\sin^2\theta_{12} \cong \sin^2\theta^{\nu}_{12} + \sin 2\theta^{\nu}_{12}\ \sin\theta_{13}\ \cos\phi\,. \tag{3.1.26}$$

The first equation leads (in the leading order approximation used to derive it and using $\sin 2\theta_{12} \cong \sin 2\theta^{\nu}_{12}$) to eq. (3.1.23), while from the second equation we find:

$$\sin\theta_{12} \cong \sin\theta^{\nu}_{12} + \frac{\sin 2\theta^{\nu}_{12}}{2\sin\theta^{\nu}_{12}} \sin\theta_{13}\cos\phi\,, \tag{3.1.27}$$

and correspondingly,

$$\theta_{12} \cong \theta^{\nu}_{12} + \theta_{13}\cos\phi\,. \tag{3.1.28}$$

This implies that in the leading order approximation adopted in ref. [86] we have [75] $\cos\delta = \cos\phi$. Note, however, that the sum rules for $\cos\delta$ and $\cos\phi$ given in eqs. (3.1.25) and (3.1.26), differ somewhat by the factors multiplying the terms $\sim \sin\theta_{13}$.

As was shown in [75], the leading order sum rule (3.1.23) leads in the cases of the TBM, GRA, GRB and HG forms of $\tilde{U}_{\nu}$ to largely imprecise predictions for the value of $\cos\delta$: for the best fit values of $\sin^2\theta_{12} = 0.308$, $\sin^2\theta_{13} = 0.0234$ and $\sin^2\theta_{23} = 0.425$ used in [75], they differ approximately by factors (1.4 – 1.9) from the values found from the exact sum rule. The same result holds for $\cos\phi$. Moreover, the predicted values of $\cos\delta$ and $\cos\phi$ differ approximately by factors of (1.5 – 2.0), in contrast to the prediction $\cos\delta \cong \cos\phi$ following from the leading order sum rules. The large differences between the results for $\cos\delta$ and $\cos\phi$, obtained using the leading order and the exact sum rules, are a consequence [75] of the quantitative importance of the next-to-leading order terms which are neglected in the leading order sum rules (3.1.23) – (3.1.28). The next-to-leading order terms are significant for the TBM, GRA, GRB and HG forms of $\tilde{U}_{\nu}$ because in all these cases the "dominant" terms $|\theta_{12} - \theta^{\nu}_{12}| \sim \sin^2\theta_{13}$, or equivalently [4] $|\sin^2\theta_{12} - \sin^2\theta^{\nu}_{12}| \sim \sin^2\theta_{13}$. It was shown also in [75] that in the case of the BM (LC) form of $\tilde{U}_{\nu}$ we have $|\theta_{12} - \theta^{\nu}_{12}| \sim \sin\theta_{13}$ and the leading order sum rules provide rather precise predictions for $\cos\delta$ and $\cos\phi$.

The results quoted above were obtained in [75] for the best fit values of the neutrino mixing parameters $\sin^2\theta_{12}$, $\sin^2\theta_{23}$ and $\sin^2\theta_{13}$. In the present chapter we investigate in detail the predictions for $\cos\delta$ and $\cos\phi$ in the cases of the TBM, BM (LC), GRA, GRB and HG forms of $\tilde{U}_{\nu}$ using the exact sum rules given in eqs. (3.1.17) (or (3.1.16)) and (3.1.18) and the leading order sum rules in eqs. (3.1.25) and (3.1.26), taking into account also the uncertainties in the measured values of $\sin^2\theta_{12}$, $\sin^2\theta_{23}$ and $\sin^2\theta_{13}$. This allows us to better assess the accuracy of the predictions for $\cos\delta$ and $\cos\phi$ based on the leading order

[4] Note that [75] since $\cos\delta$ and $\cos\phi$ in eqs. (3.1.23) – (3.1.28) are multiplied by $\sin\theta_{13}$, the "dominant" terms $|\theta_{12} - \theta^{\nu}_{12}|$ and the next-to-leading order terms $\sim \sin^2\theta_{13}$ give contributions to $\cos\delta$ and $\cos\phi$, which are both of the same order and are $\sim \sin\theta_{13}$.

sum rules and its dependence on the values of the neutrino mixing angles. We investigate also how the predictions for $\cos\delta$ and $\cos\phi$, obtained using the exact and the leading order sum rules, vary when the PMNS neutrino mixing parameters $\sin^2\theta_{12}$, $\sin^2\theta_{23}$ and $\sin^2\theta_{13}$ are varied in their respective experimentally allowed 3σ ranges.

In what follows we will present numerical results using the values of $\sin^2\theta_{12}$, $\sin^2\theta_{23}$ and $\sin^2\theta_{13}$ quoted in eqs. (1.2.6) – (1.2.8) and corresponding to NO spectrum of neutrino masses, unless another choice is explicitly specified. The results we obtain in the case of IO spectrum differ insignificantly from those found for NO spectrum.

3.2 The Case of Negligible θ_{23}^e

The case of negligible $\theta_{23}^e \cong 0$ was investigated by many authors (see, e.g., [76,84–90,125]). It corresponds to a large number of theories and models of charged lepton and neutrino mass generation (see, e.g., [76,86,88–91,100,101]). For $\theta_{23}^e \cong 0$, the sum rules of interest given in eqs. (3.1.17) (or (3.1.16)), (3.1.18) and in eqs. (3.1.25), (3.1.26) were analysed in detail in ref. [75].

In the limit of negligibly small θ_{23}^e we find from eqs. (3.1.8), (3.1.10) and (3.1.11):

$$\sin^2\hat{\theta}_{23} = \frac{1}{2}\,,\ \gamma = -\psi + \pi\,,\ \phi = -\psi = \delta_{12}^{\nu} - \delta_{12}^{e} - \pi\,,\ \beta = \gamma - \phi = \pi\,. \tag{3.2.1}$$

The phase ω is unphysical.

In the limiting case of negligible θ_{23}^e the exact sum rules for $\cos\delta$ and $\cos\phi$ take the following form [75]:

$$\cos\delta = \frac{(1-2\sin^2\theta_{13})^{\frac{1}{2}}}{\sin 2\theta_{12}\sin\theta_{13}}\left[\cos 2\theta_{12}^{\nu} + \left(\sin^2\theta_{12} - \cos^2\theta_{12}^{\nu}\right)\frac{1-3\sin^2\theta_{13}}{1-2\sin^2\theta_{13}}\right]\,, \tag{3.2.2}$$

$$\cos\phi = \frac{1-\sin^2\theta_{13}}{\sin 2\theta_{12}^{\nu}\,\sin\theta_{13}\,(1-2\sin^2\theta_{13})^{\frac{1}{2}}}\left[\sin^2\theta_{12} - \sin^2\theta_{12}^{\nu} - \cos 2\theta_{12}^{\nu}\,\frac{\sin^2\theta_{13}}{1-\sin^2\theta_{13}}\right]\,. \tag{3.2.3}$$

From the above equations, to leading order in $\sin\theta_{13}$ we get:

$$\cos\delta = \frac{1}{\sin 2\theta_{12}\sin\theta_{13}}\left(\sin^2\theta_{12} - \sin^2\theta_{12}^{\nu}\right) + O(\sin\theta_{13})\,, \tag{3.2.4}$$

$$\cos\phi = \frac{1}{\sin 2\theta_{12}^{\nu}\sin\theta_{13}}\left(\sin^2\theta_{12} - \sin^2\theta_{12}^{\nu}\right) + O(\sin\theta_{13})\,, \tag{3.2.5}$$

or equivalently,

$$\sin^2\theta_{12} = \sin^2\theta_{12}^{\nu} + \sin 2\theta_{12}\sin\theta_{13}\cos\delta + O(\sin^2\theta_{13})\,, \tag{3.2.6}$$

$$\sin^2\theta_{12} = \sin^2\theta_{12}^{\nu} + \sin 2\theta_{12}^{\nu}\sin\theta_{13}\cos\phi + O(\sin^2\theta_{13})\,. \tag{3.2.7}$$

The last two equations coincide with eqs. (3.1.25) and (3.1.26) which were derived from the exact sum rules keeping the leading order corrections in both $\sin\theta_{13}$ and $\sin\theta_{23}^{e}$. This implies, in particular, that the correction due to $|\sin\theta_{23}^{e}| \ll 1$ appears in the sum rules of interest only in the next-to-leading order terms. Casting the results obtained in a form we are going to use in our numerical analysis, we obtain:

$$\sin\theta_{12} = \sin\theta_{12}^{\nu} + \frac{\sin 2\theta_{12}}{2\sin\theta_{12}^{\nu}}\sin\theta_{13}\cos\delta + O(\sin^2\theta_{13}) \tag{3.2.8}$$

$$= \sin\theta_{12}^{\nu} + \frac{\sin 2\theta_{12}^{\nu}}{2\sin\theta_{12}^{\nu}}\sin\theta_{13}\cos\delta + O(\sin^2\theta_{13})\,, \tag{3.2.9}$$

$$\sin\theta_{12} = \sin\theta_{12}^{\nu} + \frac{\sin 2\theta_{12}^{\nu}}{2\sin\theta_{12}^{\nu}}\sin\theta_{13}\cos\phi + O(\sin^2\theta_{13})\,. \tag{3.2.10}$$

We have replaced $\sin 2\theta_{12}$ with $\sin 2\theta_{12}^{\nu}$ in eq. (3.2.9), so that it corresponds to eqs. (3.1.23) and (3.1.24). In the cases of the TBM, GRA, GRB and HG symmetry forms of $\tilde{U}_{\nu}$ we are considering and for the best fit value of $\sin^2\theta_{12} = 0.308$ we indeed have $|\sin\theta_{12} - \sin\theta_{12}^{\nu}| \sim \sin^2\theta_{13}$. Thus, if one applies consistently the approximations employed in [86], which lead to eqs. (3.1.23) – (3.1.28) (or to eqs. (3.2.4) and (3.2.5)), one should neglect also the difference between θ_{12} and θ_{12}^{ν}. This leads to $\cos\delta = \cos\phi = 0$.

In Fig. 3.1 we show predictions for $\cos\delta$ and $\cos\phi$ in the cases of the TBM, GRA, GRB and HG forms of the matrix $\tilde{U}_{\nu}$, as functions of $\sin\theta_{13}$ which is varied in the 3σ interval given in eq. (1.2.8) and corresponding to NO neutrino mass spectrum. The predictions are obtained for the best fit value of $\sin^2\theta_{12} = 0.308$ using the exact sum rules eqs. (3.2.2) and (3.2.3) for $\cos\delta$ (solid lines) and $\cos\phi$ (dashed lines) and the leading order sum rules eqs. (3.2.9) and (3.2.10) (dash-dotted lines). As we see in Fig. 3.1, the predictions for $\cos\delta$ vary in magnitude and sign when one varies the symmetry form of $\tilde{U}_{\nu}$. More specifically, from the exact sum rule in eq. (3.2.2), using the best fit value of $\sin^2\theta_{13} = 0.0234$ we get for $\cos\delta$ in the cases of the TBM, BM (LC), GRA, GRB and HG forms of $\tilde{U}_{\nu}$, respectively: $\cos\delta = (-0.114);\ (-1.29);\ 0.289;\ (-0.200);\ 0.476$.

The unphysical value of $\cos\delta$ in the case of the BM (LC) form of $\tilde{U}_{\nu}$ is a reflection of the fact that the scheme under discussion with the BM (LC) form of the matrix $\tilde{U}_{\nu}$ does not provide a good description of the current data on θ_{12}, θ_{23} and θ_{13} [74]. One gets a physical result for $\cos\delta$, $\cos\delta = -0.973$, for, e.g., values of $\sin^2\theta_{12} = 0.32$, and $\sin\theta_{13} = 0.16$, lying in the 2σ experimentally allowed intervals of these neutrino mixing parameters. We have checked that for the best fit value of $\sin^2\theta_{13}$, physical values of $(\cos\delta)_{\rm E}$, $(\cos\delta)_{\rm LO}$ and $(\cos\phi)_{\rm E}$ in the BM (LC) case can be obtained for relatively large values of $\sin^2\theta_{12}$. For, e.g., $\sin^2\theta_{12} = 0.359$ and $\sin^2\theta_{13} = 0.0234$ we find $(\cos\delta)_{\rm E} = -0.915$, $(\cos\delta)_{\rm LO} = -0.998$ and $(\cos\phi)_{\rm E} = -0.922$. In this case the differences between the exact and leading order sum rule results for $\cos\delta$ and $\cos\phi$ are relatively small.

The above results imply that it would be possible to distinguish between the different symmetry forms of $\tilde{U}_{\nu}$ considered by measuring $\cos\delta$ [75], provided $\sin^2\theta_{12}$ is known with

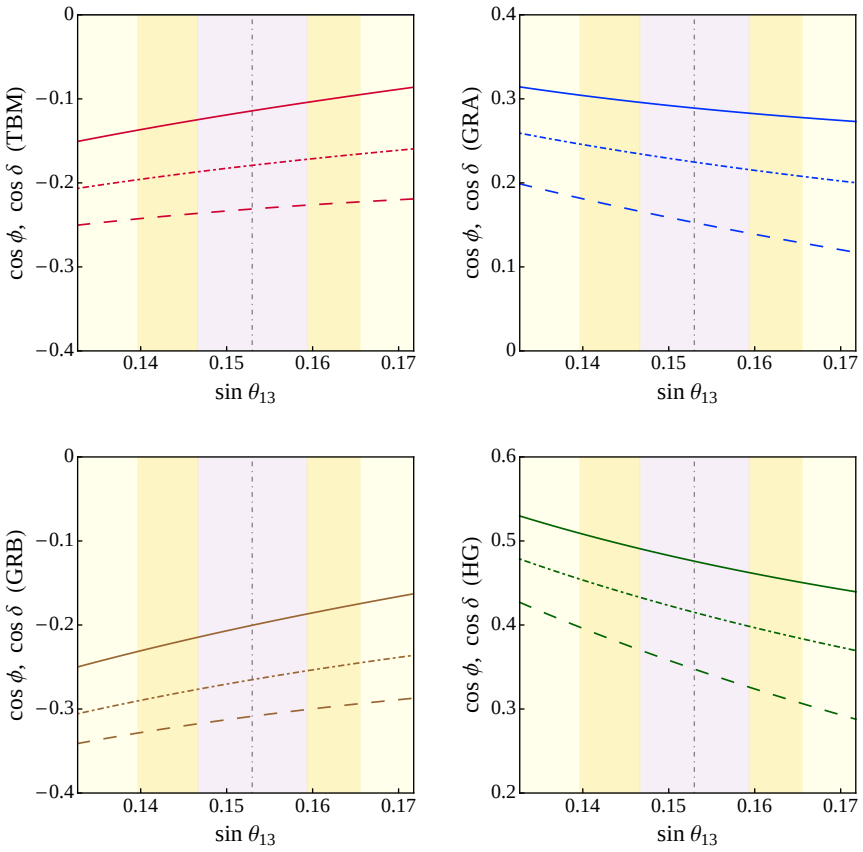

Figure 3.1: Predictions for $\cos\delta$ and $\cos\phi$ in the cases of the TBM (upper left panel), GRA (upper right panel), GRB (lower left panel) and HG (lower right panel) forms of the matrix $\tilde{U}_\nu$, as functions of $\sin\theta_{13}$ and for the best fit value of $\sin^2\theta_{12} = 0.308$. The solid lines (dashed lines) correspond to $\cos\delta$ ($\cos\phi$) determined from the exact sum rule given in eq. (3.2.2) (eq. (3.2.3)). The dash-dotted line in each of the 4 panels represents $(\cos\delta)_{\rm LO} = (\cos\phi)_{\rm LO}$ obtained from the leading order sum rule in eq. (3.2.9). The vertical dash-dotted line corresponds to the best fit value of $\sin^2\theta_{13} = 0.0234$; the three coloured vertical bands indicate the 1σ, 2σ and 3σ experimentally allowed ranges of $\sin\theta_{13}$ (see text for further details).

sufficiently high precision. Even determining the sign of $\cos\delta$ will be sufficient to eliminate some of the possible symmetry forms of $\tilde{U}_\nu$.

The leading order sum rules eqs. (3.2.9) and (3.2.10) lead to values of $\cos\delta$ and $\cos\phi$, $(\cos\delta)_{\rm LO}$ and $(\cos\phi)_{\rm LO}$, which coincide: $(\cos\delta)_{\rm LO} = (\cos\phi)_{\rm LO}$. These values differ, however, from the values obtained employing the exact sum rules: $(\cos\delta)_{\rm E} \neq (\cos\delta)_{\rm LO}$, $(\cos\phi)_{\rm E} \neq (\cos\phi)_{\rm LO}$. The exact sum rule values of $\cos\delta$ and $\cos\phi$ also differ: $(\cos\delta)_{\rm E} \neq (\cos\phi)_{\rm E}$. We are interested both in the predictions for the values of $(\cos\delta)_{\rm E}$, $(\cos\delta)_{\rm LO}$, $(\cos\phi)_{\rm E}$ and $(\cos\phi)_{\rm LO}$, and in the differences between the exact and the leading order sum

$\sin^2\theta_{12} = 0.308$	TBM	GRA	GRB	HG
$(\cos\delta)_{\rm E}$	-0.114	0.289	-0.200	0.476
$(\cos\delta)_{\rm LO}$	-0.179	0.225	-0.265	0.415
$(\cos\delta)_{\rm E}/(\cos\delta)_{\rm LO}$	0.638	1.29	0.756	1.15
$(\cos\phi)_{\rm E}$	-0.231	0.153	-0.309	0.347
$(\cos\delta)_{\rm E}/(\cos\phi)_{\rm E}$	0.494	1.89	0.649	1.37
$(\cos\phi)_{\rm E}/(\cos\phi)_{\rm LO}$	1.29	0.680	1.16	0.837

Table 3.1: The predicted values of $\cos\delta$ and $\cos\phi$, obtained from the exact sum rules in eqs. (3.2.2) and (3.2.3), $(\cos\delta)_{\rm E}$ and $(\cos\phi)_{\rm E}$, and from the leading order sum rule in eq. (3.2.9), $(\cos\delta)_{\rm LO} = (\cos\phi)_{\rm LO}$, using the best fit values of $\sin^2\theta_{13} = 0.0234$ and $\sin^2\theta_{12} = 0.308$, for the TBM, GRA, GRB and HG forms of the matrix $\tilde{U}_\nu$. The values of the ratios $(\cos\delta)_{\rm E}/(\cos\delta)_{\rm LO}$, $(\cos\delta)_{\rm E}/(\cos\phi)_{\rm E}$ and $(\cos\phi)_{\rm E}/(\cos\phi)_{\rm LO}$ are also shown.

rule predictions. In Table 3.1 we give the values of $(\cos\delta)_{\rm E}$, $(\cos\phi)_{\rm E}$, $(\cos\delta)_{\rm LO} = (\cos\phi)_{\rm LO}$, and of the ratios $(\cos\delta)_{\rm E}/(\cos\phi)_{\rm E}$, $(\cos\delta)_{\rm E}/(\cos\delta)_{\rm LO}$ and $(\cos\phi)_{\rm E}/(\cos\phi)_{\rm LO}$, calculated for the best fit values of $\sin^2\theta_{13} = 0.0234$ and $\sin^2\theta_{12} = 0.308$.

As Fig. 3.1 indicates, the differences $|(\cos\delta)_{\rm E} - (\cos\delta)_{\rm LO}|$ and $|(\cos\phi)_{\rm E} - (\cos\phi)_{\rm LO}|$ exhibit weak dependence on the value of $\sin\theta_{13}$ when it is varied in the 3σ interval quoted in eq. (1.2.8). The values of $\cos\delta$, obtained using the exact sum rule eq. (3.2.2) in the TBM, GRA, GRB and HG cases, differ from those calculated using the approximate sum rule eq. (3.2.9) by the factors 0.638, 1.29, 0.756 and 1.15, respectively. The largest difference is found to hold in the TBM case. As was shown in [75], the correction to $(\cos\delta)_{\rm LO}$ — the leading order sum rule result for $\cos\delta$ — is given approximately by $\cos 2\theta^\nu_{12}\sin\theta_{13}/(\sin 2\theta_{12})$. For given θ^ν_{12}, the relative magnitude of the correction depends on the magnitude of the ratio $|\sin^2\theta_{12} - \sin^2\theta^\nu_{12}|/\sin\theta_{13}$. The largest correction occurs for the symmetry form of $\tilde{U}_\nu$, for which this ratio has the smallest value. For the best fit value of $\sin^2\theta_{12}$, the smallest value of the ratio of interest corresponds to the TBM form of $\tilde{U}_\nu$ and is equal approximately to 0.166.

The absolute values of the difference $|(\cos\delta)_{\rm E} - (\cos\delta)_{\rm LO}|$ for the TBM, GRB, GRA and HG symmetry forms, as it follows from Table 3.1, lie in the narrow interval (0.061 – 0.065). These differences seem to be rather small. However, they are sufficiently large to lead to misleading results. Indeed, suppose $\cos\delta$ is measured and the value determined experimentally reads: $\cos\delta = -0.18 \pm 0.025$. If one compares this value with the value of $\cos\delta$ predicted using the leading order sum rule, $(\cos\delta)_{\rm LO}$, one would conclude that data are compatible with the TBM form of $\tilde{U}_\nu$ and that all the other forms considered by us are ruled out. Using the prediction based on the exact sum rule, i.e., $(\cos\delta)_{\rm E}$, would lead to a completely different conclusion, namely, that the data are compatible only with the GRB form of $\tilde{U}_\nu$ [5]. In this hypothetical example, which is included to illustrate the significance of the difference between the predictions for $\cos\delta$ obtained using the exact and

[5]The same hypothetical example can be used to illustrate the significance of the difference between the exact and the leading order sum rule predictions for $\cos\delta$ also in the case of $\theta^e_{23} \neq 0$ (see Table 3.4).

the leading order sum rules, we have assumed that the prospective uncertainties in the predicted values of $(\cos\delta)_{\rm LO}$ and $(\cos\delta)_{\rm E}$ due to the uncertainties in the measured values of $\sin^2\theta_{12}$, $\sin^2\theta_{13}$ and $\sin^2\theta_{23}$ are sufficiently small. These uncertainties will be discussed in Section 3.4 (see Fig. 3.13). The relative difference between $(\cos\delta)_{\rm E}$ and $(\cos\delta)_{\rm LO}$, i.e., the ratio $|(\cos\delta)_{\rm E} - (\cos\delta)_{\rm LO}|/|(\cos\delta)_{\rm E}|$, is also significant. For the TBM, GRA, GRB and HG symmetry forms it reads: 57.0%, 22.1%, 32.5% and 12.8%, respectively.

The behaviour of $\cos\delta$ and $\cos\phi$ when $\sin\theta_{13}$ increases is determined by the sign of $(\sin^2\theta_{12} - \sin^2\theta^{\nu}_{12})$: $\cos\delta$ and $\cos\phi$ increase (decrease) when this difference is negative (positive). For the best fit value of $\sin^2\theta_{12} = 0.308$, this difference is negative in the TBM and GRB cases, while it is positive in the GRA and HG ones. For the four symmetry forms of $\tilde{U}_{\nu}$, TBM, GRB, GRA and HG, and the best fit values of $\sin^2\theta_{13} = 0.0234$ and $\sin^2\theta_{12} = 0.308$, the ratio $(\sin^2\theta_{12} - \sin^2\theta^{\nu}_{12})/\sin\theta_{13}$ reads, respectively: (-0.166), (-0.245), 0.207 and 0.379.

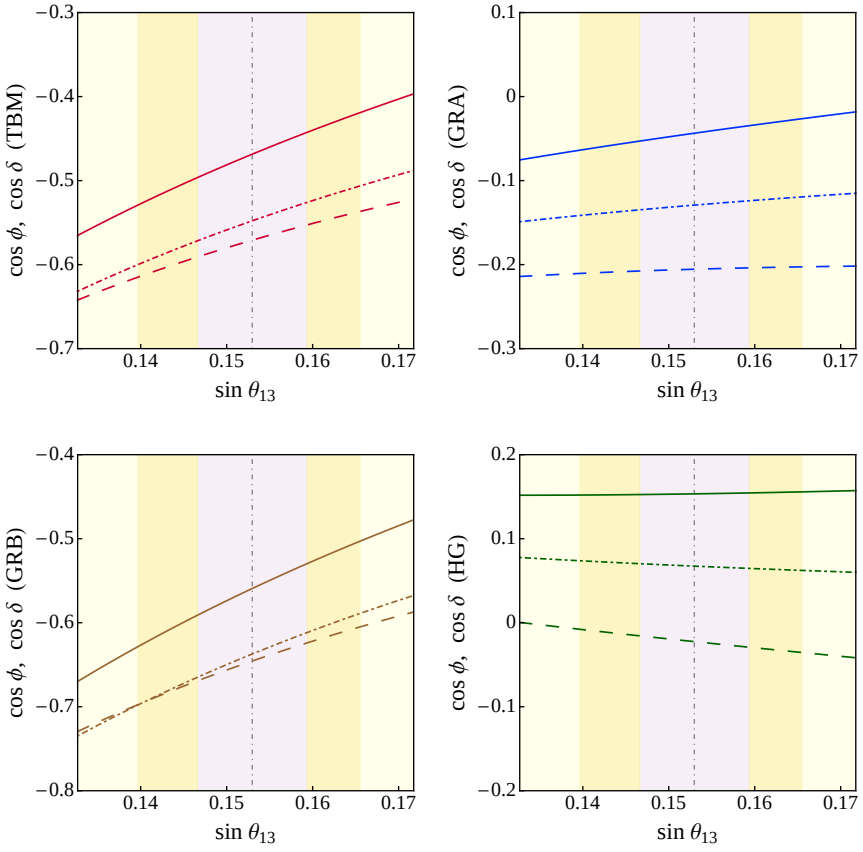

Figure 3.2: The same as in Fig. 3.1, but for $\sin^2\theta_{12} = 0.259$ (see text for further details).

Given the fact that the magnitude of the ratio $(\sin^2\theta_{12} - \sin^2\theta^{\nu}_{12})/\sin\theta_{13}$ determines the factor by which $(\cos\delta)_{\rm E}$ and $(\cos\delta)_{\rm LO}$ (and $(\cos\phi)_{\rm E}$ and $(\cos\phi)_{\rm LO}$) differ, we have checked

$\sin^2\theta_{12} = 0.259$	TBM	GRA	GRB	HG
$(\cos\delta)_{\rm E}$	-0.469	-0.0436	-0.559	0.153
$(\cos\delta)_{\rm LO}$	-0.548	-0.129	-0.637	0.0673
$(\cos\delta)_{\rm E}/(\cos\delta)_{\rm LO}$	0.855	0.338	0.878	2.28
$(\cos\phi)_{\rm E}$	-0.571	-0.206	-0.646	-0.0225
$(\cos\delta)_{\rm E}/(\cos\phi)_{\rm E}$	0.821	0.212	0.866	-6.82
$(\cos\phi)_{\rm E}/(\cos\phi)_{\rm LO}$	1.04	1.59	1.01	-0.334

Table 3.2: The same as in Table 3.1, but for $\sin^2\theta_{12} = 0.259$.

how the results described above change when $\sin^2\theta_{12}$ is varied in its 3σ allowed region, eq. (1.2.6). In Figs. 3.2 and 3.3 we show the dependence of the predicted values of $(\cos\delta)_{\rm E}$, $(\cos\phi)_{\rm E}$ and $(\cos\delta)_{\rm LO} = (\cos\phi)_{\rm LO}$ on $\sin\theta_{13}$ for the minimal and maximal 3σ allowed values of $\sin^2\theta_{12}$, $\sin^2\theta_{12} = 0.259$ and 0.359. The results shown correspond to the TBM, GRA, GRB, HG forms of $\tilde{U}_\nu$. For $\sin^2\theta_{12} = 0.259$ ($\sin^2\theta_{12} = 0.359$) and $\sin^2\theta_{13} = 0.0234$, the ratio $(\sin^2\theta_{12} - \sin^2\theta^\nu_{12})/\sin\theta_{13}$ in the TBM, GRA, GRB and HG cases takes respectively the values: (-0.486), (-0.114), (-0.565) and 0.059 (0.168, 0.540, 0.088 and 0.713). As in the preceding case, we give the predicted values of $(\cos\delta)_{\rm E}$, $(\cos\phi)_{\rm E}$, $(\cos\delta)_{\rm LO} = (\cos\phi)_{\rm LO}$, and the ratios between them, for $\sin^2\theta_{12} = 0.259$ ($\sin^2\theta_{12} = 0.359$) and $\sin^2\theta_{13} = 0.0234$ in Table 3.2 (Table 3.3).

It follows from the results presented in Tables 3.1 – 3.3 that the exact sum rule predictions of $\cos\delta$, $(\cos\delta)_{\rm E}$, for the three values of $\sin^2\theta_{12} = 0.308$, 0.259 and 0.359, differ drastically. For the TBM form of $\tilde{U}_\nu$, for instance, we get, respectively, the values: $(\cos\delta)_{\rm E} = (-0.114)$, (-0.469) and 0.221. For the GRA and GRB forms of $\tilde{U}_\nu$ we have, respectively, $(\cos\delta)_{\rm E} = 0.289$, (-0.044), 0.609, and $(\cos\delta)_{\rm E} = (-0.200)$, (-0.559), 0.138. Similarly, for the HG form we find for the three values of $\sin^2\theta_{12}$: $(\cos\delta)_{\rm E} = 0.476$, 0.153, 0.789. Thus, in the cases of the symmetry forms of $\tilde{U}_\nu$ considered, the exact sum rule predictions for $\cos\delta$ not only change significantly in magnitude when $\sin^2\theta_{12}$ is varied in its 3σ allowed range, but also the sign of $\cos\delta$ changes in the TBM, GRA and GRB cases (see Fig. 3.4).

We observe also that for $\sin^2\theta_{12} = 0.259$, the values of $\cos\delta$, obtained using the exact sum rule eq. (3.2.2) in the TBM, GRA, GRB and HG cases differ from those calculated using the leading order sum rule in eq. (3.2.9) by the factors 0.855, 0.338, 0.878 and 2.28, respectively; in the case of $\sin^2\theta_{12} = 0.359$ the same factors read: 1.27, 1.08, 1.50 and 1.05.

For $\sin^2\theta_{12} = 0.259$, the largest difference between the exact and leading order sum rule results for $\cos\delta$ occurs for the GRA and HG forms of $\tilde{U}_\nu$, while if $\sin^2\theta_{12} = 0.359$, the largest difference holds for the TBM and GRB forms.

As Figs. 3.1 – 3.3 and Tables 3.1 – 3.3 show, similar results are valid for $\cos\phi$ obtained from the exact and the leading order sum rules.

It is worth noting also that the values of $\cos\phi$ and $\cos\delta$, derived from the respective exact sum rules differ significantly for the TBM, GRA, GRB and HG forms of $\tilde{U}_\nu$ considered. As pointed out in [75], for the best fit values of $\sin^2\theta_{13}$ and $\sin^2\theta_{12}$ they differ by

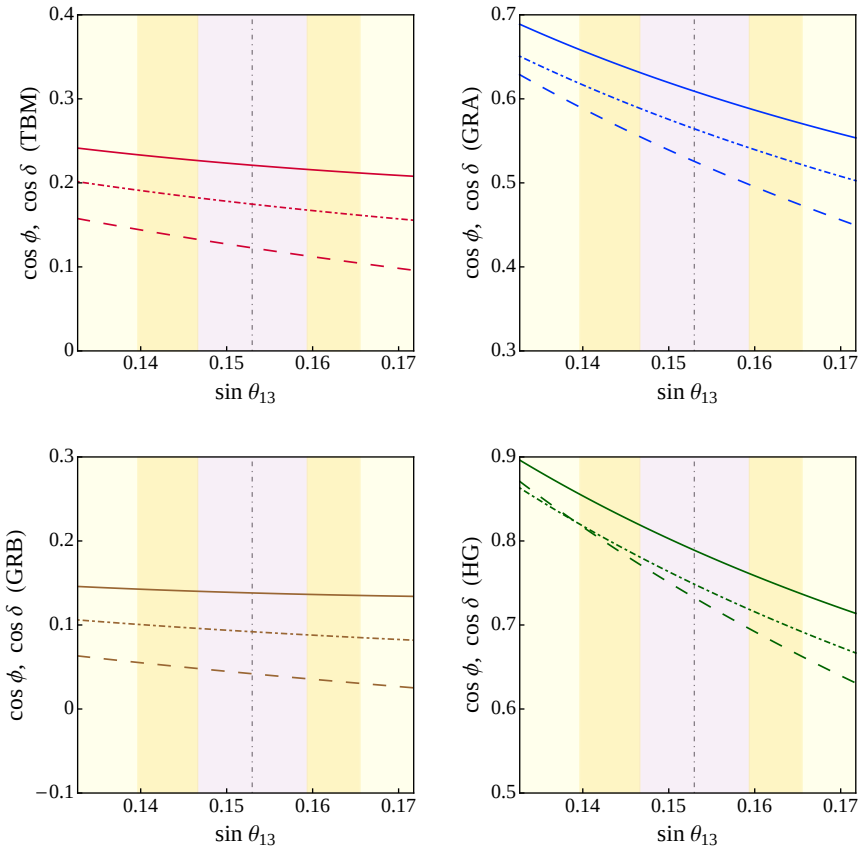

Figure 3.3: The same as in Fig. 3.1, but for $\sin^2\theta_{12} = 0.359$ (see text for further details).

$\sin^2\theta_{12} = 0.359$	TBM	GRA	GRB	HG
$(\cos\delta)_{\rm E}$	0.221	0.609	0.138	0.789
$(\cos\delta)_{\rm LO}$	0.175	0.564	0.092	0.749
$(\cos\delta)_{\rm E}/(\cos\delta)_{\rm LO}$	1.27	1.08	1.50	1.05
$(\cos\phi)_{\rm E}$	0.123	0.526	0.042	0.733
$(\cos\delta)_{\rm E}/(\cos\phi)_{\rm E}$	1.80	1.16	3.29	1.08
$(\cos\phi)_{\rm E}/(\cos\phi)_{\rm LO}$	0.702	0.931	0.456	0.979

Table 3.3: The same as in Table 3.1, but for $\sin^2\theta_{12} = 0.359$.

factors (1.4 – 2.0), as can be seen also from Table 3.1. This difference can be much larger for $\sin^2\theta_{12} = 0.259$ and 0.359: for these two values of $\sin^2\theta_{12}$, $\cos\delta$ and $\cos\phi$ differ in the cases of the different symmetry forms of interest approximately by factors (1.2 – 6.8) and (1.1 – 3.3), respectively.

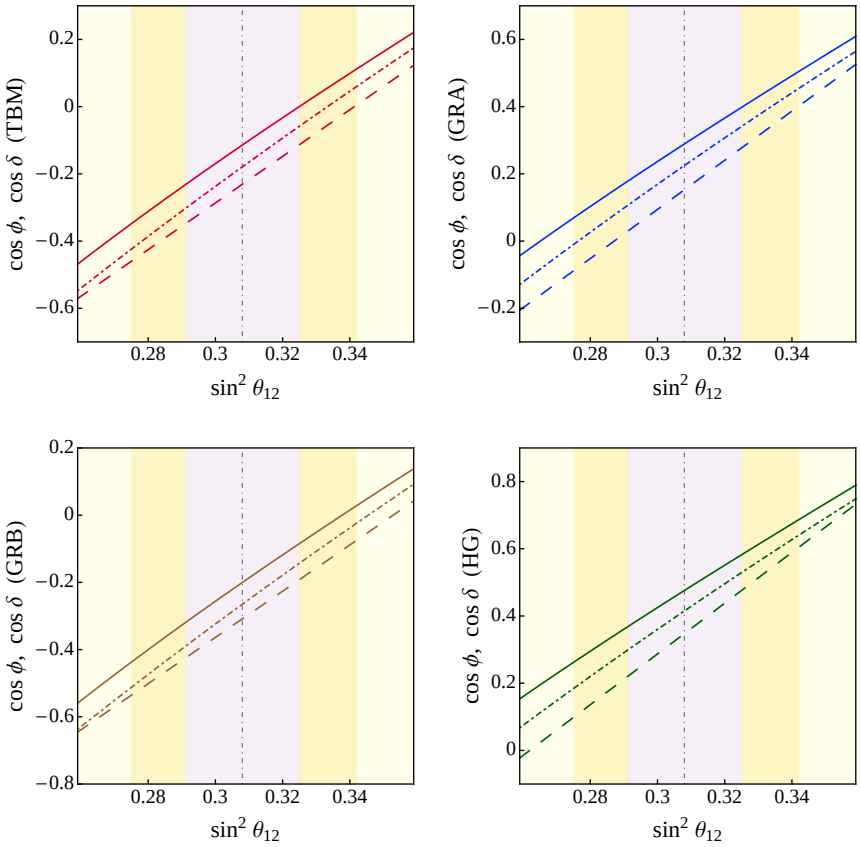

Figure 3.4: The same as in Fig. 3.1, but for $\sin^2\theta_{13} = 0.0234$ and varying $\sin^2\theta_{12}$ in the 3σ range. The vertical dash-dotted line corresponds to the best fit value of $\sin^2\theta_{12} = 0.308$ (see text for further details).

3.3 The Case of Nonzero θ_{23}^e

For $\theta_{23}^e = 0$ we have in the scheme we are considering: $\theta_{23} \cong \pi/4 - 0.5\sin^2\theta_{13}$. A nonzero value of θ_{23}^e allows for a significant deviation of θ_{23} from $\pi/4$. Such deviation is not excluded by the current data on $\sin^2\theta_{23}$, eq. (1.2.7): at 3σ, values of $\sin^2\theta_{23}$ in the interval (0.37 – 0.64) are allowed, the best fit value being $\sin^2\theta_{23} = 0.437$ (0.455). The exact sum rules for $\cos\delta$ and $\cos\phi$, eqs. (3.1.16), (3.1.17) and (3.1.18), depend on θ_{23}, while the leading order sum rules, eqs. (3.1.23) and (3.1.28), are independent of θ_{23}. In this Section we are going to investigate how the dependence on θ_{23} affects the predictions for $\cos\delta$ and $\cos\phi$, based on the exact sum rules.

We note first that from the exact sum rules in eqs. (3.1.17) and (3.1.18) we get to

leading order in $\sin\theta_{13}$:

$$\sin^2\theta_{12} = \sin^2\theta_{12}^{\nu} + \frac{\sin 2\theta_{12}}{\tan\theta_{23}}\sin\theta_{13}\cos\delta + O(\sin^2\theta_{13})\,, \tag{3.3.1}$$

$$\sin^2\theta_{12} = \sin^2\theta_{12}^{\nu} + \frac{\sin 2\theta_{12}^{\nu}}{\tan\theta_{23}}\sin\theta_{13}\cos\phi + O(\sin^2\theta_{13})\,. \tag{3.3.2}$$

It follows from eqs. (3.1.8) and (3.1.14) that in the case of $|\sin\theta_{23}^{e}| \ll 1$ considered in ref. [86], we have [75] $(\tan\theta_{23})^{-1} \cong 2\cos^2\theta_{23} = 1 + O(\sin\theta_{23}^{e})$. Applying the approximation employed in ref. [86], in which terms of order of, or smaller than, $\sin^2\theta_{13}$, $\sin^2\theta_{23}^{e}$ and $\sin\theta_{13}\sin\theta_{23}^{e}$, in the sum rules of interest are neglected, we have to set $(\tan\theta_{23})^{-1} = 1$ in eqs. (3.3.1) and (3.3.2). This leads to eqs. (3.1.25) and (3.1.26) and, correspondingly, to eqs. (3.1.23) and (3.1.28).

In Fig. 3.5 we show the predictions for $\cos\delta$ and $\cos\phi$ in the cases of the TBM, GRA, GRB and HG forms of the matrix $\tilde{U}_{\nu}$, derived from the exact sum rules in eqs. (3.1.17) and (3.1.18), $(\cos\delta)_{\rm E}$ (solid line) and $(\cos\phi)_{\rm E}$ (dashed line), and from the leading order sum rule in eq. (3.1.24) (eq. (3.1.27)), $(\cos\delta)_{\rm LO} = (\cos\phi)_{\rm LO}$ (dash-dotted line). The results presented in Fig. 3.5 are obtained for the best fit values of $\sin^2\theta_{12} = 0.308$ and $\sin^2\theta_{23} = 0.437$. The parameter $\sin^2\theta_{13}$ is varied in its 3σ allowed range, eq. (1.2.8). In Table 3.4 we give the values of $(\cos\delta)_{\rm E}$, $(\cos\delta)_{\rm LO}$, $(\cos\phi)_{\rm E}$ and of their ratios, corresponding to the best fit values of $\sin^2\theta_{12}$, $\sin^2\theta_{23}$ and $\sin^2\theta_{13}$. We see from Table 3.4 that for the TBM, GRA, GRB and HG forms of $\tilde{U}_{\nu}$, $\cos\delta$ determined from the exact sum rule takes respectively the values (-0.091), 0.275, (-0.169) and 0.445. The values of $\cos\delta$, found using the exact sum rule, eq. (3.1.17), differ in the TBM, GRA, GRB and HG cases from those calculated using the leading order sum rule, eq. (3.1.24), by the factors 0.506, 1.22, 0.636 and 1.07, respectively. Thus, the largest difference between the predictions of the exact and the leading order sum rules occurs for the TBM form of $\tilde{U}_{\nu}$.

Since the predictions of the sum rules depend on the value of θ_{12}, we show in Fig. 3.6 and Fig. 3.7 also results for the values of $\sin^2\theta_{12}$, corresponding to the lower and the upper bounds of the 3σ allowed range of $\sin^2\theta_{12}$, $\sin^2\theta_{12} = 0.259$ and 0.359, keeping $\sin^2\theta_{23}$ fixed to its best fit value. The predictions for $(\cos\delta)_{\rm E}$, $(\cos\phi)_{\rm E}$, $(\cos\delta)_{\rm LO} = (\cos\phi)_{\rm LO}$ and their ratios, obtained for the best fit values of $\sin^2\theta_{13} = 0.0234$ and $\sin^2\theta_{23} = 0.437$, and for $\sin^2\theta_{12} = 0.259$ ($\sin^2\theta_{12} = 0.359$) are given in Table 3.5 (Table 3.6). For $\sin^2\theta_{12} = 0.259$, the exact sum rule predictions of $\cos\delta$ for the TBM, GRA, GRB and HG forms of $\tilde{U}_{\nu}$ read (see Table 3.5): $(\cos\delta)_{\rm E} = (-0.408)$, (-0.022), (-0.490) and 0.156. As in the case of negligible θ_{23}^{e} analysed in the preceding Section, these values differ drastically (in general, both in magnitude and sign) from the exact sum rule values of $\cos\delta$ corresponding to the best fit value and the 3σ upper bound of $\sin^2\theta_{12} = 0.308$ and 0.359. The dependence of $(\cos\delta)_{\rm E}$, $(\cos\delta)_{\rm LO}$ and $(\cos\phi)_{\rm E}$ on $\sin^2\theta_{12}$ under discussion is shown graphically in Fig. 3.8.

Further, for $\sin^2\theta_{12} = 0.259$, the ratio $(\cos\delta)_{\rm E}/(\cos\delta)_{\rm LO}$ in the TBM, GRA, GRB and HG cases reads, respectively, 0.744, 0.172, 0.769 and 2.32 (see Table 3.5). Thus, the predictions for $\cos\delta$ of the exact and the leading order sum rules differ by the factors of 5.8 and 2.3 in the GRA and HG cases. For the upper bound of the 3σ range of $\sin^2\theta_{12} = 0.359$,

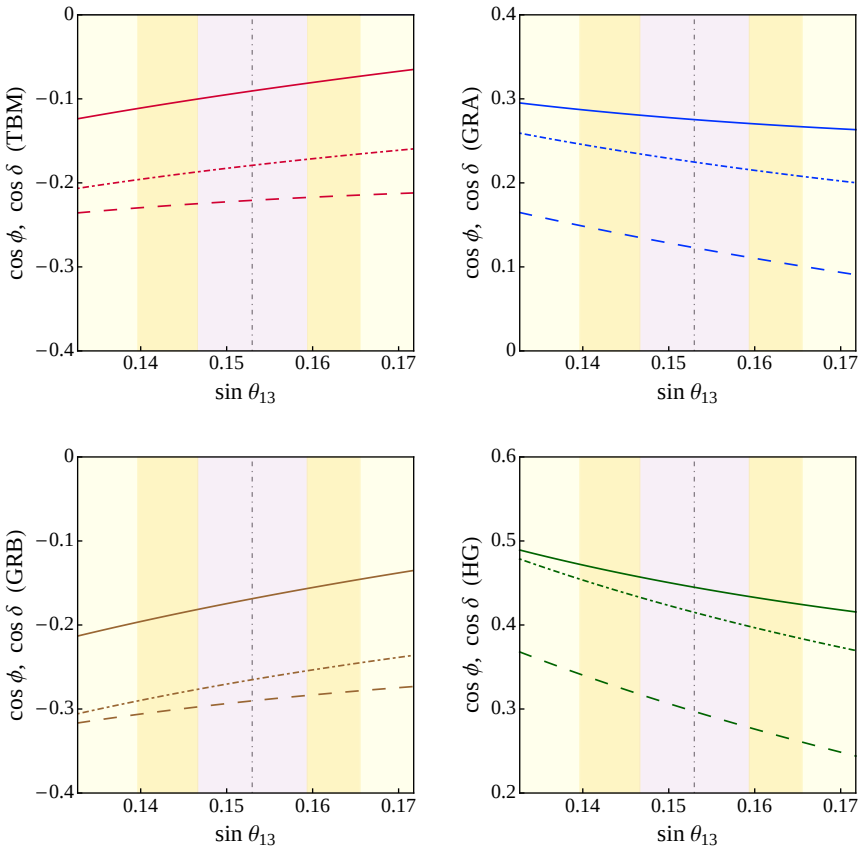

Figure 3.5: Predictions for $\cos\delta$ and $\cos\phi$ in the cases of the TBM (upper left panel), GRA (upper right panel), GRB (lower left panel) and HG (lower right panel) forms of the matrix $\tilde{U}_\nu$, as functions of $\sin\theta_{13}$ and for the best fit values of $\sin^2\theta_{12} = 0.308$ and $\sin^2\theta_{23} = 0.437$. The solid lines (dashed lines) correspond to $\cos\delta$ ($\cos\phi$) determined from the exact sum rule given in eq. (3.1.17) (eq. (3.1.18)). The dash-dotted line in each of the 4 panels represents $(\cos\delta)_{\rm LO} = (\cos\phi)_{\rm LO}$ obtained from the leading order sum rule in eq. (3.1.24) (eq. (3.1.27)). The vertical dash-dotted line corresponds to the best fit value of $\sin^2\theta_{13} = 0.0234$; the three coloured vertical bands indicate the 1σ, 2σ and 3σ experimentally allowed ranges of $\sin\theta_{13}$ (see text for further details).

the ratio $(\cos\delta)_{\rm E}/(\cos\delta)_{\rm LO}$ takes the values 1.2, 0.996, 1.46 and 0.969 for the TBM, GRA, GRB and HG forms of $\tilde{U}_\nu$, respectively (see Table 3.6). For the GRA and HG symmetry forms the leading order sum rule prediction for $\cos\delta$ is very close to the exact sum rule prediction, which can also be seen in Fig. 3.7.

We will investigate next the dependence of the predictions for $\cos\delta$ and $\cos\phi$ on the value of θ_{23} given the facts that i) $\sin^2\theta_{23}$ is determined experimentally with a relatively large uncertainty, and ii) in contrast to the leading order sum rule predictions for $\cos\delta$ and $\cos\phi$, the exact sum rule predictions depend on θ_{23}. In Figs. 3.9 and 3.10 we show the

$(\sin^2\theta_{12}, \sin^2\theta_{23}) = (0.308, 0.437)$	TBM	GRA	GRB	HG
$(\cos\delta)_{\rm E}$	-0.0906	0.275	-0.169	0.445
$(\cos\delta)_{\rm LO}$	-0.179	0.225	-0.265	0.415
$(\cos\delta)_{\rm E}/(\cos\delta)_{\rm LO}$	0.506	1.22	0.636	1.07
$(\cos\phi)_{\rm E}$	-0.221	0.123	-0.290	0.297
$(\cos\delta)_{\rm E}/(\cos\phi)_{\rm E}$	0.41	2.24	0.581	1.50
$(\cos\phi)_{\rm E}/(\cos\phi)_{\rm LO}$	1.23	0.547	1.10	0.716

Table 3.4: The predicted values of $\cos\delta$ and $\cos\phi$, obtained from the exact sum rules in eqs. (3.1.17) and (3.1.18), $(\cos\delta)_{\rm E}$ and $(\cos\phi)_{\rm E}$, and from the leading order sum rule in eq. (3.1.24) (eq. (3.1.27)), $(\cos\delta)_{\rm LO} = (\cos\phi)_{\rm LO}$, using the best fit values of $\sin^2\theta_{13} = 0.0234$, $\sin^2\theta_{12} = 0.308$ and $\sin^2\theta_{23} = 0.437$, for the TBM, GRA, GRB and HG forms of the matrix $\tilde{U}_\nu$. The values of the ratios $(\cos\delta)_{\rm E}/(\cos\delta)_{\rm LO}$, $(\cos\delta)_{\rm E}/(\cos\phi)_{\rm E}$ and $(\cos\phi)_{\rm E}/(\cos\phi)_{\rm LO}$ are also shown.

dependence of predictions for $\cos\delta$ and $\cos\phi$ on $\sin\theta_{13}$ for the best fit value of $\sin^2\theta_{12} = 0.308$ and the 3σ lower and upper bounds of $\sin^2\theta_{23} = 0.374$ and 0.626, respectively. For $\sin^2\theta_{23} = 0.374$ (0.626) and the best fit values of $\sin^2\theta_{13}$ and $\sin^2\theta_{12}$, the exact and the leading order sum rule results $(\cos\delta)_{\rm E}$, $(\cos\phi)_{\rm E}$, $(\cos\delta)_{\rm LO} = (\cos\phi)_{\rm LO}$ and their ratios are given in Tables 3.7 and 3.8. Comparing the values of $(\cos\delta)_{\rm E}$ quoted in Tables 3.7 and 3.8 with the values given in Table 3.4 we note that the exact sum rule predictions for $\cos\delta$ for $\sin^2\theta_{23} = 0.374$ (lower 3σ bound) and $\sin^2\theta_{23} = 0.437$ (best fit value) do not differ significantly in the cases of the TBM, GRA, GRB and HG forms of $\tilde{U}_\nu$ considered. However, the differences between the predictions for $\sin^2\theta_{23} = 0.437$ and $\sin^2\theta_{23} = 0.626$ are rather large — by factors of 2.05, 1.25, 1.77 and 1.32 in the TBM, GRA, GRB and HG cases, respectively.

In what concerns the difference between the exact and leading order sum rules predictions for $\cos\delta$, for the best fit values of $\sin^2\theta_{13}$ and $\sin^2\theta_{12}$, and for $\sin^2\theta_{23} = 0.374$, the ratio $(\cos\delta)_{\rm E}/(\cos\delta)_{\rm LO} = 0.345$, 1.17, 0.494 and 0.993 for TBM, GRA, GRB and HG forms of $\tilde{U}_\nu$. For $\sin^2\theta_{23} = 0.626$ we have for the same ratio $(\cos\delta)_{\rm E}/(\cos\delta)_{\rm LO} = 1.04$, 1.52, 1.13 and 1.42. Thus, for $\sin^2\theta_{23} = 0.374$ (0.626), the leading order sum rule prediction for $\cos\delta$ is rather precise in the HG (TBM) case. For the other symmetry forms of $\tilde{U}_\nu$ the leading order sum rule prediction for $\cos\delta$ is largely incorrect. As can be seen from Figs 3.5 – 3.10 and Tables 3.4 – 3.8, we get similar results for $\cos\phi$.

In the case of the BM (LC) form of $\tilde{U}_\nu$, physical values of $(\cos\delta)_{\rm E}$, $(\cos\phi)_{\rm E}$ and $(\cos\delta)_{\rm LO}$ can be obtained for the best fit values of $\sin^2\theta_{13}$ and $\sin^2\theta_{23}$ if $\sin^2\theta_{12}$ has a relatively large value. For, e.g., $\sin^2\theta_{12} = 0.359$, $\sin^2\theta_{13} = 0.0234$ and $\sin^2\theta_{23} = 0.437$ we find $(\cos\delta)_{\rm E} = -0.821$, $(\cos\delta)_{\rm LO} = -0.998$, $(\cos\phi)_{\rm E} = -0.837$, and $(\cos\delta)_{\rm E}/(\cos\delta)_{\rm LO} = 0.823$.

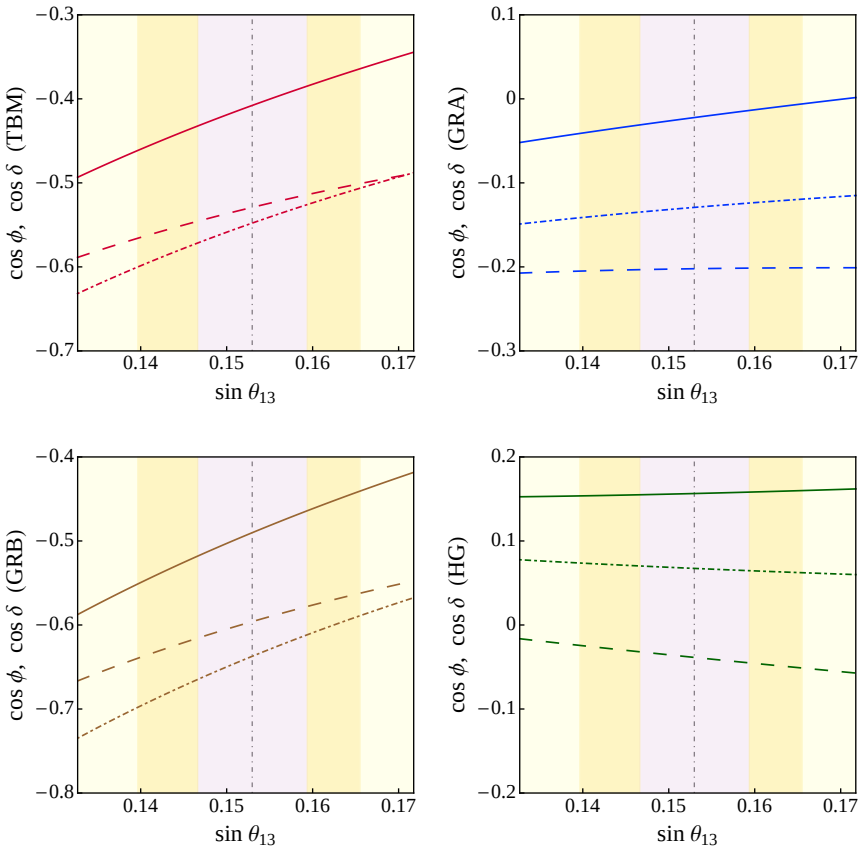

Figure 3.6: The same as in Fig. 3.5, but for $\sin^2\theta_{12} = 0.259$ (lower bound of the 3σ interval in eq. (1.2.6)) and $\sin^2\theta_{23} = 0.437$ (best fit value).

$(\sin^2\theta_{12}, \sin^2\theta_{23}) = (0.259, 0.437)$	TBM	GRA	GRB	HG
$(\cos\delta)_{\rm E}$	-0.408	-0.0223	-0.490	0.156
$(\cos\delta)_{\rm LO}$	-0.548	-0.129	-0.637	0.0673
$(\cos\delta)_{\rm E}/(\cos\delta)_{\rm LO}$	0.744	0.172	0.769	2.32
$(\cos\phi)_{\rm E}$	-0.529	-0.202	-0.596	-0.0386
$(\cos\delta)_{\rm E}/(\cos\phi)_{\rm E}$	0.771	0.110	0.822	-4.05
$(\cos\phi)_{\rm E}/(\cos\phi)_{\rm LO}$	0.966	1.57	0.935	-0.573

Table 3.5: The same as in Table 3.4, but for $\sin^2\theta_{13} = 0.0234$ (best fit value), $\sin^2\theta_{12} = 0.259$ (lower bound of the 3σ range) and $\sin^2\theta_{23} = 0.437$ (best fit value).

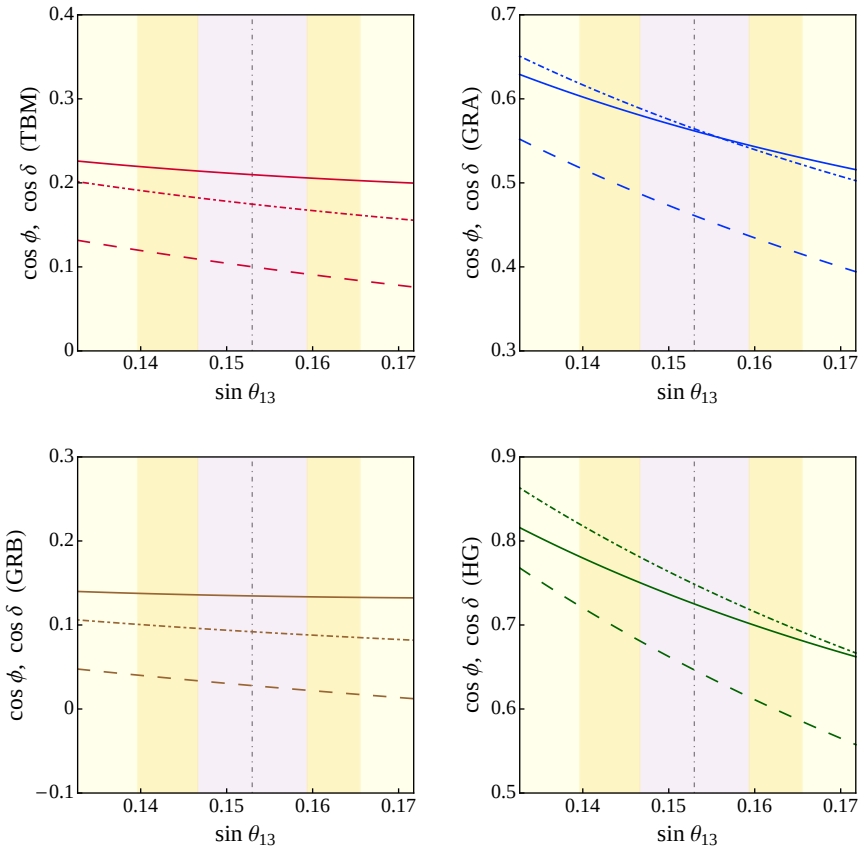

Figure 3.7: The same as in Fig. 3.5, but for $\sin^2\theta_{12} = 0.359$ (upper bound of the 3σ interval in eq. (1.2.6)) and $\sin^2\theta_{23} = 0.437$ (best fit value).

$(\sin^2\theta_{12}, \sin^2\theta_{23}) = (0.359, 0.437)$	TBM	GRA	GRB	HG
$(\cos\delta)_{\rm E}$	0.210	0.562	0.135	0.725
$(\cos\delta)_{\rm LO}$	0.175	0.564	0.092	0.749
$(\cos\delta)_{\rm E}/(\cos\delta)_{\rm LO}$	1.20	0.996	1.46	0.969
$(\cos\phi)_{\rm E}$	0.100	0.461	0.0279	0.647
$(\cos\delta)_{\rm E}/(\cos\phi)_{\rm E}$	2.09	1.22	4.83	1.12
$(\cos\phi)_{\rm E}/(\cos\phi)_{\rm LO}$	0.573	0.817	0.303	0.864

Table 3.6: The same as in Table 3.4, but for $\sin^2\theta_{13} = 0.0234$ (best fit value), $\sin^2\theta_{12} = 0.359$ (upper bound of the 3σ range) and $\sin^2\theta_{23} = 0.437$ (best fit value).

3.4 Statistical Analysis

In the present Section we perform a statistical analysis of the predictions for δ, $\cos\delta$ and the rephasing invariant $J_{\rm CP}$ which controls the magnitude of CPV effects in neutrino

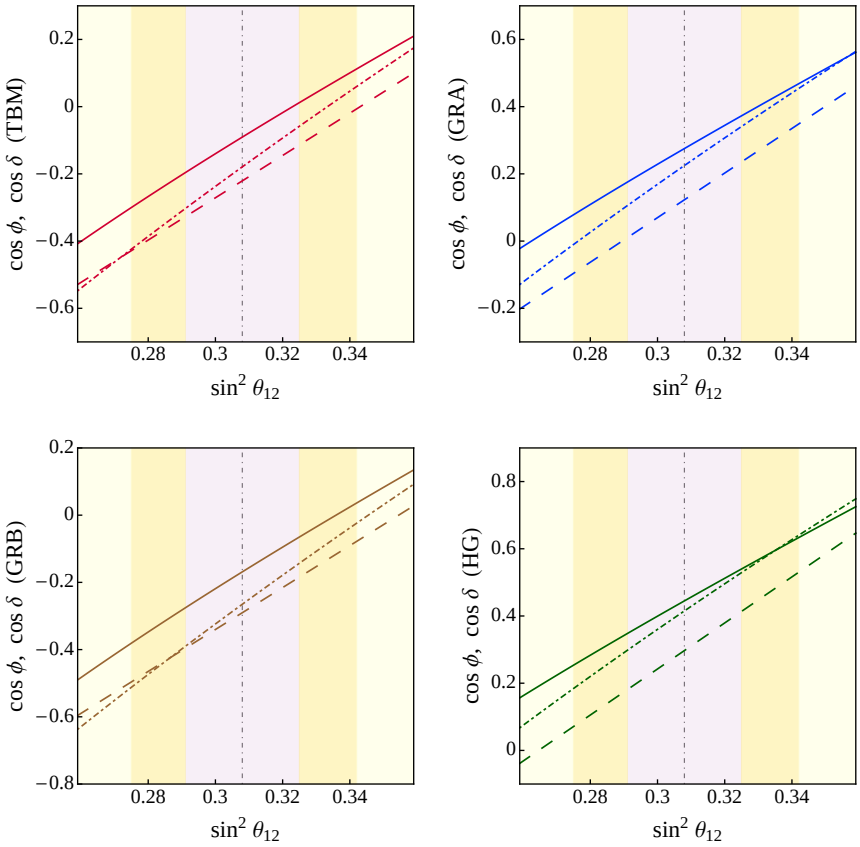

Figure 3.8: The same as in Fig. 3.5, but for $\sin^2\theta_{13} = 0.0234$, $\sin^2\theta_{23} = 0.437$ (best fit values) and varying $\sin^2\theta_{12}$ in the 3σ range. The vertical dash-dotted line corresponds to the best fit value of $\sin^2\theta_{12} = 0.308$.

$(\sin^2\theta_{12}, \sin^2\theta_{23}) = (0.308, 0.374)$	TBM	GRA	GRB	HG
$(\cos\delta)_{\rm E}$	-0.0618	0.262	-0.131	0.412
$(\cos\delta)_{\rm LO}$	-0.179	0.225	-0.265	0.415
$(\cos\delta)_{\rm E}/(\cos\delta)_{\rm LO}$	0.345	1.17	0.494	0.993
$(\cos\phi)_{\rm E}$	-0.211	0.0866	-0.271	0.237
$(\cos\delta)_{\rm E}/(\cos\phi)_{\rm E}$	0.293	3.03	0.483	1.74
$(\cos\phi)_{\rm E}/(\cos\phi)_{\rm LO}$	1.18	0.385	1.02	0.572

Table 3.7: The same as in Table 3.4, but for $\sin^2\theta_{13} = 0.0234$ (best fit value), $\sin^2\theta_{12} = 0.308$ (best fit value) and $\sin^2\theta_{23} = 0.374$ (lower bound of the 3σ range).

oscillations [11], in the cases of the TBM, BM (LC), GRA, GRB and HG symmetry forms of the matrix $\tilde{U}_\nu$ (see eq. (3.1.2)). In this analysis we use as input the latest results on

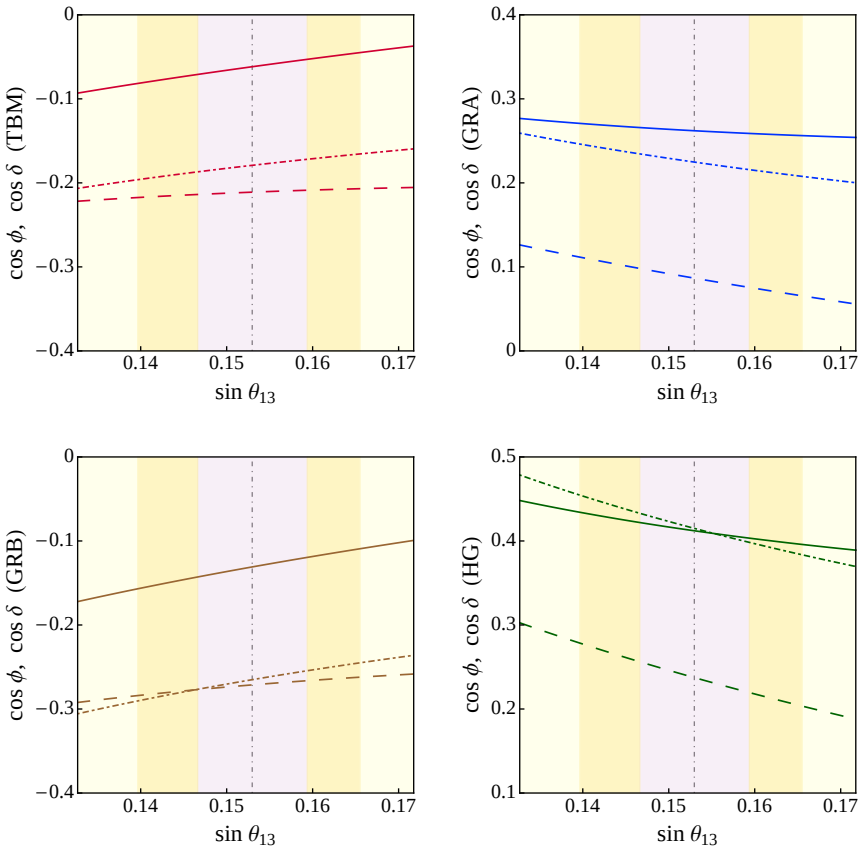

Figure 3.9: The same as in Fig. 3.5, but for $\sin^2\theta_{12} = 0.308$ (best fit value) and $\sin^2\theta_{23} = 0.374$ (lower bound of the 3σ interval in eq. (1.2.7)).

$(\sin^2\theta_{12}, \sin^2\theta_{23}) = (0.308, 0.626)$	TBM	GRA	GRB	HG
$(\cos\delta)_{\rm E}$	-0.186	0.343	-0.299	0.588
$(\cos\delta)_{\rm LO}$	-0.179	0.225	-0.265	0.415
$(\cos\delta)_{\rm E}/(\cos\delta)_{\rm LO}$	1.04	1.52	1.13	1.42
$(\cos\phi)_{\rm E}$	-0.272	0.244	-0.376	0.506
$(\cos\delta)_{\rm E}/(\cos\phi)_{\rm E}$	0.684	1.41	0.794	1.16
$(\cos\phi)_{\rm E}/(\cos\phi)_{\rm LO}$	1.52	1.09	1.42	1.22

Table 3.8: The same as in Table 3.4, but for $\sin^2\theta_{13} = 0.0234$ (best fit value), $\sin^2\theta_{12} = 0.308$ (best fit value) and $\sin^2\theta_{23} = 0.626$ (upper bound of the 3σ range).

$\sin^2\theta_{12}$, $\sin^2\theta_{13}$, $\sin^2\theta_{23}$ and δ, obtained in the global analysis of the neutrino oscillation data performed in [8]. Our goal is to derive the allowed ranges for δ, $\cos\delta$ and $J_{\rm CP}$, predicted on the basis of the current data on the neutrino mixing parameters for each of

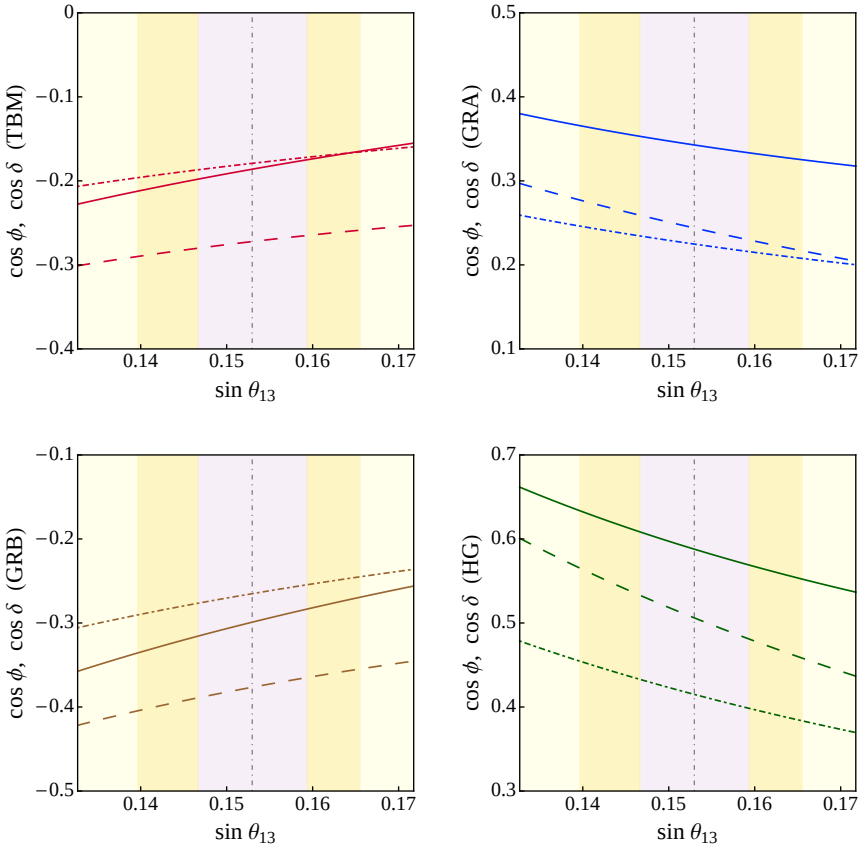

Figure 3.10: The same as in Fig. 3.5, but for $\sin^2\theta_{12} = 0.308$ (best fit value) and $\sin^2\theta_{23} = 0.626$ (upper bound of the 3σ interval in eq. (1.2.7)).

the symmetry forms of $\tilde{U}_\nu$ considered. We recall that in the standard parametrisation of the PMNS matrix, the $J_{\rm CP}$ factor reads (see, e.g., [1]):

$$J_{\rm CP} = {\rm Im}\left\{U^*_{e1}U^*_{\mu 3}U_{e3}U_{\mu 1}\right\} = \frac{1}{8}\sin\delta\sin 2\theta_{13}\sin 2\theta_{23}\sin 2\theta_{12}\cos\theta_{13}\,. \tag{3.4.1}$$

We construct χ^2 for the schemes considered — TBM, BM (LC), GRA, GRB and HG — as described in Appendix B.2. We will focus on the general case of non-vanishing θ^e_{23} in order to allow for possible sizeable deviations of θ_{23} from the symmetry value $\pi/4$.

In the five panels in Fig. 3.11 we show $N_\sigma \equiv \sqrt{\chi^2}$ as a function of δ for the five symmetry forms of $\tilde{U}_\nu$ we have studied. The dashed lines correspond to the results of the global fit [8]. The solid lines represent the results we obtain by minimising the value of χ^2 in $\sin^2\theta_{13}$ and $\sin^2\theta_{23}$ (or, equivalently, in $\sin^2\theta^e_{12}$ and $\sin^2\hat{\theta}_{23}$) for a fixed value of δ [6].

[6] We note that in the scheme considered by us, fixing the value of δ implies that one of the three neutrino mixing angles is expressed in terms of the other two. We choose for convenience this angle to be θ_{12}.

The blue (red) lines correspond to NO (IO) neutrino mass spectrum. The value of χ^2 at the minimum, $\chi^2_{\rm min}$, which determines the best fit value of δ predicted for each symmetry form of $\tilde{U}_\nu$, allows us to make conclusions about the compatibility of a given symmetry form of $\tilde{U}_\nu$ with the current global neutrino oscillation data.

It follows from the results shown in Fig. 3.11 that the BM (LC) symmetry form is disfavoured by the data at approximately 1.8σ, all the other symmetry forms considered being compatible with the data. We note that for the TBM, GRA, GRB and HG symmetry forms, a value of δ in the vicinity of $3\pi/2$ is preferred statistically. For the TBM symmetry form this result was first obtained in [74] while for the GRA, GRB and HG symmetry forms it was first found in [75]. In contrast, in the case of the BM (LC) form the best fit value is very close to π [74, 75]. The somewhat larger value of χ^2 at the second local minimum in the vicinity of $\pi/2$ in the TBM, GRA, GRB and HG cases, is a consequence of the fact that the best fit value of δ obtained in the global analysis of the current neutrino oscillation data is close to $3\pi/2$ and that the value of $\delta = \pi/2$ is statistically disfavoured (approximately at 2.5σ). In the absence of any information on δ, the two minima would have exactly the same value of χ^2, because they correspond to the same value of $\cos\delta$. In the schemes considered, as we have discussed, $\cos\delta$ is determined by the values of θ_{12}, θ_{13} and θ_{23}. The degeneracy in the sign of $\sin\delta$ can only be solved by an experimental input on δ. In Table 3.9 we give the best fit values of δ and the corresponding 3σ ranges for the TBM, BM (LC), GRA, GRB and HG forms of $\tilde{U}_\nu$, found by fixing $\sqrt{\chi^2 - \chi^2_{\rm min}} = 3$.

In Fig. 3.12 we show the likelihood function versus $\cos\delta$ for NO neutrino mass spectrum. The results shown are obtained by marginalising over all the other relevant parameters of the scheme considered (see Appendix B.2 for details). The dependence of the likelihood function on $\cos\delta$ in the case of IO neutrino mass spectrum differs little from that shown in Fig. 3.12. Given the global fit results, the likelihood function, i.e.,

$$L(\cos\delta) \propto \exp\left(-\frac{\chi^2(\cos\delta)}{2}\right), \tag{3.4.2}$$

represents the most probable value of $\cos\delta$ for each of the considered symmetry forms of $\tilde{U}_\nu$. The $n\sigma$ confidence level region corresponds to the interval of values of $\cos\delta$ in which $L(\cos\delta) \geq L(\chi^2 = \chi^2_{\rm min}) \cdot L(\chi^2 = n^2)$.

As can be observed from Fig. 3.12, a rather precise measurement of $\cos\delta$ would allow one to distinguish between the different symmetry forms of $\tilde{U}_\nu$ considered by us. For the TBM and GRB forms there is a significant overlap of the corresponding likelihood functions. The same observation is valid for the GRA and HG forms. However, the overlap of the likelihood functions of these two groups of symmetry forms occurs only at 3σ level in a very small interval of values of $\cos\delta$, as can also be seen from Table 3.9. This implies that in order to distinguish between TBM/GRB, GRA/HG and BM symmetry forms a not very demanding measurement (in terms of accuracy) of $\cos\delta$ might be sufficient. The value of the non-normalised likelihood function at the maximum in Fig. 3.12 is equal to $\exp(-\chi^2_{\rm min}/2)$, which allows us to make conclusions about the compatibility of the symmetry schemes with the current global data, as has already been pointed out.

In the left panel of Fig. 3.13 we present the likelihood function versus $\cos\delta$ within the Gaussian approximation (see Appendix B.2 for details), using the current best fit values of the mixing angles for NO neutrino mass spectrum in eqs. (1.2.6) – (1.2.8) and the prospective 1σ uncertainties in the determination of $\sin^2\theta_{12}$ (0.7% from JUNO [133]), $\sin^2\theta_{13}$ (almost 3% derived from an expected error on $\sin^2 2\theta_{13}$ of 3% from Daya Bay, see A. de Gouvea *et al.* in [134]) and $\sin^2\theta_{23}$ (5% [7] derived from the potential sensitivity of NOvA and T2K on $\sin^2 2\theta_{23}$ of 2%, see A. de Gouvea *et al.* in [134]). The BM case is very sensitive to the best fit values of $\sin^2\theta_{12}$ and $\sin^2\theta_{23}$ and is disfavoured at more than 2σ for the current best fit values quoted in eqs. (1.2.6) – (1.2.8). This case might turn out to be compatible with the data for larger (smaller) measured values of $\sin^2\theta_{12}$ ($\sin^2\theta_{23}$), as can be seen from the right panel of Fig. 3.13, which was obtained for $\sin^2\theta_{12} = 0.332$. With the increase of the value of $\sin^2\theta_{23}$ the BM form becomes increasingly disfavoured, while the TBM/GRB (GRA/HG) predictions for $\cos\delta$ are shifted somewhat — approximately by 0.1 — to the left (right) with respect to those shown in the left panel of Fig. 3.13. This shift is illustrated in Fig. 3.14, which is obtained for $\sin^2\theta_{23} = 0.579$, more precisely, for the best fit values found in [9] and corresponding to IO neutrino mass spectrum. The measurement of $\sin^2\theta_{12}$, $\sin^2\theta_{13}$ and $\sin^2\theta_{23}$ with the quoted precision will open up the possibility to distinguish between the BM, TBM/GRB, GRA and HG forms of $\tilde{U}_\nu$. Distinguishing between the TBM and GRB forms would require relatively high precision measurement of $\cos\delta$.

We have performed also a statistical analysis in order to derive predictions for $J_{\rm CP}$. In Fig. 3.15 we present $N_\sigma \equiv \sqrt{\chi^2}$ as a function of $J_{\rm CP}$ for NO and IO neutrino mass spectra. Similarly to the case of δ, we minimise the value of χ^2 for a fixed value of $J_{\rm CP}$ by varying $\sin^2\theta_{13}$ and $\sin^2\theta_{23}$ (or, equivalently, $\sin^2\theta^e_{12}$ and $\sin^2\hat{\theta}_{23}$). The best fit value of $J_{\rm CP}$ and the corresponding 3σ range for each of the considered symmetry forms of $\tilde{U}_\nu$ are summarised in Table 3.9. As Fig. 3.15 shows, the CP-conserving value of $J_{\rm CP} = 0$ is excluded in the cases of the TBM, GRA, GRB and HG neutrino mixing symmetry forms, respectively, at approximately 5σ, 4σ, 4σ and 3σ confidence levels with respect to the confidence level of the corresponding best fit values [8]. These results correspond to those we have obtained for δ, more specifically to the confidence levels at which the CP-conserving values of $\delta = 0$, π, 2π, are excluded (see Fig. 3.11).

In contrast, for the BM (LC) symmetry form, the CP-conserving value of δ, namely, $\delta \cong \pi$, is preferred and therefore the CP-violating effects in neutrino oscillations are predicted to be suppressed. At the best fit point we obtain a value of $J_{\rm CP} = -0.005\,(-0.002)$ for NO (IO) neutrino mass spectrum, which corresponds to the best fit value of $\delta/\pi = 1.04\,(1.02)$. The allowed range of the $J_{\rm CP}$ factor in the BM (LC) includes the CP-conserving value $J_{\rm CP} = 0$ at practically any confidence level. As can be seen from Table 3.9, the 3σ allowed intervals of values of δ and $J_{\rm CP}$ are rather narrow for all the symmetry forms considered, except for the BM (LC) form.

[7] This sensitivity can be achieved in future neutrino facilities [135].

[8] The confidence levels under discussion differ in the cases of NO and IO neutrino mass spectra, but as Fig. 3.15 indicates, in the cases considered these differences are rather small and we have not given them.

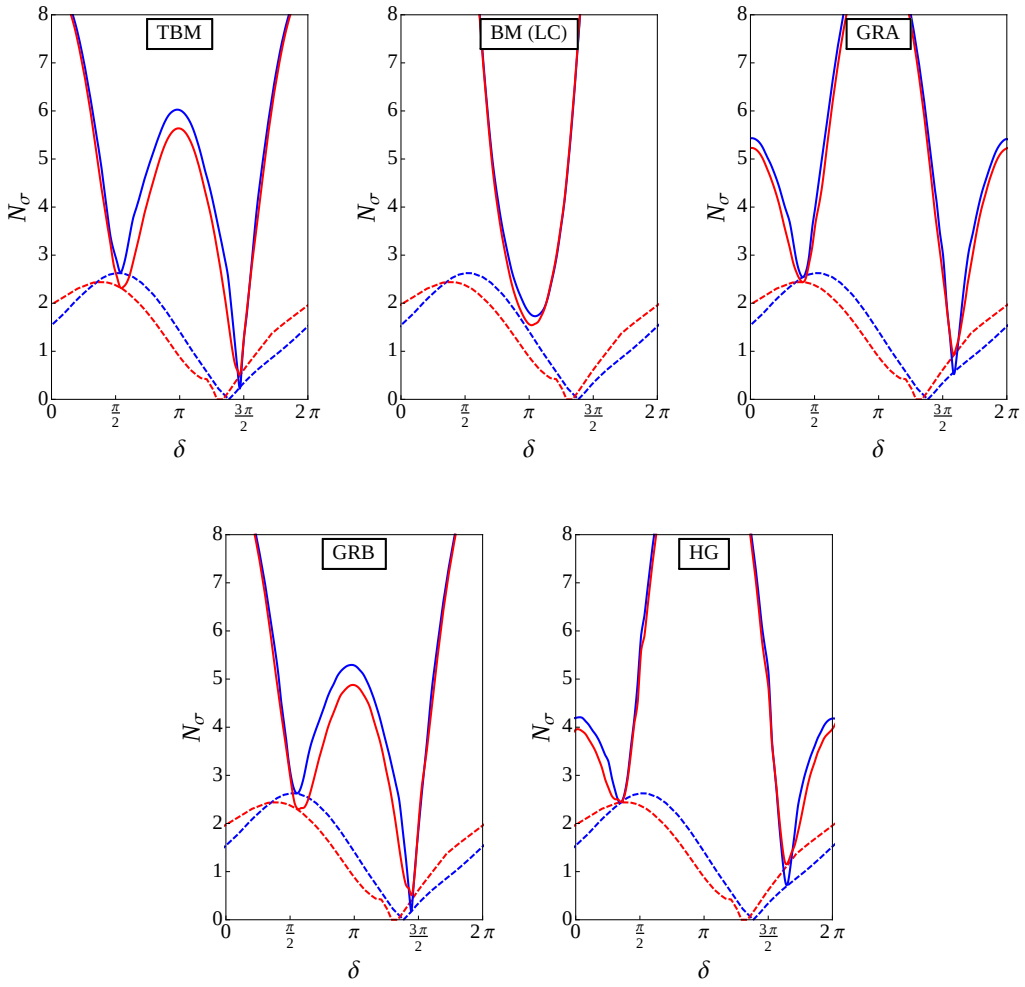

Figure 3.11: $N_\sigma \equiv \sqrt{\chi^2}$ as a function of δ. The dashed lines represent the results of the global fit [8], while the solid lines represent the results we obtain for the TBM, BM (LC), GRA (upper left, central, right panels), GRB and HG (lower left and right panels) symmetry forms of $\tilde{U}_\nu$. The blue (red) lines are for NO (IO) neutrino mass spectrum (see text for further details).

Finally, for completeness, we present in Appendix B.3 also results of a statistical analysis of the predictions for the values of $\sin^2\theta_{23}$ for the TBM, BM (LC), GRA, GRB and HG neutrino mixing symmetry forms considered. We recall that of the three neutrino mixing parameters, $\sin^2\theta_{12}$, $\sin^2\theta_{13}$ and $\sin^2\theta_{23}$, $\sin^2\theta_{23}$ is determined in the global analyses of the neutrino oscillation data with the largest uncertainty.

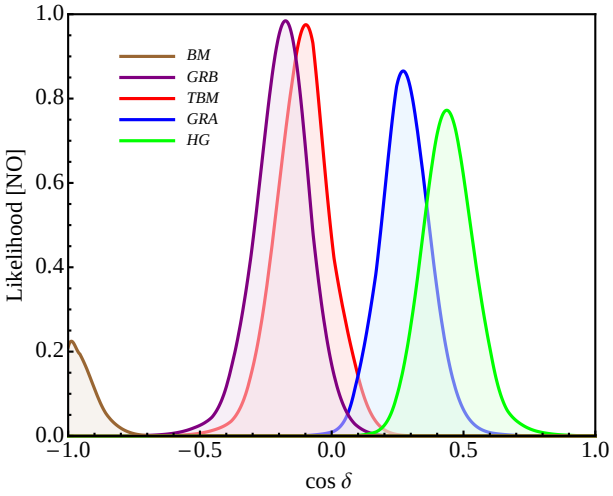

Figure 3.12: The likelihood function versus $\cos\delta$ for NO neutrino mass spectrum after marginalising over $\sin^2\theta_{13}$ and $\sin^2\theta_{23}$ for the TBM, BM (LC), GRA, GRB and HG symmetry forms of the mixing matrix $\tilde{U}_\nu$ (see text for further details).

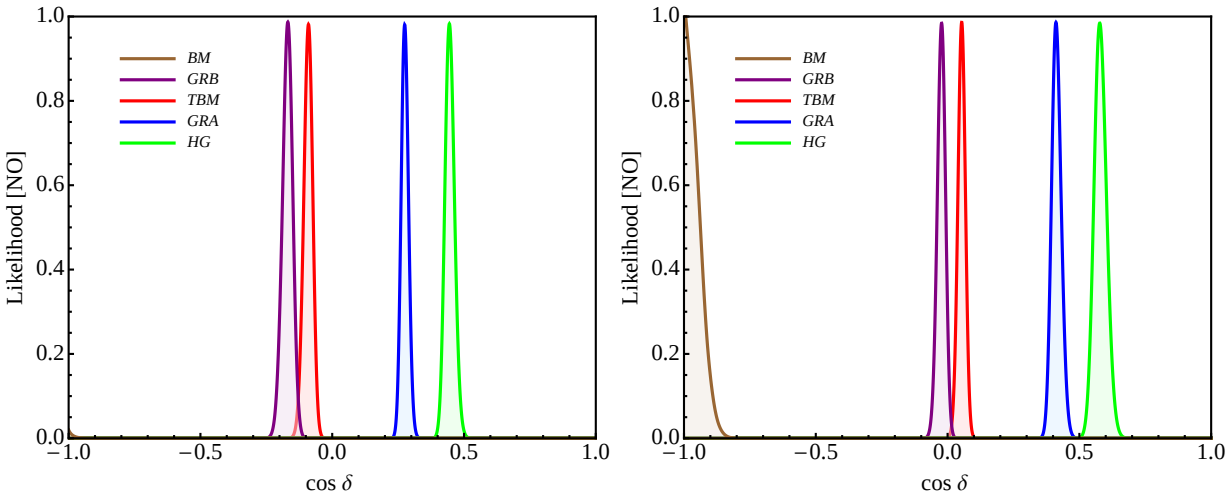

Figure 3.13: The same as in Fig. 3.12, but using the prospective 1σ uncertainties in the determination of the neutrino mixing angles within the Gaussian approximation (see text for further details). In the left (right) panel $\sin^2\theta_{12} = 0.308$ (0.332), the other mixing angles being fixed to their NO best fit values.

3.5 Summary and Conclusions

Using the fact that the neutrino mixing matrix $U = U_e^\dagger U_\nu$, where U_e and U_ν result from the diagonalisation of the charged lepton and neutrino mass matrices, we have analysed the sum rules which the Dirac phase δ present in U satisfies when U_ν has a form dictated by, or associated with, discrete symmetries and U_e has a "minimal" form (in terms of angles and

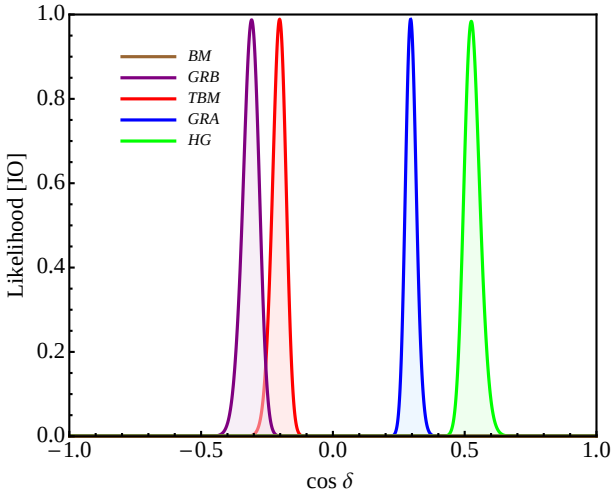

Figure 3.14: The same as in Fig. 3.13, but using the IO best fit values taken from [9].

phases it contains) that can provide the requisite corrections to U_ν, so that the reactor, atmospheric and solar neutrino mixing angles θ_{13}, θ_{23} and θ_{12} have values compatible with the current data.

We have considered the following symmetry forms of U_ν: i) tri-bimaximal (TBM), ii) bimaximal (BM) (or corresponding to the conservation of the lepton charge $L' = L_e - L_\mu - L_\tau$ (LC)), iii) golden ratio type A (GRA), iv) golden ratio type B (GRB), and v) hexagonal (HG). For all these symmetry forms U_ν can be written as $U_\nu = \Psi_1 \tilde{U}_\nu Q_0 = \Psi_1 R_{23}(\theta^\nu_{23}) R_{12}(\theta^\nu_{12}) Q_0$, where $R_{23}(\theta^\nu_{23})$ and $R_{12}(\theta^\nu_{12})$ are orthogonal matrices describing rotations in the 2-3 and 1-2 planes, respectively, and Ψ_1 and Q_0 are diagonal phase matrices each containing two phases. The phases in the matrix Q_0 give contribution to the Majorana phases in the PMNS matrix. The symmetry forms of $\tilde{U}_\nu$ of interest, TBM, BM (LC), GRA, GRB and HG, are characterised by the same value of the angle $\theta^\nu_{23} = -\pi/4$, but correspond to different fixed values of the angle θ^ν_{12} and thus of $\sin^2\theta^\nu_{12}$, namely, to i) $\sin^2\theta^\nu_{12} = 1/3$ (TBM), ii) $\sin^2\theta^\nu_{12} = 1/2$ (BM (LC)), iii) $\sin^2\theta^\nu_{12} = (2+r)^{-1} \cong 0.276$ (GRA), r being the golden ratio, $r = (1+\sqrt{5})/2$, iv) $\sin^2\theta^\nu_{12} = (3-r)/4 \cong 0.345$ (GRB), and v) $\sin^2\theta^\nu_{12} = 1/4$ (HG).

The minimal form of U_e of interest that can provide the requisite corrections to U_ν, so that the neutrino mixing angles θ_{13}, θ_{23} and θ_{12} have values compatible with the current data, including a possible sizeable deviation of θ_{23} from $\pi/4$, includes a product of two orthogonal matrices describing rotations in the 2-3 and 1-2 planes [74], $R_{23}(\theta^e_{23})$ and $R_{12}(\theta^e_{12})$, θ^e_{23} and θ^e_{12} being two (real) angles. This leads to the parametrisation of the PMNS matrix U given in eq. (3.1.5), which can be recast in the form [74]: $U = R_{12}(\theta^e_{12})\Phi(\phi) R_{23}(\hat{\theta}_{23})\, R_{12}(\theta^\nu_{12})\, \hat{Q}$, where $\Phi = \mathrm{diag}\left(1, \mathrm{e}^{i\phi}, 1\right)$, ϕ being a CP violation phase, $\hat{\theta}_{23}$ is a function of θ^e_{23} (see eq. (3.1.8)), and $\hat{Q}$ is a diagonal phase matrix. The phases in $\hat{Q}$ give contributions to the Majorana phases in the PMNS matrix. The angle $\hat{\theta}_{23}$, however, can be expressed in terms of the angles θ_{23} and θ_{13} of the PMNS matrix

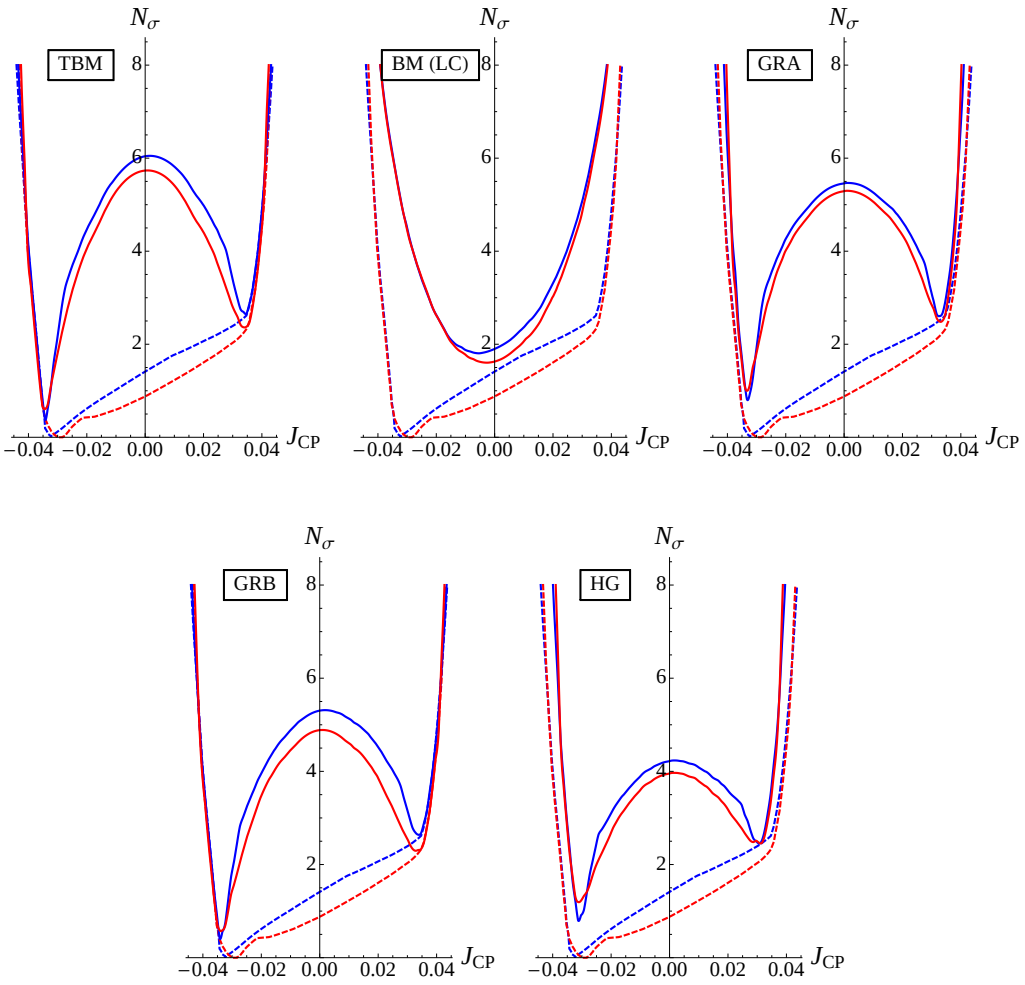

Figure 3.15: $N_\sigma \equiv \sqrt{\chi^2}$ as a function of $J_{\rm CP}$. The dashed lines represent the results of the global fit [8], while the solid lines represent the results we obtain for the TBM, BM (LC), GRA (upper left, central, right panels), GRB and HG (lower left and right panels) neutrino mixing symmetry forms. The blue (red) lines are for NO (IO) neutrino mass spectrum (see text for further details).

(eq. (3.1.14)) and the value of $\hat{\theta}_{23}$ is fixed by the values of θ_{23} and θ_{13}.

In this scheme the four observables θ_{12}, θ_{23}, θ_{13} and the Dirac phase δ in the PMNS matrix are functions of three parameters θ^e_{12}, $\hat{\theta}_{23}$ and ϕ. As a consequence, the Dirac phase δ can be expressed as a function of the three PMNS angles θ_{12}, θ_{23} and θ_{13}, leading to a new "sum rule" relating δ and θ_{12}, θ_{23} and θ_{13}. This sum rule is exact within the scheme considered. Its explicit form depends on the symmetry form of the matrix $\tilde{U}_\nu$, i.e., on the value of the angle θ^ν_{12}. For arbitrary fixed value of θ^ν_{12} the sum rule of interest is given in eq. (3.1.16) (or the equivalent eq. (3.1.17)) [75]. A similar exact sum rule can be derived

Symmetry form		Best fit	3σ range
TBM	$J_{\rm CP}$ (NO)	-0.034	$-0.038 \div -0.028 \oplus 0.031 \div 0.036$
	$J_{\rm CP}$ (IO)	-0.034	$-0.039 \div -0.025 \oplus 0.029 \div 0.037$
	δ/π (NO)	1.48	$0.49 \div 0.58 \oplus 1.34 \div 1.57$
	δ/π (IO)	1.48	$0.47 \div 0.65 \oplus 1.30 \div 1.57$
	$\cos\delta$ (NO)	-0.07	$-0.47 \div 0.21$
	$\cos\delta$ (IO)	-0.07	$-0.60 \div 0.23$
BM (LC)	$J_{\rm CP}$ (NO)	-0.005	$-0.026 \div 0.021$
	$J_{\rm CP}$ (IO)	-0.002	$-0.025 \div 0.023$
	δ/π (NO)	1.04	$0.80 \div 1.24$
	δ/π (IO)	1.02	$0.79 \div 1.23$
	$\cos\delta$ (NO)	-0.99	$-1.00 \div -0.72$
	$\cos\delta$ (IO)	-1.00	$-1.00 \div -0.72$
GRA	$J_{\rm CP}$ (NO)	-0.033	$-0.037 \div -0.027 \oplus 0.030 \div 0.035$
	$J_{\rm CP}$ (IO)	-0.033	$-0.037 \div -0.025 \oplus 0.028 \div 0.036$
	δ/π (NO)	1.58	$0.35 \div 0.46 \oplus 1.50 \div 1.70$
	δ/π (IO)	1.58	$0.31 \div 0.48 \oplus 1.47 \div 1.74$
	$\cos\delta$ (NO)	0.25	$-0.08 \div 0.69$
	$\cos\delta$ (IO)	0.25	$-0.08 \div 0.69$
GRB	$J_{\rm CP}$ (NO)	-0.034	$-0.039 \div -0.026 \oplus 0.031 \div 0.036$
	$J_{\rm CP}$ (IO)	-0.033	$-0.039 \div -0.022 \oplus 0.026 \div 0.037$
	δ/π (NO)	1.45	$0.51 \div 0.61 \oplus 1.31 \div 1.54$
	δ/π (IO)	1.45	$0.50 \div 0.70 \oplus 1.25 \div 1.54$
	$\cos\delta$ (NO)	-0.15	$-0.57 \div 0.13$
	$\cos\delta$ (IO)	-0.15	$-0.70 \div 0.13$
HG	$J_{\rm CP}$ (NO)	-0.031	$-0.035 \div -0.020 \oplus 0.026 \div 0.034$
	$J_{\rm CP}$ (IO)	-0.031	$-0.036 \div -0.015 \oplus 0.019 \div 0.034$
	δ/π (NO)	1.66	$0.27 \div 0.41 \oplus 1.55 \div 1.80$
	δ/π (IO)	1.63	$0.19 \div 0.42 \oplus 1.55 \div 1.86$
	$\cos\delta$ (NO)	0.47	$0.16 \div 0.80$
	$\cos\delta$ (IO)	0.40	$0.16 \div 0.80$

Table 3.9: Best fit values of $J_{\rm CP}$, δ and $\cos\delta$ and corresponding 3σ ranges (found fixing $\sqrt{\chi^2 - \chi^2_{\rm min}} = 3$) in our setup using the data from [8].

for the phase ϕ (eq. (3.1.18)) [75].

A parametrisation of the PMNS matrix, similar to that given in eq. (3.1.5), has been effectively employed in ref. [86]. Treating $\sin\theta^e_{12}$ and $\sin\theta^e_{23}$ as small parameters, $|\sin\theta^e_{12}| \ll 1$, $|\sin\theta^e_{23}| \ll 1$, and neglecting terms of order of, or smaller than, $O((\theta^e_{12})^2)$, $O((\theta^e_{23})^2)$ and $O(\theta^e_{12}\theta^e_{23})$, the following "leading order" sum rule was obtained in [86]: $\theta_{12} \cong \theta^\nu_{12} +$

$\theta_{13}\cos\delta$. This sum rule, in the approximation used to obtain it, is equivalent to the sum rule $\sin\theta_{12} \cong \sin\theta^{\nu}_{12} + \cos\theta^{\nu}_{12}\sin\theta_{13}\cos\delta$, which was shown in ref. [75] to be the leading order approximation of the exact sum rule given in eq. (3.1.16) (or the equivalent eq. (3.1.17)). In the present chapter we have investigated the predictions for $\cos\delta$ in the cases of TBM, BM (LC), GRA, GRB and HG symmetry forms of the matrix $\tilde{U}_\nu$ using the exact and the leading order sum rules for $\cos\delta$ discussed above and given in eqs. (3.1.17) and (3.1.24). It was shown in [75], in particular, using the best fit values of the neutrino mixing parameters $\sin^2\theta_{12}$, $\sin^2\theta_{23}$ and $\sin^2\theta_{13}$ and the exact sum rule results for $\cos\delta$ derived for the TBM, GRA, GRB and HG forms of $\tilde{U}_\nu$, that the leading order sum rule provides largely imprecise predictions for $\cos\delta$. Here we have performed a thorough study of the exact and leading order sum rule predictions for $\cos\delta$ in the TBM, BM (LC), GRA, GRB and HG cases taking into account the uncertainties in the measured values of $\sin^2\theta_{12}$, $\sin^2\theta_{23}$ and $\sin^2\theta_{13}$. This allowed us, in particular, to assess the accuracy of the predictions for $\cos\delta$ based on the leading order sum rules and its dependence on the values of the indicated neutrino mixing parameters when the latter are varied in their respective 3σ experimentally allowed ranges. In contrast to the leading order sum rule, the exact sum rule for $\cos\delta$ depends not only on θ_{12} and θ_{13}, but also on θ_{23}, and we have investigated this dependence as well.

In the present study we have analysed both the cases of $\theta^{e}_{23} = 0$, in which $\sin^2\theta_{23} \cong 0.5(1-\sin^2\theta_{13})$, and of arbitrary θ^{e}_{23}. In the second case θ_{23} can deviate significantly from $\pi/4$.

We confirm the result found in [75] that the exact sum rule predictions for $\cos\delta$ vary significantly with the symmetry form of $\tilde{U}_\nu$. This result implies that the measurement of $\cos\delta$ can allow us to distinguish between the different symmetry forms of $\tilde{U}_\nu$ [75] provided $\sin^2\theta_{12}$, $\sin^2\theta_{13}$ and $\sin^2\theta_{23}$ are known with a sufficiently good precision. Even determining the sign of $\cos\delta$ will be sufficient to eliminate some of the possible symmetry forms of $\tilde{U}_\nu$.

We find also that the exact sum rule predictions for $\cos\delta$ exhibit strong dependence on the value of $\sin^2\theta_{12}$ when the latter is varied in its 3σ experimentally allowed range $(0.259-0.359)$ (Tables 3.1 – 3.6). The predictions for $\cos\delta$ change significantly not only in magnitude, but in the cases of TBM, GRA and GRB forms of $\tilde{U}_\nu$ also the sign of $\cos\delta$ can change. These significant changes take place both for $\theta^{e}_{23} = 0$ and $\theta^{e}_{23} \neq 0$.

We have investigated the dependence of the exact sum rule predictions for $\cos\delta$ in the cases of the symmetry forms of $\tilde{U}_\nu$ considered on the value of $\sin^2\theta_{23}$ varying the latter in the respective 3σ allowed interval $0.374 \leq \sin^2\theta_{23} \leq 0.626$ (Figs. 3.9 and 3.10, and Tables 3.7 and 3.8). The results we get for $\sin^2\theta_{23} = 0.374$ and $\sin^2\theta_{23} = 0.437$, setting $\sin^2\theta_{12}$ and $\sin^2\theta_{13}$ to their best fit values, do not differ significantly. However, the differences between the predictions for $\cos\delta$ obtained for $\sin^2\theta_{23} = 0.437$ and for $\sin^2\theta_{23} = 0.626$ are relatively large (they differ by the factors of 2.05, 1.25, 1.77 and 1.32 in the TBM, GRA, GRB and HG cases, respectively).

In all cases considered, having the exact sum rule results for $\cos\delta$, we could investigate the precision of the leading order sum rule predictions for $\cos\delta$. We found that the leading order sum rule predictions for $\cos\delta$ are, in general, imprecise and in many cases are largely incorrect, the only exception being the case of the BM (LC) form of $\tilde{U}_\nu$ [75].

We have performed a similar analysis of the predictions for the cosine of the phase ϕ.

The phase ϕ is related to, but does not coincide with, the Dirac phase δ. The parameter $\cos\phi$ obeys a leading order sum rule which is almost identical to the leading order sum rule satisfied by $\cos\delta$. This leads to the confusing identification of ϕ with δ: the exact sum rules satisfied by $\cos\phi$ and $\cos\delta$ differ significantly. Correspondingly, the predicted values of $\cos\phi$ and $\cos\delta$ in the cases of the TBM, GRA, GRB and HG symmetry forms of $\tilde{U}_\nu$ considered by us also differ significantly (see Figs. 3.1 – 3.10 and Tables 3.1 – 3.8). This conclusion is not valid for the BM (LC) form: for this form the exact sum rule predictions for $\cos\phi$ and $\cos\delta$ are rather similar. The phase ϕ appears in a large class of models of neutrino mixing and neutrino mass generation and serves as a "source" for the Dirac phase δ in these models.

Finally, we have performed a statistical analysis of the predictions for δ, $\cos\delta$ and the rephasing invariant $J_{\rm CP}$ which controls the magnitude of CPV effects in neutrino oscillations [11], in the cases of the TBM, BM (LC), GRA, GRB and HG symmetry forms of the matrix $\tilde{U}_\nu$ considered. In this analysis we have used as input the latest results on $\sin^2\theta_{12}$, $\sin^2\theta_{13}$, $\sin^2\theta_{23}$ and δ, obtained in the global analysis of the neutrino oscillation data performed in [8]. Our goal was to derive the allowed ranges for δ, $\cos\delta$ and $J_{\rm CP}$, predicted on the basis of the current data on the neutrino mixing parameters for each of the symmetry forms of $\tilde{U}_\nu$ considered. The results of this analysis are shown in Figs. 3.11, 3.12 and 3.15, and are summarised in Table 3.9, in which we give the predicted best fit values and 3σ ranges of $J_{\rm CP}$, δ and $\cos\delta$ for each of the symmetry forms of $\tilde{U}_\nu$ considered. We have shown, in particular, that the CP-conserving value of $J_{\rm CP} = 0$ is excluded in the cases of the TBM, GRA, GRB and HG neutrino mixing symmetry forms, respectively, at approximately 5σ, 4σ, 4σ and 3σ confidence levels with respect to the confidence level of the corresponding best fit values (Fig. 3.15). These results reflect the predictions we have obtained for δ, more specifically, the confidence levels at which the CP-conserving values of $\delta = 0$, π, 2π, are excluded in the discussed cases (see Fig. 3.11). We have found also that the 3σ allowed intervals of values of δ and $J_{\rm CP}$ are rather narrow for all the symmetry forms considered, except for the BM (LC) form (Table 3.9). More specifically, for the TBM, GRA, GRB and HG symmetry forms we have obtained at 3σ: $0.020 \leq |J_{\rm CP}| \leq 0.039$. For the best fit values of $J_{\rm CP}$ we have found, respectively: $J_{\rm CP} = (-0.034)$, (-0.033), (-0.034), and (-0.031). Our results indicate that distinguishing between the TBM, GRA, GRB and HG symmetry forms of the neutrino mixing would require extremely high precision measurement of the $J_{\rm CP}$ factor.

Using the likelihood method, we have derived also the ranges of the predicted values of $\cos\delta$ for the different forms of $\tilde{U}_\nu$ considered, using the prospective 1σ uncertainties in the determination of $\sin^2\theta_{12}$, $\sin^2\theta_{13}$ and $\sin^2\theta_{23}$ respectively in JUNO, Daya Bay and accelerator and atmospheric neutrino experiments (Fig. 3.13). In this analysis the current best fit values of $\sin^2\theta_{12}$, $\sin^2\theta_{13}$ and $\sin^2\theta_{23}$ have been utilised (left panel of Fig. 3.13). The results thus obtained show that i) the measurement of the sign of $\cos\delta$ will allow to distinguish between the TBM/GRB, BM and GRA/HG forms of $\tilde{U}_\nu$, ii) for a best fit value of $\cos\delta = -1\,(-0.1)$ distinguishing at 3σ between the BM (TBM/GRB) and the other forms of $\tilde{U}_\nu$ would be possible if $\cos\delta$ is measured with 1σ uncertainty of $0.3\,(0.1)$.

The predictions for δ, $\cos\delta$ and $J_{\rm CP}$ in the case of the BM (LC) symmetry form of $\tilde{U}_\nu$,

as the results of the statistical analysis performed by us showed, differ significantly from those found for the TBM, GRA, GRB and HG forms: the best fit value of $\delta \cong \pi$, and, correspondingly, of $J_{\rm CP} \cong 0$. For the 3σ range of $J_{\rm CP}$ we have obtained in the case of NO (IO) neutrino mass spectrum: -0.026 $(-0.025) \leq J_{\rm CP} \leq 0.021$ (0.023), i.e., it includes a sub-interval of values centred on zero, which does not overlap with the 3σ allowed intervals of values of $J_{\rm CP}$ in the TBM, GRA, GRB and HG cases.

The results obtained in the present study, in particular, reinforce the conclusion reached in ref. [75] that the experimental measurement of the cosine of the Dirac phase δ of the PMNS neutrino mixing matrix can provide unique information about the possible discrete symmetry origin of the observed pattern of neutrino mixing.

CHAPTER 4

Non-Standard Neutrino Interactions

4.1 Introduction

An important aspect of the current studies in neutrino physics is the use of the high precision data of neutrino oscillation experiments to test models of neutrino related physics beyond the Standard Theory of particle interactions. In the present Chapter we investigate the possible effects of the existence of non-standard neutrino interactions on the interpretation of the results of the rector neutrino experiments Daya Bay, RENO and Double Chooz and of the T2K accelerator neutrino experiment [136].

Recently the T2K collaboration reported a measurement of the reactor neutrino mixing angle θ_{13} based on their latest $\nu_\mu \to \nu_e$ oscillation data [137]. Fixing the values of i) the Dirac CP violation (CPV) phase $\delta = 0$, ii) the atmospheric neutrino mixing angle $\theta_{23} = \pi/4$, iii) $\sin^2\theta_{12} = 0.306$, iv) $\Delta m^2_{21} = 7.6 \times 10^{-5}$ eV^2 and v) $|\Delta m^2_{32}| = 2.4 \times 10^{-3}$ eV^2, the T2K collaboration found:

$$\sin^2 2\theta_{13} = 0.140^{+0.038}_{-0.032}\,(0.170^{+0.045}_{-0.037})\,, \tag{4.1.1}$$

where the value (the value in brackets) corresponds to neutrino mass spectrum with normal (inverted, IO) ordering (NO). The best fit value of $\sin^2 2\theta_{13}$ reported by the T2K collaboration is significantly larger than that measured in the reactor neutrino experiments Daya Bay, RENO and Double Chooz [102, 104, 138]. The most precise determination of $\sin^2 2\theta_{13}$ was reported by the Daya Bay collaboration [138]:

$$\sin^2 2\theta_{13} = 0.090^{+0.008}_{-0.009}\,. \tag{4.1.2}$$

Given the uncertainty in the T2K result, Eq. (4.1.1), the difference between the values of $\sin^2 2\theta_{13}$ obtained in the T2K and Daya Bay experiments does not seem to be irreconcilable and the most natural explanation of this difference can be attributed to setting $\delta = 0$ and $\theta_{23} = \pi/4$. Indeed, the global analyses of the neutrino oscillation data, including the data from T2K and Daya Bay, performed in [7, 8] found a hint for non-zero value of δ and for a deviation of θ_{23} from $\pi/4$: for the best fit values of δ and $\sin^2\theta_{23}$ the authors of [8] obtained

$\delta \simeq 3\pi/2$ and $\sin^2\theta_{23} = 0.42 - 0.43$. Similar results were obtained in [7].
On-going and future neutrino experiments [137, 139, 140] have the physics potential to improve the data on the leptonic CP violation phase δ and thus to test the indications for $\delta \sim 3\pi/2$ found in the global analyses [7, 8].

In this chapter we would like to entertain a different possibility, namely, that the difference between the values of $\sin^2 2\theta_{13}$ found in the T2K experiment for $\delta = 0$, $\theta_{23} = \pi/4$, etc., and in the Daya Bay experiment is due to the presence of new physics in the neutrino sector. More specifically, we consider the effects of non-standard neutrino interactions (NSI) [141, 142] on the $\bar{\nu}_e \to \bar{\nu}_e$ and $\nu_\mu \to \nu_e$ oscillation probabilities and show how the values obtained in the two experiments can be reconciled.

4.2 Basic formalism

In what follows we consider the analytic treatment of Non Standard Interactions (NSI) as described in [143], where it was assumed that NSI can affect both neutrino production and detection processes. Matter effects can be safely neglected in the $\bar{\nu}_e \to \bar{\nu}_e$ and $\nu_\mu \to \nu_e$ oscillation probabilities, relevant for the interpretation of the Daya Bay and T2K data of interest.

Effects of NSI can appear at low energy through unknown couplings $\varepsilon_{\alpha\beta}$, generated after integrating out heavy degrees of freedom. These new couplings can affect neutrino production s and detection d [142], so the neutrino states are a superposition of the orthonormal flavor eigenstates $|\nu_e\rangle$, $|\nu_\mu\rangle$ and $|\nu_\tau\rangle$ [144–146]:

$$|\nu^{\rm s}_\alpha\rangle = |\nu_\alpha\rangle + \sum_{\beta=e,\mu,\tau} \varepsilon^s_{\alpha\beta}|\nu_\beta\rangle = \left[(1+\varepsilon^s)|\nu\rangle\right]_\alpha , \tag{4.2.1}$$

$$\langle\nu^{\rm d}_\beta| = \langle\nu_\beta| + \sum_{\alpha=e,\mu,\tau} \varepsilon^d_{\alpha\beta}\langle\nu_\alpha| = \left[\langle\nu|(1+\varepsilon^d)\right]_\beta . \tag{4.2.2}$$

The oscillation probability can be obtained by squaring the amplitude $\langle\nu^d_\beta|e^{-iHL}|\nu^s_\alpha\rangle$:

$$\begin{aligned} P_{\nu^s_\alpha\to\nu^d_\beta} &= |\langle\nu^d_\beta|e^{-iHL}|\nu^s_\alpha\rangle|^2 \\ &= \left|(1+\epsilon^d)_{\gamma\beta}\left(e^{-iHL}\right)_{\gamma\delta}(1+\epsilon^s)_{\alpha\delta}\right|^2 . \end{aligned}$$

Since the parameters $\epsilon^s_{e\alpha}$ and $\epsilon^d_{\alpha e}$ receive contributions from the same higher dimensional operators, one can constrain them by the relation:

$$\epsilon^s_{e\alpha} = \epsilon^{d*}_{\alpha e} \equiv \epsilon_{e\alpha} e^{{\rm i}\,\phi_{e\alpha}} , \tag{4.2.3}$$

$\epsilon_{e\alpha}$ and $\phi_{e\alpha}$ being the modulus and the argument of $\epsilon^s_{e\alpha}$. For $\epsilon_{\alpha\beta}$ there exist model independent bounds derived in [147], which at 90% C.L. read:

$$\begin{aligned} &\varepsilon_{ee} < 0.041, \quad \varepsilon_{e\mu} < 0.025, \quad \varepsilon_{e\tau} < 0.041 , \\ &|\varepsilon^{s,d}_{\mu e}| < 0.026, \quad |\varepsilon^{s,d}_{\mu\mu}| < 0.078, \quad |\varepsilon^{s,d}_{\mu\tau}| < 0.013 , \end{aligned} \tag{4.2.4}$$

whereas for the CP violation phases $\phi_{e\alpha}$ no constraints have been obtained so far. These bounds can be further improved, e.g., by future reactor neutrino experiments [144] and at neutrino factories [148], especially the bounds on non-diagonal couplings which are expected to be constrained at the level of $\mathcal{O}(10^{-3})$. Recently it was shown in Ref. [72] that the bound on ε_{ee} can be improved by almost an order of magnitude by the most recent data of the Daya Bay experiment [138], i.e. $\varepsilon_{ee} \lesssim 3.6 \times 10^{-3}$ at 90% confidence level.

In the case of the Daya Bay setup, the relevant features of the $\bar{\nu}_e \to \bar{\nu}_e$ survival probability at the far and near detectors can be already caught keeping terms up to $O(\epsilon)$ in the expansion in the small couplings $|\epsilon^{s,d}_{\alpha\beta}|$ and neglecting terms of $\mathcal{O}(\Delta m^2_{21}/\Delta m^2_{31})$ and of $\mathcal{O}(\epsilon \sin^2\theta_{13}, \sin^3\theta_{13})$.
On the other hand, for the T2K setup, the correct dependence on the Dirac phase δ is reproduced keeping the first order terms in Δm^2_{21}, as discussed in [143].
In the limiting case $\epsilon_{ee} = 0$ (which is a good approximation since $|\epsilon_{ee}\cos\phi_{ee}| < O(10^{-3})$ [72]), the $\overline{\nu}_e \to \overline{\nu}_e$ survival probability can be written for $\delta = 0$ as:

$$P(\overline{\nu}_e \to \overline{\nu}_e) = 1 - \sin^2 2\hat{\theta}_{13} \sin^2\left[\frac{\Delta m^2_{31}\, L}{4E_\nu}\right] , \tag{4.2.5}$$

where [68]

$$\begin{aligned}\sin^2 2\hat{\theta}_{13} = {} & \sin^2 2\theta_{13} + 4\epsilon_{e\mu} \sin 2\theta_{13} \sin\theta_{23} \cos 2\theta_{13} \cos(\phi_{e\mu}) \\ & + 4\epsilon_{e\tau} \sin 2\theta_{13} \cos\theta_{23} \cos 2\theta_{13} \cos(\phi_{e\tau}) \ .\end{aligned} \tag{4.2.6}$$

The terms involving the parameters $\epsilon_{e\mu}$ and $\epsilon_{e\tau}$ can affect significantly the determination of the reactor angle θ_{13}, as pointed out in [68, 72]. Depending on the phases $\phi_{e\mu}$ and $\phi_{e\tau}$, relatively large values of $\epsilon_{e\mu}$ and $\epsilon_{e\tau}$ can lead to smaller (for $\phi_{e\mu} = \phi_{e\tau} \simeq 0$), equal (for $\phi_{e\mu} \simeq \phi_{e\tau} + \pi$ and $\epsilon_{e\mu} \simeq \epsilon_{e\tau}$) or larger (for $\phi_{e\mu} = \phi_{e\tau} \simeq \pi$) values of θ_{13} than those obtained in the standard case of absence of NSI.

The oscillation probability $P(\nu_\mu \to \nu_e)$ relevant for the interpretation of the T2K data on $\sin^2 2\theta_{13}$, can be written for $\delta = 0$, $\Delta m^2_{21}/|\Delta m^2_{31} \ll 1$ and taking into account the NSI as:

$$P(\nu_\mu \to \nu_e) \simeq \sin^2\theta_{23} \sin^2 2\theta_{13} \sin^2 \frac{\Delta m^2_{31} L}{4E} + P_0 + P_1 \ , \tag{4.2.7}$$

where P_0 and P_1 include respectively the zero and the first order contributions of the NSI, derived for $\Delta m^2_{21} L/(4E_\nu) \ll 1$. Indeed, for the neutrino energy of $E_\nu = 0.1$ GeV we have: $\Delta m^2_{21} L/(4E_\nu) = 2.7 \times 10^{-4}$ for $L = 0.28$ km, and $\Delta m^2_{21} L/(4E_\nu) = 0.28$ for $L = 295$ km.

Using the constraints given in Eq. (4.2.3) and defining $\epsilon^{s,d}_{\alpha\beta} = |\epsilon^{s,d}_{\alpha\beta}| \exp(i\phi^{s,d}_{\alpha\beta})$, we get:

$$\begin{aligned}
P_0 = &- 4|\epsilon^s_{\mu e}| \sin\theta_{13} \sin\theta_{23} \cos(\phi^s_{\mu e}) \sin^2\left[\frac{\Delta m^2_{31} L}{4E_\nu}\right] \\
&- 4|\epsilon^s_{\mu e}| \sin\theta_{13} \sin\theta_{23} \sin(\phi^s_{\mu e}) \sin\left[\frac{\Delta m^2_{31} L}{4E_\nu}\right] \cos\left[\frac{\Delta m^2_{31} L}{4E_\nu}\right] \\
&- 4\epsilon_{e\mu} \sin\theta_{13} \sin\theta_{23} \cos(\phi_{e\mu}) \cos 2\theta_{23} \sin^2\left[\frac{\Delta m^2_{31} L}{4E_\nu}\right] \\
&- 4\epsilon_{e\mu} \sin\theta_{13} \sin\theta_{23} \sin(\phi_{e\mu}) \sin\left[\frac{\Delta m^2_{31} L}{4E_\nu}\right] \cos\left[\frac{\Delta m^2_{31} L}{4E_\nu}\right] \\
&+ 8\epsilon_{e\tau} \sin\theta_{13} \sin^2\theta_{23} \cos\theta_{23} \cos(\phi_{e\tau}) \sin^2\left[\frac{\Delta m^2_{31} L}{4E_\nu}\right] + O(\epsilon \sin^2\theta_{13}) + O(\epsilon^2) \,,
\end{aligned} \tag{4.2.8}$$

$$\begin{aligned}
P_1 = &- |\epsilon^s_{\mu e}| \sin 2\theta_{12} \cos\theta_{23} \sin\phi^s_{\mu e} \frac{\Delta m^2_{21} L}{2E_\nu} \\
&+ 2\epsilon_{e\mu} \sin 2\theta_{12} \sin^2\theta_{23} \cos\theta_{23} \cos\phi_{e\mu} \frac{\Delta m^2_{21} L}{4E_\nu} \sin\left[\frac{\Delta m^2_{31} L}{2E_\nu}\right] \\
&+ \epsilon_{e\mu} \sin 2\theta_{12} \cos\theta_{23} \sin\phi_{e\mu} \frac{\Delta m^2_{21} L}{2E_\nu} \left[1 - 2\sin^2\theta_{23} \sin^2\left[\frac{\Delta m^2_{31} L}{4E_\nu}\right]\right] \\
&+ 2\epsilon_{e\tau} \sin 2\theta_{12} \sin\theta_{23} \cos^2\theta_{23} \cos\phi_{e\tau} \frac{\Delta m^2_{21} L}{4E_\nu} \sin\left[\frac{\Delta m^2_{31} L}{2E_\nu}\right] \\
&- 2\epsilon_{e\tau} \sin 2\theta_{12} \sin\theta_{23} \cos^2\theta_{23} \sin\phi_{e\tau} \frac{\Delta m^2_{21} L}{2E_\nu} \sin^2\left[\frac{\Delta m^2_{31} L}{4E_\nu}\right] \\
&+ O\left(\epsilon \sin\theta_{13} \frac{\Delta m^2_{21} L}{4E_\nu}\right) + O(\epsilon^2) \,.
\end{aligned} \tag{4.2.9}$$

In the previous equations, the P_0 term encodes the correlations between θ_{13} and the new physics parameters so, as in the Daya Bay case, we expect a significant impact of degeneracies on the determination of the reactor angle. The term P_1 is subleading, whose magnitude is controlled by $\Delta m^2_{21} L/(4E_\nu) \ll 1$.

4.3 Fit results

As we can see from the previous formulae, the parameter space for NSI relevant for our analysis consists of six parameters, the moduli $\epsilon_{e\mu}$, $\epsilon_{e\tau}$, $\epsilon^s_{\mu e}$ and the phases $\phi_{e\mu}$, $\phi_{e\tau}$, $\phi^s_{\mu e}$. However, for the illustrative purposes of the present study it is sufficient to consider a smaller parameter space with just two independent NSI parameters, specified below. We consider two different scenarios: one in which a large $\sin^2 2\theta_{13} = 0.14$ ($\sin^2 2\theta_{13} = 0.17$) for NO (IO) can be reconciled with both the Daya Bay and T2K data and a second where we assume that $\sin^2 2\theta_{13} = 0.09$.

4.3.1 The case of $\sin^2 2\theta_{13} = 0.14\,(0.17)$

In this case we reduced the parameter space assuming:

$$\epsilon = \epsilon_{e\mu} = \epsilon_{e\tau} = \epsilon^s_{\mu e}, \quad \phi = \phi_{e\mu} = \phi_{e\tau}, \quad \phi^s_{\mu e} = 0. \tag{4.3.1}$$

The choice of the parameter space is not completely arbitrary. For the large θ_{13} case we need relatively large NSI effects to obtain an effective reactor angle satisfying the Daya Bay measurement.

In Fig. 4.1 we show the best fit points and the 1, 2 and 3σ confidence level regions for 1 degree of freedom (dof) after performing a combined fit to the Daya Bay [138] and T2K [137] data (see the Appendix C.1 for a detailed description of the fitting procedure). In the left panel of Fig. 4.1 we fixed $\sin^2\theta_{12} = 0.306$, $\Delta m^2_{21} = 7.6\times10^{-5}$ eV^2, $\sin^2\theta_{23} = 0.5$, $|\Delta m^2_{32}| = 2.4\times10^{-3}$ eV^2, $\delta = 0$ and $\sin^2 2\theta_{13} = 0.140$, whereas in the right panel we allowed θ_{13} to vary freely, using the mean value and the 1σ error as determined in the T2K experiment, $\sin^2 2\theta^{T2K}_{13} = 0.140 \pm 0.038$.
Results in the case of inverted hierarchy are shown in Fig. 4.2; the procedure adopted is the same as the one used to obtain Fig. 4.1, the only difference being that the fixed value of the reactor angle is now at $\sin^2 2\theta_{13} = 0.170$ and that, when θ_{13} is left free to vary, we used $\sin^2 2\theta^{T2K}_{13} = 0.170 \pm 0.045$.
As it can be seen, in the left panels of Figs. 4.1 and 4.2, the same value of θ_{13} can give a good description of both Daya Bay and T2K data under the hypothesis of relatively large ε and for a phase ϕ which is almost CP conserving.
Since we are adopting the preferred T2K value of θ_{13}, it is necessary to allow for relatively large NSI couplings to reconcile $\sin^2 2\theta_{13} = 0.14$ ($\sin^2 2\theta_{13} = 0.17$) with the Daya Bay event distribution. On the other hand, our choice of couplings, Eq. (4.3.1), does not lead to a significant change of the fit to the T2K data.
In the case we vary freely θ_{13} (see Appendix C.1 for details) the sensitivity to ϵ is significantly reduced (with the smallest statistical sensitivity at $\phi \sim \pi$), due to the strong correlation between θ_{13} and the NSI parameters [72]. That means that there exist a vast parameter space for NSI for which the data can be fitted simultaneously at the price of changing accordingly the value of θ_{13}. To give an example, at the best fit point we get: $\sin^2 2\theta_{13} = 0.113$ ($\sin^2 2\theta_{13} = 0.130$) for the NO (IO) spectrum.
The values of ϵ , ϕ at the NO(IO) best fit point are given in Table 4.1. We notice that the

$(\log_{10}\epsilon\,,\,\phi)$ **best fit**	**left panel**	**right panel**
NO	$(-1.64\,,\,3.18)$	$(-1.98\,,\,3.20)$
IO	$(-1.44\,,\,3.34)$	$(-1.74\,,\,3.32)$

Table 4.1: Best fit points for the $(\log_{10}\epsilon\,,\,\phi)$ parameters obtained in our analysis. NO refers to Fig. 4.1, IO to Fig. 4.2.

confidence level regions are slightly shifted to the left (right) if instead of the assumption in

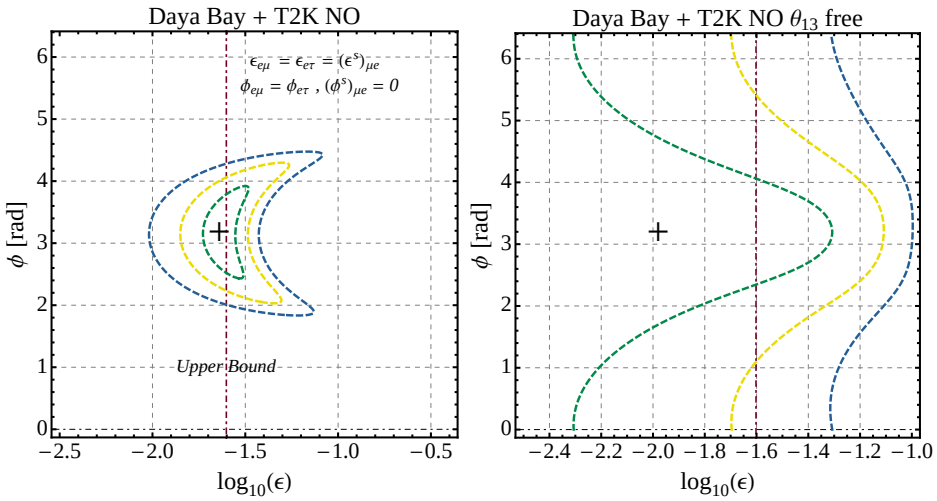

Figure 4.1: Allowed regions in the $\phi - \log_{10}(\epsilon)$ plane, where ϵ and ϕ are respectively the modulus and the phase of the NSI parameter, at 1σ, 2σ and 3σ confidence level (C.L.) for 1 dof fitting the data of the Daya Bay and the T2K experiments in the case of NSI with NO. The best fit points correspond to the crossed points. The vertical lines are at $\log_{10}\epsilon = \log_{10} 0.025$.

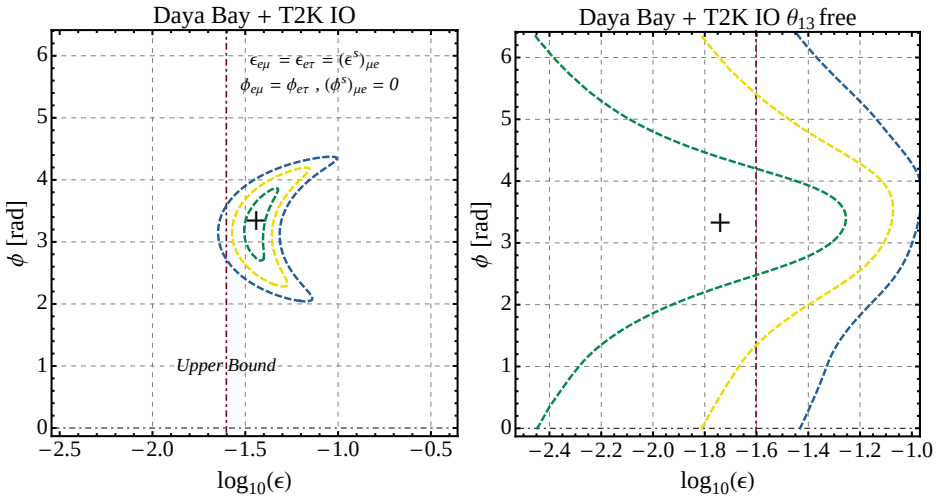

Figure 4.2: Same as Fig. 4.1 but for IO.

Eq. (4.3.1) we impose: $\epsilon_{e\mu} = 2\,\epsilon_{e\tau} = \epsilon^s_{\mu e}$, $\phi_{e\mu} = \phi_{e\tau}$ and $\phi^s_{\mu e} = 0$ ($\epsilon_{e\mu} = \epsilon_{e\tau} = \epsilon^s_{\mu e}$, $\phi_{e\mu} = \phi_{e\tau}$ and $\phi^s_{\mu e} = \pi/2$).
To demonstrate that for the obtained values of the NSI parameters one can describe both the Daya Bay and T2K results, including the spectra, in the Left Panel of Fig. 4.3 we show the oscillation probability $P(\overline{\nu}_e \to \overline{\nu}_e)$ as a function of $L_{\rm eff}/E_\nu$ [138] for the NSI model (solid red line) for NO spectrum and in the absence of NSI ("standard result"

(SR)) (dotted black line); the mixing parameters are fixed as follows: $\sin^2\theta_{12} = 0.306$, $\Delta m^2_{21} = 7.6\times10^{-5}$ eV^2, $\sin^2\theta_{23} = 0.5$, $|\Delta m^2_{32}| = 2.4\times10^{-3}$ eV^2, $\delta = 0$ and $\sin^2 2\theta_{13} = 0.140$, $\epsilon_{e\mu} = \epsilon_{e\tau} = \epsilon^s_{\mu e} = 10^{-1.64}$, $\phi_{e\mu} = \phi_{e\tau} = 3.18$ and $\phi^s_{\mu e} = 0$. The triangular, square and circular data points refer to the EH1, EH2 (near detectors) and EH3 (far detector) Daya Bay locations and have been taken from [138]. The Right Panel of Fig. 4.3 has been obtained using the same values for the standard oscillation and NSI parameters and shows the number of candidate events in the appearance channel of the T2K experiment. The SR result with $\sin^2 2\theta_{13} = 0.090$ is shown with the dot-dashed line in the left panel and the T2K best fit curve is represented with the blue line in the right panel. As it is clear from these figures, the Daya Bay and the T2K spectral data are well reproduced.

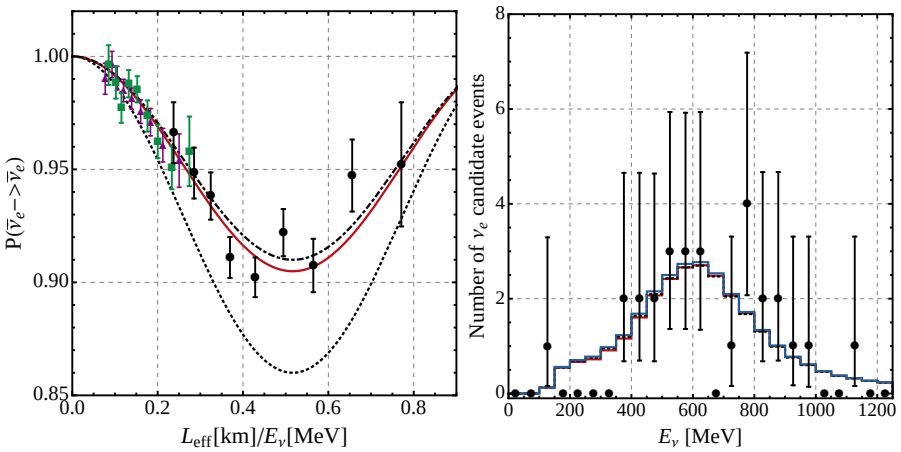

Figure 4.3: Left Panel. Oscillation probability $P(\overline{\nu}_e \to \overline{\nu}_e)$ as a function of $L_{\rm eff}/E_\nu$ for the NSI model (solid red line) and the SR with $\sin^2 2\theta_{13} = 0.140$ (dashed black line) and with $\sin^2 2\theta_{13} = 0.090$ (dot-dashed black line). The triangular, square and circular data points refer to the EH1, EH2 and EH3 locations and have been taken from [138]. Right Panel. Number of ν_e candidate events as a function of the neutrino energy for the NSI model (solid red line), the SR (dashed black line) and the T2K best fit curve (solid blue line), the three curves being almost superimposed. The T2K data and the errors have been taken from [137]. See the text for further details.

4.3.2 The case of $\sin^2 2\theta_{13} = 0.09$

In the case of small θ_{13} we reduced the parameter space assuming:

$$\epsilon = \epsilon_{e\mu} = \epsilon^s_{\mu e}, \quad \epsilon_{e\tau} \neq 0, \quad \phi_{e\mu} = \phi^s_{\mu e} = \pi, \quad \phi_{e\tau} = 0. \tag{4.3.2}$$

In the case of small θ_{13} the choice in Eq. (13) is dictated by the need of minimizing the NSI effects in the $\bar{\nu}_e \to \bar{\nu}_e$ survival probability, so that the results of the Daya Bay fit remain unaffected. In the Left Panel of Fig. 4.4 we show the best fit points and the 1, 2

and 3σ confidence level regions for 1 dof after performing a combined fit to the Daya Bay and to the T2K data for NO fixing $\sin^2\theta_{12} = 0.306$, $\Delta m^2_{21} = 7.6 \times 10^{-5}$ eV^2, $\sin^2\theta_{23} = 0.5$, $|\Delta m^2_{32}| = 2.4 \times 10^{-3}$ eV^2, $\delta = 0$ and $\sin^2 2\theta_{13} = 0.09$. In the Right Panel of Fig. 4.4 we allowed θ_{13} to vary freely.
We do not show the results for the IO spectrum, because, under the assumptions made for the parameter space, Eq. 4.3.2, they are the same as in the NO case.
In contrast to the large θ_{13} case, in order to reconcile the Daya Bay and the T2K spectral data requires that the phase $\phi_{e\mu}$ and $\phi_{e\tau}$ are related through $\phi_{e\mu} \simeq \phi_{e\tau} - \pi$. This ensures that sizeable NSI effects do not spoil the Daya Bay measurement of the reactor angle when $\epsilon_{e\mu} \sim \epsilon_{e\tau}$: in fact, $P(\overline{\nu}_e \to \overline{\nu}_e)$ is reduced essentially to the standard expression and no significant effect has to be expected from the NSI parameters at leading order. On the other hand, it is clear that relatively large values of ε are needed to fit the T2K data.

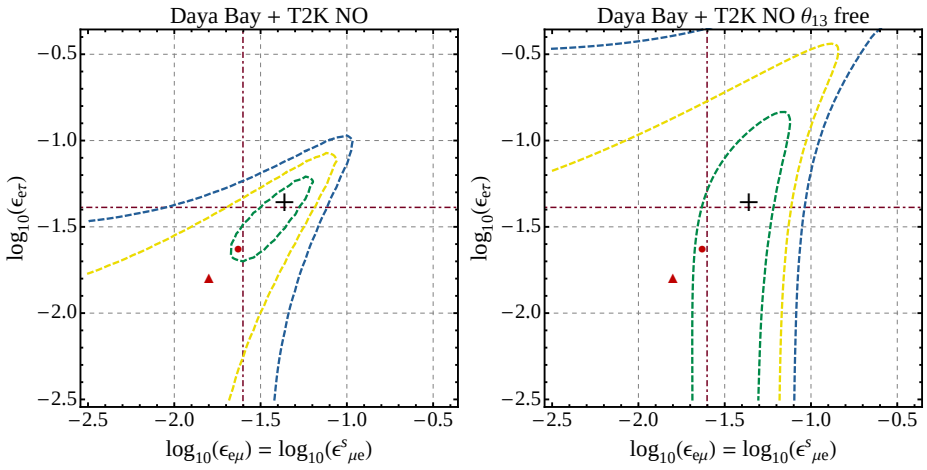

Figure 4.4: Allowed regions in the $\log_{10}\epsilon_{e\tau} - \log_{10}\epsilon$ plane, where ϵ and ϕ are respectively the modulus and the phase of the NSI parameter, at 1σ, 2σ and 3σ confidence level (C.L.) for 1 dof fitting the data of the Daya Bay and the T2K experiments in the case of NSI with NO. The best fit points correspond to the crossed points; the vertical lines are at $\log_{10}\epsilon = \log_{10} 0.025$, the horizontal lines at $\log_{10}\epsilon_{e\tau} = \log_{10} 0.041$. The circular and triangular points are at $(\log_{10}\epsilon\,,\,\log_{10}\epsilon_{e\tau}) = (-1.63\,,\,-1.63)\,,\,(-1.80\,,\,-1.80)$, respectively.

We give in Table 4.2 the best fit points we obtained in our analysis for Fig. 4.4. Notice that they are close to the current upper limits, reported with dot-dashed lines.

best fit	**left panel**	**right panel**
$(\log_{10}\epsilon\,,\,\log_{10}\epsilon_{e\tau})$	$(-1.36\,,\,-1.36)$	$(-1.36\,,\,-1.36)$

Table 4.2: Best fit points for the $(\log_{10}\epsilon\,,\,\log_{10}\epsilon_{e\tau})$ parameters obtained in our analysis.

Finally, in Fig. 4.5 we show the number of candidate events in the appearance channel of

the T2K experiment (with mixing parameters fixed at the values discussed below Eq. 4.3.2). Since the best fit points are outside the current 90% C.L. bounds on the NSI parameters, we show the spectra for two points within the NSI bounds: one point is located in the 1σ region, while the second is located in the 2σ region (see Fig. 4.4). In the Left Panel of Fig. 4.5 we fixed $(\log_{10}\epsilon\,,\,\log_{10}\epsilon_{e\tau}) = (-1.63\,,\,-1.63)$, in the Right Panel $(\log_{10}\epsilon\,,\,\log_{10}\epsilon_{e\tau}) = (-1.80\,,\,-1.80)$. The T2K best fit curve is represented with the blue line. As it is clear from these figures, the T2K spectral data are well reproduced.

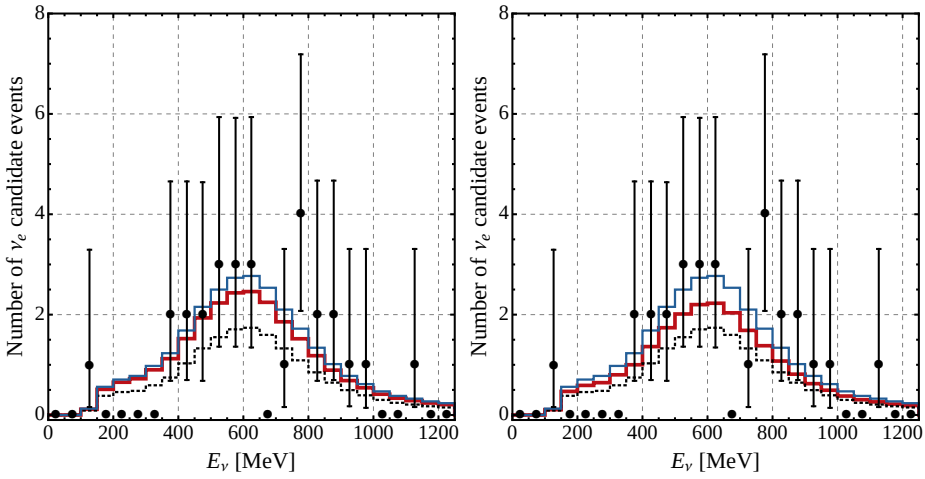

Figure 4.5: Left Panel. Number of ν_e candidate events as a function of the energy for the NSI model (solid red line) with $(\log_{10}\epsilon\,,\,\log_{10}\epsilon_{e\tau}) = (-1.63\,,\,-1.63)$, the SR (dashed black line) and the T2K best fit curve (solid thin blue line). The T2K data and the errors have been taken from [137]. Right Panel. As in the Left Panel but using $(\log_{10}\epsilon\,,\,\log_{10}\epsilon_{e\tau}) = (-1.80\,,\,-1.80)$. See the text for further details.

4.4 Summary and Conclusions

In the present chapter we have analyzed the most recent data of the Daya Bay [138] and the T2K [137] experiments with the aim to study the possibility that NSI effects can reconcile the different values of the reactor angle reported by the two experiments. We recall that the best fit values of $\sin^2 2\theta_{13}$ found in the experiments, $\sin^2 2\theta_{13} = 0.090$ [138] and $\sin^2 2\theta_{13} = 0.140$ (0.170) [137], differ by a factor 1.6 (1.9) in the case of NO (IO) neutrino mass spectrum. The T2K result was obtained under the assumptions: i) the Dirac CP violation phase $\delta = 0$, ii) the atmospheric neutrino mixing angle $\theta_{23} = \pi/4$, iii) $\sin^2\theta_{12} = 0.306$, iv) $\Delta m^2_{21} = 7.6 \times 10^{-5}$ eV^2 and v) $|\Delta m^2_{32}| = 2.4 \times 10^{-3}$ eV^2. Given the uncertainty in the T2K result, the difference between the values of $\sin^2 2\theta_{13}$ obtained in the T2K and Daya Bay experiments does not seem to be irreconcilable and the most natural explanation can be attributed to setting $\delta = 0$ and $\theta_{23} = \pi/4$. Here we have entertained

a different possibility, namely, that the difference between the values of $\sin^2 2\theta_{13}$ found in the T2K experiment for $\delta = 0$ and in the Daya Bay experiment are due to the presence of new physics in the neutrino sector in the form of non-standard neutrino interactions (NSI). There are altogether six NSI parameters which can affect the $\bar{\nu}_e \to \bar{\nu}_e$ and $\nu_\mu \to \nu_e$ oscillation probabilities, relevant for the interpretation of the Daya Bay and T2K data on $\sin^2 2\theta_{13}$: three complex, in general, NSI effective couplings, whose absolute values and phases are $\epsilon_{e\mu}$, $\epsilon_{e\tau}$, $\epsilon^s_{\mu e}$ and $\phi_{e\mu}$, $\phi_{e\tau}$, $\phi^s_{\mu e}$. We have considered two extreme cases: one where the true value of θ_{13} is $\sin^2 2\theta_{13} = 0.140$ for NO ($\sin^2 2\theta_{13} = 0.170$ for IO), and the other where the true value is $\sin^2 2\theta_{13} = 0.090$. With the aim of finding a minimal model with few new degrees of freedom for each of the two cases, we have simplified the NSI parameter spaces, assuming $\epsilon = \epsilon_{e\mu} = \epsilon_{e\tau} = \epsilon^s_{\mu e}, \phi = \phi_{e\mu} = \phi_{e\tau}, \phi^s_{\mu e} = 0$ for the large θ_{13} case and $\epsilon = \epsilon_{e\mu} = \epsilon^s_{\mu e}, \epsilon_{e\tau} \neq 0, \phi_{e\mu} = \phi^s_{\mu e} = \pi, \phi_{e\tau} = 0$ for the small θ_{13} one. All other mixing parameters are fixed to $\sin^2\theta_{12} = 0.306$, $\Delta m^2_{21} = 7.6 \times 10^{-5}$ eV^2, $\sin^2\theta_{23} = 0.5$, $|\Delta m^2_{32}| = 2.4 \times 10^{-3}$ eV^2, $\delta = 0$. We have found that, contrary to the interpretation that $\delta = 0$ is disfavoured in the standard case, following from the global analysis of the neutrino oscillation data [7, 8], it is possible to find a good agreement with both the hypothesis of large, $\sin^2 2\theta_{13} = 0.14$ (0.17), and small, $\sin^2 2\theta_{13} = 0.09$, for $\delta = 0$, in well defined regions of the NSI parameter space. In a more general situation in which the NSI can affect the neutrino flux in the near detector and without the restrictions we considered on the parameter space, it will be possible to reconcile the Daya Bay and T2K data in a bigger region of the NSI parameter space within the current upper bounds.

Given the relatively low statistics of the T2K $\nu_\mu \to \nu_e$ oscillation data, our results on the possible NSI effects should be considered as very preliminary. Future experiments searching the CP violation and/or NSI effects in neutrino oscillations will certainly provide a critical test of the possible NSI effects we have discussed.

CHAPTER 5

Neutrinoless Double Beta Decay

5.1 Introduction

As we have discussed in the Introduction, at present there are a number of experimental evidences for existence of sterile neutrinos with masses at the eV scale. We have also noted that the relevant data is usually interpreted in terms of the "3+1" and "3+2" schemes, which contain one — ν_4 — or two — $\nu_{4,5}$ — massive neutrinos beyond the three light neutrinos. The neutrinos ν_4, or $\nu_{4,5}$, are assumed to have masses $m_4 \sim 1$ eV, or $m_{4,5} \sim 1$ eV. In the minimal versions of the "$3+1$" and "$3+2$" schemes the massive neutrinos ν_j, $j = 1, 2, 3, 4$, and 5 are Majorana particles. In this the neutrinoless double beta decay is allowed: it is triggered by the exchange of virtual Majorana neutrinos ν_j. In the Introduction we have briefly discussed the predictions for the $(\beta\beta)_{0\nu}$-decay effective Majorana mass in the reference 3-neutrino mixing scheme with the light Majorana neutrinos $\nu_{1,2,3}$. In the present chapter we investigate the predictions for $|\langle m \rangle|$ in the $3+1$ and $3+2$ schemes, which have been discussed in the Introduction. More specifically, we analyze in detail the possibility of a complete or partial cancellation between the different terms in $|\langle m \rangle|$, leading to a strong suppression of $|\langle m \rangle|$ [149]. Whenever possible (e.g., in the cases of the $3+1$ scheme and for the CP conserving values of the CP violation (CPV) phases in the $3+2$ scheme), we determine analytically the region of the relevant parameter spaces where such a suppression can occur. In both the $3+1$ and $3+2$ schemes we perform also a numerical analysis to derive the values of the CPV phases for which a complete cancellation can take place. This allows us to derive the conditions under which the effective Majorana mass satisfies $|\langle m \rangle| > 0.01$ eV, which is the range planned to be exploited by the next generation of $(\beta\beta)_{0\nu}$-experiments. Our study is a natural continuation of the earlier studies [55, 56] and [57–59] on the subject.

5.2 One Sterile Neutrino: the 3+1 Model

In this Section we study the case of existence of one extra sterile neutrino. We will use the parametrisation of the PMNS matrix adopted in [53]:

$$U = O_{24}O_{23}O_{14}V_{13}V_{12}\ diag(1, e^{i\alpha/2}, e^{i\beta/2}, e^{i\gamma/2}), \tag{5.2.1}$$

where O_{ij} and V_{kl} describe real and complex rotations in $i-j$ and $k-l$ planes, respectively, and α, β and γ are three CP violation (CPV) Majorana phases [2]. Each of the matrices V_{12} and V_{13} contains one CPV phase, δ_{12} and δ_{13}, respectively, in their only two nonzero nondiagonal elements. The phases δ_{12} and δ_{13} enter into the expression for $|\langle m\rangle|$ in the combinations $\alpha/2 - \delta_{12}$ and $\beta/2 - \delta_{13}$. Therefore for the purposes of the present study we can set $\delta_{12} = 0$ and $\delta_{13} = 0$ without loss of generality. With this set-up for the CPV phases, the elements of the first row of the PMNS matrix, which are relevant for our further discussion, are given by

$$\begin{aligned} U_{e1} &= c_{12}c_{13}c_{14}, \\ U_{e2} &= e^{i\alpha/2}c_{13}c_{14}s_{12}, \\ U_{e3} &= e^{i\beta/2}c_{14}s_{13}, \\ U_{e4} &= e^{i\gamma/2}s_{14}\,, \end{aligned} \tag{5.2.2}$$

where we have used the standard notation $c_{ij} \equiv \cos\theta_{ij}$ and $s_{ij} \equiv \sin\theta_{ij}$. The element U_{e4}, and thus the angle θ_{14}, describes the coupling of 4th neutrino ν_4 to the electron in the weak charged lepton current.

The masses of all neutrinos of interest for the present study satisfy $m_j \ll 1$ MeV, $j = 1, 2, 3, 4$. Therefore, the expression for the effective Majorana mass in the $3+1$ model has the form (see, e.g., [17–19]):

$$|\langle m\rangle| = \left|m_1|U_{e1}|^2 + m_2|U_{e2}|^2 e^{i\alpha} + m_3|U_{e3}|^2 e^{i\beta} + m_4|U_{e4}|^2 e^{i\gamma}\right|. \tag{5.2.3}$$

In this study we will use two reference sets of values of the two sterile neutrino oscillation parameters $\sin^2\theta_{14}$ and Δm^2_{41}, which enter into the expression for $|\langle m\rangle|$ and which are obtained in the analyses performed in [53, 54]. Some of the results obtained in [53] using different data sets are given in Table 5.1. We will use the best fit values[1]

$$\sin^2\theta_{14} = 0.0225\,, \quad \Delta m^2_{41} = 0.93\ \text{eV}^2 \quad \text{(A)}\,, \tag{5.2.4}$$

found in [53] in the global analysis of all the data (positive evidences and negative results) relevant for the tests of the sterile neutrino hypothesis, and

$$\sin^2\theta_{14} = 0.023\,, \quad \Delta m^2_{41} = 1.78\ \text{eV}^2 \quad \text{(B)}\,, \tag{5.2.5}$$

[1] We will use throughout all the text the notation Δm^2_{41} in the case of NO spectrum and Δm^2_{43} for the IO spectrum.

obtained in [53] from the fit of all the ν_e and $\bar{\nu}_e$ disappearance data (reactor neutrino and Gallium anomalies, etc.) and quoted in Table 5.1. Global analysis of the sterile neutrino related data was performed recently, as we have already noticed, also in [54] (for earlier analyses see, e.g., [150]). The authors of [54] did not include in the data set used the MiniBooNE results at $E_\nu \leq 0.475$ GeV, which show an excess of events over the estimated background [36, 151]. The nature of this excess is not well understood at present. For the best values of $\sin^2\theta_{14}$ and Δm^2_{41} the authors [54] find: $\sin^2\theta_{14} = 0.028$ and $\Delta m^2_{41} = 1.60$ eV^2, which are close to the best fit values found in [53] in the analysis of the ν_e and $\bar{\nu}_e$ disappearance data (see Table 5.1). Actually, in what concerns the problem we are going to investigate, these two sets of values of $\sin^2\theta_{14}$ and Δm^2_{41} lead practically to the same results.

	$\sin^2 2\theta_{14}$	Δm^2_{41} eV
SBL rates only	0.13	0.44
SBL incl. Bugey3 spectr.	0.10	1.75
SBL + Gallium	0.11	1.80
SBL + LBL	0.09	1.78
global ν_e disapp.	0.09	1.78
	$\sin\theta_{14}$	Δm^2_{41} eV
global data	0.15	0.93

Table 5.1: The best fit values of the oscillation parameters $\sin^2 2\theta_{14}$ and Δm^2_{41} obtained in the 3+1 scheme in [53] using different data sets. The values in the last row are obtained from the global fit of all available data and are reported in Table 8 in [53].

The authors of ref. [54] give also the allowed intervals of values of Δm^2_{41} and $\sin^2\theta_{14}$ at 95% C.L., which are correlated. The two values of Δm^2_{41} correspond approximately to the two extreme points of the Δm^2_{41} interval. For $\Delta m^2_{41} = 0.9$ eV^2, the 2σ interval of allowed values of $\sin^2\theta_{14}$ reads: $0.022 \leq \sin^2\theta_{14} \leq 0.028$. This interval is very narrow. Varying $\sin^2\theta_{14}$ in it in our analysis leads practically to the same results as those obtained for $\sin^2\theta_{14} = 0.0225$ and we will present results only for $\sin^2\theta_{14} = 0.0225$. In the case of $\Delta m^2_{41} = 1.78$ eV^2, the corresponding 2σ interval of $\sin^2\theta_{14}$ is:

$$\Delta m^2_{41} = 1.78 \text{ eV}^2 : \quad 0.017 \leq \sin^2\theta_{14} \leq 0.047\,, \quad 95\% \text{ C.L.}\,. \tag{5.2.6}$$

In this case the value we are using $\sin^2\theta_{14} = 0.023$ is approximately by a factor 1.35 bigger (a factor of 2.04 smaller) then the 2σ minimal (maximal) allowed value of $\sin^2\theta_{14}$. In what follows we will present results for the best fit values $\Delta m^2_{41} = 1.78$ eV^2 and $\sin^2\theta_{14} = 0.023$ and will comment how the results change if one varies $\sin^2\theta_{14}$ in the 2σ interval (5.2.6).

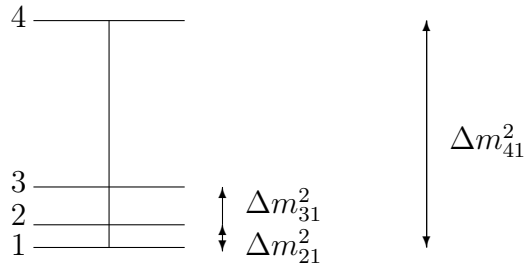

Figure 5.1: The Mass spectrum in the $3+1$ NO (NH) model.

5.2.1 The case of 3+1 Scheme with NO Neutrino Mass Spectrum

In the case of the $3+1$ scheme with NO neutrino mass spectrum, $m_1 < m_2 < m_3 < m_4$, we have:

$$|\langle m \rangle| = |m_1 c^2_{12} c^2_{13} c^2_{14} + m_2 e^{i\alpha} c^2_{13} c^2_{14} s^2_{12} + m_3 e^{i\beta} c^2_{14} s^2_{13} + m_4 e^{i\gamma} s^2_{14}| \,, \tag{5.2.7}$$

where we have used eq. (5.2.2). The masses $m_{2,3,4}$ can be expressed in terms of the lightest neutrino mass m_1 and the three neutrino mass squared differences $\Delta m^2_{21} > 0$, $\Delta m^2_{31} > 0$ and $\Delta m^2_{41} > 0$:

$$m_1 \equiv m_{min}, \quad m_2 = \sqrt{m^2_{min} + \Delta m^2_{21}}, \qquad m_3 = \sqrt{m^2_{min} + \Delta m^2_{31}} \quad \text{and} \quad m_4 = \sqrt{m^2_{min} + \Delta m^2_{41}} \,. \tag{5.2.8}$$

The mass spectrum of the $3+1$ NO (NH) model is shown schematically in Fig. 5.1.

In Fig. 5.2 we show $|\langle m \rangle|$ as a function of the lightest neutrino mass $m_{min} = m_1$. As we have already indicated and was noticed in [57] (see also [55,56]), for the two sets of values of ν_4 oscillation parameters (5.2.4) and (5.2.5) and NH 3-neutrino spectrum (i.e., $m_1 \ll m_{2,3,4}$) we have, depending on the values of the Majorana phases, $|\langle m \rangle| \cong (0.018 - 0.025)$ eV and $|\langle m \rangle| \cong (0.027 - 0.034)$ eV, respectively. This is in contrast with the prediction for $|\langle m \rangle^{(3\nu)}| \lesssim 0.005$ eV. Another important feature of the dependence of $|\langle m \rangle|$ on m_{min}, which is prominent in Fig. 5.2, is the possibility of a strong suppression of $|\langle m \rangle|$ [57–59]. Such a suppression can take place also for $|\langle m \rangle^{(3\nu)}|$ and the conditions under which it occurs have been studied in detail in [152]. In what follows we perform a similar study for $|\langle m \rangle|$. The aim is to determine the range of values of m_{min} and the Majorana phases α, β and γ for which $|\langle m \rangle| \geq 0.01$ eV.

It proves convenient for the purposes of our analysis to work with the quantity $|\langle m \rangle|^2$ rather than with $|\langle m \rangle|$, and to write $|\langle m \rangle|^2$ as

$$|\langle m \rangle|^2 = |a + e^{i\alpha} b + e^{i\beta} c + e^{i\gamma} d|^2 \,. \tag{5.2.9}$$

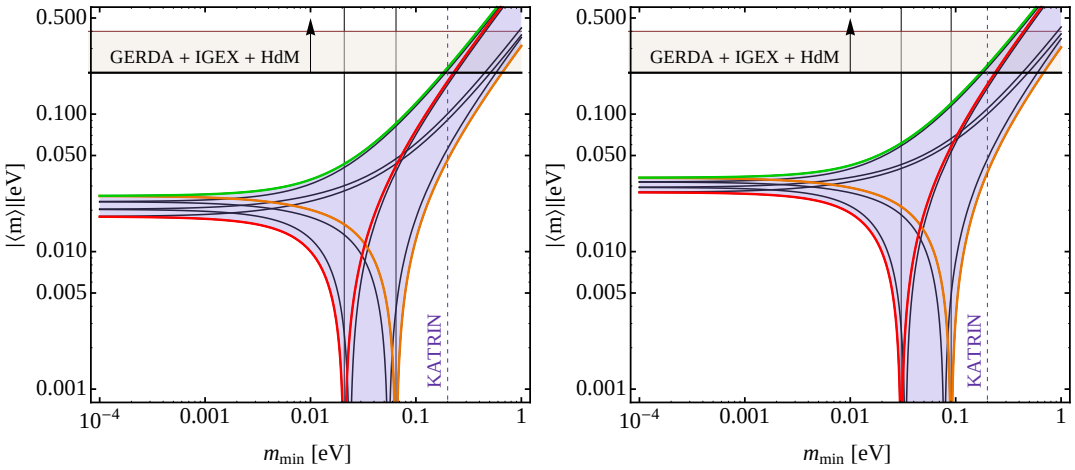

Figure 5.2: Left Panel. The value of $|\langle m\rangle|$as a function of $m_{min} \equiv m_1$ in the NO case for $\Delta m^2_{41} = 0.93\,\mathrm{eV}^2$, $\sin\theta_{14} = 0.15$ and the best fit values of the oscillation parameters given in Table 1.1. The green, red and orange lines correspond respectively to values of the three CPV Majorana phases $(\alpha, \beta, \gamma) = (0, 0, 0), (0, 0, \pi), (\pi, \pi, \pi)$. The five gray curves show $|\langle m\rangle|$computed for the other five sets of CP conserving values of the phases. The interval between the vertical left and right solid lines, corresponding to $m_1 = \underline{m}_1 \simeq 0.021\,\mathrm{eV}$ and $m_1 = \overline{m}_1 \simeq 0.065\,\mathrm{eV}$, indicates the region where $|\langle m\rangle|_{min} = 0$ for specific choices of (α, β, γ). Right Panel. The same as in the left panel but for $\Delta m^2_{41} \equiv 1.78\,\mathrm{eV}^2$. The vertical solid lines correspond to $m_1 = \underline{m}_1 \simeq 0.030\,\mathrm{eV}$ and $m_1 = \overline{m}_1 \simeq 0.091\,\mathrm{eV}$. The horizontal band indicates the upper bound $|\langle m\rangle| \sim 0.2 - 0.4$ eV obtained using the 90 % C.L. limit on the half-life of ^{76}Ge reported in [118]. See text for further details.

In the NO case under study the parameters a, b, c, and d read:

$$\begin{aligned} a &= m_{min} c^2_{12} c^2_{13} c^2_{14} \\ b &= \sqrt{m^2_{min} + \Delta m^2_{21}}\, c^2_{13} c^2_{14} s^2_{12} \\ c &= \sqrt{m^2_{min} + \Delta m^2_{31}}\, c^2_{14} s^2_{13} \\ d &= \sqrt{m^2_{min} + \Delta m^2_{41}}\, s^2_{14}\,. \end{aligned} \tag{5.2.10}$$

The first derivative of $|\langle m\rangle|^2$ with respect of α, β and γ leads to the following system of three coupled equations:

$$\begin{aligned} -2b[a\sin(\alpha) + c\sin(\alpha - \beta) + d\sin(\alpha - \gamma)] &= 0, \\ -2c[a\sin(\beta) - b\sin(\alpha - \beta) + d\sin(\beta - \gamma)] &= 0, \\ 2d[-a\sin(\gamma) + b\sin(\alpha - \gamma) + c\sin(\beta - \gamma)] &= 0. \end{aligned} \tag{5.2.11}$$

It is possible to solve this system of equations using the set of variables $v = \tan(\alpha/2)$, $t = \tan(\beta/2)$, $u = \tan(\gamma/2)$ with $\alpha,\ \beta,\ \gamma \neq \pi + 2k\pi$. We will give here only the basic

formulas and will describe the results of such minimization using the best fit values given in Table 1.1 and eqs. (5.2.4) and (5.2.5). In Appendix D.1 we describe in detail the minimization procedure of the general expression of $|\langle m\rangle|$ in the 3+1 scheme and the 16 solutions found. We give explicit expressions for the solutions and derive the domain of each of the 16 solutions. Eight of these solutions correspond to all possible combinations of the phases having values 0 or π. Obviously, the solution $(\alpha, \beta, \gamma) = (0, 0, 0)$ corresponds to an absolute maximum of the effective Majorana mass $|\langle m\rangle|$. As we show in Appendix D.1, the domains of the solutions of interest are determined by the properties of the functions f_i, $i = 1, ..., 8$:

$$\begin{aligned} f_1 &= a - b - c - d\,, & f_2 &= a + b - c - d\,, \\ f_3 &= a + b - c + d\,, & f_4 &= -a + b + c - d\,, \\ f_5 &= a + b + c + d\,, & f_6 &= a - b + c + d\,, \\ f_7 &= a - b + c - d\,, & f_8 &= a + b + c - d\,, \end{aligned} \tag{5.2.12}$$

where a, b, c and d for the NO case are defined in eq. (5.2.10).

We will focus first on the solutions which minimize $|\langle m\rangle|$ such that the minimum value is exactly zero. As is shown in Appendix D.2, there are six physical solutions for which $|\langle m\rangle|_{min} = 0$: $(u_\pm, v_\pm, t_\pm)$, $(u_3^\pm, v_3^\pm, t_3^\pm)$, $(v_4^\pm(u), t_4^\pm(u))$. In order to study the domain of existence of these solutions we define the following points $\underline{m}_1 < \hat{m}_1 < \tilde{m}_1 < \overline{m}_1$ as the zeros of the functions f_8, f_2, f_7, f_1, respectively:

$$f_8(\underline{m}_1) = 0, \quad f_2(\hat{m}_1) = 0, \quad f_7(\tilde{m}_1) = 0, \quad f_1(\overline{m}_1) = 0. \tag{5.2.13}$$

We find from the numerical analysis performed in Appendix D.2 that i) the solution $(u_\pm, v_\pm, t_\pm)$ is valid between the zeros of the function f_2 and f_1 (the region in which $f_1 f_2 f_3 f_4 > 0$), i.e. in the interval $\hat{m}_1 < m_1 < \overline{m}_1$; ii) the solution $(u_3^\pm, v_3^\pm, t_3^\pm)$ is valid between the zeros of the function f_7 and f_1, i.e. in the interval $\tilde{m}_1 < m_1 < \overline{m}_1$; and finally iii) the solution $(v_4^\pm(u), t_4^\pm(u))$ is valid in the interval between the zero of the function f_8 and f_1, i.e. for $\underline{m}_1 < m_1 < \overline{m}_1$. In Appendix D.2 we give the numerical ranges that define the domains of the solutions discussed above. Using the best fit values of the neutrino oscillation parameters given in Table 1.1 and eqs. (5.2.4) and (5.2.5), we get the following numerical values of [2] $\underline{m}_1$, $\hat{m}_1$, $\tilde{m}_1$, $\overline{m}_1$:

- for $\Delta m^2_{41} = 0.93$ eV^2 we have $(\underline{m}_1, \hat{m}_1, \tilde{m}_1, \overline{m}_1) \simeq (0.021, 0.024, 0.055, 0.065)$ eV;
- if $\Delta m^2_{41} = 1.78$ eV^2 we get $(\underline{m}_1, \hat{m}_1, \tilde{m}_1, \overline{m}_1) \simeq (0.030, 0.033, 0.078, 0.091)$ eV.

For $m_1 = \underline{m}_1$ and $m_1 = \overline{m}_1$ the value of $|\langle m\rangle|$ is exactly zero for the CP conserving values of the phases $(\alpha, \beta, \gamma) = (0, 0, \pi)$ and (π, π, π), respectively. In the intervals described above (excluding the extrema), it is possible to have $|\langle m\rangle|_{min} = 0$ for specific values of

[2] Although it will not be specified further, whenever we present numerical results in the text or in graphical form of figures in what follows, we will use the best fit values of the neutrino oscillation parameters reported in Table 1.1 to obtain them.

(α, β, γ), which are not necessarily CP conserving. This can be seen in Fig. 5.3. The numerical minima depicted in Fig. 5.3 are obtained minimizing $|\langle m \rangle|$ by performing a scan for different values of m_1 and the CPV Majorana phases.

The grey horizontal band in Fig. 5.3 corresponds to $|\langle m \rangle|_{min} \leq 10^{-8}$ eV and reflects the precision of the numerical calculation of $|\langle m \rangle|_{min} = 0$. The minima are reached at specific values of the phases (α, β, γ) that can have either CP conserving or CP nonconserving values. For $\Delta m^2_{41} = 0.93\,\mathrm{eV}^2$ and $m_1 = 0.03\,\mathrm{eV}$, for instance, we have $|\langle m \rangle| = 0$ if the three CPV phases have the following CP nonconserving values: $(\alpha, \beta, \gamma) = (1.731, 0.023, -2.711)$. Similarly, if $\Delta m^2_{41} = 1.78\ \mathrm{eV}^2$ and, e.g., $m_1 = 0.04\,\mathrm{eV}$, we find that $|\langle m \rangle| = 0$ for $(\alpha, \beta, \gamma) = (1.511, -0.365, -2.761)$.

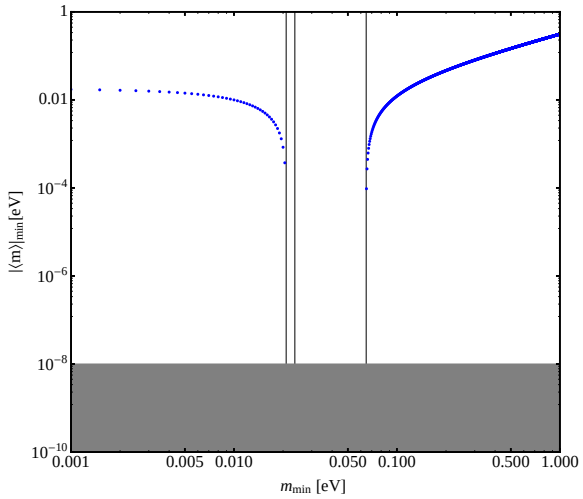

Figure 5.3: Minimum $|\langle m \rangle|$as function of $m_{min} \equiv m_1$ for $\Delta m^2_{41} = 0.93\,\mathrm{eV}^2$ and $\sin\theta_{14} = 0.15$. The plot has been obtained numerically by performing a scan over a sufficiently large sets of values of m_{min} and of each of the CPV phases (α, β, γ) in the interval $[0, \pi]$. The black vertical lines correspond respectively to $m_{min} = \underline{m}_1 \simeq 0.021$ eV, $m_{min} = \hat{m}_1 \simeq 0.024$ eV and $m_{min} = \overline{m}_1 \simeq 0.065$ eV.

Combining the results described above we can conclude that the effective Majorana mass $|\langle m \rangle|$ can be zero only for values of m_{min} from the following interval:

$$\underline{m}_1 \leq m_{min} \leq \overline{m}_1 \ . \tag{5.2.14}$$

We will derive next simple approximate analytical expressions for $\overline{m}_1$ and $\underline{m}_1$. We note first that for values of m_{min} in the range $0.02 - 0.10$ eV, the term proportional to $\sqrt{m^2_{min} + \Delta m^2_{31}} c^2_{14} s^2_{13}$ is approximately by an order of magnitude smaller than the other three terms in $|\langle m \rangle|$ (the terms with the factors a, b, d in eq. (5.2.9)). Neglecting it as well as $\Delta m^2_{21} \ll \Delta m^2_{31}, \Delta m^2_{41}$, we find the following rather simple analytic expressions for $\overline{m}_1$

and $\underline{m}_1$, which are valid up to an error of about 10%:

$$\begin{aligned} \overline{m}_1 &\approx \sqrt{\frac{\Delta m^2_{41} \sin^4\theta_{14}}{\cos^4\theta_{13}\left(-\cos^2\theta_{12}\cos^2\theta_{14}+\sin^2\theta_{12}\right)^2-\sin^4\theta_{14}}}\,, \\ \underline{m}_1 &\approx \sqrt{\frac{\Delta m^2_{41} \sin^4\theta_{14}}{\cos^4\theta_{13}\left(\cos^2\theta_{12}\cos^2\theta_{14}+\sin^2\theta_{12}\right)^2-\sin^4\theta_{14}}}\,. \end{aligned} \tag{5.2.15}$$

Using these expressions we get $(\underline{m}_1, \overline{m}_1) \simeq (0.023, 0.060)$ eV for $\Delta m^2_{41} = 0.93$ eV^2 instead of $(0.021, 0.065)$ eV, and $(\underline{m}_1, \overline{m}_1) \simeq (0.032, 0.085)$ eV for $\Delta m^2_{41} = 1.78$ eV^2 instead of $(0.030, 0.091)$ eV.

In Fig. 5.2 we show two plots of $|\langle m\rangle|$ as function of the lightest neutrino mass $m_{min} \equiv m_1$ using $\Delta m^2_{41} = 0.93$ eV^2 and $\Delta m^2_{41} = 1.78$ eV^2. The shaded area is the region of allowed values of $|\langle m\rangle|$. One can see that the green curve represents the possible maximum value for $|\langle m\rangle|$corresponding to $(\alpha, \beta, \gamma) = (0, 0, 0)$. We notice also that in the limit of $m_{min} \to 0$ the minimum value of $|\langle m\rangle| > 0.01$ eV. This limit will be analyzed in detail below. We also show in Fig. 5.2 the prospective sensitivity to m_{min} of the β-decay experiment KATRIN [29], which is under preparation.

As is well known, in the case of 3-neutrino mixing and IH (IO) neutrino mass spectrum we have $|\langle m \rangle^{(3\nu)}| > 0.01$ eV (see, e.g., [1]). We find that in the 3+1 scheme under discussion and NO neutrino mass spectrum we have always $|\langle m\rangle| > 0.01$ eV for the following ranges of m_{min}:

- $m_{min} < 0.010$ eV and $m_{min} > 0.093$ eV, if $\Delta m^2_{41} = 0.93$ eV^2;
- $m_{min} < 0.020$ eV and $m_{min} > 0.119$ eV, for $\Delta m^2_{41} = 1.78$ eV^2.

What would be the changes of our results presented for $\Delta m^2_{41} = 1.78$ eV^2 presented so far if instead of $\sin^2\theta_{14} = 0.023$ we used the minimal (maximal) value of the 2σ interval (5.2.6) of allowed values $\sin^2\theta_{14} = 0.017$ ($\sin^2\theta_{14} = 0.047$) in the analysis? Qualitatively no new features appear and the results remain the same. Quantitatively some of the numerical values of $| < m > |$, $\overline{m}_1$ and $\underline{m}_1$, quoted in the text and obtained for $\sin^2\theta_{14} = 0.023$, are just shifted. More specifically, this will lead to the decreasing (increasing) of the values of $| < m > |$ at $m_{min} \lesssim 10^{-3}$ eV and of $\overline{m}_1$ and $\underline{m}_1$ approximately by the same factor 1.35 (2.04).

For $0 \leq m_1 < \underline{m}_1$ and $m_1 > \overline{m}_1$, there are no physical solutions for the phases for which $|\langle m\rangle| = 0$. Moreover, $(u_\pm, v_\pm, t_\pm)$, $(u_3^\pm, v_3^\pm, t_3^\pm)$ and $(v_4^\pm(u), t_4^\pm(u))$ are not well defined in the indicated intervals. However, by studying the Hessian of $|\langle m\rangle|^2$, we find that there are physical solutions (among those listed in eq. (D.1.13) of Appendix D.1) for which $|\langle m\rangle|_{min} \neq 0$. These solutions are realised for specific values of the phases, i.e., for $(\alpha, \beta, \gamma) = (0, 0, \pi)$ or (π, π, π). The analysis performed in Appendix D.1 allowed to find the minima of $|\langle m\rangle|$at $m_{min} < \underline{m}_1$ for $(\alpha, \beta, \gamma) = (0, 0, \pi)$, and at $m_{min} > \overline{m}_1$ for $(\alpha, \beta, \gamma) = (\pi, \pi, \pi)$. The domain of the solution at $m_{min} < \underline{m}_1$, corresponding to $(\alpha, \beta, \gamma) = (0, 0, \pi)$, is the common interval of values of m_{min} in which the three inequalities $c < d$, $b < d - c$ and $f_8 = a + b + c - d < 0$

hold. The domain of the solution at $m_{min} > \overline{m}_1$ with $(\alpha, \beta, \gamma) = (\pi, \pi, \pi)$ is determined by the inequality $f_1 = a - b - c - d > 0$. Actually, as it is possible to show, we have, in particular, $f_8 < 0$ at $m_{min} < \underline{m}_1$, and $f_1 > 0$ for $m_{min} > \overline{m}_1$.
The analysis of the Hessian of $|\langle m \rangle|^2$ performed in Appendix D.1 shows that there can be two more solutions for which $|\langle m \rangle|_{min} \neq 0$. They correspond two i) $(\alpha, \beta, \gamma) = (0, \pi, 0)$ and ii) $(\pi, 0, 0)$. The domains of these solutions (following from the Sylvester's criterion) are determined by i) $c > d$, $b < c - d$, $-f_3 = -a - b + c - d > 0$, and ii) $b > c + d$, $-f_6 = -a + b - c - d > 0$. However, it is not difficult to convince oneself that for the values of the neutrino oscillation parameters, including those of Δm^2_{41} and $\sin^2\theta_{14}$ used by us in the present analysis, there are no physical values of $m_{min} \geq 0$ for which the inequalities in i) or in ii) are satisfied.

In Fig. 5.4 we show all the relevant functions entering in the four sets of inequalities listed above (and in eq. (D.1.13) of Appendix D.1) which ensure that the minima $|\langle m \rangle|_{min} \neq 0$. The figure is obtained for the best fit values of the oscillation parameters given in Table 1.1 and for $\Delta m^2_{41} = 0.93\,\text{eV}^2$ (left panel) and $\Delta m^2_{41} = 1.78\,\text{eV}^2$ (right panel). One can easily check that only the two sets of conditions, corresponding to $(\alpha, \beta, \gamma) = (0, 0, \pi)$ or (π, π, π) and given above [3], are satisfied.

In Figs. 5.5 and 5.6 we show as an illustrative examples $(\tan\alpha/2, \tan\beta/2, \tan\gamma/2)$ as function of m_{min} for two of the physical solutions, namely, (u_-, t_-, v_-) and (v_4^+, t_4^+), found in Appendix D.1:

$$\begin{cases} u_\pm &= \pm\sqrt{\dfrac{(-a+b+c-d)(a+b-c+d)}{(a-b-c-d)(a+b-c-d)}}, \\ v_\pm &= \pm\dfrac{(b+c)}{(b-c)}\dfrac{[(a+b-c)^2-d^2]}{\sqrt{(-a+b+c-d)(a+b-c+d)(a-d-c-b)(a-d-c+b)}}, \\ t_\pm &= \pm\dfrac{a^2+b^2-c^2-d^2}{\sqrt{(a-b-c-d)(a+b-c-d)(-a+b+c-d)(a+b-c+d)}}, \end{cases} \tag{5.2.16}$$

$$\begin{cases} v_4^\pm(u) &= \dfrac{4bdu \pm F(a,b,c,d,u)}{-u^2(a-b-c-d)(a-b+c-d)-(a-b+d)^2+c^2}, \\ t_4^\pm(u) &= \dfrac{-4cdu \pm F(a,b,c,d,u)}{u^2(a-b-c-d)(a+b-c-d)+(a-c+d)^2-b^2}, \end{cases} \tag{5.2.17}$$

where a, b, c and d are given in eq. (5.2.10) and

$$F(a,b,c,d,u) = \Big\{\Big[-u^2(a+b-c-d)(a-b+c-d)-(a+d)^2+(b-c)^2\Big]\times \\ \times\Big[a^2\left(u^2+1\right)-2ad\left(u^2-1\right)-\left(u^2+1\right)(b+c-d)(b+c+d)\Big]\Big\}^{1/2}.$$

[3] These are the first two conditions in eq. (D.1.13) of Appendix D.1 following from the Sylvester's criterion for a minimum.

The corresponding figures for, e.g., the solutions (v_+, t_+, u_+) and (v_4^-, t_4^-) are obtained from Figs. 5.5 and 5.6 by reversing the $y-$axis.

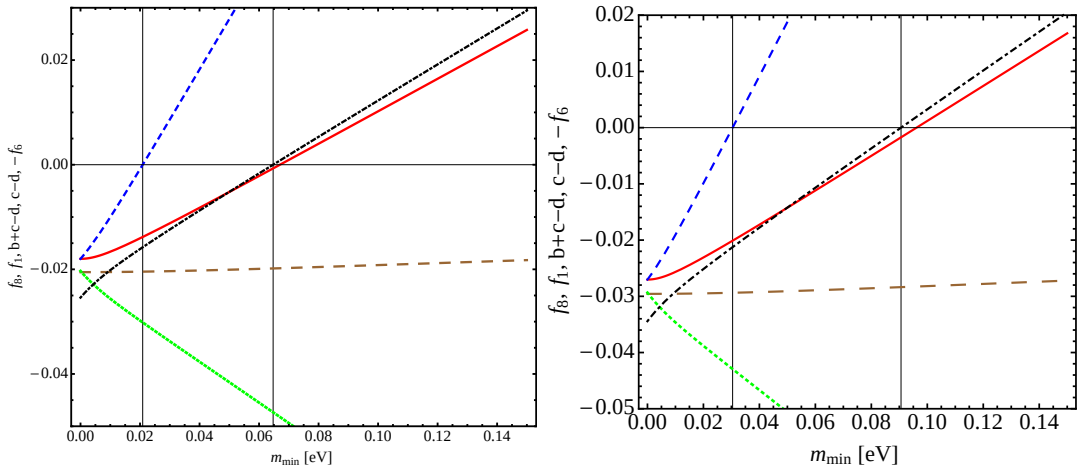

Figure 5.4: Left Panel. The functions f_8 (short-dashed blue), f_1 (dot-dashed black), $b+c-d$ (solid red), $c-d$ (large dashed brown), $-f_6$ (dotted green) versus $m_{min} \equiv m_1$ for $\Delta m^2_{41} = 0.93\,\text{eV}^2$ and $\sin\theta_{14} = 0.15$. The vertical lines correspond to $m_{min} = \underline{m}_1 \simeq 0.021\,\text{eV}$ and $m_{min} = \overline{m}_1 \simeq 0.065\,\text{eV}$. Right Panel. The same as in the left panel, but for $\Delta m^2_{41} = 1.78\ \text{eV}^2$. The vertical lines now are at $m_{min} = \underline{m}_1 \simeq 0.030\,\text{eV}$ and $m_{min} = \overline{m}_1 \simeq 0.091\,\text{eV}$.

5.2.2 The Case of $m_1 = 0$

The investigation of the minima of $|\langle m\rangle|$ in the NH case in the limit of $m_1 = 0$ and arbitrary values of the relevant parameters $b_0, c_0, d_0 = b(m_1 = 0), c(m_1 = 0), d(m_1 = 0)$, can be done following the general analysis presented in Appendix D.1 and, more specifically, using the system eq. (D.1.2) that can be written as

$$\begin{aligned} c_0 \sin(\alpha - \beta + \gamma - \gamma) + d_0 \sin(\alpha - \gamma) = 0 \\ -b_0 \sin(\alpha - \beta + \gamma - \gamma) + d_0 \sin(\beta - \gamma) = 0\,, \end{aligned} \tag{5.2.18}$$

with

$$b_0 = \sqrt{\Delta m^2_{21} c^2_{13} c^2_{14} s^2_{12}}\,, \quad c_0 = \sqrt{\Delta m^2_{31} c^2_{14} s^2_{13}}\,, \quad d_0 = \sqrt{\Delta m^2_{41} s^2_{14}}\,. \tag{5.2.19}$$

We have solved the system eq. (5.2.18) in $(\alpha - \gamma)$ and $(\beta - \gamma)$ and found the solution $\sin(\alpha-\gamma) = 0$, $\sin(\beta-\gamma) = 0$. The solution value of $(\alpha-\gamma, \beta-\gamma) = (0, 0)$ is a maximum, while the second one $(\alpha - \gamma, \beta - \gamma) = (\pi, \pi)$ is a minimum. In other words, solving the system of two equations we find a unique minimum at $(\alpha-\gamma, \beta-\gamma) = (\pi, \pi)$ independently

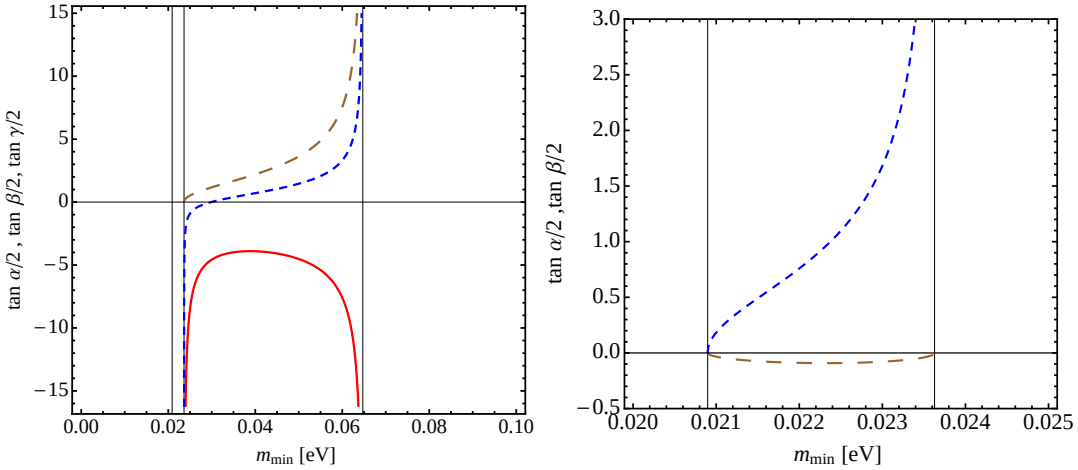

Figure 5.5: Left Panel. The values of $(\tan\alpha/2, \tan\beta/2, \tan\gamma/2)$ – the large dashed (brown), short dashed (blue), solid (red) lines – corresponding to the solution (v_-, t_-, u_-) as functions of m_1 for $\Delta m^2_{41} = 0.93$ eV^2. The 2nd and the 3rd vertical lines from the left are at $\hat{m}_1 = 0.024$ eV and $\overline{m}_1 = 0.065$ eV, and indicate the domain of existence of this solution. The 1st vertical line from the left corresponds to $\underline{m}_1 = 0.021$ eV. Right Panel. The values of $(\tan\alpha/2, \tan\beta/2)$ – large dashed (brown), solid (red) lines – corresponding to the solution (t_4^+, v_4^+) as functions of m_1 for $\gamma \simeq \pi$ $(u >> 1)$. The other parameters are the same as in the left panel. The vertical lines from the left are respectively at $\underline{m}_1$ and $\hat{m}_1$. This solution is well defined only for $\underline{m}_1 \leq m_1 \leq \hat{m}_1$.

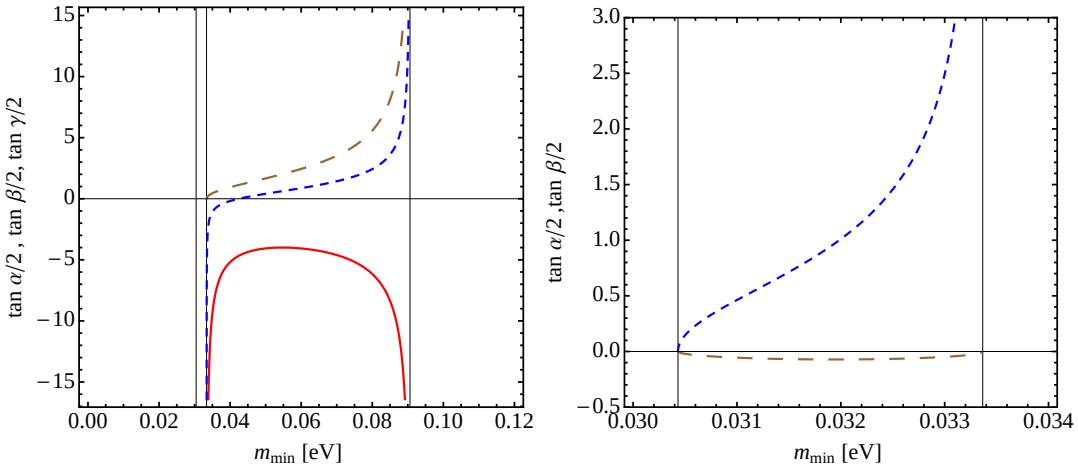

Figure 5.6: Left Panel. The same as in Fig. 5.5, left panel, for $\Delta m^2_{41} = 1.78$ eV^2. The 2nd and the 3rd vertical lines from the left are at $\hat{m}_1 = 0.033$ eV and $\overline{m}_1 = 0.091$ eV and indicate the domain of existence of the solution (u_-, t_-, v_-). The 1st vertical line from the left corresponds to $\underline{m}_1 = 0.030$ eV. Right Panel. The same as in Fig. 5.5, right panel, for $\Delta m^2_{41} = 1.78$ eV^2. The vertical lines from the left are at $\underline{m}_1$ and $\hat{m}_1$. The solution considered (t_4^+, v_4^+) is well defined only in the interval $\underline{m}_1 \leq m_1 \leq \hat{m}_1$.

of the value of [4] Δm^2_{41}. The corresponding minimum value of $|\langle m\rangle|$is 0.018 (0.027) eV in the case of $\Delta m^2_{41} = 0.93$ eV^2 (1.78 eV^2). This result is depicted in Fig. 5.7. The darkest region in the figure corresponds to the minimum of $|\langle m\rangle|$and the red cross indicates the precise value of $(\alpha - \gamma, \beta - \gamma)$ at the minimum.

It follows from the results of our analysis that for $m_1 = 0$ and any values of the CPV phases $(\alpha - \gamma, \beta - \gamma)$ we have:

- $|\langle m\rangle| \geq 0.018\, eV$ if $\Delta m^2_{41} = 0.93$ eV^2;
- $|\langle m\rangle| \geq 0.027\, eV$ for $\Delta m^2_{41} = 1.78$ eV^2. If instead of $\sin^2\theta_{14} = 0.0223$ we use $\sin^2\theta_{14} = 0.017$ (0.047), we get $|\langle m\rangle| \geq 0.019$ (0.059) eV.

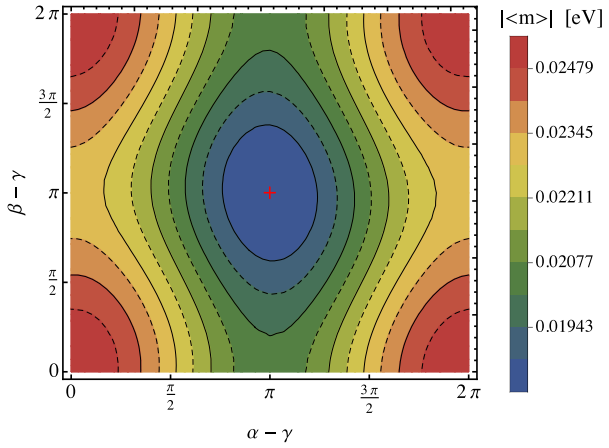

Figure 5.7: The value of $|\langle m\rangle|$for NH spectrum in the 3+1 scheme and $m_{min} = 0$. The minimum corresponds to $(\alpha - \gamma, \beta - \gamma) = (\pi, \pi)$. At the minimum (the point with the cross) $|\langle m\rangle| = 1.80 \times 10^{-2}$ eV. The values in the first four contours are, respectively, $(1.88, 1.94, 2.01, 2.08) \times 10^{-2}$ eV and obtained for $\Delta m^2_{41} = 0.93$ eV^2. See text for further details.

5.3 The case of IO Spectrum in the 3+1 Scheme

In the case of 3+1 scheme with IO 3-neutrino mass spectrum, $m_3 < m_1 < m_2 < m_4$, one can write the effective Majorana mass following the notation in [1] as:

$$|\langle m\rangle| = |m_1 c^2_{12} c^2_{13} c^2_{14} + m_2 e^{i\alpha} c^2_{13} c^2_{14} s^2_{12} + m_3 e^{i\beta} c^2_{14} s^2_{13} + m_4 e^{i\gamma} s^2_{14}|\,. \tag{5.3.1}$$

[4] For the specific values of the neutrino oscillation parameters used in the present analysis, the fact that the minimum of $|\langle m\rangle|$is reached for just one set of values of $(\alpha - \gamma, \beta - \gamma) = (\pi, \pi)$ follows from the explicit expression for $|\langle m\rangle|$, eqs. (5.2.7), in the case of $m_1 = 0$.

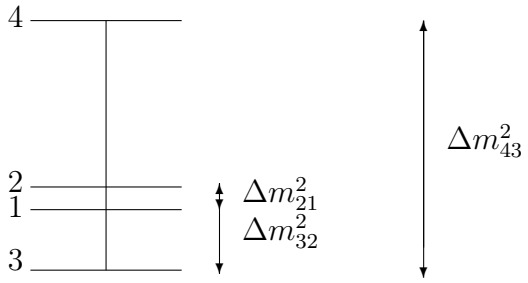

Figure 5.8: The mass spectrum in the 3+1 IO scheme.

The masses $m_{1,2,4}$ can be expressed in terms of the lightest neutrino mass $m_{min} = m_3$ and the neutrino mass squared differences as follows:

$$\begin{aligned} m_1 =& \sqrt{m^2_{min} + |\Delta m^2_{32}| - \Delta m^2_{21}}, \quad m_2 = \sqrt{m^2_{min} + |\Delta m^2_{32}|}, \quad m_4 = \sqrt{m^2_{min} + \Delta m^2_{43}}\,, \\ m_3 =& m_{min}\,, \quad \Delta m^2_{21} > 0\,, \quad \Delta m^2_{32} < 0\,, \quad \Delta m^2_{43} > 0\,. \end{aligned} \tag{5.3.2}$$

The neutrino mass spectrum of this scheme is depicted schematically in Fig. 5.8.

The parameters a, b, c and d are given by:

$$\begin{aligned} a &= \sqrt{m^2_{min} + |\Delta m^2_{32}| - \Delta m^2_{21}}\; c^2_{12} c^2_{13} c^2_{14} \\ b &= \sqrt{m^2_{min} + |\Delta m^2_{32}|}\; c^2_{13} c^2_{14} s^2_{12} \\ c &= m_{min}\; c^2_{14} s^2_{13} \\ d &= \sqrt{m^2_{min} + \Delta m^2_{43}}\; s^2_{14} \end{aligned} \tag{5.3.3}$$

In this case only a few solutions among those found in Appendix D.1 are relevant and their existence depends on the numerical values of the parameters a, b, c and d. In Appendix D.2 we list the domain of existence of all the solutions. Here we will analyze the solutions $(u_\pm, v_\pm, t_\pm)$, given in eq. (5.2.16) with the parameters a, b, c and d defined in eq. (5.3.3), because their domain is the largest (the numerical details are given in Appendix D.2).

We observe that the solutions $(u_\pm, v_\pm, t_\pm)$ are well defined when the product $f_1 f_2 f_3 f_4$ is positive, where $f_{1,2,3,4}$ are given in eq. (5.2.12). Defining $\overline{m}_3$ as the zero of the function f_1, $f_1(\overline{m}_3) = 0$, we find that the effective Majorana mass can be zero for $m_3 < \overline{m}_3$ for specific CP non-conserving values of the CPV phases α, β and γ. For $\Delta m^2_{43} = 0.93$ (1.78) eV^2 and the best fit values of Table 1.1, we find $\overline{m}_3 \simeq 0.038$ (0.074) eV. These results are presented graphically in Fig. 5.9, where we show the numerically calculated $|\langle m \rangle|_{min}$ as function of m_3. The numerical minima depicted in Fig. 5.9 are obtained by performing a scan over the

values of m_3 and of each of the phases (α, β, γ) in the interval $[0, 2\pi]$. The grey horizontal band in Fig. 5.9, corresponding to $|\langle m\rangle|_{min} < 10^{-8}$ eV, reflect the precision of the numerical calculation of $|\langle m\rangle|_{min} = 0$. The minima of $|\langle m\rangle|$under discussion are reached for values of the phases (α, β, γ) that can be either CP conserving or CP non-conserving.

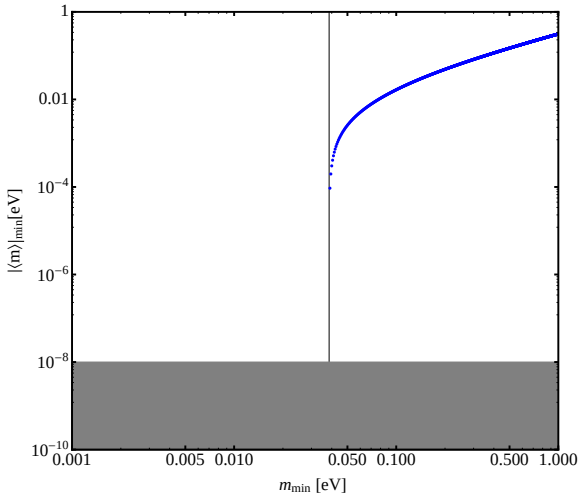

Figure 5.9: Minimum $|\langle m\rangle|$as function of $m_{min} \equiv m_3$. The figure has been obtained numerically for $\Delta m^2_{43} = 0.93\,\text{eV}^2$, $\sin\theta_{14} = 0.15$. The vertical line corresponds to $m_{min} = \overline{m}_3 \simeq 0.038\,\text{eV}$. See text for details.

We will find next an analytical approximation of $\overline{m}_3$. We observe that for values m_3 in the range $m_3 \approx 0.05 - 0.10\,eV$ the term $\propto m_3 \cos^2\theta_{14}\sin^2\theta_{13}$ is by approximately an order of magnitude smaller then the other three terms in $|\langle m\rangle|$. Neglecting it as well the term $\propto \Delta m^2_{21}$, we find the following expression for $\overline{m}_3$, which is valid up to an error of about the 15%:

$$\overline{m}_3 \approx \sqrt{\frac{\Delta m^2_{43}\sin^4\theta_{14} - |\Delta m^2_{32}|\cos^2 2\theta_{12}\cos^4\theta_{13}\cos^4\theta_{14}}{\cos^2 2\theta_{12}\cos^4\theta_{13}\cos^4\theta_{14} - \sin^4\theta_{14}}}\,. \tag{5.3.4}$$

Using this approximation we get $\overline{m}_3 \simeq 0.032\,\text{eV}$ for $\Delta m^2_{43} = 0.93\,\text{eV}^2$, and $\overline{m}_3 \simeq 0.068\,\text{eV}$ for $\Delta m^2_{43} = 1.78\,\text{eV}^2$, instead of 0.038 eV and 0.074 eV found numerically.

To find the minima of $|\langle m\rangle|$for values of $m_3 > \overline{m}_3$ we have to study the Hessian of $|\langle m\rangle|$. From the analysis in Appendix D.1 it follows that in the region in which $f_1 > 0$ (corresponding to the region $m_3 > \overline{m}_3$), the minimum of $|\langle m\rangle|$(according to the Sylvester's criterion) takes place at $(\alpha, \beta, \gamma) = (\pi, \pi, \pi)$. In Fig. 5.10 we show all the relevant functions entering in the conditions determining the minima, which are listed in eq. (5.2.12) (and eq. (D.1.13)), with the parameters a, b, c and d defined in eq. (5.3.3).

In Fig. 5.11 we show as an example the values of the three phases versus m_{min} for the solution (u_-, v_-, t_-). The analogous figure for the solution (u_+, v_+, t_+) is obtained formally from Fig. 5.11 by reversing the $y-$axis.

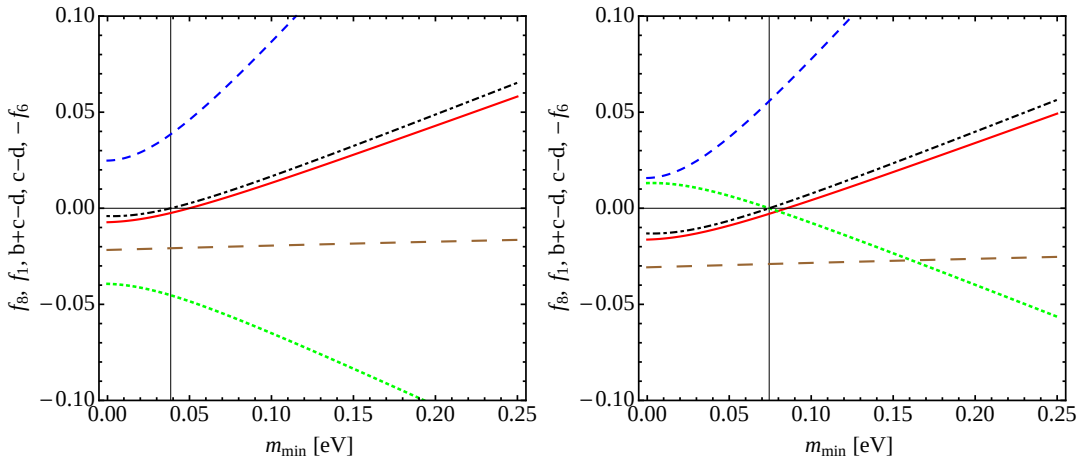

Figure 5.10: Left Panel. The functions f_8 (short-dashed blue), f_1 (dot-dashed black), $b+c-d$ (solid red), $c-d$ (large dashed brown), $-f_6$ (dotted green) versus $m_{min} \equiv m_3$ for $\Delta m^2_{43} = 0.93\,\mathrm{eV}^2$, $\sin\theta_{14} = 0.15$. The vertical line corresponds to $m_{min} = \overline{m}_3 \simeq 0.038\,\mathrm{eV}$. Right Panel. The same as in the left panel, but for $\Delta m^2_{43} = 1.78\,\mathrm{eV}^2$. The vertical line corresponds to $m_{min} = \overline{m}_3 \simeq 0.074\,\mathrm{eV}$.

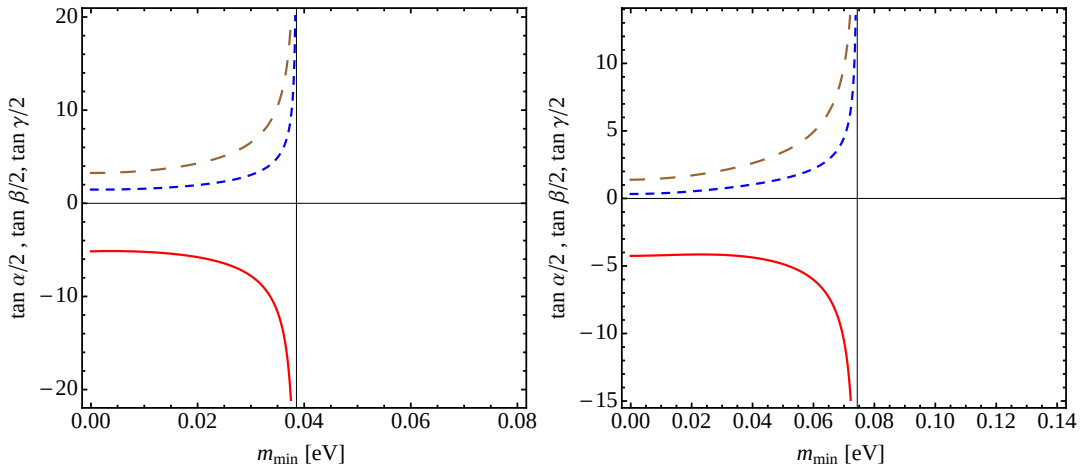

Figure 5.11: Left Panel. The values of $(\tan\alpha/2, \tan\beta/2, \tan\gamma/2)$ – large dashed (brown), short dashed (blue), solid (red) lines – corresponding to the solution (v_-, t_-, u_-), eq. (5.2.16), as functions of m_3 for $\Delta m^2_{43} = 0.93\,\mathrm{eV}^2$, $\sin\theta_{14} = 0.15$. The vertical line is at $\overline{m}_3 = 0.038\,\mathrm{eV}$, indicating the domain of existence of this solution, $m_3 \leq \overline{m}_3$. Right Panel. The same as in the left panel, but for $\Delta m^2_{43} = 1.78\,\mathrm{eV}^2$. The vertical line is at $\overline{m}_3 = 0.074\,\mathrm{eV}$, indicating the domain of existence of the solution (v_-, t_-, u_-), $m_3 \leq \overline{m}_3$.

Finally, we show in Fig. 5.12 $|\langle m\rangle|$as function of the lightest neutrinos mass, m_{min}. In this case the region of allowed values of $|\langle m\rangle|$(the shaded area) is larger than in the NO case since $|\langle m\rangle|$can reach zero for any $m_{min} \leq \overline{m}_3$. This is due to the fact that, depending on the values of the CPV phases α, β and γ, a complete cancellation among the terms in

the expression for $|\langle m\rangle|$can occur.

The results of the analysis performed in this section show that we always have $|\langle m\rangle| > 0.01$ eV for:

- $m_{min} > 0.078$ eV, if $\Delta m^2_{43} = 0.93$ eV^2;
- $m_{min} > 0.108$ eV, if $\Delta m^2_{43} = 1.78$ eV^2.

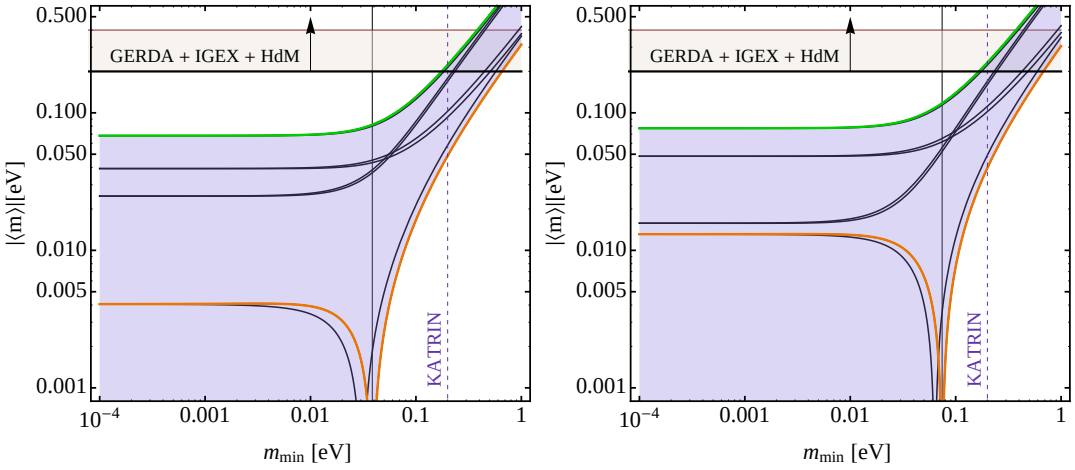

Figure 5.12: Left Panel. The value of $|\langle m\rangle|$as function of $m_{min} = m_3$ for $\Delta m^2_{43} = 0.93\,\text{eV}^2$, $\sin\theta_{14} = 0.15$. The green and orange lines correspond respectively to $(\alpha,\beta,\gamma) = (0,0,0)$ and (π,π,π). The six gray curves correspond to the other possible sets of CP conserving values 0 or π of the CPV phases (α,β,γ). The vertical line is at $m_3 = \overline{m}_3 \simeq 0.038\,\text{eV}$. If $m_3 \leq \overline{m}_3$, we can have $|\langle m\rangle|_{min} = 0$ at any fixed m_3 for specific values of (α,β,γ), while for $m_3 > \overline{m}_3$, the minimum of $|\langle m\rangle|$is realized at $(\alpha,\beta,\gamma) = (\pi,\pi,\pi)$ and $|\langle m\rangle|_{min} \neq 0$. Right Panel. The same as in the left panel, but for $\Delta m^2_{43} \equiv 1.78\,\text{eV}^2$. The vertical line is at $m_3 = \overline{m}_3 \simeq 0.074\,\text{eV}$. The horizontal band indicates the upper bound $|\langle m\rangle| \sim 0.2 - 0.4$ eV obtained using the 90 % C.L. limit on the half-life of ^{76}Ge reported in [118].

If in the case of $\Delta m^2_{41} = 1.78$ eV^2, instead of $\sin^2\theta_{14} = 0.023$ we used the extreme value of the 2σ allowed interval quoted in eq. (5.2.6), $\sin^2\theta_{14} = 0.017$ ($\sin^2\theta_{14} = 0.047$), this will lead to the decreasing (increasing) of the numerical values of $|<m>|$ at $m_{min} \lesssim 10^{-3}$ eV and of $\overline{m}_3$, obtained for $\sin^2\theta_{14} = 0.023$, approximately by the factors 1.1 (1.4) and 2.0 (2.4), respectively.

5.3.1 The Case of $m_3 = 0$

The effective Majorana mass in this case is

$$|\langle m\rangle| = \left|\sqrt{|\Delta m^2_{32}| - \Delta m^2_{21}}\,(c_{12}c_{13}c_{14})^2 + \sqrt{|\Delta m^2_{32}|}\,(c_{13}c_{14}s_{12})^2 e^{i\alpha} + \sqrt{\Delta m^2_{43}}\,s^2_{14}e^{i\gamma}\right| . \tag{5.3.5}$$

Now only two phases enter into the expression of $|\langle m\rangle|$: α and γ. In this case the minima of $|\langle m\rangle|$can be obtained from the general solutions derived in Appendix D.1 and take place for

$$\begin{aligned}\sin\gamma_{\pm} &= \mp\frac{\sqrt{-[(a_0-d_0)^2-b_0^2][(a_0+d_0)^2-b_0^2]}}{2a_0d_0}\\ \sin\alpha_{\pm} &= \pm\frac{\sqrt{-[(a_0-d_0)^2-b_0^2][(a_0+d_0)^2-b_0^2]}}{2a_0b_0}\end{aligned} \tag{5.3.6}$$

where

$$\begin{aligned}a_0 &= \sqrt{|\Delta m^2_{32}|-\Delta m^2_{21}}\;\; c^2_{12}c^2_{13}c^2_{14}\,,\\ b_0 &= \sqrt{|\Delta m^2_{32}|}\;\, c^2_{13}c^2_{14}s^2_{12}\,,\\ d_0 &= \sqrt{\Delta m^2_{43}}\;\, s^2_{14}\,.\end{aligned} \tag{5.3.7}$$

Both minima correspond to $|\langle m\rangle| = 0$ independently of the value of Δm^2_{43}. However, the location of the minima on the $\alpha-\gamma$ plane depends on Δm^2_{43}. For instance, if we use $\Delta m^2_{43} = 0.93$ eV^2, the minima are at $(\sin\alpha, \sin\gamma) = (\mp 0.562, \pm 0.373)$. This result is shown in Fig. 5.13. We notice that the existence of solutions for (α,γ) such that $|\langle m\rangle| \sim 0$ is clear from the expression in eq. (5.3.5) since for the values of the oscillation parameters used in the present study a complete cancellation among the three terms in $|\langle m\rangle|$can take place. Indeed, in the case of the best fit values, for instance,

the first term $\propto \sqrt{|\Delta m^2_{32}|-\Delta m^2_{21}}\,(c_{12}c_{13}c_{14})^2 \approx 0.032$, can be compensated completely by the sum of the other two terms which are of the order of $\sqrt{|\Delta m^2_{32}|}\,(c_{13}c_{14}s_{12})^2 \approx 0.014$ and $\sqrt{\Delta m^2_{43}}\,s^2_{14} \approx 0.022$, respectively.

It follows from our analysis that in the case of $m_3 = 0$ we have $|\langle m\rangle| > 0.01$ eV for values of the phases α and γ outside the region delimited by the red line in Figure 5.13.

We note finally that in the limit $m_3 \to 0$ (or equivalently $c \to 0$) there are four out of the nine solutions determined analytically, which admit $|\langle m\rangle| = 0$ (this can be seen in Table D.2 in the Appendix D.2). The four solutions are $(u_{\pm}, v_{\pm}, t_{\pm})$ and $(v_4^{\pm}(u), t_4^{\pm}(u))$. If the solutions $(v_4^{\pm}(u), t_4^{\pm}(u))$ are evaluated at $u^{\pm}$, i.e., $v_4^{\pm}(u^{\pm}) \to v_{\pm}$, in this case the two minima of the first solution coincide with the two minima of the second one.

5.4 The 3+2 Scheme: Two Sterile Neutrinos

In this Section we analyze the case of two extra sterile neutrino states. In this case the PMNS mixing matrix is a 5×5 unitary matrix. Following the parametrization used in [53] it can be written as:

$$U = V_{35}O_{34}V_{25}V_{24}O_{23}O_{15}O_{14}V_{13}V_{12}\;\; diag(1, e^{i\alpha/2}, e^{i\beta/2}, e^{i\gamma/2}, e^{i\eta/2})\,, \tag{5.4.1}$$

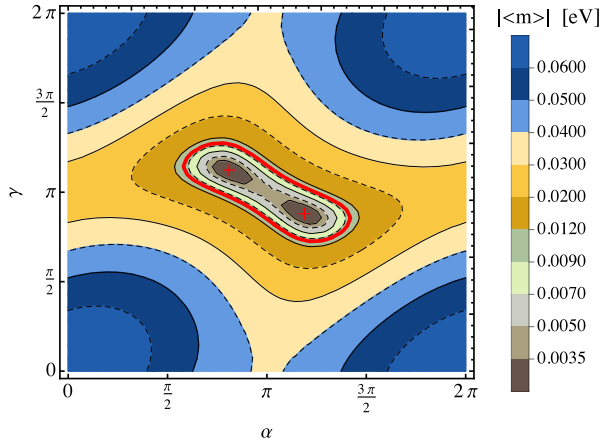

Figure 5.13: The values of $|\langle m\rangle|$for the IH spectrum in the 3+1 scheme versus α and γ in the case of $m_{min} = m_3 = 0$, $\Delta m^2_{43} = 0.93\,\text{eV}^2$ and $\sin\theta_{14} = 0.15$. In this case there are two minima in the crossed points at $(\sin\alpha, \sin\gamma) = (\mp 0.562, \pm 0.373)$, and $|\langle m\rangle|$in these minima is exactly zero. The red line corresponds to $|\langle m\rangle| = 0.01$ eV. See text for details.

$\Delta m^2_{41(43)}$ [eV^2]	$\Delta m^2_{51(53)}$ [eV^2]	θ_{14}	θ_{15}
0.47	0.87	0.13	0.14

Table 5.2: Best global fit values of the sterile neutrino oscillation parameters in the 3+2 scheme with NO (IO) neutrino mass spectrum (from [53]). The relation to the mixing matrix elements is $|U_{e4}| = \cos\theta_{15}\sin\theta_{14}$ and $|U_{e5}| = \sin\theta_{15}$.

where η is an additional Majorana CPV phase. As in the case of the 3+1 scheme, we can set to zero the phases in the matrices V_{25}, V_{24}, V_{13} and V_{12} without loss of generality. In this case the elements of the first row of the PMNS matrix of interest for our analysis are given by:

$$\begin{aligned} U_{e1} &= c_{12}c_{13}c_{14}c_{15} \\ U_{e2} &= e^{i\alpha/2}c_{13}c_{14}c_{15}s_{12} \\ U_{e3} &= e^{i\beta/2}c_{14}c_{15}s_{13} \\ U_{e4} &= e^{i\gamma/2}c_{15}s_{14} \\ U_{e5} &= e^{i\eta/2}s_{15} \end{aligned} \tag{5.4.2}$$

The $(\beta\beta)_{0\nu}$-decay effective Majorana mass reads:

$$|\langle m\rangle| = \left|m_1|U_{e1}|^2 + m_2|U_{e2}|^2 e^{i\alpha} + m_3|U_{e3}|^2 e^{i\beta} + m_4|U_{e4}|^2 e^{i\gamma} + m_5|U_{e5}|^2 e^{i\eta}\right|. \tag{5.4.3}$$

The values for θ_{14}, $\Delta m^2_{41(43)}$, θ_{15} and $\Delta m^2_{51(53)}$ — for NO (IO)—, obtained in the global analysis performed in [53], are summarized in Table 5.2.

5.5 The 3+2 Scheme with NO Spectrum

In the case of the 3+2 scheme with NO spectrum, $m_1 < m_2 < m_3 < m_4 < m_5$, one can write the effective Majorana mass as:

$$|\langle m\rangle| = |m_1 c_{12}^2 c_{13}^2 c_{14}^2 c_{15}^2 + m_2 e^{i\alpha} c_{13}^2 c_{14}^2 c_{15}^2 s_{12}^2 + m_3 e^{i\beta} c_{14}^2 c_{15}^2 s_{13}^2 + m_4 e^{i\gamma} c_{15}^2 s_{14}^2 + m_5 e^{i\eta} s_{15}^2| \quad (5.5.1)$$

As in the case of the 3+1 scheme, it proves convenient to express the masses $m_{2,3,4,5}$ in terms of the lightest neutrino mass m_1 and the neutrino mass squared differences:

$$\begin{aligned} m_{min} \equiv m_1, \quad m_2 = \sqrt{m_1^2 + \Delta m_{21}^2}, \quad m_3 = \sqrt{m_1^2 + \Delta m_{31}^2}, \quad m_4 = \sqrt{m_1^2 + \Delta m_{41}^2}, \\ m_5 = \sqrt{m_1^2 + \Delta m_{51}^2}, \quad \Delta m_{21}^2 > 0, \quad \Delta m_{31}^2 > 0, \quad \Delta m_{41}^2 > 0 \text{ and } \Delta m_{51}^2 > 0 \, . \end{aligned} \quad (5.5.2)$$

The neutrino mass spectrum in 3+2 NO scheme is shown in Fig. 5.14.

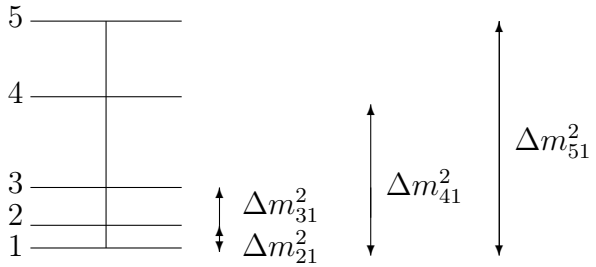

Figure 5.14: The neutrino mass spectrum in the 3+2 NO scheme.

In what follows we will analyze the conditions for minimization of $|\langle m\rangle|$. As in the 3+1 case, we will work with $|\langle m\rangle|^2$ rather than with $|\langle m\rangle|$:

$$|\langle m\rangle|^2 = |a + e^{i\alpha} b + e^{i\beta} c + e^{i\gamma} d + e^{i\eta} e|^2 \, , \quad (5.5.3)$$

where

$$\begin{aligned} a &= m_{min} c_{12}^2 c_{13}^2 c_{14}^2 c_{15}^2 \, , \\ b &= \sqrt{m_{min}^2 + \Delta m_{21}^2} c_{13}^2 c_{14}^2 c_{15}^2 s_{12}^2 \, , \\ c &= \sqrt{m_{min}^2 + \Delta m_{31}^2} c_{14}^2 c_{15}^2 s_{13}^2 \, , \\ d &= \sqrt{m_{min}^2 + \Delta m_{41}^2} c_{15}^2 s_{14}^2 \, , \\ e &= \sqrt{m_{min}^2 + \Delta m_{51}^2} s_{15}^2 \, . \end{aligned} \quad (5.5.4)$$

The analytical study of the minima of $|\langle m\rangle|^2$ in this case is a non-trivial task since four phases are involved and the non-linearity of the system of the first derivatives of $|\langle m\rangle|^2$ with respect to the four phases makes the analysis rather complicated. Therefore finding all possible solutions of the minimization procedure in analytical form is a complex problem. Thus, we have performed the general analysis of the minimization of $|\langle m\rangle|$numerically. It is possible, however, to perform analytically the analysis of the minima of $|\langle m\rangle|$, corresponding to the 16 sets of CP conserving values (either 0 or π) of the four phases α, β, γ and η. This analysis is described in Appendix D.3. It follows from the results found in Appendix D.3 that only $(\alpha,\beta,\gamma,\eta) = (\pi,\pi,\pi,\pi)$, $(0,0,0,\pi)$, $(0,0,\pi,0)$, $(0,\pi,0,0)$ and $(\pi,0,0,0)$ can correspond to minima of $|\langle m\rangle|$. These minima take place in intervals of values of m_1 which are determined by the following sets of inequalities:

$$
\begin{aligned}
&(\alpha,\beta,\gamma,\eta) = (\pi,\pi,\pi,\pi) \quad if \quad F_1 = a-b-c-d-e > 0,\\
&(\alpha,\beta,\gamma,\eta) = (0,0,0,\pi) \quad if \quad (d<e)\wedge(c<e-d)\wedge(b<-c-d+e)\wedge\\
&\qquad\qquad\qquad\qquad \wedge\,(F_8 = a+b+c+d-e<0),\\
&(\alpha,\beta,\gamma,\eta) = (0,0,\pi,0) \quad if \quad (d>e)\wedge(c<d-e)\wedge(b<-c+d-e)\wedge\\
&\qquad\qquad\qquad\qquad \wedge\,(F_3 = a+b+c-d+e<0),\\
&(\alpha,\beta,\gamma,\eta) = (0,\pi,0,0) \quad if \quad (c>d+e)\wedge(b<c-d-e)\wedge\\
&\qquad\qquad\qquad\qquad \wedge\,(G_3 = a+b-c+d+e<0),\\
&(\alpha,\beta,\gamma,\eta) = (\pi,0,0,0) \quad if \quad (b>c+d+e)\wedge(F_6 = a-b+c+d+e<0)\,.
\end{aligned}
\tag{5.5.5}
$$

The dependence of F_1, F_8, F_3, G_3, F_6 and $(d-e)$ on m_1 is shown in the right panel of Fig. 5.15.

It is not difficult to check that for the values of the oscillation parameters quoted in Tables 1.1 and 5.2, the sets of inequalities listed above in each of the cases of $(\alpha,\beta,\gamma,\eta) = (0,0,\pi,0)$, $(0,\pi,0,0)$ and $(\pi,0,0,0)$ cannot simultaneously be fulfilled for $m_1 \geq 0$. Thus, only $(\alpha,\beta,\gamma,\eta) = (\pi,\pi,\pi,\pi)$ and $(0,0,0,\pi)$ correspond to true minima of $|\langle m\rangle|$. Defining $\overline{m}_1$ and $\underline{m}_1$ as the zero of the functions F_1 and F_8,

$$
F_1(\overline{m}_1) = a-b-c-d-e = 0, \qquad F_8(\underline{m}_1) = a+b+c+d-e = 0\,, \tag{5.5.6}
$$

we find that the minima of $|\langle m\rangle|$for $m_1 > \overline{m}_1$ take place only at $(\alpha,\beta,\gamma,\eta) = (\pi,\pi,\pi,\pi)$, while for $m_1 < \underline{m}_1$ they occur at $(\alpha,\beta,\gamma,\eta) = (0,0,0,\pi)$. Further, the numerical analysis performed by us shows that in the interval of $\overline{m}_1 < m_{min} < \underline{m}_1$, the minimum value of $|\langle m\rangle|$is exactly zero and is reached, in general, for CP nonconserving values of the phases $(\alpha,\beta,\gamma,\eta)$. These results are presented graphically in the left panel of Fig. 5.15. Figure 5.15 shows also, in particular, that at $m_{min} \to 0$ we have $|\langle m\rangle| \neq 0$.

In Fig. 5.16 we show $|\langle m\rangle|$as a function of the lightest neutrino mass m_{min}. The shaded area indicates the allowed values for $|\langle m\rangle|$. The red, orange, green and gray lines correspond to the different sets of CP conserving values (0 or π) of the CPV phases (α,β,γ). The vertical solid lines are at $m_1 = \underline{m}_1 \simeq 4.44\times10^{-3}\,\text{eV}$ (and $(\alpha,\beta,\gamma,\eta) = (0,0,0,\pi)$) and $m_1 = \overline{m}_1 \simeq 8.84\times10^{-2}\,\text{eV}$ (and $(\alpha,\beta,\gamma,\eta) = (\pi,\pi,\pi,\pi)$). It is clear from the figure that $|\langle m\rangle|$can be zero in the interval $\underline{m}_1 \leq m_{min} \leq \overline{m}_1$, while for $m_{min} \to 0$ we

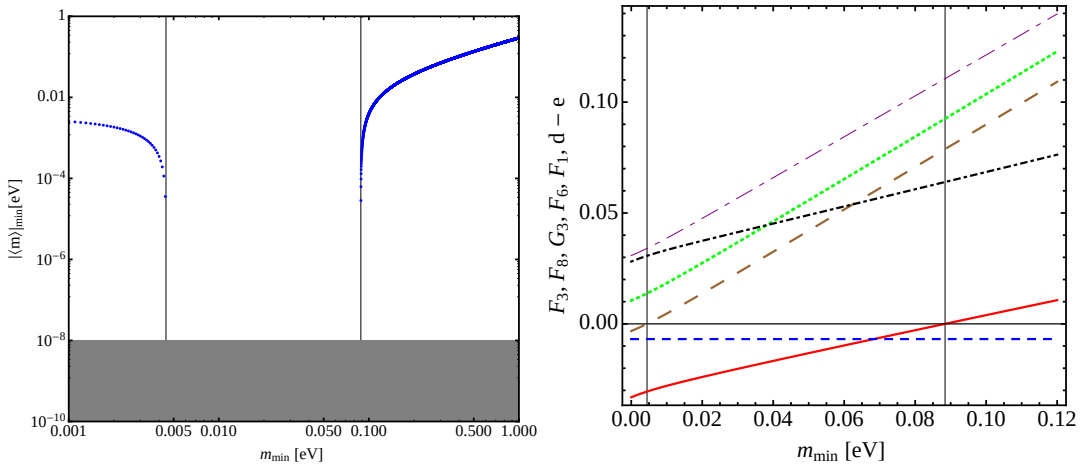

Figure 5.15: Left Panel. Minimum $|\langle m\rangle|$as function of $m_{min} \equiv m_1$. The figure has been obtained numerically for $\Delta m^2_{41} = 0.47\,\text{eV}^2$, $\Delta m^2_{51} = 0.87\,\text{eV}^2$, $\sin\theta_{14} = 0.13$, $\sin\theta_{15} = 0.14$ (see Table 5.2) and performing a scan over a sufficiently large sets of values of m_{min}. The vertical lines correspond to $\overline{m}_1 \simeq 8.84 \times 10^{-2}$ eV and $\underline{m}_1 \simeq 4.44 \times 10^{-3}$ eV. In the interval $\underline{m}_1 \leq m_1 \leq \overline{m}_1$ we have $\min(|\langle m\rangle|) = 0$. Right Panel. The functions F_3 (dotted green), F_8 (large dashed brown), G_3 (short-large dashed purple), F_6 (dot-dashed black), F_1 (solid red), $d - e$ (short-dashed blue), defined in eq. (5.5.6) as function of m_{min} for the best fit values of Table 5.2. The vertical lines are at $\overline{m}_1 \simeq 8.84 \times 10^{-2}$ eV and $\underline{m}_1 \simeq 4.44 \times 10^{-3}$ eV.

have $|\langle m\rangle|_{min} \to 3.21 \times 10^{-3}$ eV and $\max(|\langle m\rangle|) = 0.033$ eV. The indicated $|\langle m\rangle|_{min}$ and $\max(|\langle m\rangle|)$ values at $m_{min} = 0$ in Fig. 5.16 are reached for $(\alpha, \beta, \gamma, \eta) = (0, 0, 0, \pi)$ and $(\alpha, \beta, \gamma, \eta) = (0, 0, 0, 0)$ (corresponding to the red and green lines). At $m_1 = \overline{m}_1$ and $m_1 = \underline{m}_1$, we have $|\langle m\rangle|_{min} = 0$: at $m_1 = \underline{m}_1$ the first four terms in the expression for $|\langle m\rangle|$are positive and their sum is compensated by the last term, $\sqrt{\Delta m^2_{51}}\sin^2\theta_{15}$, while at $m_1 = \overline{m}_1$ a cancellation occurs between the first term proportional to m_{min} and the sum of all the other terms. We have also indicated in the figure with a dotted vertical line the prospective constraint on m_{min} that might be obtained in the β-decay experiment KATRIN [29]. We find that in 3+2 NO scheme under discussion one always has

- $|\langle m\rangle| > 0.01$ eV for $m_{min} > 0.118$ eV.

5.5.1 The Case of $m_1 = 0$

In the case of $m_{min} \equiv m_1 = 0$, the expression of $|\langle m\rangle|$symplifies to:

$$|\langle m\rangle|^2\Big|_{m_1=0} = |e^{i\alpha}b_0 + e^{i\beta}c_0 + e^{i\gamma}d_0 + e^{i\eta}e_0|^2\,, \tag{5.5.7}$$

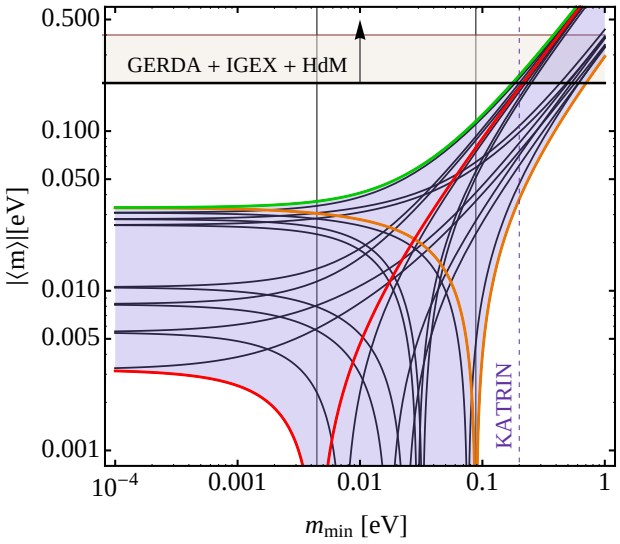

Figure 5.16: The value of $|\langle m\rangle|$versus the lightest neutrino mass m_1 for $\Delta m^2_{41} = 0.47\,\mathrm{eV}^2$, $\Delta m^2_{51} = 0.87\,\mathrm{eV}^2$, $\sin\theta_{14} = 0.13$, $\sin\theta_{15} = 0.14$. The green, red and orange lines correspond to $(\alpha,\beta,\gamma,\eta) = (0,0,0,0), (0,0,0,\pi), (\pi,\pi,\pi,\pi)$, while the blue lines are obtained for the other 13 sets of CP conserving values (0 or π) of the four CPV phases. The vertical solid lines are at $m_1 = \underline{m}_1 \simeq 0.004\,\mathrm{eV}$ and $m_1 = \overline{m}_1 \simeq 0.088\,\mathrm{eV}$. The minimum of $|\langle m\rangle|$in the interval $\underline{m}_1 \leq m_1 \leq \overline{m}_1$ is exactly zero. The horizontal band indicates the upper bound $|\langle m\rangle| \sim 0.2 - 0.4$ eV obtained using the 90 % C.L. limit on the half-life of ^{76}Ge reported in [118]. See text for further details.

where the parameters b_0, c_0, d_0 and e_0 read:

$$\begin{aligned} b_0 &= \sqrt{\Delta m^2_{21} c^2_{13} c^2_{14} s^2_{12}}\,, \\ c_0 &= \sqrt{\Delta m^2_{31} c^2_{14} c^2_{15} s^2_{13}}\,, \\ d_0 &= \sqrt{\Delta m^2_{41} c^2_{15} s^2_{14}}\,, \\ e_0 &= \sqrt{\Delta m^2_{51} s^2_{15}}\,. \end{aligned} \tag{5.5.8}$$

The minimum of the effective Majorana mass is reached in this case for $(\alpha, \beta, \gamma, \eta) = (0, 0, 0, \pi)$ and at the minimum $|\langle m \rangle| \neq 0$. Indeed, numerically we have $b_0 \simeq 2.51 \times 10^{-3}$ eV, $c_0 \simeq 1.14 \times 10^{-3}$ eV, $d_0 \simeq 1.13 \times 10^{-2}$ eV and $e_0 \simeq 1.82 \times 10^{-2}$ eV, and it is clear that the four terms in the expression for $|\langle m \rangle|$cannot compensate each other completely. For the minimum value of $|\langle m \rangle|$in the case under study we get $|\langle m \rangle| = 0.0032$ eV. In Fig. 5.17 we show the values of $|\langle m \rangle|$versus $\alpha - \eta$ and $\beta - \eta$, fixing for convenience $\gamma - \eta = \pi$. The minimum is at the crossed point corresponding to at $\alpha - \eta = \pi$, $\beta - \eta = \pi$. It follows from

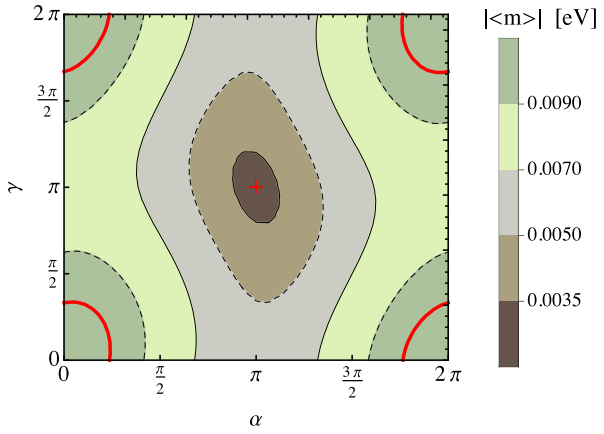

Figure 5.17: The value of $|\langle m \rangle|$in the 3+2 scheme with NO spectrum at $m_{min} = 0$ for $\gamma - \eta = \pi$. The minimum of $|\langle m \rangle|$corresponds to $(\alpha - \eta, \beta - \eta) = (\pi, \pi)$ (the crossed point). The values of $|\langle m \rangle|$at this minimum is 3.21 $\times 10^{-3}$ eV. The red line corresponds to $|\langle m \rangle| = 0.01$ eV.

our analysis that in the case of $m_1 = 0$ and $\gamma - \eta = \pi$ we have $|\langle m \rangle| > 0.01$ eV for values of the phases $\alpha - \eta$ and $\beta - \eta$ in the region delimited by the red lines in Figure 5.17.

5.6 The 3+2 Scheme with IO Spectrum

In the case of the 3+2 scheme with IO spectrum, $m_3 < m_1 < m_2 < m_4 < m_5$, $|\langle m \rangle|$can be written as:

$$|\langle m \rangle| = |m_1 c^2_{12} c^2_{13} c^2_{14} c^2_{15} + m_2 e^{i\alpha} c^2_{13} c^2_{14} c^2_{15} s^2_{12} + m_3 e^{i\beta} c^2_{14} c^2_{15} s^2_{13} + m_4 e^{i\gamma} c^2_{15} s^2_{14} + m_5 e^{i\eta} s^2_{15}|\,. \tag{5.6.1}$$

We have:

$$m_1 = \sqrt{m_3^2 - \Delta m_{32}^2 - \Delta m_{21}^2}, \quad m_2 = \sqrt{m_3^2 - \Delta m_{32}^2}, \quad m_3 \equiv m_{min}, \quad m_4 = \sqrt{m_3^2 + \Delta m_{43}^2},$$
$$m_5 = \sqrt{m_3^2 + \Delta m_{53}^2}, \quad \Delta m_{21}^2 > 0\,, \quad \Delta m_{32}^2 < 0\,, \quad \Delta m_{43}^2 > 0\,, \qquad \Delta m_{53}^2 > 0\,. \tag{5.6.2}$$

The neutrino mass spectrum in 3+2 IO scheme is shown schematically in Fig. 5.18.

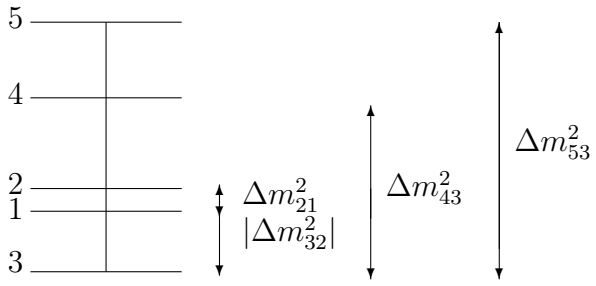

Figure 5.18: The neutrino mass spectrum in the 3+2 IO scheme.

We define:

$$|\langle m \rangle|^2 = |a + e^{i\alpha} b + e^{i\beta} c + e^{i\gamma} d + e^{i\eta} e|^2\ , \tag{5.6.3}$$

where the parameters a, b, c, d and e in this case read:

$$\begin{aligned} a &= \sqrt{m_{min}^2 + |\Delta m_{32}^2| - \Delta m_{21}^2}\, c_{12}^2 c_{13}^2 c_{14}^2 c_{15}^2\,, \\ b &= \sqrt{m_{min}^2 + |\Delta m_{32}^2|}\, c_{13}^2 c_{14}^2 c_{15}^2 s_{12}^2\,, \\ c &= m_{min} c_{14}^2 c_{15}^2 s_{13}^2\,, \\ d &= \sqrt{m_{min}^2 + \Delta m_{43}^2}\, c_{15}^2 s_{14}^2\,, \\ e &= \sqrt{m_{min}^2 + \Delta m_{53}^2}\, s_{15}^2\,. \end{aligned} \tag{5.6.4}$$

As in the case of NO spectrum, we have performed the general analysis of minimization of $|\langle m \rangle|$ numerically. Analytical results have been obtained only for the CP conserving values (0 or π) of the four CPV phases. As it follows from the analysis performed in Appendix D.3, only one set of CP conserving values of the phases corresponds to a minimum of $|\langle m \rangle|$, namely, $(\alpha, \beta, \gamma, \eta) = (\pi, \pi, \pi, \pi)$. The domain of this minimization solution is determined by the inequality $F_1(m_3) \equiv (a - b - c - d - e) > 0$. Let us define by $\overline{m}_3$ the zero of F_1: $F_1(\overline{m}_3) = 0$. As can be shown (and is seen also in Fig. D.1 in Appendix D.3), the inequality of interest $F_1(m_3) > 0$ is satisfied for $m_3 > \overline{m}_3$. Thus, for $m_3 > \overline{m}_3$, $|\langle m \rangle|$takes minimum values only for the values of the phases $(\alpha, \beta, \gamma, \eta) = (\pi, \pi, \pi, \pi)$. Moreover, the minima of $|\langle m \rangle|$at $m_3 > \overline{m}_3$ are different from zero. This follows from the

fact that the minima under discussion correspond to the contribution of the first term $\propto \sqrt{m^2_{min} + |\Delta m^2_{32}| - \Delta m^2_{21}}$ in the expression for $|\langle m \rangle|$, eq. (5.6.1), being compensated by the sum of the other terms in $|\langle m \rangle|$, and that for the values of the oscillation parameters used in the present analysis the compensation cannot be complete. For the indicated values of the phases, a complete compensation leading to $|\langle m \rangle|_{min} = 0$ is possible only in the point $m_3 = \overline{m}_3$. At any given $m_3 < \overline{m}_3$, as our numerical analysis shows, we have $|\langle m \rangle|_{min} = 0$ and the minimum takes place, in general, for CP nonconserving values of $(\alpha, \beta, \gamma, \eta)$. These results are illustrated in Fig. 5.19, where we show $|\langle m \rangle|_{min}$ as function of the lightest neutrino mass.

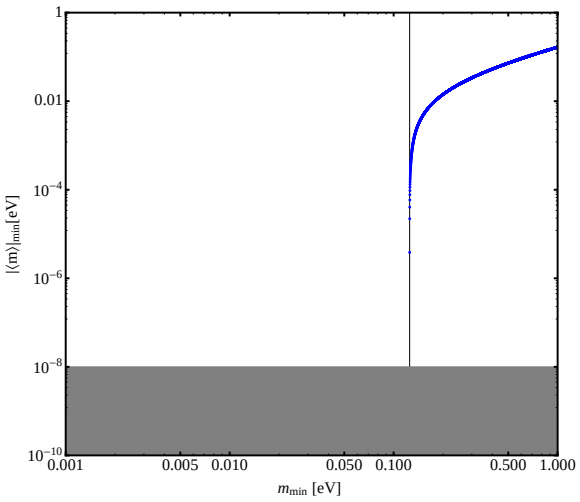

Figure 5.19: Minimum $|\langle m \rangle|$as a function of $m_{min} \equiv m_3$. The plot has been obtained numerically for $\Delta m^2_{43} = 0.47\,\text{eV}^2$, $\Delta m^2_{53} = 0.87\,\text{eV}^2$, $\sin\theta_{14} = 0.13$, $\sin\theta_{15} = 0.14$ (see Table 5.2) by varying m_{min} in the interval [0.001, 1.000] eV and each of the four CPV phases in the interval $[0, 2\pi]$. The vertical line corresponds to $\overline{m}_3 \simeq 1.25 \times 10^{-1}$ eV ($F_1(\overline{m}_3) = 0$). For any given $m_3 \leq \overline{m}_3$ we have $|\langle m \rangle|_{min} = 0$. For the different $m_3 < \overline{m}_3$, the minima of $|\langle m \rangle|$occur at different sets of CP nonconserving values of $(\alpha, \beta, \gamma, \eta)$ (see text for further details).

In Fig. 5.20 we show $|\langle m \rangle|$as function of the lightest neutrino mass $m_{min} = m_3$. The gray lines correspond to $|\langle m \rangle|$computed for CP conserving values of the phases $(\alpha, \beta, \gamma, \eta)$ (either 0 or π). The shaded area indicates the possible allowed values of $|\langle m \rangle|$and is obtained for the values of the oscillation parameters quoted in Tables 1.1 and 5.2. The vertical solid line corresponds to $m_{min} = \overline{m}_3 \simeq 0.125$ eV and $(\alpha, \beta, \gamma, \eta) = (\pi, \pi, \pi, \pi)$. At $m_{min} \leq \overline{m}_3$, we can have $|\langle m \rangle|_{min} = 0$ for specific, in general CP nonconserving, values of the phases $(\alpha, \beta, \gamma, \eta)$. This behaviour of $|\langle m \rangle|_{min}$ is very different from the behavior in the case of NO spectrum discussed in the previous Section, where $|\langle m \rangle|_{min}$ can be zero only in a limited interval of values of m_{min}.

We find also that in the 3+2 IO scheme under discussion and the values of the neutrino oscillation parameters used in the present analysis one always has

- $|\langle m\rangle| > 0.01$ eV for $m_{min} > 0.178$ eV.

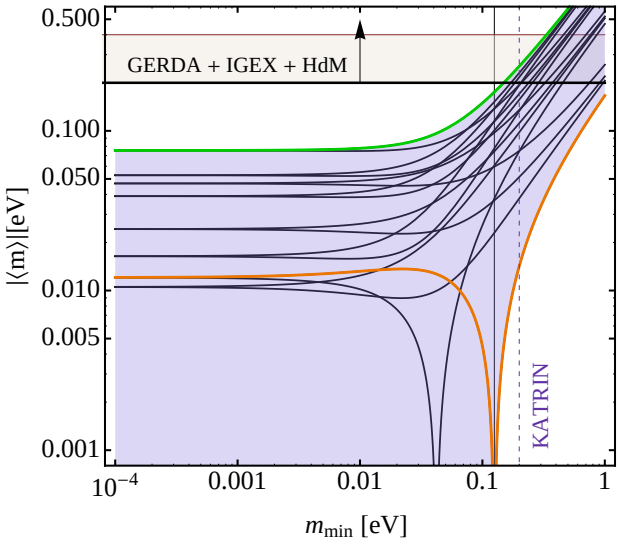

Figure 5.20: The value of $|\langle m\rangle|$as function of $m_{min} = m_3$ for $\Delta m^2_{43} = 0.47$ eV^2, $\Delta m^2_{53} = 0.87$ eV^2, $\sin\theta_{14} = 0.13$, $\sin\theta_{15} = 0.14$ (see Table 5.2). The green and orange lines correspond to $(\alpha, \beta, \gamma) = (0, 0, 0, 0)$ and (π, π, π, π), while the gray lines corresponding to the other 14 sets of CP conserving values (0 or π) of the four CPV phases. The vertical solid line corresponds to $m_{min} = \overline{m}_3 \simeq 0.125$ eV. At $m_{min} \leq \overline{m}_3$ we can have $|\langle m\rangle|_{min} = 0$. The dotted line represents the prospective upper limit from the β-decay experiment KATRIN [29]. The horizontal band indicates the upper bound $|\langle m\rangle| \sim 0.2-0.4$ eV obtained using the 90 % C.L. limit on the half-life of ^{76}Ge given in [118].

5.6.1 The case of $m_3 = 0$

In the limit $m_{min} \equiv m_3 = 0$, (which implies $c = 0$ in eq. (5.6.3)), the analysis of the minimization of the effective Majorana mass is exactly the same as in the case of the 3+1 scheme. This becomes clear after a redefinition of the phases and the coefficients involved. For $m_{min} \equiv m_3 = 0$, $|\langle m\rangle|^2$ can be written as:

$$|\langle m\rangle|^2\Big|_{m_3=0} = |a_0 + e^{i\alpha}b_0 + e^{i\gamma}d_0 + e^{i\eta}e_0|^2 \ , \tag{5.6.5}$$

where

$$\begin{aligned} a_0 &= \sqrt{|\Delta m^2_{32}| - \Delta m^2_{21}}\, c^2_{12} c^2_{13} c^2_{14} c^2_{15}\,, \\ b_0 &= \sqrt{|\Delta m^2_{32}|}\, c^2_{13} c^2_{14} c^2_{15} s^2_{12}\,, \\ d_0 &= \sqrt{\Delta m^2_{43}}\, c^2_{15} s^2_{14}\,, \\ e_0 &= \sqrt{\Delta m^2_{53}}\, s^2_{15}\,. \end{aligned} \tag{5.6.6}$$

Using the analysis performed in Appendix D.1 for the 3+1 scheme we find that the solutions which minimize $|\langle m\rangle|$, such that $|\langle m\rangle|_{min}$ is exactly zero, are: $(u_\pm, v_\pm, t_\pm) \equiv (\tan(\gamma_\pm/2), \tan(\alpha_\pm/2), \tan(\eta_\pm/2))$, $(u_3^\pm, v_3^\pm, t_3^\pm) \equiv (\tan(\gamma_3^\pm/2), \tan(\alpha_3^\pm/2), \tan(\eta_3^\pm/2))$, and $(v_4^\pm(u), t_4^\pm(u)) \equiv (\tan(\alpha_4^\pm/2), \tan(\eta_4^\pm/2))$. The solutions $(u_\pm, v_\pm, t_\pm)$ and $(v_4^\pm(u), t_4^\pm(u))$ can be obtained formally from eqs. (5.2.16) and (5.2.17) by replacing, respectively, a, b, c and d with a_0, b_0, e_0 and d_0 defined in eq. (5.6.6), while the solution $(u_3^\pm, v_3^\pm, t_3^\pm)$ is given by:

$$\begin{cases} u_3^\pm &= \pm \dfrac{\sqrt{(-a_0+b_0-d_0+e_0)(a_0-b_0+d_0+e_0)}}{\sqrt{(a_0-b_0-d_0-e_0)(a_0-b_0-d_0+e_0)}}\,, \\ v_3^\pm &= \pm \dfrac{a_0^2 - b_0^2 - d_0^2 + e_0^2}{\sqrt{(a_0-b_0-d_0-e_0)(a_0-b_0-d_0+e_0)}\sqrt{(-a_0+b_0-d_0+e_0)(a_0-b_0+d_0+e_0)}}\,, \\ t_3^\pm &= \pm \dfrac{(b_0+e_0)(-a_0+b_0+d_0-e_0)\sqrt{(-a_0+b_0-d_0+e_0)(a_0-b_0+d_0+e_0)}}{(b_0-e_0)\sqrt{(a_0-b_0-d_0-e_0)(a_0-b_0-d_0+e_0)}(-a_0+b_0-d_0+e_0)}\,. \end{cases} \tag{5.6.7}$$

Using the best fit values $\Delta m^2_{43} = 0.47\,\mathrm{eV}^2$, $\Delta m^2_{53} = 0.87\,\mathrm{eV}^2$, $\sin\theta_{14} = 0.13$, $\sin\theta_{15} = 0.14$ we find that the minima corresponding to $(u_\pm, v_\pm, t_\pm)$ and to eq. (5.6.7) are given numerically by:

$$u_\pm \simeq \pm 1.44, \quad v_\pm \simeq \pm 18.5, \quad t_\pm \simeq \mp 2.61 \tag{5.6.8}$$

and

$$u_3^\pm \simeq \pm 1.30, \quad v_3^\pm \simeq \mp 2.63, \quad t_3^\pm \simeq \mp 24.7\,. \tag{5.6.9}$$

The third minimum corresponding to the solution $(v_4^\pm(u), t_4^\pm(u))$ is not determined uniquely since it depends on u. However, one can define the minimum for a specific choice of u, or equivalently, for a value for one of the other phases, because the expressions of this solution are invertible. In order to check numerically whether the three solutions are minima we plot the dependence of $|\langle m\rangle|$on two of the CPV phases (α, γ, η), fixing the value of the third phase. It proves convenient to set the value of η, i.e. of t, equal to the values of the solution $(u_\pm, v_\pm, t_\pm)$. One can, of course, do the same using the solutions $(u_3^\pm, v_3^\pm, t_3^\pm)$, or choosing an arbitrary value of η. Our aim is to show that in the 3+2 IO scheme with $m_3 = 0$, the two solutions (u^+, v^+, t^+) and $(v_4^+(u), t_4^+(u))$ represent two different minima, in contrast to the case of 3+1 IO scheme with $m_3 = 0$.

More specifically, if we fix $t \simeq -2.61$, we find $v_4^+ \simeq 1.68$ at a value of $u_4^+ \simeq -59.3$. The Left Panel of Fig. 5.21 shows the values of $|\langle m\rangle|$with $t = t_+ \simeq -2.61$. The marked points

correspond to the two different minima: the first corresponds to the solution (u_+, v_+, t_+) and takes place at $(\alpha, \gamma) = (3.03, 1.93)$, while the second one is associated with the solution $(v_4^+(u), t_4^+(u))$ and occurs at $(\alpha, \gamma) = (2.07, 3.17)$. In these two minima the effective Majorana mass is exactly zero. Repeating the same analysis with $t \simeq 2.61$, we find $v_4^- \simeq -1.68$ at the value of $u_4^- \simeq 59.3$. The Right Panel of Fig. 5.21 shows the values of $|\langle m \rangle|$ with $t = t_- \simeq 2.61$. The points marked with a cross correspond to the two different minima, one evaluated from the function (u_-, v_-, t_-) and corresponding to $(\alpha, \gamma) = (3.25, 4.35)$, and the second evaluated from the function $(v_4^-(u), t_4^-(u))$ and corresponding to $(\alpha, \gamma) = (4.21, 3.11)$. As in the previous case, in these two minima the effective Majorana mass is exactly zero. The existence of two minima in the 3+2 scheme in the limit of $m_3 = 0$ is very different from the 3+1 case where the two minima coincide.

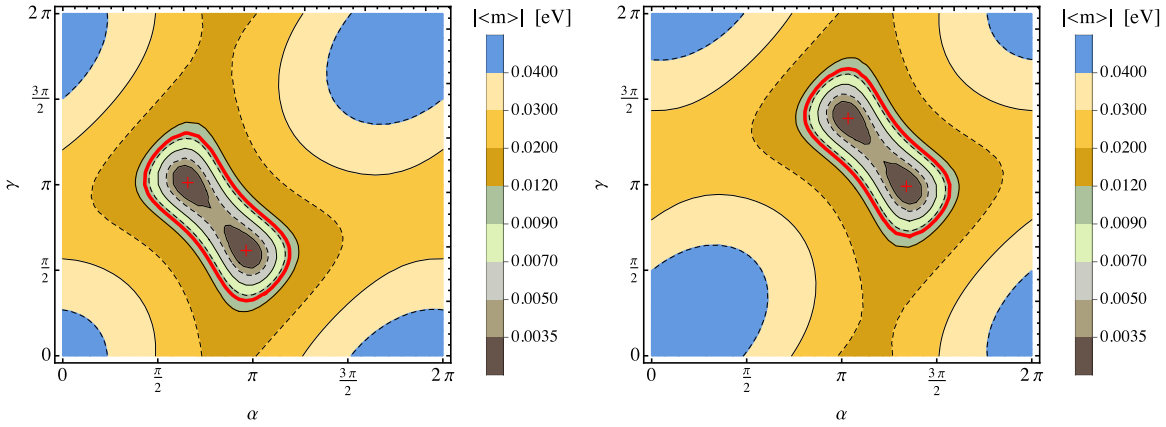

Figure 5.21: Left Panel. The value of $|\langle m \rangle|$in the 3+2 IO scheme for $m_3 \equiv m_{min} = 0$ and the best fit values of Table 5.2. The phase η is set to the value η_+, $\tan \eta_+/2 \simeq -2.61$. The values of $|\langle m \rangle|$ in the marked points $(\alpha, \gamma) = (3.03, 1.93), (2.07, 3.17)$, are zero. The red contour line corresponds to $|\langle m \rangle| = 0.01$ eV. Right Panel. The same as in the left panel, but setting η to the value η_-, $\tan \eta_-/2 \simeq 2.61$. The values of $|\langle m \rangle|$ in the marked points $(\alpha, \gamma) = (3.25, 4.35), (4.21, 3.11)$, are zero. The red contour line corresponds to $|\langle m \rangle| = 0.01$ eV. See text for details.

Finally, it follows from our analysis that for $m_3 = 0$ in the cases we have considered and which are illustrated in Fig. 5.21 we have $|\langle m \rangle| > 0.01$ eV for values of the phases α and γ outside the region delimited by the red line in Fig. 5.21.

5.7 Summary and Conclusions

In the present chapter we have investigated the predictions for neutrinoless double beta ($(\beta\beta)_{0\nu}$-) decay effective Majorana mass $|\langle m \rangle|$ in the $3 + 1$ and $3 + 2$ schemes with one and two additional sterile neutrinos with masses at the eV scale. These two schemes are

widely used in the interpretation of the reactor neutrino and Gallium anomalies as well as of the data of the LSND and MiniBooNE experiments in terms of active-sterile neutrino oscillations. Due to the assumed active-sterile neutrino mixing, the "3 + 1" and "3 + 2" models have altogether 4 and 5 light massive neutrinos ν_j coupled to the electron and muon in the weak charged lepton current. In the minimal versions of these models the massive neutrinos are Majorana particles. The additional neutrinos ν_4 and ν_4, ν_5, should have masses m_4 and m_4, m_5 at the eV scale. It follows from the data that if ν_4 or ν_4, ν_5 exist, they should couple to the electron and muon in the weak charged lepton current with couplings $U_{ek} \sim 0.1$ and $U_{\mu k} \sim 0.1$, $k = 4;\ 4, 5$.

As was shown in [55, 56] and more recently in [57–59], the contribution of the additional light Majorana neutrinos ν_4 or $\nu_{4,5}$ to the $(\beta\beta)_{0\nu}$-decay amplitude, and thus to the $(\beta\beta)_{0\nu}$-decay effective Majorana mass $|\langle m \rangle|$, can change drastically the predictions for $|\langle m \rangle|$ obtained in the reference 3-flavour neutrino mixing scheme, $|\langle m \rangle^{(3\nu)}|$. Using the values of the neutrino oscillation parameters of the $3 + 1$ and $3 + 2$ schemes, obtained in the global analyses of the data relevant for the active-sterile neutrino oscillation hypothesis (positive evidence and negative results), performed in [53, 54] (see Tables 1.1, 5.1 and 5.2), we have investigated in detail in the present chapter the possibility of a complete or partial cancellation among the different terms in $|\langle m \rangle|$, leading to a strong suppression of $|\langle m \rangle|$. This was done in the $3 + 1$ and $3 + 2$ schemes both in the cases of 3-neutrino mass spectra with normal ordering (NO) and inverted ordering (IO), as well as in the cases of normal hierarchical (NH) and inverted hierarchical (IH) spectra with $\min(m_j) = 0$, where $j = 1, 2, 3, 4$ ($j = 1, 2, 3, 4, 5$) for the $3 + 1$ ($3 + 2$) scheme. In this type of analysis the free parameters are the CP violation (CPV) Majorana phases and the lightest neutrino mass. In the case of the $3 + 1$ scheme, in which there are three physical CPV Majorana phases, we have found all the solutions of the system of equations which determine the minima of $|\langle m \rangle|$ as well as their domains (i.e., the regions of their validity), in analytic form. This was done for all types of neutrino mass spectra we have considered. In the more complicated case of $3 + 2$ scheme with four physical CPV Majorana phases, the non-linearity of the system of four equations which determine the extrema of $|\langle m \rangle|$ makes the analytical study of the extrema of interest a complicated problem. Thus, in this case we have performed the general analysis of the minimization of $|\langle m \rangle|$ numerically. It was possible, however, to perform analytically the analysis of the minima of $|\langle m \rangle|$, corresponding to the 16 sets of CP conserving values (either 0 or π) of the four phases.

We have found that if the neutrino mass spectrum is of the NO type, we can have $|\langle m \rangle| = 0$, and thus strongly suppressed $|\langle m \rangle|$, in a specific interval of values of $\min(m_j) \equiv m_{min}$, $\underline{m}_1 \leq m_{min} \leq \overline{m}_1$. This results is valid both for the $3 + 1$ and $3 + 2$ schemes. The specific values of $\underline{m}_1$ and $\overline{m}_1$ depend on the scheme: they are determined by the values of the oscillation parameters in each of the two schemes. For the best fit values reported in Tables 1, 2 and 3, in the $3+1$ with $\Delta m^2_{41} = 0.93\,\mathrm{eV}^2$, $3+1$ with $\Delta m^2_{41} = 1.78\,\mathrm{eV}^2$ and $3+2$ schemes they read, respectively: $(\underline{m}_1, \overline{m}_1) = (0.021, 0.065)$ eV, $(\underline{m}_1, \overline{m}_1) = (0.030, 0.091)$ eV and $(0.004, 0.088)$ eV. For the different values of m_{min} from the indicated interval, the minimum $|\langle m \rangle| = 0$ is reached for different sets of CP nonconserving, in general, values of

the CPV Majorana phases.

For the best fit values reported in Tables 1, 2 and 3, we find that we always have $|\langle m\rangle| > 0.01$ eV,

- in the $3+1$ scheme with $\Delta m^2_{41} = 0.93$ eV^2 – for $m_{min} < 0.010$ eV and $m_{min} > 0.093$ eV;
- in the $3+1$ scheme with $\Delta m^2_{41} = 1.78$ eV^2 – for $m_{min} < 0.020$ eV and $m_{min} > 0.119$ eV;
- in the $3+2$ scheme – for $m_{min} > 0.118$ eV.

The results we have obtained for IO spectrum are different. In this case one can have $|\langle m\rangle| = 0$ in the interval $m_{min} \leq \overline{m}_3$, where $\overline{m}_3$ is determined by the values of neutrino oscillation parameters. For a given m_{min} from the indicated interval, $|\langle m\rangle| = 0$ takes place for specific, in general, CP nonconserving values of the relevant Majorana phases. The values of $\overline{m}_3$ in the two schemes, $3+1$ and $3+2$, differ. Using the values of the oscillation parameters given in Tables 1, 2 and 3, we find: $\overline{m}_3 = 0.038\,(0.074)$ eV for $\Delta m^2_{41} = 0.93\,(1.78)\,\text{eV}^2$ in the $3+1$ scheme, and $\overline{m}_3 = 0.125$ in the $3+2$ scheme.

Using the values of the oscillation parameters given in Tables 1, 2 and 3, we find also that one has always $|\langle m\rangle| > 0.01$ eV,

- in the $3+1$ scheme with $\Delta m^2_{43} = 0.93$ eV^2 – for $m_{min} > 0.078$ eV;
- in the $3+1$ scheme with $\Delta m^2_{43} = 1.78$ eV^2 – for $m_{min} > 0.108$ eV;
- in the $3+2$ scheme – for $m_{min} > 0.178$ eV.

We have investigated also the specific cases of NH and IH spectra in the limit $m_{min} = 0$, which present certain peculiarities both in the $3+1$ and $3+2$ schemes.

The analysis performed by us allowed to derive the general conditions under which the effective Majorana mass satisfies $|\langle m\rangle| > 0.01$ eV, and thus to determine the regions of values m_{min} for which $|\langle m\rangle|$ is predicted to lie in the range planned to be explored by the next generation of $(\beta\beta)_{0\nu}$-experiments. The results of these experiments will provide additional tests of the hypothesis of existence of sterile neutrinos with masses at the eV scale, and couplings ~ 0.1 to the electron and muon in the weak charged lepton current.

CHAPTER 6

Constraining Sterile Neutrinos

6.1 Neutrino Oscillation Probabilities

In the preceding Chapter we have analysed the effects of existence of one or two sterile neutrinos with Majorana masses at the eV scale on the predictions for the effective Majorana mass in neutrinoless double beta decay. Here we use the high precision data of the Daya Bay experiment and the prospective precision data from the JUNO experiment to derive constraints on the parameters which drive the oscillations of active electron antineutrinos into sterile neutrinos [153]. In contrast to the results obtained in the preceding Chapter, which are valid only in the case of massive neutrinos being Majorana particles, the results derived in the present Chapter are valid independently of the nature — Dirac or Majorana — of massive neutrinos.

In the presence of n sterile neutrinos, the neutrino mass matrix is an $(n+3)\times(n+3)$ matrix, which can be diagonalized by means of an $(n+3)\times(n+3)$ unitary matrix U. In general, one has $(n+3)(n+2)/2$ mixing angles and $(n+2)(n+1)/2$ Dirac phases. In the case of only one sterile neutrino, U is typically parameterized by

$$U = R_{34}\tilde{R}_{24}\tilde{R}_{14}R_{23}\tilde{R}_{13}R_{12}P\,, \tag{6.1.1}$$

where the matrix R_{ij} is a rotation by the angle θ_{ij} in the corresponding ij space, e.g.

$$R_{34} = \begin{pmatrix} 1 & 0 & 0 & 0 \\ 0 & 1 & 0 & 0 \\ 0 & 0 & c_{34} & s_{34} \\ 0 & 0 & -s_{34} & c_{34} \end{pmatrix} \quad \text{or} \quad \tilde{R}_{14} = \begin{pmatrix} c_{14} & 0 & 0 & s_{14}e^{-i\delta_{14}} \\ 0 & 1 & 0 & 0 \\ 0 & 0 & 1 & 0 \\ -s_{14}e^{i\delta_{14}} & 0 & 0 & c_{14} \end{pmatrix} \tag{6.1.2}$$

with $s_{ij} = \sin\theta_{ij}$ and $c_{ij} = \cos\theta_{ij}$. The diagonal matrix P contains three Majorana phases, which are irrelevant to our discussion. In this parametrization, one can figure out that

$$|U_{e1}| = c_{14}c_{13}c_{12}\,, \quad |U_{e2}| = c_{14}c_{13}s_{12}\,, \quad |U_{e3}| = c_{14}s_{13}\,, \quad |U_{e4}| = s_{14}\,, \tag{6.1.3}$$

indicating that only the mixing angle θ_{14} enters reactor electron antineutrino oscillations.

The survival probability of electron antineutrinos from nuclear reactors can be written as

$$P_{\bar{e}\bar{e}} \equiv P_{ee} = 1 - 4 \sum_{i<j} |U_{ei}|^2 |U_{ej}|^2 \sin^2 \Delta_{ji} \ , \tag{6.1.4}$$

where $\Delta_{ji} \equiv \Delta m^2_{ji} L/(4E)$ denote the oscillation phases, L the baseline length, E the neutrino energy, and $\Delta m^2_{ji} \equiv m^2_j - m^2_i$ the mass-squared difference of two neutrino mass eigenstates i and j. Using Eq. (6.1.3), we can rewrite the survival probability (6.1.4) as

$$\begin{aligned} P_{ee} \ = \ & 1 - c^4_{14} s^2_{12} \sin^2 2\theta_{13} \sin^2 \Delta_{32} - c^4_{14} c^2_{12} \sin^2 2\theta_{13} \sin^2 \Delta_{31} - c^4_{14} c^4_{13} \sin^2 2\theta_{12} \sin^2 \Delta_{21} \\ & - s^2_{13} \sin^2 2\theta_{14} \sin^2 \Delta_{43} - c^2_{13} s^2_{12} \sin^2 2\theta_{14} \sin^2 \Delta_{42} - c^2_{13} c^2_{12} \sin^2 2\theta_{14} \sin^2 \Delta_{41} \end{aligned} \tag{6.1.5}$$

where the oscillation terms are cast into two rows. The first row collects the contributions from active neutrinos, while the second row from sterile neutrinos. In what follows, we will concentrate on the oscillation probability at the Daya Bay and JUNO setups, in which one of the standard oscillation modes in the first row of Eq. (6.1.5) dominates the probability. In addition, the Δ_{43} mode is further suppressed by both θ_{13} and θ_{14}, and can therefore be safely neglected. Thus, the oscillation probability (6.1.5), in the limit $c^2_{13} = c^2_{14} = 1$, approximates to

$$\begin{aligned} P_{ee} \ \simeq \ & 1 - s^2_{12} \sin^2 2\theta_{13} \sin^2 \Delta_{32} - c^2_{12} \sin^2 2\theta_{13} \sin^2 \Delta_{31} - \sin^2 2\theta_{12} \sin^2 \Delta_{21} \\ & - s^2_{12} \sin^2 2\theta_{14} \sin^2 \Delta_{42} - c^2_{12} \sin^2 2\theta_{14} \sin^2 \Delta_{41} \ . \end{aligned} \tag{6.1.6}$$

6.1.1 The Electron Antineutrino Survival Probability at Daya Bay

Since the baseline length of the Daya Bay detectors is relatively short, the Δ_{21} related modes are strongly suppressed by L, and it is a good approximation to use $\Delta_{32} \simeq \Delta_{31}$ and $\Delta_{42} \simeq \Delta_{41}$. Hence, the oscillation probability (6.1.6) is simplified to

$$P_{ee} \simeq 1 - \sin^2 2\theta_{13} \sin^2 \Delta_{31} - \sin^2 2\theta_{14} \sin^2 \Delta_{41} \ , \tag{6.1.7}$$

where terms like $s^2_{13} s^2_{14}$ have been dropped. The last term appears in short-baseline reactor neutrino experiments when $|\Delta m^2_{41}| \gtrsim 10^{-3}$ eV^2, and may play an important role in explaining the reactor neutrino anomaly. Furthermore, the sterile neutrino contributions would make significant modifications to the electron antineutrino spectrum. In case of a larger active-sterile mass-squared difference, the second term leads to fast oscillations, which result in a shift of the total observed events.

In the interesting situation that $\Delta m^2_{31} \simeq \Delta m^2_{41}$, the two terms in the oscillation probability can be combined, and one can define an effective mixing angle as $\sin^2 2\tilde{\theta}_{13} = \sin^2 2\theta_{13} + \sin^2 2\theta_{14}$. In this case, sterile neutrinos induce mimicking effects that add a correction to the observed mixing angle θ_{13}. Accordingly, Daya Bay loses its sensitivity to sterile neutrinos.

In Fig. 6.1, we illustrate the oscillation probability at the Daya Bay far detector with baseline length $L = 2$ km and mixing $\sin^2 2\theta_{14} = 0.1$ [cf. Eq. (6.2.2) for the other standard

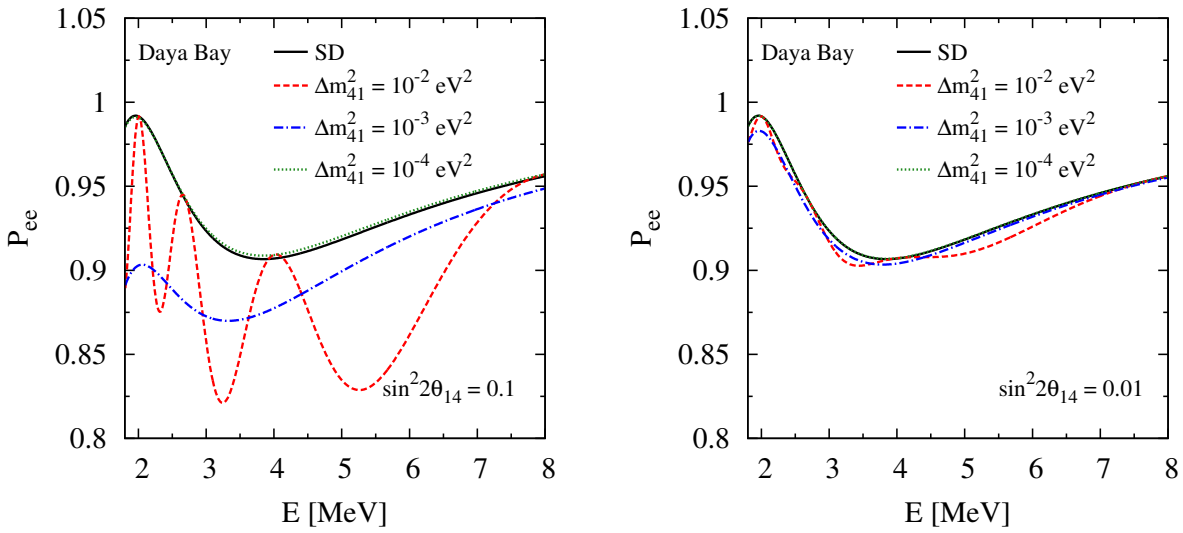

Figure 6.1: The oscillation probability P_{ee} at Daya Bay as a function of neutrino energy E for $L = 2$ km and $\sin^2 2\theta_{14} = 0.1$ (left plot) as well as $\sin^2 2\theta_{14} = 0.01$ (right plot). SD refers to the standard oscillation probability.

oscillation parameters]. As one can read off from the plot, in the limit $|\Delta m^2_{41}| \ll |\Delta m^2_{32}|$, the black solid and green dotted curves almost overlap, and hence, Daya Bay has no sensitivity to sterile neutrinos in this mass regime. In the limit $\Delta m^2_{41} \sim \Delta m^2_{31}$, the sterile polluted curve differs from the standard one. However, this difference can be compensated by taking a smaller value for θ_{13}. A combined analysis of reactor and long-baseline experiments are therefore needed to discriminate this ambiguity. In the regime $|\Delta m^2_{41}| \gg |\Delta m^2_{32}|$, the fast oscillations induced by sterile neutrinos lead to a clear distinction to the standard oscillation behavior, and can be well constrained using the current Daya Bay data.

6.1.2 The Electron Antineutrino Survival Probability at JUNO

Different from the Daya Bay setup, the JUNO detector will be located around 50 km away from the nuclear power plant, indicating that the Δ_{21} oscillation mode is dominating, whereas the Δ_{31} and Δ_{32} related oscillation modes become fast oscillations. The sterile neutrino related oscillation modes Δ_{4i} induce corrections to the neutrino spectrum. Since the JUNO energy resolution is optimized for the determination of the neutrino mass hierarchy, the JUNO detector turns out to be sensitive to mass-squared differences between 10^{-5} eV^2 and 10^{-2} eV^2. Above this mass range, the oscillation frequency is too fast to be distinguished, whereas, below this range, the oscillation behavior does not manifest due to the suppression of baseline length and neutrino energy. Therefore, one may consider the following three cases:

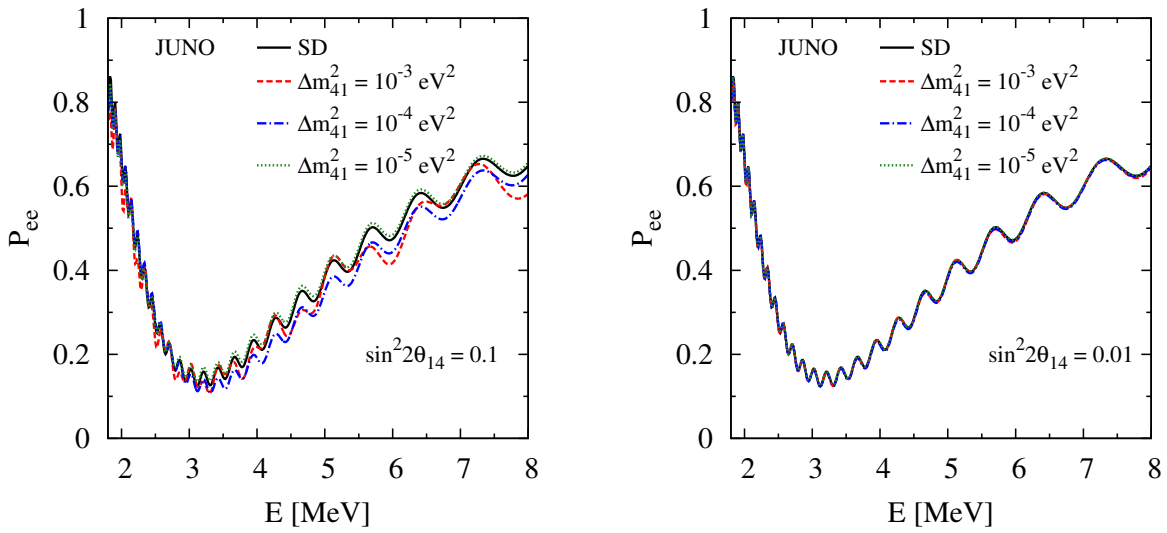

Figure 6.2: The oscillation probability P_{ee} at JUNO as a function of neutrino energy E for $L = 52.5$ km and $\sin^2 2\theta_{14} = 0.1$ (left plot) as well as $\sin^2 2\theta_{14} = 0.01$ (right plot). Here the normal mass hierarchy is assumed. SD refers to the standard oscillation probability.

1. The sterile neutrino is nearly degenerate with one of the three active neutrinos, i.e. $|\Delta m^2_{4i}| < 10^{-5}$ eV^2 (for $i = 1, 2$, or 3). The active-sterile mass-squared differences can be ignored in this case, and the Δ_{42} and Δ_{41} terms in Eq. (6.1.6) can always be absorbed into the standard oscillation terms. The role of sterile neutrinos is simply to correct the standard neutrino mixing angles, implying loss of sensitivity to sterile neutrinos.

2. In the case of a much larger active-sterile mass-squared difference, i.e. $|\Delta m^2_{4i}| > 10^{-2}$ eV^2, the fast active-sterile oscillations are actually beyond the resolution limit of JUNO. In this regime, the Daya Bay setup performs a better probe of sterile neutrinos. The reason is that the baseline length of Daya Bay is much shorter than that of JUNO (the Daya Bay baseline is only about 2 % of the JUNO baseline), and hence, the fast oscillations at Daya Bay is milder, which provides us with a better chance to distinguish the sterile neutrino induced oscillations from the standard ones.

3. In the range 10^{-5} eV$^2 < |\Delta m^2_{4i}| < 10^{-2}$ eV^2, the observed neutrino spectrum obtains corrections from sterile neutrinos and one would expect a better sensitivity at JUNO.

In Fig. 6.2, the sterile neutrino corrections are illustrated for the JUNO setup. When the active-sterile mixing is sizable, the effects of sterile neutrinos become more significant in the large energy regime, in particular for the cases $\Delta m^2_{41} = 10^{-3}$ eV^2 and $\Delta m^2_{41} = 10^{-4}$ eV^2. The shift of the energy spectrum provides us with the possibility to search for sterile neutrinos. For the case of a small value for θ_{14}, the deviation from the standard oscillations

is less pronounced, and one needs in principle a challenging experimental setup with a very high precision to detect sterile neutrinos.

Since the major purpose of JUNO is to settle the neutrino mass hierarchy, one may wonder if the presence of sterile neutrinos may affect the determination of the neutrino mass hierarchy at JUNO. To this end, we present the probability difference between the normal and inverted mass hierarchy cases:

$$\begin{aligned} \Delta P &= P_{ee}^{\rm NH} - P_{ee}^{\rm IH} \\ &\simeq 2 \sin 2\Delta_{21} \left(s_{12}^2 \sin^2 2\theta_{13} \cos\Delta_{31} \sin\Delta_{31} - c_{12}^2 \sin^2 2\theta_{14} \cos\Delta_{42} \sin\Delta_{42} \right) \end{aligned} \tag{6.1.8}$$

where NH stands for the normal mass hierarchy ($m_3 > m_1$) and IH the inverted mass hierarchy ($m_3 < m_1$). One can clearly observe from Eq. (6.1.8) that there exists a very interesting situation that in the limit

$$\Delta_{42} \simeq \Delta_{31} \,, \tag{6.1.9}$$

$$s_{12}^2 \sin^2 2\theta_{13} \simeq c_{12}^2 \sin^2 2\theta_{14} \,, \tag{6.1.10}$$

the probability difference is equal to zero, i.e. $\Delta P = 0$. In this special case, both normal and inverted mass hierarchy fits would give the same minimal χ^2, and the JUNO setup loses its ability to determine the neutrino mass hierarchy. In other words, if JUNO cannot discriminate between its normal and inverted mass hierarchy analyses, a light sterile neutrino with mass of the order $\Delta m_{41}^2 \simeq \Delta m_{32}^2$ and mixing $\sin^2 2\theta_{14} \simeq 0.04$ could then be the underlying reason.

In Fig. 6.3, the impact of sterile neutrinos on the mass hierarchy determination is shown. One can observe from the left plot that when the conditions given in Eq. (6.1.10) are fulfilled, normal and inverted mass hierarchy fits will give equally good or equally bad fits to experimental data. In contrast, in the general case, the wrong-hierarchy oscillation probability gives a worse fit, which is clearly seen in the right plot of Fig. 6.3.

6.2 Fit to Daya Bay data

In this section, we present the relevant features of the Daya Bay experiment and some of the details of our statistical analysis. The Daya Bay experimental setup that we take into account consists of six reactors [154], emitting antineutrinos $\bar{\nu}_e$ whose spectra have been recently estimated in Refs. [155, 156]. The total flux of arriving $\bar{\nu}_e$ at the six antineutrino detectors has been estimated using the convenient parametrization discussed in Ref. [155] and taking into account all the distances between the detectors and the reactors (summarised in Tab. 2 of Ref. [154]). For this analysis we use the data set accumulated during 217 days, which are extracted from Fig. 2 of Ref. [138]. The antineutrino energy E is reconstructed by the prompt energy deposited by the positron $E_{\rm prompt}$ using the approximated relation [154] $E \simeq E_{\rm prompt} + 0.8$ MeV. The energy resolution function is a Gaussian

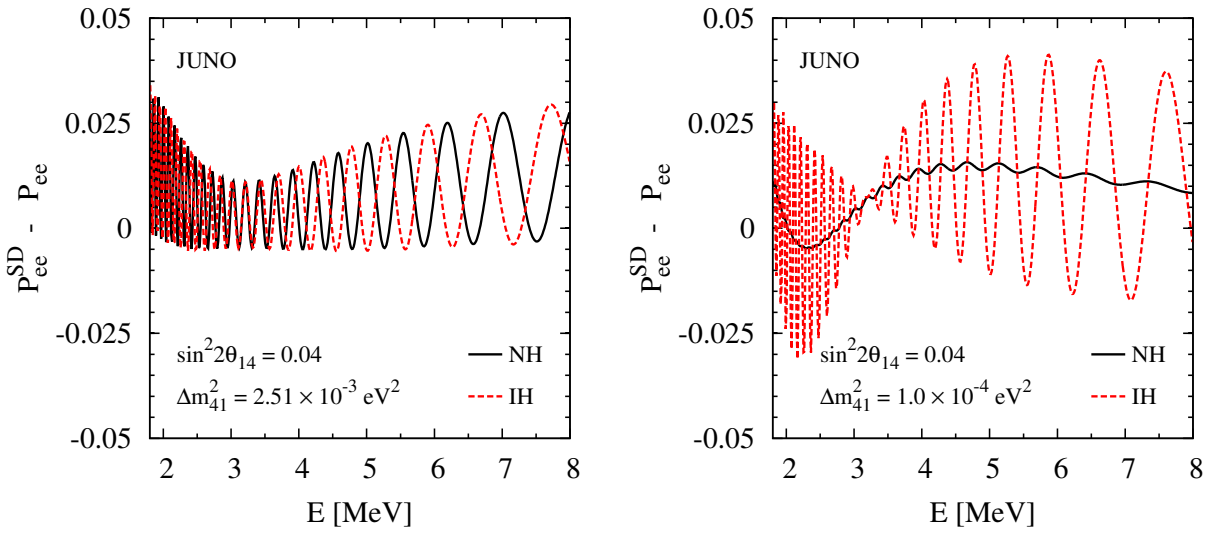

Figure 6.3: The probability differences $(P_{ee}^{\rm SD})^{\rm NH} - P_{ee}$ (solid curves) and $(P_{ee}^{\rm SD})^{\rm IH} - P_{ee}$ (dotted curves) as functions of neutrino energy E for $\sin^2 2\theta_{14} = 0.04$ and $\Delta m^2_{42} = \Delta m^2_{31}$ (left plot) as well as $\Delta m^2_{42} = 10^{-4}$ eV^2 (right plot), where $P_{ee}^{\rm SD}$ is the standard neutrino oscillation probability. Here the normal mass hierarchy for P_{ee} is assumed.

function, parametrized according to

$$\sigma(E)[\text{MeV}] = \begin{cases} \gamma\sqrt{E/\text{MeV} - 0.8}\,, & \text{for } E > 1.8 \text{ MeV}\,, \\ \gamma\,, & \text{for } E \leq 1.8 \text{ MeV}\,, \end{cases} \tag{6.2.1}$$

with $\gamma = 0.08$ MeV. The antineutrino cross section for the inverse beta decay process has been taken from Ref. [157].

The statistical analysis is performed using a modified version of the GLoBES software [158–160] and a χ^2 function which takes into account several sources of systematic errors and retrace the one used by the Daya Bay collaboration. Details can be found in Ref. [72]. We analyze the sensitivity of the Daya Bay experiment on the sterile parameters and the effect of θ_{14} and Δm^2_{41} on the determination of θ_{13} and Δm^2_{31}. Fit results have been obtained after a marginalization over the parameters that are not shown in the figures.

In particular, we use Gaussian priors defined through the mean value and the 1σ error as follows:

$$\begin{aligned} \sin^2\theta_{12} &= 0.306(1 \pm 5\ \%)\,, \\ \sin^2\theta_{13} &= 0.021(1 \pm 20\ \%)\,, \\ \Delta m^2_{21} &= [7.58(1 \pm 5\ \%)] \times 10^{-5}\ \text{eV}^2\,, \\ \left|\Delta m^2_{31}\right| &= [(2.35(1 \pm 20\ \%)] \times 10^{-3}\ \text{eV}^2\,. \end{aligned} \tag{6.2.2}$$

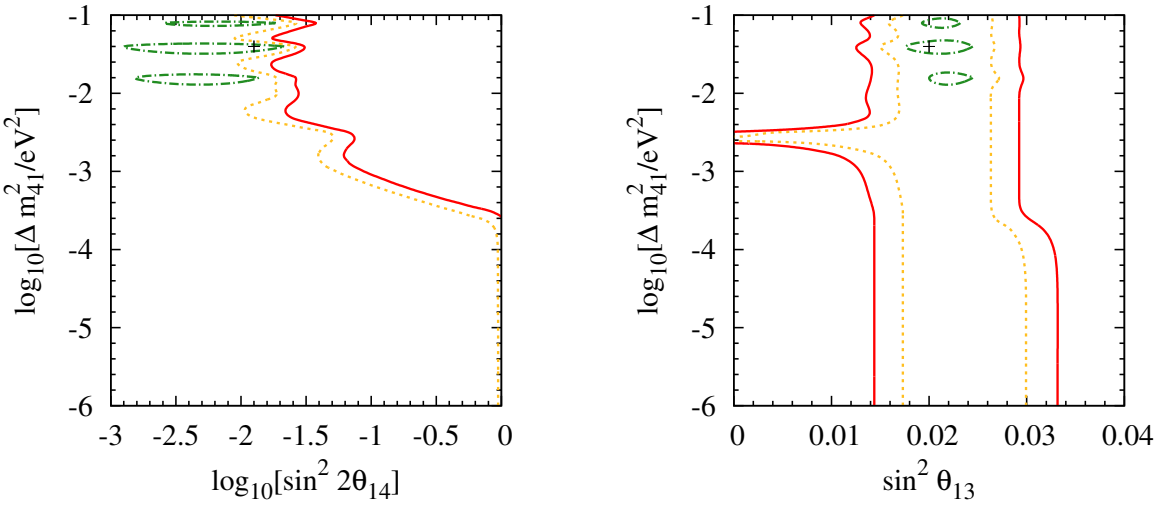

Figure 6.4: Confidence level regions at 1σ, 2σ, and 3σ for 2 dof, after performing a fit to the Daya Bay data, in the $(\sin^2 2\theta_{14}, \Delta m^2_{41})$ and $(\sin^2 \theta_{13}, \Delta m^2_{41})$-planes presented in the left and right plots, respectively.

The central values in Eq. (6.2.2) have been obtained from Ref. [161], although with 1σ errors slightly larger to account for possible (unevaluated) effects due to the presence of sterile neutrinos. The new parameters θ_{14} and Δm^2_{41} are considered as free parameters: the mass-squared difference is completely unconstrained in the range $(10^{-6}, 1)$ eV^2, while for the mixing angle we only considered the upper bound $\theta_{14} < 20°$. In all figures the green dotted-dashed, yellow dotted, and red solid curves refer to 1σ, 2σ, and 3σ regions in 2 degrees of freedom (dof), respectively. The results in the $(\sin^2 2\theta_{14}, \Delta m^2_{41})$-plane is shown in the left plot of Fig. 6.4 after a marginalization over all the standard oscillation parameters using the priors defined in Eq. (6.2.2), in which we can clearly see that at the smallest confidence level a best fit point emerges at $(\sin^2 2\theta_{14}, \Delta m^2_{41}) = (0.012, 0.039\,\text{eV}^2)$. However, since a relatively large part of the parameter space is still allowed at 2σ, it is interesting to analyze the impact of the presence of a third independent mass-squared difference Δm^2_{41} on the measurement of θ_{13}. This is shown in the right plot of Fig. 6.4, obtained after marginalizing over the undisplayed θ_{14} (limited by $\theta_{14} < 20°$) and the other standard parameters with priors as in Eq. (6.2.2). We can easily recognize the presence of two distinct regions. One for $\Delta m^2_{41} \lesssim 10^{-3}\,\text{eV}^2$ and $\Delta m^2_{41} \gtrsim 5 \times 10^{-3}\,\text{eV}^2$ (at 3σ) where, as also outlined in Ref. [79], the measurement of θ_{13} is quite robust and almost unaffected by sterile neutrinos. The other for $10^{-3}\,\text{eV}^2 \lesssim \Delta m^2_{41} \lesssim 5 \times 10^{-3}\,\text{eV}^2$ in which, given the strong interplay between θ_{13} and θ_{14} for $\Delta m^2_{41} \sim \Delta m^2_{31}$ in the oscillation probability, θ_{13} can also become vanishingly small. For our purposes, it is enough to study three different cases, shown in Fig. 6.5 (obtained marginalizing over the other standard parameters and on θ_{14}): $(\sin^2 2\theta_{14}, \Delta m^2_{41}) = (10^{-2}, 10^{-4}\,\text{eV}^2)$ (upper left plot), $(\sin^2 2\theta_{14}, \Delta m^2_{41}) = (0.012, 0.039\,\text{eV}^2)$ (upper right plot, corresponding to

the best-fit point shown in the left plot of Fig. 6.4) and $\Delta m^2_{41} = 2.5 \times 10^{-3}$ eV^2 with free θ_{14} (lower plot). As can be observed from the left and the right upper plots of Fig. 6.5, the presence of sterile neutrinos does not affect significantly the determination of the standard oscillation parameters θ_{13} and Δm^2_{31} for mass-squared differences away from the region $10^{-3}\,\text{eV}^2 \lesssim \Delta m^2_{41} \lesssim 5 \times 10^{-3}\,\text{eV}^2$. On the other hand, for a mass-squared difference within this range we observe in the lower plot a much larger spread of the allowed values of θ_{13} and Δm^2_{31}, as a consequence of $\Delta m^2_{41} \approx \Delta m^2_{31}$. As we have mentioned below Eq. (7), the existence of a sterile neutrino could mimick the effects of a large θ_{13} in this case. The best-fit θ_{13} and Δm^2_{31} are however in consistent with their true values. Concretely, we have the best-fit values ($\sin^2\theta_{13}$, Δm^2_{31})= (0.022, 2.7×10^{-3} eV^2), (0.020, 2.7×10^{-3} eV^2) and (0.021, 2.7×10^{-3} eV^2) for the upper left, upper right and lower plots, respectively.

6.3 Sensitivity at JUNO

The JUNO experiment [162] has been designed to determine the neutrino mass hierarchy, i.e., the sign of Δm^2_{31}, by observing the disappearance of reactor electron antineutrinos at a distance of 52.5 km. With high statistics of one hundred thousand $\bar{\nu}_e$ events in six years and an excellent energy resolution $\gamma = 0.03$ MeV, the JUNO setup will also have a very good sensitivity to the other standard neutrino oscillation parameters, in particular to θ_{12} and Δm^2_{21}. In this section, we explore the impact of sterile neutrinos with a mass-squared difference Δm^2_{41} ranging from 10^{-6} eV^2 to 10^{-1} eV^2 on precision measurements of (θ_{12}, Δm^2_{21}) and (θ_{13}, Δm^2_{31}), and the determination of the neutrino mass hierarchy at JUNO. Moreover, the JUNO sensitivity to sterile neutrinos will be studied and compared with the constraint from the Daya Bay data presented in Sec. 6.2.

Following the approach in Ref. [144], we perform our simulations for the JUNO setup by using the GLoBES software [158–160]. The true values of the relevant standard parameters are taken from the latest global-fit analysis of neutrino oscillation experiments [8]:

$$\begin{aligned} \sin^2\theta_{12} &= 0.308 \pm 0.017 \,, \\ \sin^2\theta_{13} &= 0.0234 \pm 0.002 \,, \\ \Delta m^2_{21} &= (7.54 \pm 0.26) \times 10^{-5}\ \text{eV}^2 \,, \\ \left|\Delta m^2_{31}\right| &= (2.43 \pm 0.06) \times 10^{-3}\ \text{eV}^2 \,, \end{aligned} \tag{6.3.1}$$

where 1σ errors are assumed to be Gaussian and will be incorporated into our simulations as priors for the corresponding parameters. It is worth mentioning that the true values and uncertainties in Eq. (6.3.1) have been obtained by including the Daya Bay data [8], in contrast to those in Eq. (6.2.2). Since JUNO is very sensitive to $(\theta_{12}, \Delta m^2_{21})$, the priors on these are not relevant here. However, the prior knowledge on $(\theta_{13}, \Delta m^2_{31})$ from existing reactor neutrino experiments, such as Daya Bay, is important and will be taken into account.

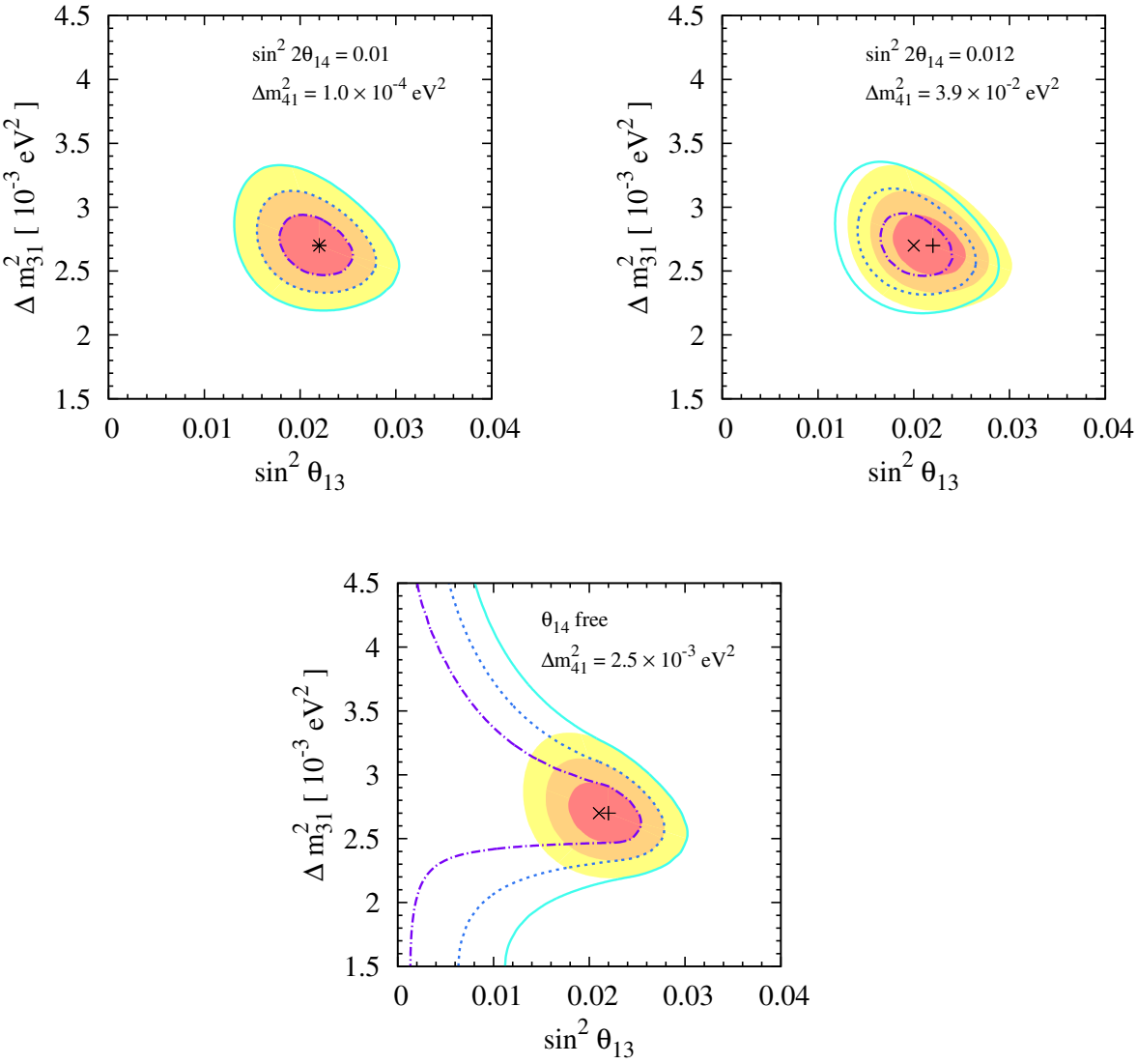

Figure 6.5: Confidence level regions at 1σ, 2σ, and 3σ for 2 dof in the $(\sin^2\theta_{13}, \Delta m^2_{31})$-plane after performing a fit to the Daya Bay data. For the left and the right upper plots, the sterile oscillation parameters are fixed to $(\sin^2 2\theta_{14}, \Delta m^2_{41}) = (10^{-2}, 10^{-4}\,\mathrm{eV}^2)$ and $(\sin^2 2\theta_{14}, \Delta m^2_{41}) = (0.012, 0.039\,\mathrm{eV}^2)$, respectively. The lower plot has been obtained fixing $\Delta m^2_{41} = 2.5 \times 10^{-3}\,\mathrm{eV}^2$ and varying freely θ_{14}.

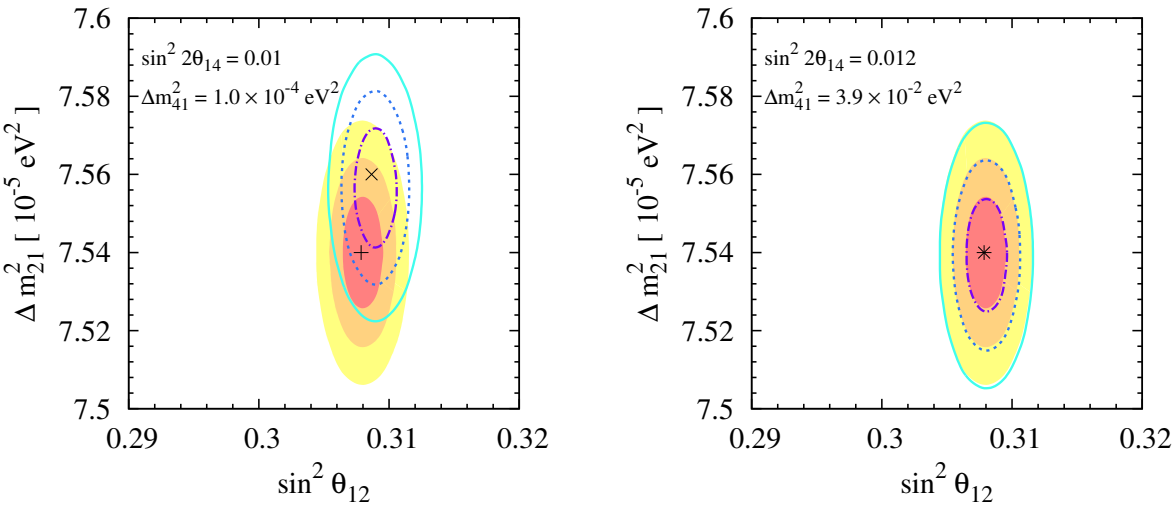

Figure 6.6: Illustration for the impact of sterile neutrinos on the experimental sensitivities to $(\sin^2\theta_{12}, \Delta m^2_{21})$ at JUNO. In our simulations, the true values in Eq. (6.3.1) have been used. The red (dark-gray), orange (gray), and yellow (light-gray) areas stand respectively for the 1σ, 2σ, and 3σ regions for 2 dof in the case of no sterile neutrinos, while the fit results in the presence of sterile neutrinos are represented by the purple (dotted-dashed), blue (dotted), and cyan (solid) curves. Left plot: For $(\sin^2 2\theta_{14}, \Delta m^2_{41}) = (0.01, 1.0 \times 10^{-4}\ \text{eV}^2)$, the best-fit values are $(\sin^2\theta_{12}, \Delta m^2_{21}) = (0.309, 7.56 \times 10^{-5}\ \text{eV}^2)$. Right plot: For $(\sin^2 2\theta_{14}, \Delta m^2_{41}) = (0.012, 3.9 \times 10^{-2}\ \text{eV}^2)$, the best-fit values coincide with those in the case of no sterile neutrinos.

6.3.1 The Parameters θ_{12} and Δm^2_{21}

In order to illustrate how sterile neutrinos affect the precision measurement of $(\theta_{12}, \Delta m^2_{21})$, we generate neutrino data at JUNO by assuming a light sterile neutrino with $(\sin^2 2\theta_{14}, \Delta m^2_{41}) = (0.01, 1.0 \times 10^{-4}\ \text{eV}^2)$. In addition, the true values of the relevant standard parameters are given in Eq. (6.3.1). Then, the generated data are fitted by the standard parameters, with θ_{13} and Δm^2_{31} being marginalized over. As shown in the left plot of Fig. 6.6, the best-fit values in this case turn out to be $(\sin^2\theta_{12}, \Delta m^2_{21}) = (0.309, 7.56 \times 10^{-5}\ \text{eV}^2)$ denoted by "×", which are significantly different from the best-fit values $(\sin^2\theta_{12}, \Delta m^2_{21}) = (0.308, 7.54 \times 10^{-5})$ denoted by "+" in the standard case. The purple dotted-dashed, blue dotted, and cyan solid curves stand for the 1σ, 2σ, and 3σ contour curves, respectively. The difference between best-fit and true values of θ_{12} can be well understood from Eq. (6.1.6), where Δ_{42} and Δ_{41} are of the same order of Δ_{21} and lead to excessive disappearance of reactor antineutrinos. The latter can also be explained by a larger value of θ_{12}, but without sterile neutrinos. On the other hand, for the chosen true values, $|\Delta_{41}| > |\Delta_{21}| > |\Delta_{42}|$ and $\cos^2\theta_{12} > \sin^2\theta_{12}$ indicate that sterile neutrinos introduce an

additional term of faster oscillations, which can be mimicked by a larger Δm^2_{21}. However, if the 1σ errors of the priors of θ_{13} and Δm^2_{31} are taken of the order of 20%, the difference between the standard and the nonstandard fits becomes insignificant. For comparison, we present an analysis of JUNO sensitivity in the standard case without sterile neutrinos, and the shaded areas correspond to the 1σ, 2σ, and 3σ regions, respectively. Given the true values $(\sin^2 2\theta_{14}, \Delta m^2_{41}) = (0.01, 1.0 \times 10^{-4}\ \text{eV}^2)$, it is obvious from Fig. 6.6 that the JUNO sensitivity to $(\theta_{12}, \Delta m^2_{21})$ is essentially not changed, although the best-fit values may deviate from the true values.

If the best-fit values $(\sin^2 2\theta_{14}, \Delta m^2_{41}) = (0.012, 3.9 \times 10^{-2}\ \text{eV}^2)$ from Daya Bay data are taken as true values in our simulations, the JUNO sensitivities to θ_{12} and Δm^2_{21} are almost unchanged, as shown in the right plot of Fig. 6.6. According to Eq. (6.1.6), $\Delta m^2_{41} > \Delta m^2_{31} \gg \Delta m^2_{21}$ implies that the contributions from sterile neutrinos can be hidden by the uncertainties of $(\theta_{13}, \Delta m^2_{31})$, in particular for $\sin^2 2\theta_{14} \ll \sin^2 2\theta_{13}$ in our case. For this set of parameters, JUNO is not sensitive enough to place a restrictive constraint.

It is worthwhile to make a comparison between the sensitivity to $(\sin^2\theta_{12}, \Delta m^2_{21})$ from our simulations and that given by the JUNO Collaboration. In Fig. 6.6, the 1σ error on $\sin^2\theta_{12}$ is 0.0015 and that on Δm^2_{21} is $0.014 \times 10^{-5}\ \text{eV}^2$, corresponding to a precision of 0.49% and 0.19%, respectively. In our simulations, only one reactor with thermal power of 35.8 GW and a flux normalization uncertainty of 3% are considered, and we have ignored the background and other systematics. For the nominal setup and systematic uncertainties considered in Ref. [162], the estimates of the sensitivity to $(\sin^2\theta_{12}, \Delta m^2_{21})$ from the JUNO Collaboration are 0.54% and 0.24%, which are in reasonably good agreement with ours. However, when the bin-to-bin energy uncorrelated uncertainty (1%), the energy linear scale uncertainty (1%), the energy nonlinear uncertainty (1%), and the background (1%) are taken into account, the precisions will be 0.67% and 0.59% [133]. Therefore, our simulated sensitivity will be reduced if the background and the above systematic uncertainties are included.

6.3.2 The Parameters θ_{13} and Δm^2_{31}

In a similar way, we now consider the impact of sterile neutrinos on the measurement of $(\theta_{13}, \Delta m^2_{31})$ at JUNO. In Fig. 6.7, we show the fit of standard parameters to the data generated by oscillation probabilities in the presence of sterile neutrinos. The fit to the data generated with $(\sin^2 2\theta_{14}, \Delta m^2_{41}) = (0.01, 1.0 \times 10^{-4}\ \text{eV}^2)$ is given in the left plot, while that with $(\sin^2 2\theta_{14}, \Delta m^2_{41}) = (0.012, 3.9 \times 10^{-2}\ \text{eV}^2)$ in the right plot.

In the former case, the best-fit value of θ_{13} in the sterile neutrino case coincides exactly with that in the standard case. Moreover, the 1σ, 2σ, and 3σ contour curves overlap with the edges of shaded regions, which are obtained by generating neutrino data without sterile neutrinos. The reason is two-fold. First, $\Delta_{41} \approx \Delta_{21} \ll \Delta_{31}$ and the corrections to the standard oscillation probability of three active neutrinos can be absorbed into the uncertainties of $(\theta_{12}, \sin^2\Delta_{21})$. Second, the JUNO setup itself has limited sensitivity to $(\theta_{13}, \Delta m^2_{31})$.

In the latter case, the deviation from the fit without sterile neutrinos is visible, but

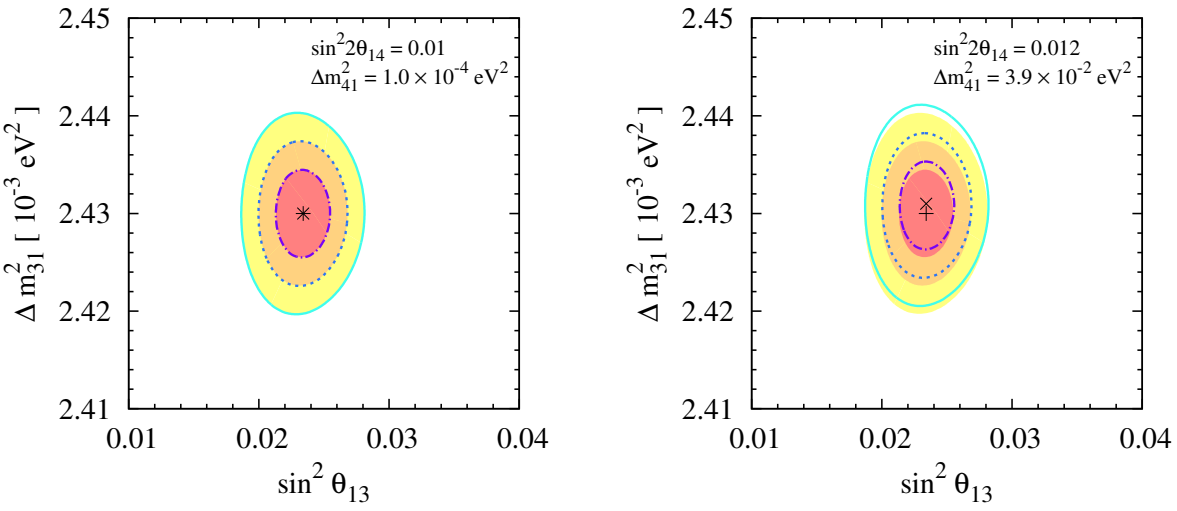

Figure 6.7: Illustration for the impact of sterile neutrinos on the experimental sensitivities to $(\sin^2\theta_{13}, \Delta m^2_{31})$ at JUNO. In our simulations, the true values in Eq. (6.3.1) have been used. The red (dark-gray), orange (gray), and yellow (light-gray) areas stand respectively for the 1σ, 2σ, and 3σ regions for 2 dof in the case of no sterile neutrinos, while the fit results in the presence of sterile neutrinos are denoted by the purple (dotted-dashed), blue (dotted), and cyan (solid) curves. Left plot: For $(\sin^2 2\theta_{14}, \Delta m^2_{41}) = (0.01, 1.0\times10^{-4}\ \text{eV}^2)$, the best-fit values coincide with those in the case of no sterile neutrinos. Right plot: For $(\sin^2 2\theta_{14}, \Delta m^2_{41}) = (0.012, 3.9\times10^{-2}\ \text{eV}^2)$, the best-fit values deviate slightly from those in the standard case.

insignificant. Due to $\Delta_{41} > \Delta_{31}$, the best-fit point is now shifted to a larger value of Δm^2_{31}. It is now evident that a light sterile neutrino does not affect the measurement of $(\theta_{13}, \Delta m^2_{31})$ at JUNO, which in any event is not very sensitive to these two parameters.

6.3.3 The Neutrino Mass Hierarchy

In Fig. 6.8, we show the JUNO sensitivity to the neutrino mass hierarchy in the presence of sterile neutrinos. In our simulations, the neutrino data are generated in the NH case and the true values of the standard parameters are given in Eq. (6.3.1). Additionally, the true values of Δm^2_{41} are specified in the plot, and the black solid, red dashed, blue double-dotted, green dotted-dashed, and brown dotted curves correspond to $\Delta m^2_{41} = 1.0\times10^{-4}\ \text{eV}^2$, $5.0\times10^{-4}\ \text{eV}^2$, $2.49\times10^{-3}\ \text{eV}^2$, $2.51\times10^{-3}\ \text{eV}^2$, and $1.0\times10^{-2}\ \text{eV}^2$, respectively. The fit to the generated neutrino data has been carried out both in the NH and IH cases. In the upper plot, the values χ^2_{min} of the IH fits are denoted by thick curves, while those of the NH fits by thin curves of the same kind. The absolute values of the differences between the IH and NH fits, namely $\Delta\chi^2_{\text{min}} \equiv |\chi^2_{\text{min}}(\text{IH}) - \chi^2_{\text{min}}(\text{NH})|$, are shown in the lower plot. The

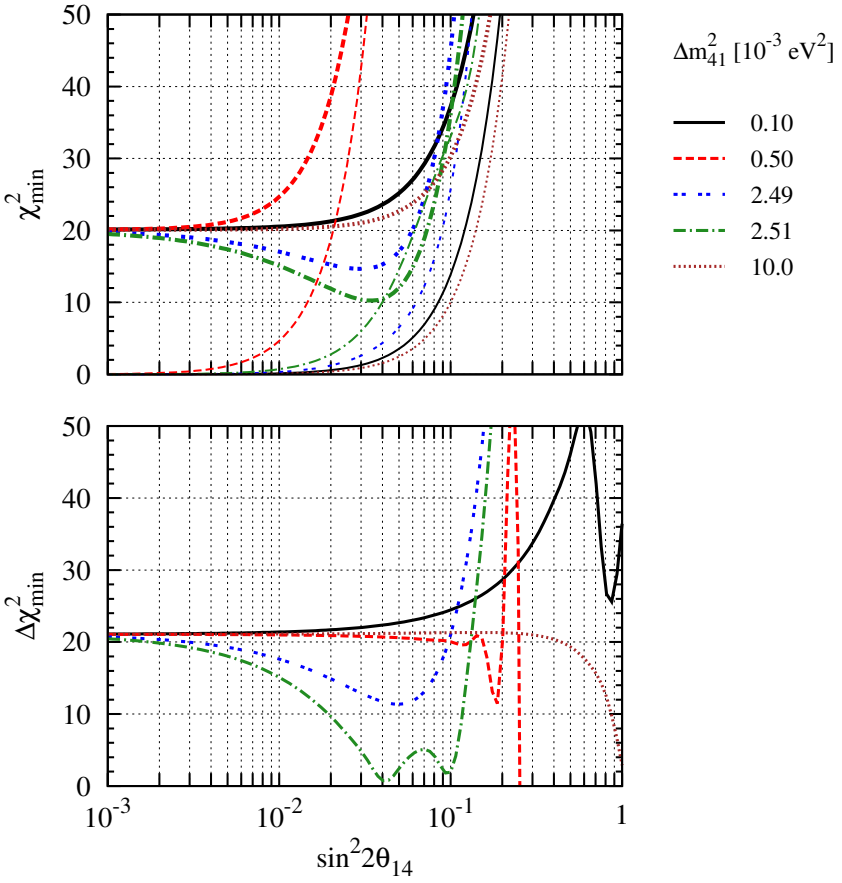

Figure 6.8: Impact on the determination of neutrino mass hierarchy at JUNO. In our simulations, neutrino data are generated in the NH case. In the upper plot, thick curves refer to the fits with IH, while the corresponding thin curves to those with NH. In the lower plot, the absolute values of differences between the IH and NH fits $\Delta\chi^2_{\rm min} \equiv |\chi^2_{\rm min}({\rm IH}) - \chi^2_{\rm min}({\rm NH})|$ have been given for $\Delta m^2_{41} = 1.0 \times 10^{-4}$ eV^2 (solid), 5.0×10^{-4} eV^2 (dashed), 2.49×10^{-3} eV^2 (double-dotted), 2.51×10^{-3} eV^2 (dotted-dashed), and 1.0×10^{-2} eV^2 (dotted).

value of $\Delta\chi^2_{\rm min}$ can be used to measure the capability of the JUNO setup to discriminate between NH and IH.

It is interesting to observe from the lower plot of Fig. 6.8 that $\Delta\chi^2_{\rm min}$ approximately vanishes at $\sin^2 2\theta_{14} = 0.04$ for $\Delta m^2_{41} = 2.51 \times 10^{-3}$ eV^2, which corresponds to the green dotted-dashed curve. This can be perfectly understood with the help of Eqs. (6.1.8) and (6.1.10), where one can see that the oscillation probabilities in the NH and IH cases are

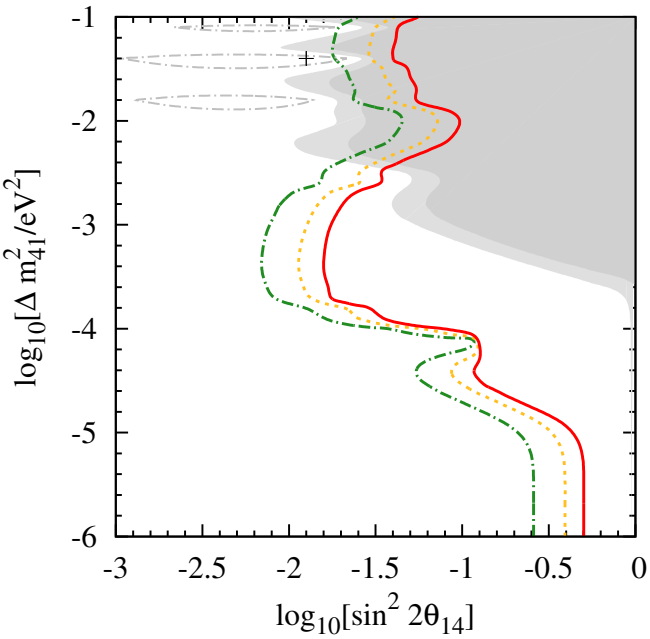

Figure 6.9: Experimental sensitivity to sterile neutrinos at JUNO. The green (dotted-dashed), yellow (dotted), and red (solid) curves correspond to the 1σ, 2σ, and 3σ contours for 2 dof, respectively. For comparison, the fit to Daya Bay data in Fig. 6.4 has been reproduced, where the dark (light) shaded area is excluded by Daya Bay at the 3σ (2σ) confidence level.

equal at this point in parameter space. Therefore, JUNO is unable to pin down the neutrino mass hierarchy in this case. Note that there will be another zero point for $\Delta\chi^2_{\rm min}$ around $\sin^2 2\theta_{14} \approx 0.1$. However, now both $\chi^2_{\rm min}$(IH) and $\chi^2_{\rm min}$(NH) are quite large, implying that three active neutrino oscillations in both the NH and IH cases cannot fit the data well. This indicates that the JUNO setup is sensitive enough to constrain or discover a light sterile neutrino with the corresponding mixing parameters. Except for the mass region $\Delta m^2_{41} \approx \Delta m^2_{31}$, sterile neutrinos have little impact on the determination of the neutrino mass hierarchy.

6.3.4 The Sensitivity at JUNO

Finally, let us proceed to explore the sensitivity of the JUNO setup to the mixing parameters of sterile neutrinos. In our simulations, neutrino data are generated by the standard oscillation probabilities and the true values are given in Eq. (6.3.1). The data are fitted by the general oscillation probability with sterile neutrinos, and all the relevant standard oscillation parameters $(\theta_{12}, \Delta m^2_{21})$ and $(\theta_{13}, \Delta m^2_{31})$ are marginalized over. Our results have been depicted in Fig. 6.9, and compared with the fit to the Daya Bay data. The dark

(light) shaded area is excluded by Daya Bay at the 3σ (2σ) confidence level. At the 3σ confidence level, compared to the JUNO setup, the Daya Bay experiment has a better sensitivity to sterile neutrinos with $\Delta m^2_{41} \gtrsim 4.0 \times 10^{-3}$ eV^2. In the low-mass region, i.e., $\Delta m^2_{41} < 4.0 \times 10^{-3}$ eV^2, JUNO always dominates over Daya Bay in constraining light sterile neutrinos. In this sense, it is therefore clear that reactor neutrino experiments at short and medium baselines are complementary to each other.

The JUNO setup is most sensitive to the mass region from $\Delta m^2_{41} = 10^{-4}$ eV^2 to $\Delta m^2_{41} = 10^{-3}$ eV^2, where the limit $\sin^2 2\theta_{14} < 10^{-2}$ can be reached. The sensitivity is significantly diminished for $\Delta m^2_{41} \approx \Delta m^2_{21}$. In this case, the oscillation probability in Eq. (6.1.5) is reduced to the standard one with two independent neutrino mass-squared differences, where the spectral information is not useful in constraining sterile neutrinos. In the limit of a vanishing Δm^2_{41}, we obtain $\sin^2 \Delta_{43} \approx \sin^2 \Delta_{31}$ and $\sin^2 \Delta_{42} \approx \sin^2 \Delta_{21}$, implying that the standard neutrino oscillation terms in Eq. (6.1.5) receive corrections from sterile neutrinos if θ_{14} is not vanishingly small. Since JUNO has an excellent sensitivity to θ_{12}, it will be able to set an upper bound on $\sin^2 2\theta_{14}$.

It is worthwhile to mention that the experimental constraints on sterile neutrinos exist in the disappearance channel $\bar{\nu}_e \to \bar{\nu}_e$ at reactor neutrino experiments and $\nu_e \to \nu_e$ for solar neutrino experiments. In Ref. [53], for $\Delta m^2_{41} \gg 10^{-2}$ eV^2, the upper bounds $\sin^2 2\theta_{14} < 0.215$ and $\sin^2 2\theta_{14} < 0.28$ at 95 % confidence level have been derived from long-baseline reactor experiments and from solar plus KamLAND data, respectively. Therefore, our results from the Daya Bay experiment and the future JUNO experiment in Fig. 6.9 improve the existing bounds in the high-mass region, and provide new constraints in the low-mass region.

6.4 Summary and Conclusions

One goal of reactor neutrino experiments is to probe new physics beyond the standard-oscillation paradigm as sub-leading effects in neutrino flavor transitions. Due to high statistical precision and good measurements with the Daya Bay experiment, one can obtain some insight into the hypothesis of sterile neutrinos and put limits on light sterile neutrinos when the active-sterile mass-squared difference is located between 10^{-3} and 10^{-1} eV^2. Restricted by the baseline and energy resolution, the Daya Bay experiment has poor sensitivity to sterile neutrinos with a mass-squared difference below 10^{-3} eV^2. In contrast, the future JUNO setup features a higher resolution on the neutrino spectrum and has a longer baseline compared to Daya Bay, and hence plays a complementarity role to the current measurements especially in the small mass-squared difference regime. This is particularly relevant for solar neutrinos, since the MSW solution suggests a low energy of the spectra of events at Super-Kamiokande and SNO, which is however not shown in the data. A light sterile neutrino with a mass-squared difference of the order of 10^{-5} eV^2 and a weak mixing with active neutrinos could explain this suppression [163, 164]. Furthermore, when the recent detection of B mode polarization from the BICEP2 experiment [165] is considered, an analysis of the combined CMB data in the framework of LCDM+r models gives

$N_{\rm eff} = 4.00 \pm 0.41$ [166], which also prefers the existence of extra radiation.

In this work, we have therefore focused on the 3+1 neutrino scenario with only one sterile neutrino and investigated the impact of light sterile neutrinos on short and medium-baseline reactor antineutrino experiments. In particular, we have performed a detail study of antineutrino oscillations and determined the sensitive mass regimes of sterile neutrinos for Daya Bay and JUNO. For both setups, active-sterile neutrino oscillations could in principle mimic the standard oscillations when the active-sterile mass-squared difference is close to one of the standard neutrino mass-squared differences, and hence, one looses sensitivity to sterile neutrinos. Our numerical analysis indicates that the public Daya Bay data suggests an upper limit on the sterile neutrino mixing angle $\sin^2 2\theta_{14} \lesssim 0.06$ at 3σ level for the mass-squared difference between 10^{-3} and 10^{-1} eV^2. In addition, for fixed sterile neutrino oscillation parameters, the effects of sterile neutrinos on the determination of θ_{13} and Δm^2_{31} are rather tiny and can be neglected in extracting the standard parameters. Regarding the JUNO setup, the high-energy resolution improves the sensitivity to $\sin^2 2\theta_{14} \lesssim 0.016$ for $\Delta m^2_{41} \in (10^{-4}, 10^{-3})$ eV^2 and six years of running. However, for a relatively large mass-squared difference, the JUNO sensitivity is not comparable to the one of Daya Bay, due to the longer baseline. When the active-sterile mass-squared difference is around 10^{-4} eV^2, the measured θ_{12} and Δm^2_{21} deviate from their true values, whereas θ_{13} and Δm^2_{31} are not affected by the sterile neutrino pollution. We have also found a special parameter region that, when $\sin^2 2\theta_{14} \simeq 0.04$ and $\Delta m^2_{42} \simeq \Delta m^2_{31}$, the sterile neutrino polluted oscillation probability would be almost the same for both NH and IH, indicating that the JUNO setup completely loses its power to discriminate the active neutrino mass hierarchy.

CHAPTER 7

Outlook

In the present Ph.D. thesis we have discussed certain theoretical and phenomenological aspects of neutrino related physics beyond the Standard Theory of particle interactions. Additional studies were performed in the articles [72, 172–176], the results of which were not included in the Thesis.

The experimental program of research in neutrino physics extends beyond 2030. The status of CP symmetry in the lepton sector will be elucidated by the currently running T2K [177] and NOνA [178] long baseline (LBL) neutrino oscillation experiments and in the future planned DUNE [179] and T2HK [15] LBL oscillation experiments with large scale detectors (34 kton liquid argon and ~ 500 kton ultra pure water). DUNE and T2HK, which have a very rich physics program, are planned to be operative in 2025-2026. For these measurements the high precision determination of the reactor mixing angle θ_{13} in the currently running Daya Bay experiment with reactor $\bar{\nu}_e$ [180], to be completed by 2018, will serve as a very important input. A very important input for the DUNE and T2HK measurements of the Dirac CP violation phase in the neutrino mixing matrix will be provided also by the data on the neutrino mass spectrum from the approved JUNO experiment with reactor $\bar{\nu}_e$ [181, 182], which is under construction and is scheduled to start data taking in 2021, and from the planned PINGU detector [183] (within the IceCube experiment at the South Pole) and ORCA detector [184] (in the Mediterranean sea within the KM3Net project). Both PINGU and ORCA are designed to study the oscillations of the atmospheric ν_μ, $\bar{\nu}_\mu$, ν_e and $\bar{\nu}_e$ in the energy range $\sim (2 - 10)$ GeV, in which the Earth matter effects in the oscillations of neutrinos are significant. PINGU and ORCA are planned to be operative in 2021-2022. The JUNO experiment (employing a 20 kton liquid scintillator detector) has an extremely rich physics program [182]. It will make, in particular, the most precise measurement of the solar neutrino mixing angle θ_{12} [185, 186].

The nature of massive neutrinos — Dirac or Majorana — will be probed in ongoing and future planned $(\beta\beta)_{0\nu}$-decay experiments: CUORE (with ^{130}Te), GERDA (with ^{76}Ge), KAMLAND-Zen (with ^{136}Xe), EXO (with ^{136}Xe), SNO+ (with ^{130}Te), MAJORANA (with ^{76}Ge), AMORE (with ^{100}Mo), SuperNEMO (with a number of different isotopes), to name a few (see, e.g., [20]). The goal of these experiments is to test the range of predictions of

the effective Majorana mass $|\langle m \rangle| \gtrsim 0.01$ eV, corresponding to IO neutrino mass spectrum and, possibly, even to smaller values of $|\langle m \rangle|$. The searches for $(\beta\beta)_{0\nu}$-decay will extend beyond 2020.

The hints of existence of additional neutrino states with masses at the eV scale, which induce oscillations of the active ν_μ, $\bar{\nu}_\mu$ and/or ν_e, $\bar{\nu}_e$ neutrinos into sterile neutrinos, will be tested in upcoming experiments with artificial sources (SAGE, CeSOX), with reactor neutrinos (STEREO, NUCIFER, PROSPECT, etc.) and with accelerator neutrinos (ICARUS at Fermilab (SBN), nuPRISM, nuSTORM, NESSiE, etc.) (see, e.g., [34]). We will know whether active ν_μ, $\bar{\nu}_\mu$ and/or ν_e, $\bar{\nu}_e$ neutrinos indeed oscillate into sterile neutrinos probably by 2021-2022.

Data on the absolute neutrino mass scale, or equivalently, on $\min(m_j)$, $j = 1, 2, 3, ...$, will be provided by the upcoming KATRIN experiment [187]. Future cosmological and astrophysical measurements will provide high precision information on the sum of the neutrino masses [31, 32].

In Chapters 2, 3, 4 and 5 we have made specific predictions which will be tested in the ongoing and the future planned experiments described above. It is hoped that these experiments and further theoretical developments will shed light on the fundamental aspects of neutrino mixing: the status of the CP symmetry in the lepton sector, the type of spectrum neutrino masses obey, the nature — Dirac or Majorana — of massive neutrinos, the existence of sterile neutrinos with masses at the eV scale, etc. The data that will be provided by these experiments will help us make progress in understanding the possible origin of the observed patterns of neutrino mixing and of the neutrino mass squared differences, on the connection, if any, between the neutrino mixing angles and leptonic CP violation phases and, more generally, between the quark and neutrino (lepton) mixing, in the searches for a solution of the (lepton) flavour problem, in the understanding the role the neutrinos can play, if any, in the generation of the baryon asymmetry of the Universe, etc. Obviously, the wealth of data from the ongoing and the future planned neutrino experiments will require non-trivial theoretical input. We are looking very much forward to these exciting developments.

APPENDIX A

Group Theory

A.1 Technicalities about T'

The group T' is the double covering group of A_4 and it is defined through the algebraic relations:

$$S^2 = R \quad R^2 = T^3 = (ST)^3 = E \quad RT = TR\,. \tag{A.1.1}$$

The number of the unitary irreducible representations of a discrete group is equal to the number of the conjugacy classes. For T' they are seven, which are classified given the elements T, S, because $R \equiv S^2$, we summarize them as

$$\begin{aligned}
&1\,C^1 : \{E\}\ , \quad 1'\,C^2 : \left\{S^2\right\} \\
&4\,C^3 : \left\{T, S^3TS, ST, TS\right\}\ , \quad 4'\,C^3 : \left\{T^2, S^2TST, S^2T^2S, S^3T^2\right\} \\
&4''\,C^6 : \left\{S^2T, STS, S^3T, S^2TS\right\}\ , \quad 4'''\,C^6 : \left\{S^2T^2, TST, T^2S, ST^2\right\} \\
&6\,C^4 : \left\{S, S^3, TST^2, T^2ST, S^2TST^2, S^2T^2ST\right\}
\end{aligned} \tag{A.1.2}$$

The representations of T' can be expressed as

$$
\begin{aligned}
&\mathbf{1} : T = 1 \ , \ R = 1 \ , \ S = 1 \, ; \\
&\mathbf{1'} : T = \omega \ , \ R = 1 \ , \ S = 1 \, ; \\
&\mathbf{1''} : T = \omega^2 \ , \ R = 1 \ , \ S = 1 \, ; \\
&\mathbf{2} : T = \begin{pmatrix} \omega^2 & 0 \\ 0 & \omega \end{pmatrix} \ , \ R = \begin{pmatrix} -1 & 0 \\ 0 & -1 \end{pmatrix} \ , \ S = \begin{pmatrix} -\frac{i}{\sqrt{3}} & -\sqrt{\frac{2}{3}} p \\ \sqrt{\frac{2}{3}} \bar{p} & \frac{i}{\sqrt{3}} \end{pmatrix} ; \\
&\mathbf{2'} : T = \begin{pmatrix} \omega^3 & 0 \\ 0 & \omega^2 \end{pmatrix} \ , \ R = \begin{pmatrix} -1 & 0 \\ 0 & -1 \end{pmatrix} \ , \ S = \begin{pmatrix} -\frac{i}{\sqrt{3}} & -\sqrt{\frac{2}{3}} p \\ \sqrt{\frac{2}{3}} \bar{p} & \frac{i}{\sqrt{3}} \end{pmatrix} ; \\
&\mathbf{2''} : T = \begin{pmatrix} \omega & 0 \\ 0 & 1 \end{pmatrix} \ , \ R = \begin{pmatrix} -1 & 0 \\ 0 & -1 \end{pmatrix} \ , \ S = \begin{pmatrix} -\frac{i}{\sqrt{3}} & -\sqrt{\frac{2}{3}} p \\ \sqrt{\frac{2}{3}} \bar{p} & \frac{i}{\sqrt{3}} \end{pmatrix} ; \\
&\mathbf{3} : T = \begin{pmatrix} 1 & 0 & 0 \\ 0 & \omega & 0 \\ 0 & 0 & \omega^2 \end{pmatrix} \ , \ R = \begin{pmatrix} 1 & 0 & 0 \\ 0 & 1 & 0 \\ 0 & 0 & 1 \end{pmatrix} \ , \ S = \begin{pmatrix} -\frac{1}{3} & \frac{2\omega}{3} & \frac{2\omega^2}{3} \\ \frac{2\omega^2}{3} & -\frac{1}{3} & \frac{2\omega}{3} \\ \frac{2\omega}{3} & \frac{2\omega^2}{3} & -\frac{1}{3} \end{pmatrix} .
\end{aligned}
$$

We use the definition of the representation of T' given in [97] in which ω and p are fixed to be respectively $\omega = \mathrm{e}^{\frac{2\,\mathrm{i}\,\pi}{3}}$ and $p = \mathrm{e}^{\frac{\mathrm{i}\,\pi}{12}}$. Finally T' has $n = 13$ subgroups excluding the whole group:

- Trivial subgroup
  $\mathbb{E} = \{E\}$;
- Z_2 subgroup
  $Z_2^{S^2} = \{E, S^2\}$;
- Z_3 subgroups
  $Z_3^T = \{E, T, T^2\}$, $Z_3^{S^3TS} = \{E, S^3TS, S^2TST\}$, $Z_3^{ST} = \{E, ST, S^2T^2S\}$, $Z_3^{TS} = \{E, TS, S^3T^2\}$;
- Z_4 subgroups
  $Z_4^S = \{E, S, S^2, S^3\}$, $Z_4^{TST^2} = \{E, TST^2, S^2, S^2TST^2\}$, $Z_4^{T^2ST} = \{E, T^2ST, S^2, S^2T^2ST\}$;
- Z_6 subgroups
  $Z_6^{S^2T} = \{E, S^2T, T^2, S^2, T, S^2T^2\}$, $Z_6^{STS} = \{E, STS, S^2TST, S^2, S^3TS, TST\}$,
  $Z_6^{S^3T} = \{E, S^3T, S^2T^2S, S^2, ST, T^2S\}$, $Z_6^{S^2TS} = \{E, S^2TS, S^3T^2, S^2, TS, ST^2\}$.

A complete table of the CGs coefficients can be found in [90].

APPENDIX B

Parametrisations and Statistical Details

B.1 Relations Between Phases in Two Parametrisations

In this section we present the relations between the phases of the two different parametrisations of the PMNS matrix employed in [86] and [75]. In the parametrisation used in [86] the PMNS matrix after setting $\theta_{13}^{e} = \theta_{13}^{\nu} = 0$ reads:

$$U_{\text{PMNS}} = U_{12}^{e_L\dagger}\, U_{23}^{e_L\dagger}\, U_{23}^{\nu_L}\, U_{12}^{\nu_L}\,, \tag{B.1.1}$$

where the subscripts 12 and 23 stand for the rotation plane, e.g., the matrix $U_{12}^{e_L}$ being defined as

$$U_{12}^{e_L} = \begin{pmatrix} \cos\theta_{12}^{e} & \sin\theta_{12}^{e}\, e^{-i\delta_{12}^{e}} & 0 \\ -\sin\theta_{12}^{e}\, e^{i\delta_{12}^{e}} & \cos\theta_{12}^{e} & 0 \\ 0 & 0 & 1 \end{pmatrix}, \tag{B.1.2}$$

and the others analogously. We can factorise the phases in the charged lepton and the neutrino sectors in the following way:

$$\begin{aligned} U_{12}^{e_L\dagger}\, U_{23}^{e_L\dagger} = &\begin{pmatrix} 1 & 0 & 0 \\ 0 & e^{i(\delta_{12}^{e}+\pi)} & 0 \\ 0 & 0 & e^{i(\delta_{12}^{e}+\delta_{23}^{e})} \end{pmatrix} \begin{pmatrix} \cos\theta_{12}^{e} & \sin\theta_{12}^{e} & 0 \\ -\sin\theta_{12}^{e} & \cos\theta_{12}^{e} & 0 \\ 0 & 0 & 1 \end{pmatrix} \\ &\times \begin{pmatrix} 1 & 0 & 0 \\ 0 & \cos\theta_{23}^{e} & \sin\theta_{23}^{e} \\ 0 & -\sin\theta_{23}^{e} & \cos\theta_{23}^{e} \end{pmatrix} \begin{pmatrix} 1 & 0 & 0 \\ 0 & e^{-i(\delta_{12}^{e}+\pi)} & 0 \\ 0 & 0 & e^{-i(\delta_{12}^{e}+\delta_{23}^{e})} \end{pmatrix}, \end{aligned} \tag{B.1.3}$$

$$\begin{aligned} U_{23}^{\nu_L}\, U_{12}^{\nu_L} = &\begin{pmatrix} 1 & 0 & 0 \\ 0 & e^{i\delta_{12}^{\nu}} & 0 \\ 0 & 0 & e^{i(\delta_{23}^{\nu}+\delta_{12}^{\nu})} \end{pmatrix} \begin{pmatrix} 1 & 0 & 0 \\ 0 & \cos\theta_{23}^{\nu} & \sin\theta_{23}^{\nu} \\ 0 & -\sin\theta_{23}^{\nu} & \cos\theta_{23}^{\nu} \end{pmatrix} \\ &\times \begin{pmatrix} \cos\theta_{12}^{\nu} & \sin\theta_{12}^{\nu} & 0 \\ -\sin\theta_{12}^{\nu} & \cos\theta_{12}^{\nu} & 0 \\ 0 & 0 & 1 \end{pmatrix} \begin{pmatrix} 1 & 0 & 0 \\ 0 & e^{-i\delta_{12}^{\nu}} & 0 \\ 0 & 0 & e^{-i(\delta_{23}^{\nu}+\delta_{12}^{\nu})} \end{pmatrix}. \end{aligned} \tag{B.1.4}$$

Combining eqs. (B.1.3) and (B.1.4) and comparing with the parametrisation of the PMNS matrix employed in [75] and given in eqs. (3.1.5) and (3.1.6), we find the following relations:

$$\psi = \delta^e_{12} - \delta^\nu_{12} + \pi\,, \quad \omega = \delta^e_{23} + \delta^e_{12} - \delta^\nu_{23} - \delta^\nu_{12}\,, \tag{B.1.5}$$

$$\xi_{21} = -2\delta^\nu_{12}\,, \quad \xi_{31} = -2(\delta^\nu_{12} + \delta^\nu_{23})\,. \tag{B.1.6}$$

B.2 Statistical Details

In order to perform a statistical analysis of the models considered in Chapter 3 we construct the χ^2 function in the following way:

$$\chi^2(\sin^2\theta_{12}, \sin^2\theta_{13}, \sin^2\theta_{23}, \delta) = \chi^2_1(\sin^2\theta_{12}) + \chi^2_2(\sin^2\theta_{13}) + \chi^2_3(\sin^2\theta_{23}) + \chi^2_4(\delta)\,, \tag{B.2.1}$$

in which we have neglected the correlations among the oscillation parameters, since the functions χ^2_i have been extracted from the 1-dimensional projections in [8]. In order to quantify the accuracy of our approximation we show in Fig. B.1 the confidence regions at 1σ, 2σ and 3σ for 1 degree of freedom in the planes $(\sin^2\theta_{23}, \delta)$, $(\sin^2\theta_{13}, \delta)$ and $(\sin^2\theta_{23}, \sin^2\theta_{13})$ in blue (dashed lines), purple (solid lines) and light-purple (dash-dotted lines) for NO (IO) neutrino mass spectrum, respectively, obtained using eq. (B.2.1). The parameters not shown in the plot have been marginalised. It should be noted that what is also used in the literature is the Gaussian approximation, in which χ^2 can be simplified using the best fit values and the 1σ uncertainties as follows:

$$\chi^2_{\rm G} = \sum_i \frac{(x_i - \overline{x}_i)^2}{\sigma^2_{x_i}}\,. \tag{B.2.2}$$

Here $x_i = \{\sin^2\theta_{12}, \sin^2\theta_{13}, \sin^2\theta_{23}, \delta\}$, $\overline{x}_i$ and σ_{x_i} being the best fit values and the 1σ uncertainties [1] taken from [8]. We present in Fig. B.2 the results of a similar two-dimensional analysis for the confidence level regions in the planes shown in Fig. B.1, but using the approximation for χ^2 given in eq. (B.2.2). It follows from these figures that the Gaussian approximation does not allow to reproduce the confidence regions of [8] with sufficiently good accuracy. For this reason in our analysis we use the more accurate procedure defined through eq. (B.2.1). In both the figures the best fit points are indicated with a cross and an asterisk for NO and IO spectra, respectively.

Each symmetry scheme considered in our analysis, which we label with an index m, depends on a set of parameters y^m_j, which are related to the standard oscillation parameters through expressions of the form $x_i = x^m_i(y^m_j)$. In order to produce the 1-dimensional figures we minimise

$$\chi^2\left(x^m_i(y^m_j)\right) = \sum_{i=1}^{4} \chi^2_i\left(x^m_i(y^m_j)\right) \tag{B.2.3}$$

[1] In the case of asymmetric errors we take the mean value of the two errors.

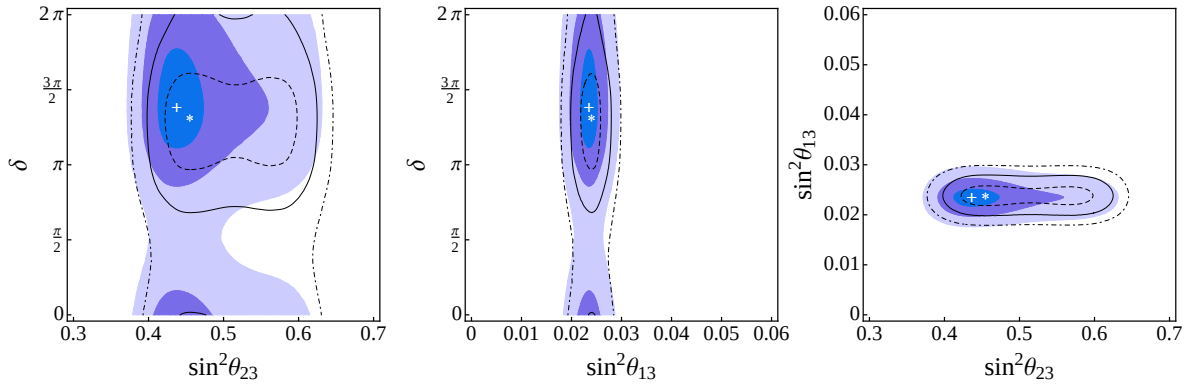

Figure B.1: Confidence regions at 1σ, 2σ and 3σ for 1 degree of freedom in the planes $(\sin^2\theta_{23}, \delta)$, $(\sin^2\theta_{13}, \delta)$ and $(\sin^2\theta_{23}, \sin^2\theta_{13})$ in the blue (dashed lines), purple (solid lines) and light-purple (dash-dotted lines) for NO (IO) neutrino mass spectrum, respectively, obtained using eq. (B.2.1). The best fit points are indicated with a cross (NO) and an asterisk (IO).

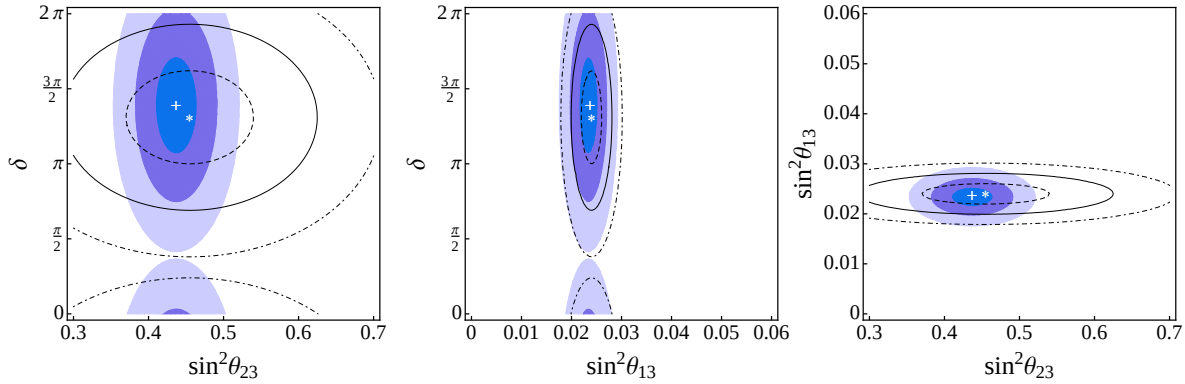

Figure B.2: The same as in Fig. B.1, but using eq. (B.2.2).

for a fixed value of the corresponding observable α, i.e.,

$$\chi^2(\alpha) = \min\left[\chi^2\left(x_i^m(y_j^m)\right)\Big|_{\alpha=\text{const}}\right], \tag{B.2.4}$$

with $\alpha = \{\delta, J_{\rm CP}, \sin^2\theta_{23}\}$. The likelihood function for $\cos\delta$ has been computed by taking

$$L(\cos\delta) \propto \exp\left(-\frac{\chi^2(\cos\delta)}{2}\right), \tag{B.2.5}$$

which was used to produce the likelihood function for the different symmetry forms in Fig. 3.12. It is worth noticing that in the case of flat priors on the mixing parameters, the posterior probability density function reduces to the likelihood function. Although we did not use the Gaussian approximation for obtaining Figs. 3.11, 3.12, 3.15 and B.3, we employed it to obtain Figs. 3.13 and 3.14.

B.3 Results for the Atmospheric Angle

For completeness of the results presented in Chapter 3 in Fig. B.3 we give $N_\sigma \equiv \sqrt{\chi^2}$ as a function of $\sin^2\theta_{23}$. The best fit values and the 3σ regions are summarised in Table B.1.

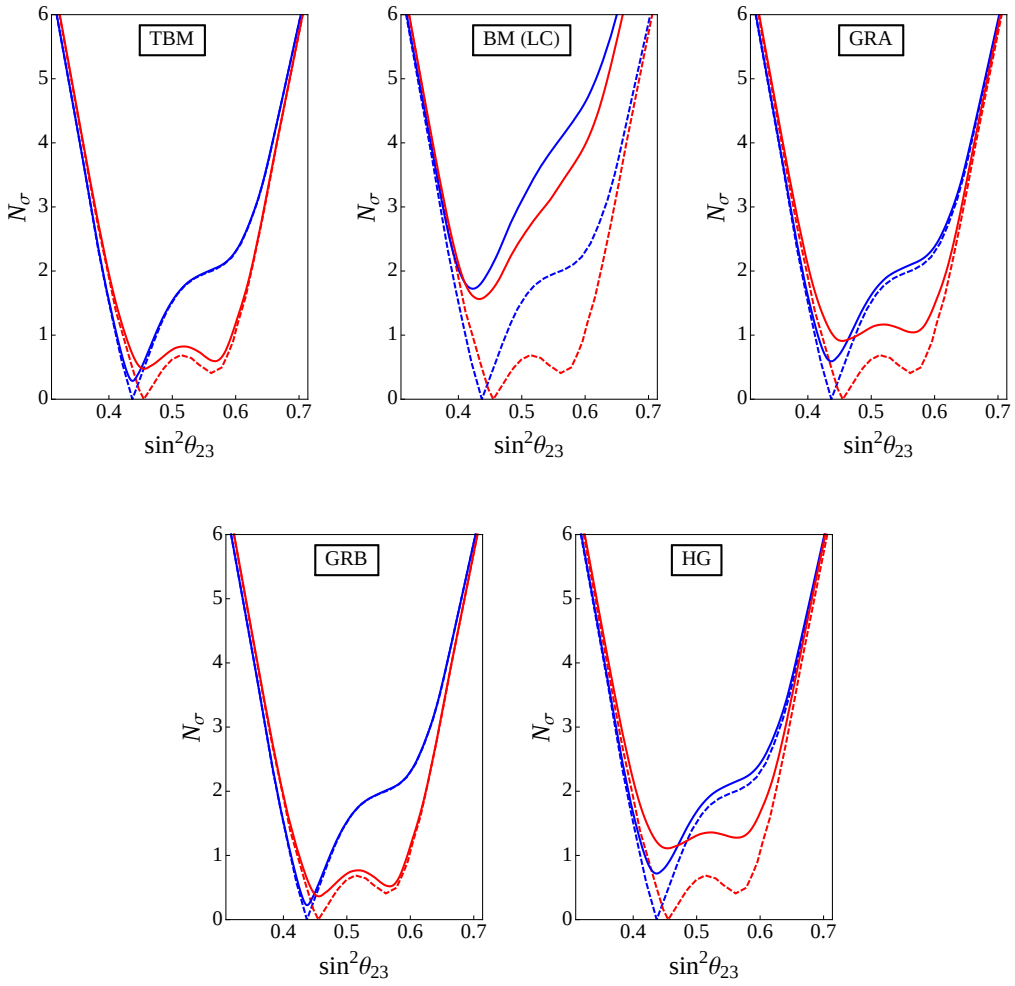

Figure B.3: $N_\sigma \equiv \sqrt{\chi^2}$ as a function of $\sin^2\theta_{23}$. The dashed lines represent the results of the global fit [8], while the solid ones represent the results we obtain for the TBM, BM (LC), GRA (upper left, central, right panels), GRB and HG (lower left and right panels) neutrino mixing symmetry forms. The blue (red) lines are for NO (IO) neutrino mass spectrum.

Symmetry form		Best fit	3σ range
TBM	$\sin^2\theta_{23}$ (NO)	0.44	$0.37 \div 0.63$
	$\sin^2\theta_{23}$ (IO)	0.46	$0.38 \div 0.65$
BM (LC)	$\sin^2\theta_{23}$ (NO)	0.42	$0.37 \div 0.52$
	$\sin^2\theta_{23}$ (IO)	0.42	$0.37 \div 0.56$
GRA	$\sin^2\theta_{23}$ (NO)	0.44	$0.37 \div 0.63$
	$\sin^2\theta_{23}$ (IO)	0.46	$0.38 \div 0.65$
GRB	$\sin^2\theta_{23}$ (NO)	0.44	$0.37 \div 0.63$
	$\sin^2\theta_{23}$ (IO)	0.46	$0.38 \div 0.65$
HG	$\sin^2\theta_{23}$ (NO)	0.44	$0.37 \div 0.63$
	$\sin^2\theta_{23}$ (IO)	0.46	$0.38 \div 0.64$

Table B.1: Best fit values of $\sin^2\theta_{23}$ and corresponding 3σ ranges (found fixing $\sqrt{\chi^2 - \chi^2_{\rm min}} = 3$) in our setup using the data from [8].

APPENDIX C

Neutrino experiment simulations

C.1 Daya Bay and T2K

The Daya Bay experimental setup we take into account [154] consists of six antineutrino detectors (ADs) and six reactors; detailed information on the antineutrino spectra emitted by the nuclear reactors and arriving to the detectors can be found in [155, 156, 167]. For our analysis we used the data set accumulated during 217 days reported in [138], where the detected antineutrino candidates are collected in the far hall, EH3 (far detector), and in the near halls EH1, EH2 (near detectors).

The antineutrino energy $E_{\overline{\nu}_e}$ is reconstructed by the prompt energy deposited by the positron E_{prompt} using the approximated relation [154]: $E_{\overline{\nu}_e} \simeq E_{\text{prompt}} + 0.8$ MeV. We adopt a Gaussian energy resolution function of the form:

$$R^c(E, E') = \frac{1}{\sigma(E)\sqrt{2\pi}} e^{-\frac{(E-E')^2}{2\sigma^2(E)}} \,. \tag{C.1.1}$$

with $\sigma(E)[\text{MeV}] = \alpha \cdot \text{E} + \beta \cdot \sqrt{\text{E}} + \gamma$ that, for Daya Bay, are $(\alpha, \beta, \gamma) = (0, 0, 0.08)$ MeV. The antineutrino cross section for the inverse beta decay (IBD) process has been taken from [157]. The statistical analysis of the data has been performed using the GLoBES software [159, 160] with the χ^2 function defined as [154]:

$$\chi^2_{DB}(\theta, \Delta m^2, \vec{S}, \alpha_r, \varepsilon_d, \eta_d) = \sum_{d=1}^{6} \sum_{i=1}^{36} \frac{\left[M_i^d - T_i^d \cdot \left(1 + \sum_r \omega_r^d \alpha_r + \varepsilon_d\right) + \eta_d\right]^2}{M_i^d + B_i^d}$$
$$+ \sum_r \frac{\alpha_r^2}{\sigma_r^2} + \sum_{d=1}^{6} \left[\frac{\varepsilon_d^2}{\sigma_d^2} + \frac{\eta_d^2}{\sigma_{B_d}^2}\right] + \text{Priors}\,, \tag{C.1.2}$$

where $\vec{S}$ is a vector containing the new physics parameters, M_i^d are the measured IBD events of the d-th detector ADs in the i-th bin, B_i^d the corresponding background and $T_i^d = T_i(\theta, \Delta m^2, \vec{S})$ are the theoretical prediction for the rates. The parameter ω_r^d is the

fraction of IBD contribution of the r-th reactor to the d-th detector AD, determined by the approximated relation $\omega_r^d \sim L_{rd}^{-2}/(\sum_{r=1}^{6} 1/L_{rd}^2)$, where L_{rd} is the distance between the d-th detector and the r-th reactor. The parameter σ_d is the uncorrelated detection uncertainty ($\sigma_d = 0.2\%$) and σ_{B_d} is the background uncertainty of the d-th detector obtained using the information given in [138]: $\sigma_{B_1} = \sigma_{B_2} = 8.21$, $\sigma_{B_3} = 5.95$, $\sigma_{B_4} = \sigma_{B_5} = \sigma_{B_6} = 1.15$ and $\sigma_r = 0.8\%$ are the uncorrelated reactor uncertainties. The corresponding pull parameters are $(\varepsilon_d, \eta_d, \alpha_r)$. With this choice of nuisance parameters we are able to reproduce the 1σ, 2σ and 3σ confidence level results presented in Fig. 3 of Ref. [138] with high accuracy. The differences are at the level of few percent (see Tab. I and Tab. II of Ref. [72]).

The T2K experiment [137] consists of two separate detectors, both of which are 2.5 degrees off axis of the neutrino beam. The far detector is located at $L_F = 295$ km from the source, the ND280 near detector is $L_N = 280$ metres from the target.

In our analysis we used the public data in [137, 168]. The neutrino flux has been estimated following [169]. We fixed the fiducial mass of the near and the far detector respectively as $FM_{\rm ND280} = 1529$ Kg and $FM_{\rm SK} = 22.5$ Kton [170]; a bin to bin normalization has been fixed in order to reproduce the T2K best fit events. For the energy resolution function we adopt the same Gaussian form of Eq. (C.1.1) with $(\alpha, \beta, \gamma) = (0, 0, 0.085)$ GeV.

The χ^2_{T2K} is defined as:

$$\chi^2_{T2K}(\theta, \Delta m^2, \vec{S}, \rho, \Omega_d, \alpha_d) = \sum_{d=1}^{2} \sum_{i=1}^{n_{bins}^d} 2 \left[M_i^d - T_i^d \cdot (1 + \rho + \Omega_d) + M_i^d \log \frac{M_i^d}{T_i^d \cdot (1 + \rho + \Omega_d)} \right] + \frac{\rho^2}{\sigma_\rho^2} + \sum_{d=1}^{2} \frac{\Omega_d^2}{\sigma_{\Omega_d}^2} + \text{Priors}\,. \tag{C.1.3}$$

In the previous formula, $\vec{S}$ is a vector containing the new physics parameters, M_i^d are the measured events, including the backgrounds (extracted from Fig. 4 of [137]), of the d-th detector in the i-th bin, $T_i^d = T_i^d(\theta, \Delta m^2, \vec{S}, \alpha_d)$ are the theoretical predictions for the rates, θ and Δm^2 are respectively the mixing angles and the squared mass differences contained in the oscillation probability, n_{bins}^d is the number of bins for the d-th detector. The parameter σ_ρ contains the flux, the uncorrelated ν interaction and the final-state interactions uncertainties ($\sigma_\rho = 8.8\%$ Tab. II of [137]), σ_{Ω_d} the fiducial mass uncertainty for the d-th detector (σ_{Ω_d} has been estimated to be $\sigma_{\Omega_d} = 1\%$ for the far and the near detectors similarly to [158]), α_d are free parameters which represent the energy scale for predicted signal events with uncertainty σ_{α_d}, ($\sigma_{\alpha_d} = 1\%$ [171]).

The corresponding pull parameters are $(\rho, \Omega_d, \alpha_d)$. The measured event rates at the near detector have been estimated rescaling the non oscillated measured event rates at the far detector using the scale factor $L_F^2/L_N^2 \times FM_{\rm ND280}/FM_{\rm SK}$. Our definition of the χ^2 allows to reproduce with high accuracy the 68% and 90% confidence level regions for $\sin^2 2\theta_{13}$ as a function of the CP violation phase δ shown in Fig. 5 of Ref. [137].

We analysed the whole Daya Bay and T2K data sample using $\chi^2_{tot} = \chi^2_{DB} + \chi^2_{T2K}$. We considered two different statistical analysis: i) we fixed all the standard oscillation

parameters, ii) we fixed all the standard oscillation parameters except θ_{13} on which we imposed a gaussian prior defined through the mean value and the 1σ error $\sin^2 2\theta_{13} = 0.140 \pm 0.038$, $\sin^2 2\theta_{13} = 0.170 \pm 0.045$ and $\sin^2 2\theta_{13} = 0.090 \pm 0.009$, for the different cases we have analyzed.

APPENDIX D

Effective Majorana Mass

D.1 The Extrema of $|\langle m \rangle|$ in the 3+1 Scheme with NO or IO Neutrino Mass Spectrum

We are interested in the minima and the maxima of $|\langle m \rangle|$. It turns out to be somewhat simpler to study the extrema of $|\langle m \rangle|^2$ which obviously coincide with those of $|\langle m \rangle|$. The expression for $|\langle m \rangle|^2$ in both the cases of NO and IO spectra can be written as:

$$|\langle m \rangle|^2 = |a + e^{i\alpha} b + e^{i\beta} c + e^{i\gamma} d|^2. \tag{D.1.1}$$

The zeros of the first derivatives of $|\langle m \rangle|^2$ with respect to the phases α, β and γ are given by the following system of three equations:

$$\begin{aligned} -2b[a\sin(\alpha) + c\sin(\alpha - \beta) + d\sin(\alpha - \gamma)] &= 0, \\ -2c[a\sin(\beta) - b\sin(\alpha - \beta) + d\sin(\beta - \gamma)] &= 0, \\ 2d[-a\sin(\gamma) + b\sin(\alpha - \gamma) + c\sin(\beta - \gamma)] &= 0. \end{aligned} \tag{D.1.2}$$

In order to solve this system we use the following parametrization:

$$\begin{aligned} \sin\alpha &= \frac{2v}{1+v^2}, & \cos\alpha &= \frac{1-v^2}{1+v^2}, \\ \sin\beta &= \frac{2t}{1+t^2}, & \cos\beta &= \frac{1-t^2}{1+t^2}, \\ \sin\gamma &= \frac{2u}{1+u^2}, & \cos\gamma &= \frac{1-u^2}{1+u^2}. \end{aligned} \tag{D.1.3}$$

where, respectively, $v \equiv \tan(\alpha/2)$, $t \equiv \tan(\beta/2)$, $u \equiv \tan(\gamma/2)$ with $\alpha,\, \beta,\, \gamma \neq \pi + 2k\pi$. In terms of the new variables the system in eq.(D.1.2) can be written as:

$$\begin{aligned}
&-\frac{2b}{1+v^2}\left[2av - \frac{2ct\,(1-v^2)}{t^2+1} + \frac{2c\,(1-t^2)\,v}{t^2+1} - \frac{2du\,(1-v^2)}{u^2+1} + \frac{2d\,(1-u^2)\,v}{u^2+1}\right] = 0,\\
&-\frac{2c}{1+t^2}\left[2at - \frac{2b\,(1-t^2)\,v}{v^2+1} + \frac{2bt\,(1-v^2)}{v^2+1} - \frac{2d\,(1-t^2)\,u}{u^2+1} + \frac{2dt\,(1-u^2)}{u^2+1}\right] = 0,\\
&\frac{2d}{1+u^2}\left[-2au + \frac{2b\,(1-u^2)\,v}{v^2+1} - \frac{2bu\,(1-v^2)}{v^2+1} + \frac{2ct\,(1-u^2)}{t^2+1} - \frac{2c\,(1-t^2)\,u}{t^2+1}\right] = 0.
\end{aligned} \tag{D.1.4}$$

The new coordinates u, v and t are singular if at least one angle α, β, γ is equal to π. We observe that seven solutions of the system in eq. (D.1.2) are given for one of the three phases equal to π, i.e., for u or v or t going to ∞:

$$\begin{aligned}
&\alpha = \beta = \pi(0) \quad \text{and} \quad \gamma = 0(\pi),\\
&\alpha = \gamma = \pi(0) \quad \text{and} \quad \beta = 0(\pi),\\
&\gamma = \beta = \pi(0) \quad \text{and} \quad \alpha = 0(\pi),\\
&\alpha = \beta = \gamma = \pi\ .
\end{aligned} \tag{D.1.5}$$

We can recover this type of solutions as a limit of the system in eq. (D.1.4) when a pair of variables u, v, t are equal. For example, in the limit in which $t = v = 0$, the system in eq. (D.1.4) is reduced to

$$\begin{cases}
(4bd)\dfrac{u}{u^2+1} = 0,\\
(4cd)\dfrac{u}{u^2+1} = 0,\\
[4d(a+b+c)]\dfrac{u}{u^2+1} = 0\,.
\end{cases} \tag{D.1.6}$$

Evidently, we have a solution in the limit $u \to \infty$. This is equivalent to say that the solutions under discussion can be found as a limit of the system (D.1.4) when the variables u, t, and v are sent to ∞.

The solutions of the system in eq. (D.1.4), assuming $\alpha, \beta, \gamma \neq \pi$ and $b, c, d \neq 0$, are the zeros of the following system of equations:

$$\begin{cases}
2av - \dfrac{2ct\,(1-v^2)}{t^2+1} + \dfrac{2c\,(1-t^2)\,v}{t^2+1} - \dfrac{2du\,(1-v^2)}{u^2+1} + \dfrac{2d\,(1-u^2)\,v}{u^2+1} = 0,\\
2at - \dfrac{2b\,(1-t^2)\,v}{v^2+1} + \dfrac{2bt\,(1-v^2)}{v^2+1} - \dfrac{2d\,(1-t^2)\,u}{u^2+1} + \dfrac{2dt\,(1-u^2)}{u^2+1} = 0,\\
-2au + \dfrac{2b\,(1-u^2)\,v}{v^2+1} - \dfrac{2bu\,(1-v^2)}{v^2+1} + \dfrac{2ct\,(1-u^2)}{t^2+1} - \dfrac{2c\,(1-t^2)\,u}{t^2+1} = 0.
\end{cases} \tag{D.1.7}$$

The solutions of this system are nine: (u_1, v_1, t_1), $(u_\pm, v_\pm, t_\pm)$, $(u_i^\pm, v_i^\pm, t_i^\pm)$ with $i = 2, 3$ and $(v_4^\pm(u), t_4^\pm(u))$. We found $(u_1, v_1, t_1) = (0, 0, 0)$ and

$$\begin{cases} u_\pm &= \pm\sqrt{\dfrac{(-a+b+c-d)(a+b-c+d)}{(a-b-c-d)(a+b-c-d)}}, \\ v_\pm &= \pm\dfrac{(b+c)}{(b-c)}\dfrac{[(a+b-c)^2-d^2]}{\sqrt{(-a+b+c-d)(a+b-c+d)(a-d-c-b)(a-d-c+b)}}, \\ t_\pm &= \pm\dfrac{a^2+b^2-c^2-d^2}{\sqrt{(a-b-c-d)(a+b-c-d)(-a+b+c-d)(a+b-c+d)}}, \end{cases}$$

$$\begin{cases} u_2^\pm &= 0, \\ v_2^\pm &= \pm\sqrt{\dfrac{(-a-b+c-d)(a+b+c+d)}{(a-b-c+d)(a-b+c+d)}}, \\ t_2^\pm &= \pm\dfrac{(a-b+c+d)(a+b+c+d)}{\sqrt{(a-b-c+d)(a-b+c+d)(-a-b+c-d)(a+b+c+d)}}, \end{cases}$$

$$\begin{cases} u_3^\pm &= \pm\sqrt{\dfrac{(-a+b+c-d)(a-b+c+d)}{(a-b-c-d)(a-b+c-d)}}, \\ v_3^\pm &= \pm\dfrac{a^2-b^2+c^2-d^2}{\sqrt{(a-b-c-d)(a-b+c-d)(-a+b+c-d)(a-b+c+d)}}, \\ t_3^\pm &= \pm\dfrac{(b+c)(-a+b-c+d)}{(b-c)(-a+b+c-d)}\sqrt{\dfrac{(-a+b+c-d)(a-b+c+d)}{(a-b-c-d)(a-b+c-d)}}, \end{cases}$$

$$\begin{cases} v_4^\pm(u) &= \dfrac{4bdu \pm F(a,b,c,d,u)}{-u^2(a-b-c-d)(a-b+c-d)-(a-b+d)^2+c^2}, \\ t_4^\pm(u) &= \dfrac{-4cdu \pm F(a,b,c,d,u)}{u^2(a-b-c-d)(a+b-c-d)+(a-c+d)^2-b^2}, \end{cases} \tag{D.1.8}$$

where

$$F(a,b,c,d,u) = \Big\{\Big[-u^2(a+b-c-d)(a-b+c-d)-(a+d)^2+(b-c)^2\Big]\times \\ \times\Big[a^2\left(u^2+1\right)-2ad\left(u^2-1\right)-\left(u^2+1\right)(b+c-d)(b+c+d)\Big]\Big\}^{1/2}.$$

We observe that in the NH case, the limit $m_1 \to 0$ corresponds to setting $a \to 0$ in eqs. (D.1.4), while the limit $m_3 \to 0$ in the IH case corresponds to $c \to 0$. We define the constants a, b, c, d in these limits respectively as b_0, c_0, d_0 and a_0, b_0, d_0. Moreover,

we observe that $|\langle m\rangle|$evaluated at the solutions $(u_i^{\pm}, v_i^{\pm}, t_i^{\pm})$ with $i = 2, 3$, $(v_4^{\pm}, t_4^{\pm})$ and $(u_{\pm}, v_{\pm}, t_{\pm})$ is exactly zero.

In the subsection 6.2 we discuss, in particular, the limiting case of $m_3 \to 0$. Therefore it is useful to show the solutions $(u_{\pm}, v_{\pm}, t_{\pm})$ in terms of $\sin\gamma_+ = -\sin\gamma_-$, $\sin\alpha_+ = -\sin\alpha_-$, $\sin\beta_+ = -\sin\beta_-$, so we can write:

$$\sin\gamma_- = \frac{\sqrt{-[(a-d-c)^2-b^2][(a+d-c)^2-b^2]}}{2(a-c)d}\,,$$

$$\sin\alpha_- = \frac{(b-c)(b+c)(a+b-c-d)\sqrt{(-a+b+c-d)(a+b-c+d)}(-a+b+c+d)}{2\left(ab\left(c(a-c)+b^2\right)-bcd^2\right)\sqrt{(-a+c+d)^2-b^2}}\,,$$

$$\sin\beta_- = \frac{\sqrt{(a-b-c-d)(a+b-c-d)}\sqrt{(-a+b+c-d)(a+b-c+d)}\,(-a^2-b^2+c^2+d^2)}{2(a-c)\left[a\left(c(a-c)+b^2\right)-cd^2\right]}\,.$$

Next, in order to study the domains of existence of the solutions given in eq. (D.1.8), which depend on the parameters a b, c and d, we need to define the following functions:

$$\begin{aligned} f_1 &= a-b-c-d\,, & f_2 &= a+b-c-d\,,\\ f_3 &= a+b-c+d\,, & f_4 &= -a+b+c-d\,,\\ f_5 &= a+b+c+d\,, & f_6 &= a-b+c+d\,,\\ f_7 &= a-b+c-d\,, & f_8 &= a+b+c-d\,. \end{aligned} \tag{D.1.9}$$

We notice that the conditions of existence for the solutions $(u_{\pm}, v_{\pm}, t_{\pm})$, $(u_2^{\pm}, v_2^{\pm}, t_2^{\pm})$ and $(u_3^{\pm}, v_3^{\pm}, t_3^{\pm})$ are respectively $f_3f_4f_5f_6 > 0$, $f_1f_4f_6f_7 > 0$ and $f_1f_2f_3f_4 > 0$. We discuss the domains of the other solutions in Appendix D.2 using numerical methods.

Finally, we would like to comment on the solutions $(v_4^{\pm}, t_4^{\pm})$ because, as can be seen from their explicit expressions, they depend on a free variable, u. Thus, we would like to provide some details about the study of the domain of such solutions. Defining $k = u^2$ and $F(a,b,c,d,k) = \sqrt{f(k)}$ we find that the function $f(k)$ is a parabola of the form:

$$f(k) = Ak^2 + Bk + C\,, \tag{D.1.10}$$

with coefficient of the term of maximum degree equal to

$$A = (a+b-c-d)(a-b+c-d)(a+b+c-d)(-a+b+c+d)\,, \tag{D.1.11}$$

and discriminant $\Delta = B^2 - 4AC = 256\,a^2b^2c^2d^2$. The discriminant Δ is always positive or equal to zero. The zeros of the function $f(k)$, namely k_1 and k_2, are given by:

$$\begin{aligned} \tilde{k}_1 &= \frac{(a-b-c+d)(a+b+c+d)}{(a+b+c-d)(-a+b+c+d)}\,,\\ \tilde{k}_2 &= -\frac{(a+b-c+d)(a-b+c+d)}{(a+b-c-d)(a-b+c-d)}\,. \end{aligned} \tag{D.1.12}$$

Depending on the values of the parameters a, b, c and d one can find a range of m_{min} for which this solution is well defined. We will discuss this in the next section D.2.

The method described above cannot be used to determine the physical domain of the minimization solutions found by us in the case in which at least one of the phases α, β, γ is equal to π (eq. (D.1.5)). In order to study these cases we use the Hessian matrix of $|\langle m \rangle|^2$, $H(\alpha, \beta, \gamma)$. The determinant of the Hessian, evaluated for the phases either 0 or π and assuming $a, b, c, d > 0$, can be positive only for $(\alpha, \beta, \gamma) = (\pi, 0, 0), (0, \pi, 0), (0, 0, \pi), (\pi, \pi, \pi)$. Therefore the local minima and maxima can correspond only to these configurations. We derive the relations among the coefficients a, b, c, d in order to have a minimum using the Sylvester's criterion. We assume that a, b, c, d are real and positive, $a, b, c, d > 0$.
We have a minima at

$$\begin{aligned}
&(\alpha, \beta, \gamma) = (\pi, \pi, \pi) \quad if \quad f_1 = a - b - c - d > 0; \\
&(\alpha, \beta, \gamma) = (0, 0, \pi) \quad if \quad (c < d) \wedge (b < d - c) \wedge (f_8 = a + b + c - d < 0); \\
&(\alpha, \beta, \gamma) = (0, \pi, 0) \quad if \quad (c > d) \wedge (b < c - d) \wedge (-f_3 = -a - b + c - d > 0); \\
&(\alpha, \beta, \gamma) = (\pi, 0, 0) \quad if \quad (b > c + d) \wedge (-f_6 = -a + b - c - d > 0).
\end{aligned} \tag{D.1.13}$$

D.2 Domains of the solutions

In this part we describe the domains of the solutions given in eq. (D.1.8). We will give the numerical intervals of values of m_{min} in which the minimization solutions are well defined for $\Delta m^2_{41(43)} = 0.93$ eV^2 and 1.78 eV^2 and using the best fit values reported in Table 1.1. In Tables D.1 and D.2 we present the results of this numerical analysis in the cases of NO and IO spectra, respectively.

D.3 Extrema of $|\langle m \rangle|$ in the 3+2 Scheme

As in the case of the 3+1 scheme, it proves somewhat easier to study the extrema of $|\langle m \rangle|^2$ than of $|\langle m \rangle|$. The expression for $|\langle m \rangle|^2$ for both NO and IO spectra has the form:

$$|\langle m \rangle|^2 = |a + e^{i\alpha} b + e^{i\beta} c + e^{i\gamma} d + e^{i\eta} e|^2. \tag{D.3.1}$$

Equating to zero the first derivatives of $|\langle m \rangle|^2$ with respect to the four phases we get the following system of four equations:

$$\begin{aligned}
a \sin(\alpha) + c \sin(\alpha - \beta) + d \sin(\alpha - \gamma) + e \sin(\alpha - \eta) = 0, \\
a \sin(\beta) - b \sin(\alpha - \beta) + d \sin(\beta - \gamma) + e \sin(\beta - \eta) = 0, \\
-a \sin(\gamma) + b \sin(\alpha - \gamma) + c \sin(\beta - \gamma) - e \sin(\gamma - \eta) = 0, \\
-a \sin(\eta) + b \sin(\alpha - \eta) + c \sin(\beta - \eta) + d \sin(\gamma - \eta) = 0.
\end{aligned} \tag{D.3.2}$$

Solution	Domain of existence in terms of m_{min}
$(u^{\pm}, v^{\pm}, t^{\pm})$	$2.363 \times 10^{-2}\,\text{eV} < m_1 < 6.473 \times 10^{-2}\,\text{eV}$ $(3.337 \times 10^{-2}\,\text{eV} < m_1 < 9.061 \times 10^{-2}\,\text{eV})$
$(u_2^{\pm}, v_2^{\pm}, t_2^{\pm})$	None (None)
$(u_3^{\pm}, v_3^{\pm}, t_3^{\pm})$	$5.485 \times 10^{-2}\,\text{eV} < m_1 < 6.473 \times 10^{-2}\,\text{eV}$ $(7.811 \times 10^{-2}\,\text{eV} < m_1 < 9.061 \times 10^{-2}\,\text{eV})$
$(v_4^{\pm}, t_4^{\pm})$ for $A > 0$	$2.090 \times 10^{-2}\,\text{eV} < m_1 < 2.363 \times 10^{-2}\,\text{eV} \vee$ $\vee\ 5.485 \times 10^{-2}\,\text{eV} < m_1 < 6.473 \times 10^{-2}\,\text{eV}$
	$\Big(3.043 \times 10^{-2}\,\text{eV} < m_1 < 3.337 \times 10^{-2}\,\text{eV} \vee$ $\vee\ 7.811 \times 10^{-2}\,\text{eV} < m_1 < 9.061 \times 10^{-2}\,\text{eV}\Big)$
$(v_4^{\pm}, t_4^{\pm})$ for $A < 0$	$2.363 \times 10^{-2}\,\text{eV} < m_1 < 5.485 \times 10^{-2}\,\text{eV}$ $(3.337 \times 10^{-2}\,\text{eV} < m_1 < 7.811 \times 10^{-2}\,\text{eV})$

Table D.1: Numerical results for the domains of existence of the solutions given in eq. (D.1.8) in the 3+1 NO case for $\Delta m^2_{41} = 0.93\,\text{eV}^2$ ($\Delta m^2_{41} = 1.78\,\text{eV}^2$). The expression of A is given in eq. (D.1.11).

The analytical study of the minima of $|\langle m \rangle|^2$ in this case is a non-trivial task since four phases are involved and the non-linearity of the system of the first derivatives of $|\langle m \rangle|^2$ with respect to the four phases makes the analysis rather complicated. Therefore finding all possible solutions of the minimization procedure in analytical form is a complicated problem. Thus, we have performed the general analysis of the minimization of $|\langle m \rangle|$numerically. This allowed to determine the intervals of values of m_{min} in which the minimal value of $|\langle m \rangle|$is exactly zero. It is possible, however, to perform analytically the analysis of the minima of $|\langle m \rangle|$, corresponding to the 16 sets of CP conserving values (either 0 or π) of the four phases α, β, γ and η. This can be done by using the Sylvester's criterion for the Hessian, evaluated for the indicated values of the phases $0, \pi$, which determines the physical domain of the minimization solutions. The minima thus found, as we show, correspond to $|\langle m \rangle| \neq 0$.

Assuming $a, b, c, d, e > 0$ and $a, b, c, d, e \in \mathbb{R}$ and using the Sylvester's criterion we find

Solution	Domain of existence in terms of m_{min}
$(u^{\pm}, v^{\pm}, t^{\pm})$	$0\,\text{eV} < m_3 < 3.855 \cdot 10^{-2}\,\text{eV}$ $(0\,\text{eV} < m_3 < 7.437 \times 10^{-2}\,\text{eV})$
$(u_2^{\pm}, v_2^{\pm}, t_2^{\pm})$	None (None)
$(u_3^{\pm}, v_3^{\pm}, t_3^{\pm})$	$3.084 \times 10^{-2}\,\text{eV} < m_3 < 3.855 \times 10^{-2}\,\text{eV}$ $(6.344 \times 10^{-2}\,\text{eV} < m_3 < 7.437 \times 10^{-2}\,\text{eV})$
$(v_4^{\pm}, t_4^{\pm})$ for $A > 0$	$3.084 \times 10^{-2}\,\text{eV} < m_3 < 3.855 \times 10^{-2}\,\text{eV}$ $(6.344 \times 10^{-2}\,\text{eV} < m_3 < 7.437 \times 10^{-2}\,\text{eV})$
$(v_4^{\pm}, t_4^{\pm})$ for $A < 0$	$0\,\text{eV} < m_3 < 3.084 \times 10^{-2}\,\text{eV}$ $(0\,\text{eV} < m_3 < 6.344 \times 10^{-2}\,\text{eV})$

Table D.2: The same as in Table D.1 but for the case of the 3+1 IO scheme.

that the minima of $|\langle m \rangle|$take place at

$$
\begin{aligned}
&(\alpha,\beta,\gamma,\eta) = (\pi,\pi,\pi,\pi) \quad if \quad F_1 = a - b - c - d - e > 0, \\
&(\alpha,\beta,\gamma,\eta) = (0,0,0,\pi) \quad if \quad (d < e) \wedge (c < e - d) \wedge (b < -c - d + e) \wedge \\
&\qquad\qquad\qquad\qquad \wedge (F_8 = a + b + c + d - e < 0), \\
&(\alpha,\beta,\gamma,\eta) = (0,0,\pi,0) \quad if \quad (d > e) \wedge (c < d - e) \wedge (b < -c + d - e) \wedge \\
&\qquad\qquad\qquad\qquad \wedge (F_3 = a + b + c - d + e < 0), \\
&(\alpha,\beta,\gamma,\eta) = (0,\pi,0,0) \quad if \quad (c > d + e) \wedge (b < c - d - e) \wedge \\
&\qquad\qquad\qquad\qquad \wedge (G_3 = a + b - c + d + e < 0), \\
&(\alpha,\beta,\gamma,\eta) = (\pi,0,0,0) \quad if \quad (b > c + d + e) \wedge (F_6 = a - b + c + d + e < 0)\,.
\end{aligned}
\tag{D.3.3}
$$

At the other CP conserving values of the phases, $(\alpha,\beta,\gamma,\eta) = (0,0,0,0)$, $(\pi,\pi,0,0)$, $(\pi,0,\pi,0)$, $(\pi,0,0,\pi)$, $(0,\pi,\pi,0)$, $(0,\pi,0,\pi)$, $(0,0,\pi,\pi)$, $(\pi,\pi,\pi,0)$, $(\pi,\pi,0,\pi)$, $(\pi,0,\pi,\pi)$ and $(0,\pi,\pi,\pi)$, $|\langle m \rangle|$cannot reach a minimum. In Fig. D.1 we show the dependence of the functions F_1, F_8, F_3, G_3 and F_6 on $m_{min} \equiv m_3$ for the best fit values of the neutrinos oscillation parameters given in Tables 1 and 3.

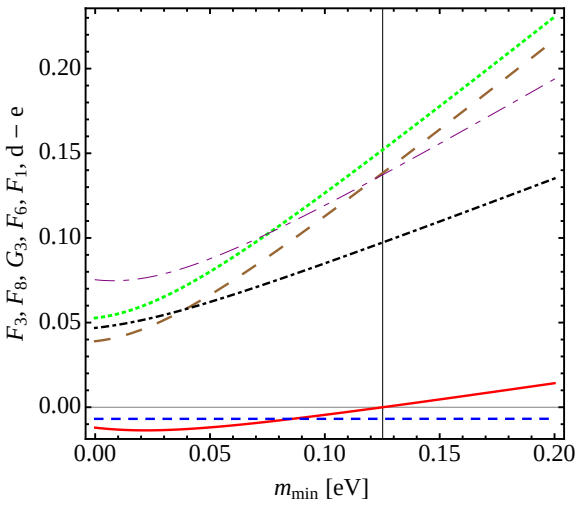

Figure D.1: The functions F_3 (dotted green line), F_8 (long-dashed brown line), G_3 (short-long-dashed purple line), F_6 (dot-dashed black line), F_1 (solid red line), $d-e$ (short-dashed blue line), defined in eq. (5.5.6), versus $m_{min} \equiv m_3$ for the oscillation parameter values reported in Table 5.2. The vertical black line corresponds to $m_{min} = \overline{m}_3 \simeq 1.25 \times 10^{-1}$ eV.

Aknowledgements

I am grateful to so many people that it is hard to thank all of them here. First of all, I would like to thank S. T. Petcov as supervisor and mentor during this years and for motivating me so many times "Su forza!" for doing better and better and more importantly for supporting me. I thank all my collaborators A. Meroni, M. Spinrath, D. Meloni, A. V. Titov, T. Ohlsson, H. Zhang, S. Zhou, A. G. Di Iura, A. J. Stuart for the fruitful works we made together.

I thank my family and my friends which guided and supported me during these years. I thank all the colleagues and friends whereby I have shared the great experience of being a Ph.D. student at SISSA: M. Valli, G. Grilli, B. L. De Souza, A. Belenchia, P. Baratella. A very special thanks to C. De Nobili as a friend, office mate, first pilot in the flight experiences, to A. V. Titov as a friend, Russian office mate (спасибо) and scientific collaborator, to A. Meroni as a friend and for suggesting me to work in neutrino physics. A very special thank to my friends A. Patacca and P. Sgobba I have been in touch with Google Hangouts.

I thank my flat mates during these years A. Pedron, F. Iseppon, L. Soltuzu and especially S. Bertola and the vis-à-vis Valeria, Amelia, Franz. I thank the "Lupus in tabula" gang Giulia, Jasmin, Martina, Linda and also Guglielmo & Aurora, Matteo & Lucia, Nicola & Cristina among the first people I met in Trieste.

Thank you.

Bibliography

[1] K. Nakamura and S. T. Petcov, *"Neutrino Masses, Mixing and Oscillations"*, in K. A. Olive *et al.* (Particle Data Group), Chin. Phys. C **38** (2014) 090001.

[2] S. M. Bilenky, J. Hosek and S. T. Petcov, *"On Oscillations of Neutrinos with Dirac and Majorana Masses"*, Phys. Lett. B **94** (1980) 495.

[3] E. Molinaro and S. T. Petcov, *"The Interplay Between the "Low" and "High" Energy CP-Violation in Leptogenesis"*, Eur. Phys. J. C **61** (2009) 93 [arXiv:0803.4120].

[4] A. Ibarra, E. Molinaro and S. T. Petcov, *"Low Energy Signatures of the TeV Scale See-Saw Mechanism"*, Phys. Rev. D **84** (2011) 013005 [arXiv:1103.6217].

[5] L. Wolfenstein, *"CP Properties of Majorana Neutrinos and Double Beta Decay"*, Phys. Lett. B **107** (1981) 77; S. M. Bilenky, N. P. Nedelcheva and S. T. Petcov, *"Some Implications of the CP Invariance for Mixing of Majorana Neutrinos"*, Nucl. Phys. B **247** (1984) 61; B. Kayser, *"CPT, CP, and C Phases and their Effects in Majorana Particle Processes"*, Phys. Rev. D **30** (1984) 1023.

[6] G. L. Fogli, E. Lisi, A. Marrone, D. Montanino, A. Palazzo and A. M. Rotunno, *"Global analysis of neutrino masses, mixings and phases: entering the era of leptonic CP violation searches"*, Phys. Rev. D **86** (2012) 013012 [arXiv:1205.5254].

[7] M. C. Gonzalez-Garcia, M. Maltoni, J. Salvado and T. Schwetz, *"Global fit to three neutrino mixing: critical look at present precision"*, JHEP **1212** (2012) 123 [arXiv:1209.3023].

[8] F. Capozzi, G. L. Fogli, E. Lisi, A. Marrone, D. Montanino and A. Palazzo, *"Status of three-neutrino oscillation parameters, circa 2013"*, Phys. Rev. D **89** (2014) 093018 [arXiv:1312.2878].

[9] M. C. Gonzalez-Garcia, M. Maltoni and T. Schwetz, *"Updated fit to three neutrino mixing: status of leptonic CP violation"*, JHEP **1411** (2014) 052 [arXiv:1409.5439].

[10] N. Cabibbo, *"Time Reversal Violation in Neutrino Oscillation"*, Phys. Lett. B **72** (1978) 333.

[11] P.I. Krastev and S. T. Petcov, *"Resonance Amplification and T-Violation Effects in Three Neutrino Oscillations in the Earth"*, Phys. Lett. B **205** (1988) 84.

[12] F. Capozzi, E. Lisi, A. Marrone, D. Montanino and A. Palazzo, *"Neutrino masses and mixings: Status of known and unknown 3ν parameters"*, Nucl. Phys. B **908** (2016) 218 [arXiv:1601.07777].

[13] R. Acciarri *et al.* [DUNE Collaboration], *"Long-Baseline Neutrino Facility (LBNF) and Deep Underground Neutrino Experiment (DUNE) Conceptual Design Report Volume 1: The LBNF and DUNE Projects"*, arXiv:1601.05471.

[14] R. Acciarri *et al.* [DUNE Collaboration], *"Long-Baseline Neutrino Facility (LBNF) and Deep Underground Neutrino Experiment (DUNE) Conceptual Design Report Volume 4: The DUNE Detectors at LBNF"*, arXiv:1601.02984.

[15] K. Abe *et al.* [Hyper-Kamiokande Proto- Collaboration], *"Physics potential of a long-baseline neutrino oscillation experiment using a J-PARC neutrino beam and Hyper-Kamiokande"*, PTEP **2015** (2015) 053C02 [arXiv:1502.05199].

[16] P. Langacker, S. T. Petcov, G. Steigman and S. Toshev, *"On the Mikheev-Smirnov-Wolfenstein (MSW) Mechanism of Amplification of Neutrino Oscillations in Matter"*, Nucl. Phys. B **282** (1987) 589.

[17] S. M. Bilenky and S. T. Petcov, *"Massive Neutrinos and Neutrino Oscillations"*, Rev. Mod. Phys. **59** (1987) 671, Erratum: [Rev. Mod. Phys. **61** (1989) 169], Erratum: [Rev. Mod. Phys. **60** (1988) 575].

[18] S. M. Bilenky, S. Pascoli and S. T. Petcov, *"Majorana neutrinos, neutrino mass spectrum, CP violation and neutrinoless double beta decay. 1. The Three neutrino mixing case"*, Phys. Rev. D **64** (2001) 053010 [arXiv:hep-ph/0102265]; S. T. Petcov, *"Theoretical prospects of neutrinoless double beta decay"*, Phys. Scripta T **121** (2005) 94 [arXiv:hep-ph/0504166].

[19] W. Rodejohann, *"Neutrinoless Double Beta Decay in Particle Physics"*, Int. J. Mod. Phys. E **20** (2011) 1833 [arXiv:1106.1334]; J. D. Vergados, H. Ejiri and F. Simkovic, *"Theory of Neutrinoless Double Beta Decay"*, Rept. Prog. Phys. **75** (2012) 106301 [arXiv:1205.0649].

[20] S. Dell'Oro, S. Marcocci, M. Viel and F. Vissani, *"Neutrinoless double beta decay: 2015 review"*, Advances in High Energy Physics, Volume 2016 (2016), Article ID 2162659 [arXiv:1601.07512].

[21] S. T. Petcov, *"The Nature of Massive Neutrinos"*, Adv. High Energy Phys. **2013** (2013) 852987 [arXiv:1303.5819].

[22] S. Pascoli, S. T. Petcov and A. Riotto, *"Connecting low energy leptonic CP-violation to leptogenesis"*, Phys. Rev. D **75** (2007) 083511 [arXiv:hep-ph/0609125].

[23] S. Pascoli, S. T. Petcov and A. Riotto, *"Leptogenesis and Low Energy CP Violation in Neutrino Physics"*, Nucl. Phys. B **774** (2007) 1 [arXiv:hep-ph/0611338].

[24] C. Weinheimer, B. Degen, A. Bleile, J. Bonn, L. Bornschein, O. Kazachenko, A. Kovalik and E. W. Otten, *"High precision measurement of the tritium beta spectrum near its endpoint and upper limit on the neutrino mass"*, Phys. Lett. B **460** (1999) 219.

[25] C. Kraus *et al.*, *"Final results from phase II of the Mainz neutrino mass search in tritium beta decay"*, Eur. Phys. J. C **40** (2005) 447 [arXiv:hep-ex/0412056].

[26] A. I. Belesev *et al.*, *"Results of the Troitsk experiment on the search for the electron anti-neutrino rest mass in tritium beta decay"*, Phys. Lett. B **350** (1995) 263.

[27] V. M. Lobashev *et al.*, *"Direct search for mass of neutrino and anomaly in the tritium beta spectrum"*, Phys. Lett. B **460** (1999) 227.

[28] V. N. Aseev *et al.* [Troitsk Collaboration], *"An upper limit on electron antineutrino mass from Troitsk experiment"*, Phys. Rev. D **84** (2011) 112003 [arXiv:1108.5034].

[29] K. Eitel, *"Direct neutrino mass experiments"*, Nucl. Phys. Proc. Suppl. **143** (2005) 197; R. G. H. Robertson *et al.*, *"KATRIN: an experiment to determine the neutrino mass from the beta decay of tritium"*, arXiv:1307.5486.

[30] P. A. R. Ade *et al.* [Planck Collaboration], *"Planck 2015 results. XIII. Cosmological parameters"*, arXiv:1502.01589.

[31] R. Laureijs, J. Amiaux, S. Arduini, J.-L. Augueres, J. Brinchmann, R. Cole, M. Cropper and C. Dabin *et al.*, *"Euclid Definition Study Report"*, arXiv:1110.3193.

[32] L. Amendola *et al.* [Euclid Theory Working Group Collaboration], *"Cosmology and fundamental physics with the Euclid satellite"*, Living Rev. Rel. **16** (2013) 6 [arXiv:1206.1225].

[33] S. Pascoli and S.T. Petcov, *"The SNO Solar Neutrino Data, Neutrinoless Double-Beta and Neutrino Mass Spectrum"*, Phys. Lett. B **544** (2002) 239 [arXiv:hep-ph/0205022]; S. Pascoli and S. T. Petcov, *"Addendum: The SNO Solar Neutrino Data, Neutrinoless Double Beta-Decay and Neutrino Mass Spectrum"*, Phys. Lett. B **580** (2004) 280 [arXiv:hep-ph/0310003].

[34] S. Gariazzo, C. Giunti, M. Laveder, Y. F. Li and E. M. Zavanin, *"Light sterile neutrinos"*, J. Phys. G **43** (2016) 033001 [arXiv:1507.08204].

[35] A. Aguilar-Arevalo *et al.* [LSND Collaboration], *"Evidence for neutrino oscillations from the observation of $\overline{\nu}_e$ appearance in a $\overline{\nu}_\mu$ beam"*, Phys. Rev. D **64** (2001) 112007 [arXiv:hep-ex/0104049].

[36] A. A. Aguilar-Arevalo *et al.* [MiniBooNE Collaboration], *"Unexplained Excess of Electron-Like Events From a 1-GeV Neutrino Beam"*, Phys. Rev. Lett. **102** (2009) 101802 [arXiv:0812.2243].

[37] A. A. Aguilar-Arevalo *et al.* [MiniBooNE Collaboration], *"Event Excess in the MiniBooNE Search for $\bar{\nu}_\mu \to \bar{\nu}_e$ Oscillations"*, Phys. Rev. Lett. **105** (2010) 181801 [arXiv:1007.1150].

[38] C. Giunti and M. Laveder, *"Short-Baseline Active-Sterile Neutrino Oscillations?"*, Mod. Phys. Lett. A **22** (2007) 2499 [arXiv:hep-ph/0610352].

[39] C. Giunti and M. Laveder, *"Statistical Significance of the Gallium Anomaly"*, Phys. Rev. C **83** (2011) 065504 [arXiv:1006.3244].

[40] C. Giunti, M. Laveder, Y. F. Li, Q. Y. Liu and H. W. Long, *"Update of Short-Baseline Electron Neutrino and Antineutrino Disappearance"*, Phys. Rev. D **86** (2012) 113014 [arXiv:1210.5715].

[41] G. Mention, M. Fechner, T. Lasserre, T. A. Mueller, D. Lhuillier, M. Cribier and A. Letourneau, *"The Reactor Antineutrino Anomaly"*, Phys. Rev. D **83** (2011) 073006 [arXiv:1101.2755].

[42] B. Armbruster *et al.* [KARMEN Collaboration], *"Upper limits for neutrino oscillations $\overline{\nu}_\mu \to \overline{\nu}_e$ from muon decay at rest"*, Phys. Rev. D **65** (2002) 112001 [arXiv:hep-ex/0203021].

[43] P. Astier *et al.* [NOMAD Collaboration], *"Search for $\nu_\mu \to \nu_e$ oscillations in the NOMAD experiment"*, Phys. Lett. B **570** (2003) 19 [arXiv:hep-ex/0306037].

[44] M. Antonello *et al.* [ICARUS Collaboration], *"Experimental search for the "LSND anomaly" with the ICARUS detector in the CNGS neutrino beam"*, Eur. Phys. J. C **73** (2013) no.3, 2345 [arXiv:1209.0122].

[45] F. Dydak *et al.* [CDHSW Collaboration], *"A search for ν_μ oscillations in the Δm^2 range $0.3 - 90$ eV^2"*, Phys. Lett. B **134** (1984) 281.

[46] P. Adamson *et al.* [MINOS Collaboration], *"Active to sterile neutrino mixing limits from neutral-current interactions in MINOS"*, Phys. Rev. Lett. **107** (2011) 011802 [arXiv:1104.3922].

[47] R. Wendell *et al.* [Super-Kamiokande Collaboration], *"Atmospheric neutrino oscillation analysis with sub-leading effects in Super-Kamiokande I, II, and III"*, Phys. Rev. D **81** (2010) 092004 [arXiv:1002.3471].

[48] P. A. R. Ade *et al.* [Planck Collaboration], *"Planck 2013 results. XVI. Cosmological parameters"*, Astron. Astrophys. **571** (2014) A16 [arXiv:1303.5076].

[49] A. Mirizzi, G. Mangano, N. Saviano, E. Borriello, C. Giunti, G. Miele and O. Pisanti, *"The strongest bounds on active-sterile neutrino mixing after Planck data"*, Phys. Lett. B **726** (2013) 8 [arXiv:1303.5368].

[50] M. Wyman, D. H. Rudd, R. A. Vanderveld and W. Hu, *"Neutrinos Help Reconcile Planck Measurements with the Local Universe"*, Phys. Rev. Lett. **112** (2014) no.5, 051302 [arXiv:1307.7715].

[51] S. Gariazzo, C. Giunti and M. Laveder, *"Light Sterile Neutrinos in Cosmology and Short-Baseline Oscillation Experiments"*, JHEP **1311** (2013) 211 [arXiv:1309.3192].

[52] N. Saviano, A. Mirizzi, O. Pisanti, P. D. Serpico, G. Mangano and G. Miele, *"Multi-momentum and multi-flavour active-sterile neutrino oscillations in the early universe: role of neutrino asymmetries and effects on nucleosynthesis"*, Phys. Rev. D **87** (2013) 073006 [arXiv:1302.1200]; S. Hannestad, R. S. Hansen and T. Tram, *"Can active-sterile neutrino oscillations lead to chaotic behavior of the cosmological lepton asymmetry?"*, JCAP **1304** (2013) 032 [arXiv:1302.7279].

[53] J. Kopp, P. A. N. Machado, M. Maltoni and T. Schwetz, *"Sterile Neutrino Oscillations: The Global Picture"*, JHEP **1305** (2013) 050 [arXiv:1303.3011].

[54] C. Giunti, M. Laveder, Y. F. Li and H. W. Long, *"Pragmatic View of Short-Baseline Neutrino Oscillations"*, Phys. Rev. D **88** (2013) 073008 [arXiv:1308.5288].

[55] S. M. Bilenky, S. Pascoli and S. T. Petcov, *"Majorana neutrinos, neutrino mass spectrum, CP violation and neutrinoless double beta decay. 2. Mixing of four neutrinos"*, Phys. Rev. D **64** (2001) 113003 [arXiv:hep-ph/0104218].

[56] S. Goswami and W. Rodejohann, *"Constraining mass spectra with sterile neutrinos from neutrinoless double beta decay, tritium beta decay and cosmology"*, Phys. Rev. D **73** (2006) 113003 [arXiv:hep-ph/0512234].

[57] J. Barry, W. Rodejohann and H. Zhang, *"Light Sterile Neutrinos: Models and Phenomenology"*, JHEP **1107** (2011) 091 [arXiv:1105.3911]; W. Rodejohann, *"Neutrinoless double beta decay and neutrino physics"*, J. Phys. G **39** (2012) 124008 [arXiv:1206.2560].

[58] Y. F. Li and S. s. Liu, *"Vanishing effective mass of the neutrinoless double beta decay including light sterile neutrinos"*, Phys. Lett. B **706** (2012) 406 [arXiv:1110.5795].

[59] M. Ghosh, S. Goswami, S. Gupta and C. S. Kim, *"Implication of a vanishing element in the 3+1 scenario"*, Phys. Rev. D **88** (2013) no.3, 033009 [arXiv:1305.0180].

[60] A. Kusenko, F. Takahashi and T. T. Yanagida, *"Dark Matter from Split Seesaw"*, Phys. Lett. B **693** (2010) 144 [arXiv:1006.1731].

[61] A. Adulpravitchai and R. Takahashi, *"A4 Flavor Models in Split Seesaw Mechanism"*, JHEP **1109** (2011) 127 [arXiv:1107.3829].

[62] M. Shaposhnikov, *"A Possible symmetry of the νMSM"*, Nucl. Phys. B **763** (2007) 49 [arXiv:hep-ph/0605047].

[63] M. Lindner, A. Merle and V. Niro, *"Soft $L_e - L_\mu - L_\tau$ flavour symmetry breaking and sterile neutrino keV Dark Matter"*, JCAP **1101** (2011) 034 Erratum: [JCAP **1407** (2014) E01] [arXiv:1011.4950].

[64] C. D. Froggatt and H. B. Nielsen, *"Hierarchy of Quark Masses, Cabibbo Angles and CP Violation"*, Nucl. Phys. B **147** (1979) 277.

[65] J. Barry, W. Rodejohann and H. Zhang, *"Sterile Neutrinos for Warm Dark Matter and the Reactor Anomaly in Flavor Symmetry Models"*, JCAP **1201** (2012) 052 [arXiv:1110.6382]; A. Merle and V. Niro, *"Deriving Models for keV sterile Neutrino Dark Matter with the Froggatt-Nielsen mechanism"*, JCAP **1107** (2011) 023 [arXiv:1105.5136].

[66] H. Zhang, *"Light Sterile Neutrino in the Minimal Extended Seesaw"*, Phys. Lett. B **714** (2012) 262 [arXiv:1110.6838]; J. Heeck and H. Zhang, *"Exotic Charges, Multicomponent Dark Matter and Light Sterile Neutrinos"*, JHEP **1305** (2013) 164 [arXiv:1211.0538]; P. S. Bhupal Dev and A. Pilaftsis, *"Light and Superlight Sterile Neutrinos in the Minimal Radiative Inverse Seesaw Model"*, Phys. Rev. D **87** (2013) no.5, 053007 [arXiv:1212.3808].

[67] F. P. An *et al.* [Daya Bay Collaboration], *"Observation of electron-antineutrino disappearance at Daya Bay"*, Phys. Rev. Lett. **108** (2012) 171803 [arXiv:1203.1669].

[68] T. Ohlsson and H. Zhang, *"Non-Standard Interaction Effects at Reactor Neutrino Experiments"*, Phys. Lett. B **671** (2009) 99 [arXiv:0809.4835].

[69] R. Leitner, M. Malinsky, B. Roskovec and H. Zhang, *"Non-standard antineutrino interactions at Daya Bay"*, JHEP **1112** (2011) 001 [arXiv:1105.5580].

[70] R. Adhikari, S. Chakraborty, A. Dasgupta and S. Roy, *"Non-standard interaction in neutrino oscillations and recent Daya Bay, T2K experiments"*, Phys. Rev. D **86** (2012) 073010 [arXiv:1201.3047].

[71] A. N. Khan, D. W. McKay and F. Tahir, *"Sensitivity of medium-baseline reactor neutrino mass-hierarchy experiments to nonstandard interactions"*, Phys. Rev. D **88** (2013) 113006 [arXiv:1305.4350].

[72] I. Girardi and D. Meloni, *"Constraining new physics scenarios in neutrino oscillations from Daya Bay data"*, Phys. Rev. D **90** (2014) no.7, 073011 [arXiv:1403.5507].

[73] P. Bakhti and Y. Farzan, *"Shedding light on LMA-Dark solar neutrino solution by medium baseline reactor experiments: JUNO and RENO-50"*, JHEP **1407** (2014) 064 [arXiv:1403.0744].

[74] D. Marzocca, S. T. Petcov, A. Romanino and M. C. Sevilla, *"Nonzero $|U_{e3}|$ from Charged Lepton Corrections and the Atmospheric Neutrino Mixing Angle"*, JHEP **1305** (2013) 073 [arXiv:1302.0423].

[75] S. T. Petcov, *"Predicting the values of the leptonic CP violation phases in theories with discrete flavour symmetries"*, Nucl. Phys. B **892** (2015) 400 [arXiv:1405.6006].

[76] G. Altarelli and F. Feruglio, *"Discrete Flavor Symmetries and Models of Neutrino Mixing"*, Rev. Mod. Phys. **82** (2010) 2701 [arXiv:1002.0211].

[77] S. F. King *et al.*, *"Neutrino Mass and Mixing: from Theory to Experiment"*, New J. Phys. **16** (2014) 045018. [arXiv:1402.4271].

[78] S. F. King and C. Luhn, *"Neutrino Mass and Mixing with Discrete Symmetry"*, Rept. Prog. Phys. **76** (2013) 056201 [arXiv:1301.1340].

[79] A. Palazzo, *"Constraints on very light sterile neutrinos from θ_{13}-sensitive reactor experiments"*, JHEP **1310** (2013) 172 [arXiv:1308.5880].

[80] P. Bakhti and Y. Farzan, *"Constraining Super-light Sterile Neutrino Scenario by JUNO and RENO-50"*, JHEP **1310** (2013) 200 [arXiv:1308.2823].

[81] A. Esmaili, E. Kemp, O. L. G. Peres and Z. Tabrizi, *"Probing light sterile neutrinos in medium baseline reactor experiments"*, Phys. Rev. D **88** (2013) 073012 [arXiv:1308.6218].

[82] S. T. Petcov and W. Rodejohann, *"Flavor Symmetry $L_e - L_\mu - L_\tau$, Atmospheric Neutrino Mixing and CP Violation in the Lepton Sector"*, Phys. Rev. **D71** (2005) 073002 [arXiv:hep-ph/0409135].

[83] P. H. Frampton, S. T. Petcov and W. Rodejohann, *"On deviations from bimaximal neutrino mixing"*, Nucl. Phys. B **687** (2004) 31 [arXiv:hep-ph/0401206].

[84] C. Giunti and M. Tanimoto, *"Deviation of neutrino mixing from bimaximal"*, Phys. Rev. D **66** (2002) 053013 [arXiv:hep-ph/0207096]; C. Giunti and M. Tanimoto, *"CP violation in bilarge lepton mixing"*, Phys. Rev. D **66** (2002) 113006 [arXiv:hep-ph/0209169].

[85] A. Romanino, *"Charged lepton contributions to the solar neutrino mixing and θ_{13}"*, Phys. Rev. D **70** (2004) 013003 [arXiv:hep-ph/0402258].

[86] S. Antusch and S. F. King, *"Charged lepton corrections to neutrino mixing angles and CP phases revisited"*, Phys. Lett. B **631** (2005) 42 [arXiv:hep-ph/0508044].

[87] K. A. Hochmuth, S. T. Petcov and W. Rodejohann, *"$U_{\rm PMNS} = U_l^\dagger U_\nu$"*, Phys. Lett B **654** (2007) 177 [arXiv:0706.2975].

[88] D. Marzocca, S. T. Petcov, A. Romanino and M. Spinrath, *"Sizeable θ_{13} from the Charged Lepton Sector in SU(5), (Tri-)Bimaximal Neutrino Mixing and Dirac CP Violation"*, JHEP **1111** (2011) 009 [arXiv:1108.0614].

[89] G. Altarelli, F. Feruglio and I. Masina, *"Can neutrino mixings arise from the charged lepton sector?"*, Nucl. Phys. B **689** (2004) 157 [arXiv:hep-ph/0402155]; I. Masina, *"A maximal atmospheric mixing from a maximal CP violating phase"*, Phys. Lett. B **633** (2006) 134 [arXiv:hep-ph/0508031]; S. Dev, S. Gupta and R. R. Gautam, *"Parametrizing the Lepton Mixing Matrix in terms of Charged Lepton Corrections"*, Phys. Lett. B **704** (2011) 527 [arXiv:1107.1125]; S. Antusch and V. Maurer, *"Large neutrino mixing angle θ_{13}^{MNS} and quark-lepton mass ratios in unified flavour models"*, Phys. Rev. D **84** (2011) 117301 [arXiv:1107.3728]; C. Duarah, A. Das and N. N. Singh, *"Dependence of $\tan^2\theta_{12}$ on Dirac CP phase δ in tri-bimaximal neutrino mixing under charged lepton correction"*, [arXiv:1210.8265].

[90] A. Meroni, S. T. Petcov and M. Spinrath, *"A SUSY $SU(5) \times T'$ Unified Model of Flavour with large θ_{13}"*, Phys. Rev. D **86** (2012) 113003 [arXiv:1205.5241].

[91] W. Chao and Y.-j. Zheng, *"Relatively Large Theta13 from Modification to the Tri-bimaximal, Bimaximal and Democratic Neutrino Mixing Matrices"*, JHEP **1302** (2013) 044 [arXiv:1107.0738]; D. Meloni, *"Large θ_{13} from a model with broken $L_e - L_\mu - L_\tau$ symmetry"*, JHEP **1202** (2012) 090 [arXiv:1110.5210]; S. Antusch, C. Gross, V. Maurer and C. Sluka, *"$\theta_{13}^{\rm PMNS} = \theta_C/\sqrt{2}$ from GUTs"*, Nucl. Phys. B **866** (2013) 255 [arXiv:1205.1051]; G. Altarelli, F. Feruglio, L. Merlo and E. Stamou, *"Discrete Flavour Groups, θ_{13} and Lepton Flavour Violation"*, JHEP **1208** (2012) 021 [arXiv:1205.4670]; G. Altarelli, F. Feruglio and L. Merlo, *"Tri-Bimaximal Neutrino Mixing and Discrete Flavour Symmetries"*, Fortsch. Phys. **61** (2013) 507 [arXiv:1205.5133]; F. Bazzocchi and L. Merlo, *"Neutrino Mixings and the S4 Discrete Flavour Symmetry"*, Fortsch. Phys. **61** (2013) 571 [arXiv:1205.5135]; S. Gollu, K. N. Deepthi and R. Mohanta, *"Charged lepton correction to tribimaximal lepton mixing and its implications to neutrino phenomenology"*, [arXiv:1303.3393].

[92] C. H. Albright, A. Dueck and W. Rodejohann, *"Possible Alternatives to Tri-bimaximal Mixing"*, Eur. Phys. J. C **70** (2010) 1099 [arXiv:1004.2798].

[93] P. F. Harrison, D. H. Perkins and W. G. Scott, *"Tri-bimaximal mixing and the neutrino oscillation data"*, Phys. Lett. B **530** (2002) 167 [arXiv:hep-ph/0202074]; *"Symmetries and generalizations of tri-bimaximal neutrino mixing"*, Phys. Lett. B **535** (2002) 163 [arXiv:hep-ph/0203209]; Z. Z. Xing, *"Nearly tri-bimaximal neutrino mixing and CP violation"*, Phys. Lett. B **533** (2002) 85 [arXiv:hep-ph/0204049]; X. G. He and A. Zee, *"Some simple mixing and mass matrices for neutrinos"*, Phys. Lett. B **560** (2003) 87

[arXiv:hep-ph/0301092]; see also L. Wolfenstein, *"Oscillations Among Three Neutrino Types and CP Violation"*, Phys. Rev. D **18** (1978) 958.

[94] S. T. Petcov, *"On pseudo-Dirac neutrinos, neutrino oscillations and neutrinoless double β-decay"*, Phys. Lett. B **110** (1982) 245.

[95] F. Vissani, *"A Study of the scenario with nearly degenerate Majorana neutrinos"*, arXiv:hep-ph/9708483; V. D. Barger, S. Pakvasa, T. J. Weiler and K. Whisnant, *"Bimaximal mixing of three neutrinos"*, Phys. Lett. B **437** (1998) 107 [arXiv:hep-ph/9806387]; A. J. Baltz, A. S. Goldhaber and M. Goldhaber, *"The Solar neutrino puzzle: An Oscillation solution with maximal neutrino mixing"*, Phys. Rev. Lett. **81** (1998) 5730 [arXiv:hep-ph/9806540].

[96] H. Ishimori *et al.*, *"Non-Abelian Discrete Symmetries in Particle Physics"*, Prog. Theor. Phys. Suppl. **183** (2010) 1 [arXiv:1003.3552].

[97] P. H. Frampton and T. W. Kephart, *"Simple non-abelian finite flavor groups and fermion masses"*, Int. J. Mod. Phys. A **10** (1995) 4689 [arXiv:hep-ph/9409330]; F. Feruglio, C. Hagedorn, Y. Lin and L. Merlo, *"Tri-bimaximal Neutrino Mixing and Quark Masses from a Discrete Flavour Symmetry"*, Nucl. Phys. B **775** (2007) 120, Erratum-ibid. **836** (2010) 127 [arXiv:hep-ph/0702194]; G. J. Ding, *"Fermion Mass Hierarchies and Flavor Mixing from T' Symmetry"*, Phys. Rev. D **78** (2008) 036011 [arXiv:0803.2278]; P. H. Frampton, T. W. Kephart and S. Matsuzaki, *"Simplified Renormalizable T' Model for Tribimaximal Mixing and Cabibbo Angle"*, Phys. Rev. D **78** (2008) 073004 [arXiv:0807.4713]; D. A. Eby, P. H. Frampton and S. Matsuzaki, *"Predictions of Neutrino Mixing Angles in a T' Model"*, Phys. Lett. B **671** (2009) 386 [arXiv:0810.4899]; P. H. Frampton and S. Matsuzaki, *"T' Predictions of PMNS and CKM Angles"*, Phys. Lett. B **679** (2009) 347 [arXiv:0902.1140].

[98] I. Girardi, A. Meroni, S. T. Petcov and M. Spinrath, *"Generalised geometrical CP violation in a T' lepton flavour model"*, JHEP **1402** (2014) 050 [arXiv:1312.1966].

[99] M.-C. Chen and K. T. Mahanthappa, *"CKM and Tri-bimaximal MNS Matrices in a $SU(5) \times^{(d)} T$ Model"*, Phys. Lett. B **652** (2007) 34 [arXiv:0705.0714].

[100] M. C. Chen and K. T. Mahanthappa, *"Group Theoretical Origin of CP Violation"*, Phys. Lett. B **681** (2009) 444 [arXiv:0904.1721].

[101] M.-C. Chen, J. Huang, K. T. Mahanthappa and A. M. Wijangco, *"Large θ_{13} in a SUSY $SU(5) \times T'$ Model"*, JHEP **1310** (2013) 112 [arXiv:1307.7711].

[102] J. K. Ahn *et al.* [RENO Collaboration], *"Observation of Reactor Electron Antineutrino Disappearance in the RENO Experiment"*, Phys. Rev. Lett. **108** (2012) 191802 [arXiv:1204.0626].

[103] K. Abe *et al.* [T2K Collaboration], *"Indication of Electron Neutrino Appearance from an Accelerator-produced Off-axis Muon Neutrino Beam"*, Phys. Rev. Lett. **107** (2011) 041801 [arXiv:1106.2822].

[104] Y. Abe *et al.* [DOUBLE-CHOOZ Collaboration], *"Indication for the disappearance of reactor electron antineutrinos in the Double Chooz experiment"*, Phys. Rev. Lett. **108** (2012) 131801 [arXiv:1112.6353]; Y. Abe *et al.* [DOUBLE-CHOOZ Collaboration], *"Reactor electron antineutrino disappearance in the Double Chooz experiment"*, Phys. Rev. D **86** (2012) 052008 [arXiv:1207.6632].

[105] P. Adamson *et al.* [MINOS Collaboration], *"Improved search for muon-neutrino to electron-neutrino oscillations in MINOS"*, Phys. Rev. Lett. **107** (2011) 181802 [arXiv:1108.0015].

[106] P. Minkowski, *"$\mu \to e\gamma$ at a rate of one out of 1-billion muon decays?"*, Phys. Lett. B **67** (1977) 421; M. Gell-Mann, P. Ramond and R. Slansky in Sanibel Talk, CALT-68-709, Feb 1979, and in *Supergravity* (North Holland, Amsterdam 1979); T. Yanagida in *Proc. of the Workshop on Unified Theory and Baryon Number of the Universe*, KEK, Japan, 1979; S. L. Glashow, Cargese Lectures (1979); R. N. Mohapatra and G. Senjanovic, *"Neutrino Mass And Spontaneous Parity Nonconservation"*, Phys. Rev. Lett. **44** (1980) 912.

[107] J.-Q. Chen and P.-D. Fan, *"Algebraic expressions of the Clebsch-Gordon coefficients of the point group $T^{\dagger}$"*, J. Math. Phys. **39** (1998) 5519.

[108] G. C. Branco, J. M. Gerard and W. Grimus, *"Geometrical T Violation"*, Phys. Lett. B **136** (1984) 383.

[109] S. Antusch, S. F. King, C. Luhn and M. Spinrath, *"Right Unitarity Triangles and Tri-Bimaximal Mixing from Discrete Symmetries and Unification"*, Nucl. Phys. B **850** (2011) 477 [arXiv:1103.5930].

[110] S. Antusch, S. F. King and M. Spinrath, *"Spontaneous CP violation in $A_4 \times SU(5)$ with Constrained Sequential Dominance 2"*, Phys. Rev. D **87** (2013) 096018 [arXiv:1301.6764]; S. F. King, *"Minimal predictive see-saw model with normal neutrino mass hierarchy"*, JHEP **1307** (2013) 137 [arXiv:1304.6264]; S. F. King, *"Minimal see-saw model predicting best fit lepton mixing angles"*, Phys. Lett. B **724** (2013) 92 [arXiv:1305.4846]; S. Antusch, C. Gross, V. Maurer and C. Sluka, *"A flavour GUT model with $\theta_{13}^{PMNS} \simeq \theta_C/\sqrt{2}$"*, Nucl. Phys. B **877** (2013) 772 [arXiv:1305.6612]; S. Antusch, C. Gross, V. Maurer and C. Sluka, *"Inverse neutrino mass hierarchy in a flavour GUT model"*, Nucl. Phys. B **879** (2014) 19 [arXiv:1306.3984].

[111] S. Antusch and M. Spinrath, *"New GUT predictions for quark and lepton mass ratios confronted with phenomenology"*, Phys. Rev. D **79** (2009) 095004 [arXiv:0902.4644]; M. Spinrath, *"New Aspects of Flavour Model Building in Supersymmetric Grand Unification"*, arXiv:1009.2511; S. Antusch, S. F. King and M. Spinrath, *"GUT predictions*

for quark-lepton Yukawa coupling ratios with messenger masses from non-singlets", Phys. Rev. D **89** (2014) no.5, 055027 [arXiv:1311.0877].

[112] M. Holthausen, M. Lindner and M. A. Schmidt, *"CP and Discrete Flavour Symmetries"*, JHEP **1304** (2013) 122 [arXiv:1211.6953].

[113] F. Feruglio, C. Hagedorn and R. Ziegler, *"Lepton Mixing Parameters from Discrete and CP Symmetries"*, JHEP **1307** (2013) 027 [arXiv:1211.5560].

[114] A. Aranda, C. D. Carone and R. F. Lebed, *"Maximal neutrino mixing from a minimal flavor symmetry"*, Phys. Rev. D **62** (2000) 016009 [arXiv:hep-ph/0002044].

[115] G.J. Ding, S. F. King and A. J. Stuart, *"Generalised CP and A_4 Family Symmetry"*, JHEP **1312** (2013) 006 [arXiv:1307.4212].

[116] W. Grimus and P. O. Ludl, *"Finite flavour groups of fermions"*, J. Phys. A **45** (2012) 233001 [arXiv:1110.6376].

[117] A. Meroni, E. Molinaro and S. T. Petcov, *"Revisiting Leptogenesis in a SUSY $SU(5)\times T'$ Model of Flavour"*, Phys. Lett. B **710** (2012) 435 [arXiv:1203.4435].

[118] M. Agostini *et al.* [GERDA Collaboration], *"Results on Neutrinoless Double-β Decay of ^{76}Ge from Phase I of the GERDA Experiment"*, Phys. Rev. Lett. **111** (2013) no.12, 122503 [arXiv:1307.4720].

[119] I. Girardi, S. T. Petcov and A. V. Titov, *"Determining the Dirac CP Violation Phase in the Neutrino Mixing Matrix from Sum Rules"*, Nucl. Phys. B **894** (2015) 733 [arXiv:1410.8056].

[120] L. L. Everett and A. J. Stuart, *"Icosahedral (A(5)) Family Symmetry and the Golden Ratio Prediction for Solar Neutrino Mixing"*, Phys. Rev. D **79** (2009) 085005 [arXiv:0812.1057].

[121] Y. Kajiyama, M. Raidal and A. Strumia, *"The Golden ratio prediction for the solar neutrino mixing"*, Phys. Rev. D **76** (2007) 117301 [arXiv:0705.4559].

[122] W. Rodejohann, *"Unified Parametrization for Quark and Lepton Mixing Angles"* Phys. Lett. B **671** (2009) 267 [arXiv:0810.5239]; A. Adulpravitchai, A. Blum and W. Rodejohann, *"Golden Ratio Prediction for Solar Neutrino Mixing"*, New J. Phys. **11** (2009) 063026 [arXiv:0903.0531].

[123] J. E. Kim and M. S. Seo, *"Quark and lepton mixing angles with a dodeca-symmetry"*, JHEP **1102** (2011) 097 [arXiv:1005.4684].

[124] C. H. Albright and M. C. Chen, *"Model Predictions for Neutrino Oscillation Parameters"*, Phys. Rev. D **74** (2006) 113006 [arXiv:hep-ph/0608137].

[125] Y. Shimizu and M. Tanimoto, *"Predicting CP violation in Deviation from Tri-bimaximal mixing of Neutrinos"*, Mod. Phys. Lett. A **30** (2015) 1550002 [arXiv:1405.1521].

[126] L. J. Hall and G. G. Ross, *"Discrete Symmetries and Neutrino Mass Perturbations for θ_{13}"*, JHEP **1311** (2013) 091 [arXiv:1303.6962]; Z. Liu and Y. L. Wu, *"Leptonic CP Violation and Wolfenstein Parametrization for Lepton Mixing"*, Phys. Lett. B **733** (2014) 226 [arXiv:1403.2440]; S. K. Garg and S. Gupta, *"Corrections for tribimaximal, bimaximal and democratic neutrino mixing matrices"*, JHEP **1310** (2013) 128 [arXiv:1308.3054].

[127] J. Gehrlein, J. P. Oppermann, D. Schäfer and M. Spinrath, *"An SU(5) $\times$ A_5 Golden Ratio Flavour Model"*, Nucl. Phys. B **890** (2015) 539 [arXiv:1410.2057].

[128] S. F. King, T. Neder and A. J. Stuart, *"Lepton mixing predictions from $\Delta(6n^2)$ family Symmetry"*, Phys. Lett. B **726** (2013) 312 [arXiv:1305.3200].

[129] C. Hagedorn, A. Meroni and E. Molinaro, *"Lepton mixing from $\Delta(3n^2)$ and $\Delta(6n^2)$ and CP"*, Nucl. Phys. B **891** (2015) 499 [arXiv:1408.7118].

[130] C. Luhn, *"Trimaximal TM_1 neutrino mixing in S_4 with spontaneous CP violation"*, Nucl. Phys. B **875** (2013) 80 [arXiv:1306.2358].

[131] S. Antusch, J. Kersten, M. Lindner and M. Ratz, *"Running neutrino masses, mixings and CP phases: Analytical results and phenomenological consequences"*, Nucl. Phys. B **674** (2003) 401 [arXiv:hep-ph/0305273]; J. A. Casas, J. R. Espinosa, A. Ibarra and I. Navarro, *"General RG equations for physical neutrino parameters and their phenomenological implications"*, Nucl. Phys. B **573** (2000) 652 [arXiv:hep-ph/9910420]; P. H. Chankowski and Z. Pluciennik, *"Renormalization group equations for seesaw neutrino masses"*, Phys. Lett. B **316** (1993) 312 [arXiv:hep-ph/9306333]; K. S. Babu, C. N. Leung and J. T. Pantaleone, *"Renormalization of the neutrino mass operator"*, Phys. Lett. B **319** (1993) 191 [arXiv:hep-ph/9309223].

[132] S. T. Petcov, T. Shindou and Y. Takanishi, *"Majorana CP-violating phases, RG running of neutrino mixing parameters and charged lepton flavor violating decays"*, Nucl. Phys. B **738** (2006) 219 [arXiv:hep-ph/0508243].

[133] Y. Wang, *"JUNO: A Multi-Purpose LS-based Experiment"*, PoS Neutel **2013** (2013) 030.

[134] S. K. Agarwalla *et al.* [LAGUNA-LBNO Collaboration], *"The mass-hierarchy and CP-violation discovery reach of the LBNO long-baseline neutrino experiment"*, JHEP **1405** (2014) 094 [arXiv:1312.6520]; C. Adams *et al.* [LBNE Collaboration], *"The Long-Baseline Neutrino Experiment: Exploring Fundamental Symmetries of the Universe"*, arXiv:1307.7335; A. de Gouvea *et al.* [Intensity Frontier Neutrino Working Group Collaboration], *"Working Group Report: Neutrinos"*, arXiv:1310.4340.

[135] P. Coloma, H. Minakata and S. J. Parke, *"Interplay between Appearance and Disappearance Channels for Precision Measurements of θ_{23} and δ"*, Phys. Rev. D **90** (2014) 9, 093003 [arXiv:1406.2551].

[136] I. Girardi, D. Meloni and S. T. Petcov, *"The Daya Bay and T2K results on $\sin^2 2\theta_{13}$ and Non-Standard Neutrino Interactions"*, Nucl. Phys. B **886** (2014) 31 [arXiv:1405.0416].

[137] K. Abe *et al.* [T2K Collaboration], *"Observation of Electron Neutrino Appearance in a Muon Neutrino Beam"*, Phys. Rev. Lett. **112** (2014) 061802 [arXiv:1311.4750].

[138] F. P. An *et al.* [Daya Bay Collaboration], *"Spectral measurement of electron antineutrino oscillation amplitude and frequency at Daya Bay"*, Phys. Rev. Lett. **112** (2014) 061801 [arXiv:1310.6732].

[139] D. S. Ayres *et al.* [NOvA Collaboration], *"NOvA: Proposal to build a 30 kiloton off-axis detector to study $\nu_\mu \to \nu_e$ oscillations in the NuMI beamline"*, arXiv:hep-ex/0503053.

[140] M. Bass *et al.* [LBNE Collaboration], *"Baseline optimization for the measurement of CP violation and mass hierarchy in a long-baseline neutrino oscillation experiment"*, Phys. Rev. D **91** (2015) no.5, 052015 arXiv:1311.0212.

[141] L. Wolfenstein, *"Neutrino Oscillations in Matter,"* Phys. Rev. D **17** (1978) 2369; M. M. Guzzo, A. Masiero and S. T. Petcov, *"On the MSW effect with massless neutrinos and no mixing in the vacuum"*, Phys. Lett. B **260** (1991) 154; E. Roulet, *"MSW effect with flavor changing neutrino interactions"*, Phys. Rev. D **44** (1991) 935.

[142] Y. Grossman, *"Nonstandard neutrino interactions and neutrino oscillation experiments"*, Phys. Lett. B **359**, 141 (1995) [arXiv:hep-ph/9507344].

[143] J. Kopp, M. Lindner, T. Ota and J. Sato, *"Non-standard neutrino interactions in reactor and superbeam experiments"*, Phys. Rev. D **77**, (2008) 013007 [arXiv:0708.0152].

[144] T. Ohlsson, H. Zhang and S. Zhou, *"Nonstandard interaction effects on neutrino parameters at medium-baseline reactor antineutrino experiments"*, Phys. Lett. B **728** (2014) 148 [arXiv:1310.5917].

[145] T. Ohlsson, *"Status of non-standard neutrino interactions"*, Rept. Prog. Phys. **76** (2013) 044201 [arXiv:1209.2710].

[146] D. Meloni, T. Ohlsson, W. Winter and H. Zhang, *"Non-standard interactions versus non-unitary lepton flavor mixing at a neutrino factory"*, JHEP **1004** (2010) 041 [arXiv:0912.2735].

[147] C. Biggio, M Blennow and E. Fernandez-Martinez *"General bounds on non-standard neutrino interactions"*, JHEP **0908**, (2009) 090 [arXiv:0907.0097].

[148] P. Coloma, A. Donini, J. Lopez-Pavon and H. Minakata, *"Non-Standard Interactions at a Neutrino Factory: Correlations and CP violation"*, JHEP **1108**, 036 (2011) [arXiv:1105.5936].

[149] I. Girardi, A. Meroni and S. T. Petcov, *"Neutrinoless Double Beta Decay in the Presence of Light Sterile Neutrinos"*, JHEP **1311** (2013) 146 [arXiv:1308.5802].

[150] M. Archidiacono, N. Fornengo, C. Giunti and A. Melchiorri, *"Testing 3+1 and 3+2 neutrino mass models with cosmology and short baseline experiments"*, Phys. Rev. D **86** (2012) 065028 [arXiv:1207.6515].

[151] A. A. Aguilar-Arevalo *et al.* [MiniBooNE Collaboration], *"A Search for electron neutrino appearance at the $\Delta m^2 \sim 1eV^2$ scale"*, Phys. Rev. Lett. **98** (2007) 231801 [arXiv:0704.1500]; A. A. Aguilar-Arevalo *et al.* [MiniBooNE Collaboration], *"Improved Search for $\bar{\nu}_\mu \to \bar{\nu}_e$ Oscillations in the MiniBooNE Experiment"*, Phys. Rev. Lett. **110** (2013) 161801 [arXiv:1207.4809, arXiv:1303.2588].

[152] S. Pascoli and S. T. Petcov, *"Majorana Neutrinos, Neutrino Mass Spectrum and the $|\langle m \rangle| \sim 10^{-3}$ eV Frontier in Neutrinoless Double Beta Decay"*, Phys. Rev. D **77** (2008) 113003 [arXiv:0711.4993].

[153] I. Girardi, D. Meloni, T. Ohlsson, H. Zhang and S. Zhou, *"Constraining Sterile Neutrinos Using Reactor Neutrino Experiments"*, JHEP **1408** (2014) 057 [arXiv:1405.6540].

[154] F. P. An *et al.* [Daya Bay Collaboration], *"Improved Measurement of Electron Antineutrino Disappearance at Daya Bay"*, Chin. Phys. C **37** (2013) 011001 [arXiv:1210.6327].

[155] T. A. Mueller, D. Lhuillier, M. Fallot, A. Letourneau, S. Cormon, M. Fechner, L. Giot and T. Lasserre *et al.*, *"Improved Predictions of Reactor Antineutrino Spectra"*, Phys. Rev. C **83** (2011) 054615 [arXiv:1101.2663].

[156] P. Huber, *"On the determination of anti-neutrino spectra from nuclear reactors"*, Phys. Rev. C **84**, 024617 (2011) [Erratum-ibid. C **85**, 029901 (2012)] [arXiv:1106.0687].

[157] P. Vogel and J. F. Beacom, *"Angular distribution of neutron inverse beta decay, $\overline{\nu}_e + p \to e^+ + n$"*, Phys. Rev. D **60** (1999) 053003 [arXiv:hep-ph/9903554].

[158] P. Huber, M. Lindner, T. Schwetz and W. Winter, *"Reactor neutrino experiments compared to superbeams"*, Nucl. Phys. B **665** (2003) 487 [arXiv:hep-ph/0303232].

[159] P. Huber, J. Kopp, M. Lindner, M. Rolinec and W. Winter, *"New features in the simulation of neutrino oscillation experiments with GLoBES 3.0: General Long Baseline Experiment Simulator"*, Comput. Phys. Commun. **177** (2007) 432 [arXiv:hep-ph/0701187].

[160] P. Huber, M. Lindner and W. Winter, *"Simulation of long-baseline neutrino oscillation experiments with GLoBES (General Long Baseline Experiment Simulator)"*, Comput. Phys. Commun. **167** (2005) 195 [arXiv:hep-ph/0407333].

[161] G. L. Fogli, E. Lisi, A. Marrone, A. Palazzo and A. M. Rotunno, *"Evidence of $\theta_{13} > 0$ from global neutrino data analysis"*, Phys. Rev. D **84** (2011) 053007 [arXiv:1106.6028].

[162] Y. F. Li, J. Cao, Y. Wang and L. Zhan, *"Unambiguous Determination of the Neutrino Mass Hierarchy Using Reactor Neutrinos"*, Phys. Rev. D **88** (2013) 013008 [arXiv:1303.6733].

[163] P. C. de Holanda and A. Y. Smirnov, *"Homestake result, sterile neutrinos and low-energy solar neutrino experiments"*, Phys. Rev. D **69** (2004) 113002 [arXiv:hep-ph/0307266].

[164] P. C. de Holanda and A. Y. Smirnov, *"Solar neutrino spectrum, sterile neutrinos and additional radiation in the Universe"*, Phys. Rev. D **83** (2011) 113011 [arXiv:1012.5627].

[165] P. A. R. Ade *et al.* [BICEP2 Collaboration], *"Detection of B-Mode Polarization at Degree Angular Scales by BICEP2"*, Phys. Rev. Lett. **112** (2014) no.24, 241101 [arXiv:1403.3985].

[166] E. Giusarma, E. Di Valentino, M. Lattanzi, A. Melchiorri and O. Mena, *"Relic Neutrinos, thermal axions and cosmology in early 2014"*, Phys. Rev. D **90** (2014) no.4, 043507 [arXiv:1403.4852].

[167] S. Jetter, talk given at *"International Workshop on Neutrino Factories, Super Beams and Beta Beams (NuFact2013)"*.

[168] K. Abe *et al.* [T2K Collaboration], *"Measurement of Neutrino Oscillation Parameters from Muon Neutrino Disappearance with an Off-axis Beam"*, Phys. Rev. Lett. **111** (2013) 211803 [arXiv:1308.0465].

[169] K. Abe *et al.* [T2K Collaboration], *"Measurement of the Inclusive NuMu Charged Current Cross Section on Carbon in the Near Detector of the T2K Experiment"*, Phys. Rev. D **87** (2013) 092003 [arXiv:1302.4908].

[170] Private communication of T2K collaboration to the authors of the article: D. Meloni and M. Martini, *"Revisiting the T2K data using different models for the neutrino-nucleus cross sections"*, Phys. Lett. B **716** (2012) 186 [arXiv:1203.3335].

[171] P. Coloma, P. Huber, J. Kopp and W. Winter, *"Systematic uncertainties in long-baseline neutrino oscillations for large θ_{13}"*, Phys. Rev. D **87** (2013) 3, 033004 [arXiv:1209.5973].

[172] A. Di Iura, I. Girardi and D. Meloni, *"Probing new physics scenarios in accelerator and reactor neutrino experiments"*, J. Phys. G **42** (2015) 065003 [arXiv:1411.5330].

[173] I. Girardi, S. T. Petcov and A. V. Titov, *"Predictions for the Leptonic Dirac CP Violation Phase: a Systematic Phenomenological Analysis"*, Eur. Phys. J. C **75** (2015) 345 [arXiv:1504.00658].

[174] I. Girardi, S. T. Petcov and A. V. Titov, *"Predictions for the Dirac CP Violation Phase in the Neutrino Mixing Matrix"*, Int. J. Mod. Phys. A **30** (2015) 1530035 [arXiv:1504.02402].

[175] I. Girardi, S. T. Petcov, A. J. Stuart and A. V. Titov, *"Leptonic Dirac CP Violation Predictions from Residual Discrete Symmetries"*, Nucl. Phys. B **902** (2016) 1 [arXiv:1509.02502].

[176] I. Girardi, S. T. Petcov and A. V. Titov, *"Predictions for the Majorana CP Violation Phases in the Neutrino Mixing Matrix and Neutrinoless Double Beta Decay"*, arXiv:1605.04172.

[177] K. Abe *et al.* [T2K Collaboration], *"Measurements of neutrino oscillation in appearance and disappearance channels by the T2K experiment with* 6.6×10^{20} *protons on target"*, Phys. Rev. D **91** (2015) no.7, 072010 [arXiv:1502.01550].

[178] P. Adamson *et al.* [NOvA Collaboration], *"First measurement of electron neutrino appearance in NOνA"*, Phys. Rev. Lett. **116** (2016) no.15, 151806 [arXiv:1601.05022]; P. Adamson *et al.* [NOvA Collaboration], *"First measurement of muon-neutrino disappearance in NOνA"*, Phys. Rev. D **93** (2016) no.5, 051104 [arXiv:1601.05037].

[179] R. Acciarri *et al.* [DUNE Collaboration], *"Long-Baseline Neutrino Facility (LBNF) and Deep Underground Neutrino Experiment (DUNE) Volume 2: The Physics Program for DUNE at LBNF"*, arXiv:1512.06148.

[180] X. Guo *et al.* [Daya Bay Collaboration], *"A Precision measurement of the neutrino mixing angle* θ_{13} *using reactor antineutrinos at Daya-Bay"*, arXiv:hep-ex/0701029.

[181] S. T. Petcov and M. Piai, *"The LMA MSW solution of the solar neutrino problem, inverted neutrino mass hierarchy and reactor neutrino experiments"*, Phys. Lett. B **533** (2002) 94 [arXiv:hep-ph/0112074].

[182] F. An *et al.* [JUNO Collaboration], *"Neutrino Physics with JUNO"*, J. Phys. G **43** (2016) no.3, 030401 [arXiv:1507.05613]; Z. Djurcic *et al.* [JUNO Collaboration], *"JUNO Conceptual Design Report"*, arXiv:1508.07166.

[183] M. G. Aartsen *et al.* [IceCube PINGU Collaboration], *"Letter of Intent: The Precision IceCube Next Generation Upgrade (PINGU)"*, arXiv:1401.2046.

[184] U. F. Katz [KM3NeT Collaboration], *"The ORCA Option for KM3NeT"*, arXiv:1402.1022.

[185] S. Choubey, S. T. Petcov and M. Piai, *"Precision neutrino oscillation physics with an intermediate baseline reactor neutrino experiment"*, Phys. Rev. D **68** (2003) 113006 [arXiv:hep-ph/0306017].

[186] A. Bandyopadhyay, S. Choubey, S. Goswami and S. T. Petcov, *"High precision measurements of $\theta_\odot$ in solar and reactor neutrino experiments"*, Phys. Rev. D **72** (2005) 033013 [arXiv:hep-ph/0410283].

[187] A. Osipowicz *et al.* [KATRIN Collaboration], *"KATRIN: A Next generation tritium beta decay experiment with sub-eV sensitivity for the electron neutrino mass. Letter of intent"*, arXiv:hep-ex/0109033.